Synthetic Aperture Sequential Beamforming and other Beamforming Techniques in Ultrasound Imaging

Kortbek, Jacob; Jensen, Jørgen Arendt; Jørgensen, Michael Ø.; Gammelmark, Kim

Publication date:
2008

Document Version
Publisher's PDF, also known as Version of record

Synthetic Aperture Sequential Beamforming and other Beamforming Techniques in Ultrasound Imaging.

Jacob Kortbek

January, 2008

B-K Medical, Denmark &
Center for Fast Ultrasound Imaging, CFU
Technical University of Denmark

SUBMITTED IN PARTIAL FULFILLMENT OF THE
REQUIREMENTS FOR THE DEGREE OF
DOCTOR OF PHILOSOPHY
AT
THE TECHNICAL UNIVERSITY OF DENMARK
JANUARY 2008

_____
Signature of Author

Contents

Preface

These words are the first of many in this thesis, but they are also some of the last words written. One thousand days, more or less, have gone by since the beginning of this Industrial PhD Project at *B-K Medical* in Herlev, Denmark and *Center for Fast Ultrasound Imaging* (CFU) at *Ørsted•DTU, Technical University of Denmark*. Days have gone spending time on gaining more knowledge in various courses with topics within digital design techniques, acoustics, radar, business-theory, and ultrasound signal processing. Days have gone assisting students in laboratory sessions, correcting student reports, and supervising students in their M.Sc projects. Many days have gone by reading literature, articles, and patents within the fascinating field of ultrasound. Many days have gone by with many different and exciting subjects in the PhD project, which has been carried out under head supervision of Professor Jørgen Arendt Jensen from CFU, and assistant supervisors Michael Ø. Jørgensen, and Kim Løkke Gammelmark at B-K Medical. Characteristic for all subjects have been ultrasound beamforming and many variations and applications have been investigated. Promising results have shown and a patent application is in the pipeline.

Jacob Kortbek
December, 2007

Acknowledgement

I would like to dedicate this project to my loving father who sadly departed half way through my PhD. He was always a great support for me during my entire education.

I would also like to show my deepest gratitude to my loving wife and daughter who has supported me, and been able to bear with me in periods of physical and mental absence.

My head supervisor Professor Jørgen Arendt Jensen from *Center for Fast Ultrasound Imaging* (CFU) has contributed with an exceptional guidance and has been a tremendous source of knowledge and insight, and also the founder of the idea of synthetic aperture sequential beamforming.

I thank my assistant supervisors Michael Ø. Jørgensen, and Kim Løkke Gammelmark at *B-K Medical* for guidance and many good discussions.

I thank Henrik Andresen for a good cooperation, and Sarah Gustavsson and Svetoslav Nikolov for the initial version of BFT2.

Henrik Laursen has solved an immense number of IT-problems during my project, and Elna Sørensen has been a great help in many other different occasions.

Gert Seerup and Christian Duun-Christensen have been a great assistance doing measurements at B-K Medical.

Last but definitely not least i would like to thank all my colleagues at Ørsted•DTU and B-K Medical for being a big part of an exciting PhD project.

The PhD project was supported by grant 9700883, 9700563 and 26-04-0024 from the Danish Science Foundation and by B-K Medical, Denmark.

Abstract

This thesis consists of various subjects and applications within beamforming in general, and subjects within synthetic aperture focusing.

An insight into the software architecture and beamformer design principles of a software beamformation toolbox is given. Some of the many considerations in relation to beamformer development and implementation are shared.

In the delay-and-sum beamformer the sample index is not necessarily discrete. Some form of interpolation is needed and the influence on image quality has been investigated. The interpolation schemes investigated include linear, polynomial, and up-sampling and FIR filtering.

Directional beamforming for angle estimation of the velocity vector has been investigated using simulations and measurements. Using the measurements more than 96% valid estimates were produced for the flow angles $\theta = \{60^\circ, 75^\circ, 90^\circ\}$ and with a bias below 2° and a standard deviation below 5°.

The two synthetic aperture imaging techniques described in this thesis are both candidates for a realistic implementation in a commercial scanner. In one technique synthetic aperture focusing (SAF) is applied to 2-dimensional imaging with a single rotating mechanically focused concave element. Emission and reception are done while the transducer element continuously rotates and the received RF signals are stored. The geometrical focal point can be considered as a point source emitting a spherical wave in a limited angular region. For each image point in a high resolution image line (HRL) it must be determined which emissions that have a wave field that encompasses the image point. These emissions contribute to the HRL, and samples from each of them are selected according to the focusing delays, and added together. Due to the rotation, the synthesized aperture only experiences a moderate expansion. This is not sufficient to reduce the extent of the wide point spread function of a single emission. The advantage of SAF is the increase in SNR. For the setup with focal depth at 20 mm the SAF SNR gain is 11 dB.

The other synthetic aperture focusing technique is similar but has been revised toward linear array imaging. The technique is realized using two beamformers, and denoted Synthetic Aperture Sequential Beamforming (SASB). The VS is now created from an electronic focused subaperture in the first beamformer. Receive focusing is a simple fixed focusing with receive focal point in the transmit focal point, and the first beamformer could easily be analog and thereby save many ADC's. The focused RF-lines from the first beamformer are stored and transferred to the 2nd beamformer. Here it is exploited that a single image point is represented in multiple output lines from the first beamformer. There is an substantial improvement in lateral resolution using SASB compared to dynamic receive focusing (DRF). The improvement in FWHM

is at least a factor of 2 and the improvement at -40 dB is at least a factor of 3. At depths until 20 mm the FWHM is superior with DRF. With SASB the resolution is almost constant throughout the range. For DRF the FWHM increases almost linearly with range and the resolution at -40 dB is fluctuating with range.

SASB has been applied to data acquired with a commercial scanner and a tissue phantom with wire targets. The images confirm the results from the simulations. At the center of the image the resolution of SASB is superior to DRF and is practically range independent. The resolution in the near field is slightly better for DRF. A decrease in performance at the transducer edges occur for both DRF and SASB. They are more profound for SASB and especially at greater depths it is obvious that the lateral resolution is laterally dependent.

CHAPTER

ONE

Introduction

The image quality and diagnostic capabilities in general of medical ultrasound imaging rely to a great extent on the beamformer, which is the primary signal processing task of an ultrasound system. The evolution of ultrasound beamformers from analog into digital implementations have been described by Thomenius[1] and numerous variations exist and new and improved methods of beamforming continue to appear. The beamformer design is a consequence of the combination of desired application, image quality demands, array type, and the processing resources available for real-time implementation.

This thesis consists of three main chapters all related to beamforming. Chapter 2 contains various subjects and applications within beamforming in general. Chapter 3, and Chapter 4 is about synthetic aperture beamforming. One application investigated is synthetic aperture focusing applied to an imaging system with a rotating single element transducer. Another application and the main focus is a new technique, that enables an uncomplicated implementation of synthetic aperture focusing for array imaging.

1.1 Beamforming

The general purpose of beamforming in terms of beam properties is to construct a narrow beam with a large range of depth. Beamforming in its simplest form is all about controlling the phase of a group of signals exploiting that the sum of these signals can be either constructive or destructive. Beamforming is used for reconstruction of image points from the received transducer signals in both conventional and synthetic aperture imaging. The delay-and-sum beamformer (DASB) is the beamformer type applied in commercial scanners of today. Even though the principle of the DASB is simple the implementation can be complex.

The basics of delay and sum beamforming, and the strategy for calculating the time-of-flight is discussed in Section 2.1. An illustration of how to define and calculate the time-of-flight using the concept of virtual sources is shown in Fig. 1.1. An insight into the software architecture, and design principles of a software beamformation toolbox is also presented in Section 2.1.

In the delay-and-sum beamformer a sample is selected from each of the receive channels corresponding to the echo of the image point target. The sample index is based on the total transmit-receive time-of-flight. Due to the continuous nature of the time-of-flight, it will not necessarily lie at the discrete time indices of the sampled channel data. Some form of interpolation is needed and it has an influences on the image quality and the hardware complexity for implementation. This is the topic of Section 2.2.

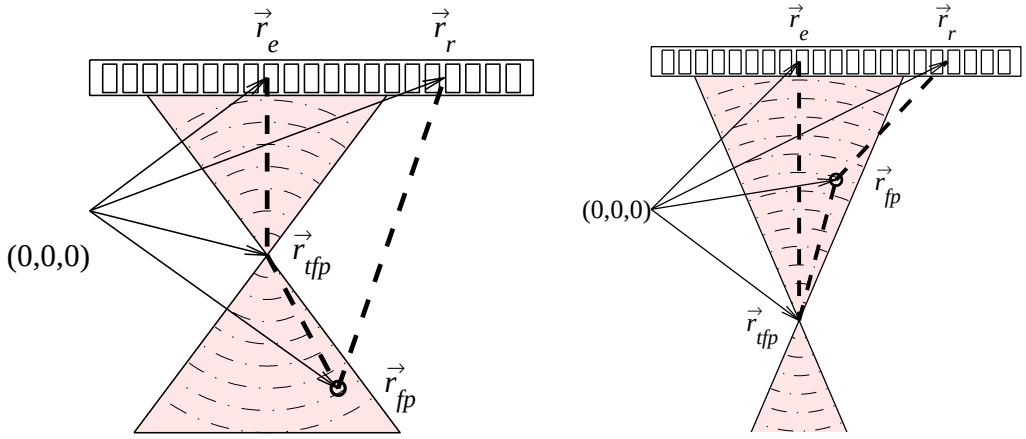

Figure 1.1: Wave propagation path (dotted line) for calculating the time-of-flight in receive focusing for a focused transmission. The transmit origin is perceived as the center element of the transmitting aperture. The TOF path is via the transmit focal point, which is perceived as a virtual source.

Modern ultrasound systems can estimate the blood velocity. The shift in phase as a function of time can be determined using an autocorrelation estimator[2]. Another approach is to determine the shift in position using the cross-correlation function[3, 4]. Both approaches only find the shift along the ultrasound beam direction. Velocities transverse to the beam are not detected, and velocities in different directions are not depicted correctly. There is, thus, a need for methods that can detect the correct velocity magnitude and direction as a function of spatial position. Directional beamforming is one approach. The concept of directional beamforming is described in Section 2.3. Lines in any arbitrary direction in 3-D space can be beamformed, as illustrated in Fig. 1.2. The signal from such a line is denoted a directional signal. When correlating directional signals from consecutive emissions a spatial shift will be present, from which the velocity can be estimated. Directional beamforming can also be used to estimate the angle of the velocity vector. The correlation between directional signals from different directions is found, and the direction of the highest correlation is assumed the direction of the velocity vector.

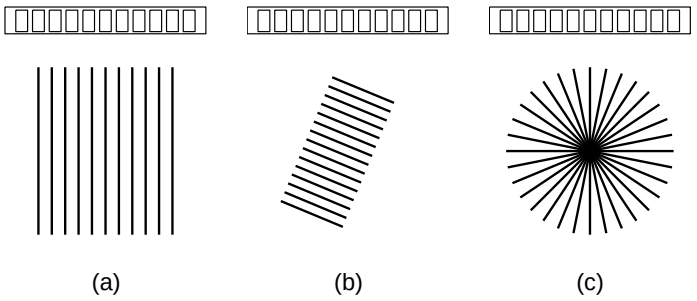

Figure 1.2: Receive points are located on straight lines. Different arrangements of lines are used for different applications. The examples shown illustrate B-mode imaging (a), directional beamforming for velocity estimation (b) and directional beamforming for velocity vector angle estimation (c).

1.2 Implementation of Synthetic Aperture Imaging

Synthetic aperture imaging is a technique, that sets high demands on processing capabilities, data transport, and storage and makes implementation of a full synthetic aperture imaging system very challenging and costly. The techniques and applications described in Chapter 3, and Chapter 4 are both examples of synthetic aperture imaging, but they are still candidates for a realistic implementation in a commercial scanner.

Chapter 3 applies the concept of virtual sources and synthetic aperture techniques to 2-dimensional imaging with a single rotating mechanically focused concave element. Such an imaging system can e.g. be found in an anorectal ultrasound transducer. With such a transducer emission and reception are done while the transducer element continuously rotates and the received RF signals are stored. It is proposed to apply mono-static synthetic aperture focusing (SAF) on these data with the objective of improving lateral resolution and signal-to-noise ratio (SNR).

The geometrical focal point can be considered as a point source emitting a spherical wave in a limited angular region. For each image point in a high resolution image line (HRL) it must be determined which emissions that have a wave field that encompasses the image point. These emissions contribute to the HRL, and samples from each of them are selected according to the focusing delays, and added together. This is illustrated in Fig. 1.3

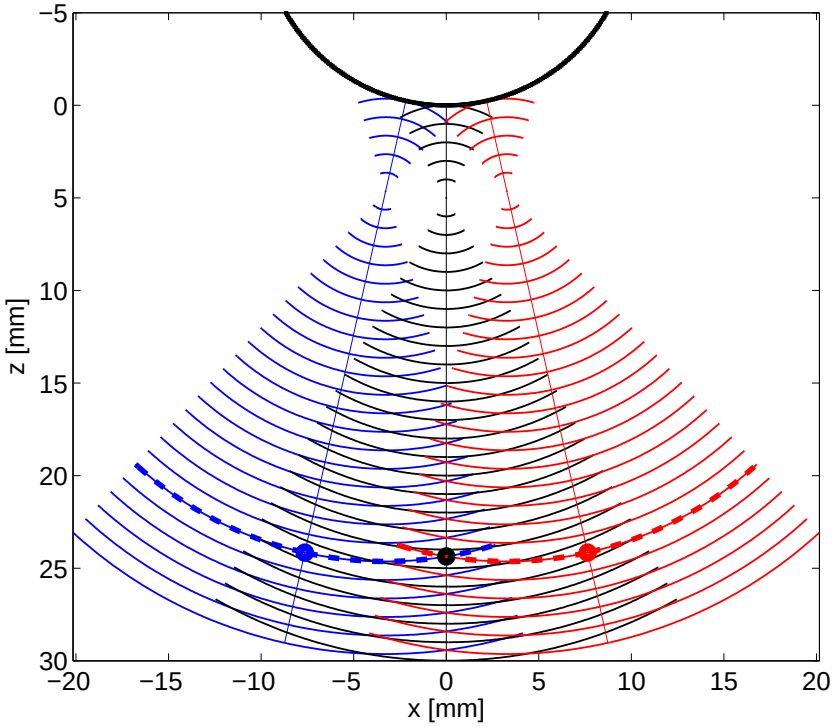

Figure 1.3: An illustration of propagating waves from 3 different emissions. A single sample of the image line from the center emission is indicated with a dot. Samples from the off-center image lines which share the same phase-information are also indicated. These samples are added in the beamformer.

The technique applied in Chapter 4 is similar to the one described in Chapter 3, but it is revised toward linear array imaging. The technique is realized using two beamformers, and denoted

Synthetic Aperture Sequential Beamforming (SASB). The VS is now created from an electronic focused sub-aperture in the first beamformer. Receive focusing is a simple fixed focusing with receive focal point in the transmit focal point. The focused RF-lines from the first beamformer are stored and transferred to the 2nd beamformer. Here it is exploited that a single image point is represented in multiple output lines from the first beamformer. The consequence of this type of focusing is a virtual aperture, which is as wide as the entire transducer. This results in an improvement in resolution compared to conventional dynamic receive focusing (DRF). This is visualized in the side-by-side comparison of simulated images in Fig. 1.4.

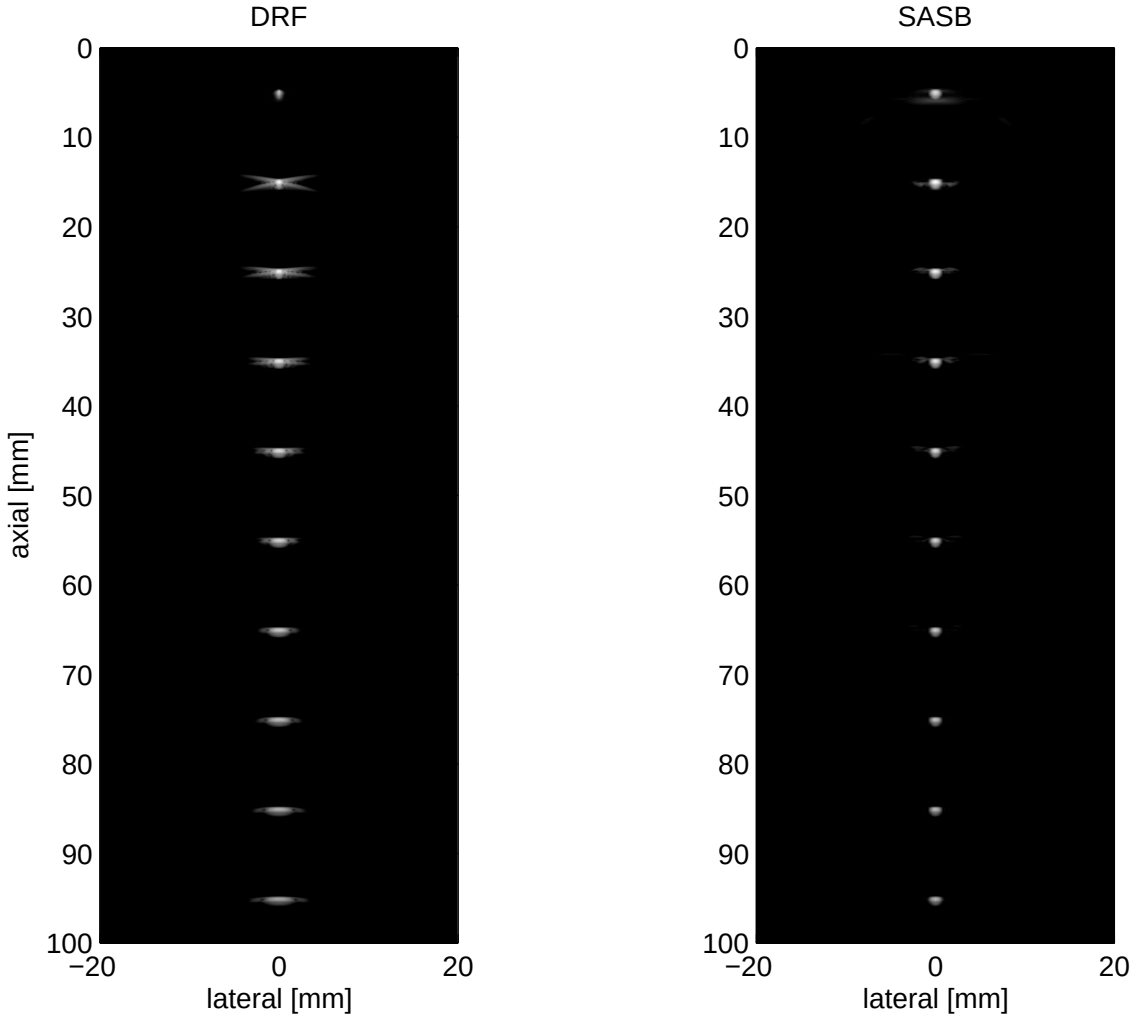

Figure 1.4: Envelope images using DRF (left) and SASB (right).

CHAPTER

TWO

Beamforming

This chapter discuss various topics within ultrasound beamforming. Beamforming is perhaps the most essential part of signal processing in ultrasound imaging. Delay and sum beamforming is in its nature a simple task but the defining parameters can take many forms. Beamforming represents a large processing task and the performance is highly dependent on the actual implementation. This includes among others the strategy for calculating the time-of-flight for the receive focusing, the interpolation scheme, and apodization calculations. This is discussed further in Section 2.1 which is an extraction from the paper in Appendix B.1. Here a software beamformation toolbox is described. The toolbox was initially developed by Sara Gustavsson[5] and Svetoslav Nikolov. It has then been revised and expanded for a more general use, and to comply to the demands of a synthetic aperture beamformer. This toolbox have been used extensively for all beamforming tasks in this thesis.

Interpolation between samples is a necessity in delay and sum beamforming. The influence of the type of interpolation has been investigated together with Henrik Andresen. This work is described in Section 2.2, which is an extraction from the paper in Appendix B.2.

Beamforming in medical ultrasound is commonly understood as image line beamforming. That is beamforming lines parallel to the propagation direction of the emitted ultrasound wave field. A completely different type of delay and sum beamforming is described in Section 2.3, which is extracted from the papers in Appendix B.3, and Appendix B.4. The co-authored papers in Appendix C.1 and Appendix C.2 is also on this subject. Directional beamforming was introduced by Jørgen Arendt Jensen and the application is vector velocity estimation. Lines in any arbitrary direction in 3-D space can be beamformed. The signal from such a line is denoted a directional signal and contains information of the scatterers positioned in the near proximity of the line. Consider a line aligned along the direction of a blood flow. When correlating directional signals from consecutive emissions a spatial shift will be present. The spatial shift is generated over a time period equal to the time between two consecutive emissions. The average velocity of the involved scatterers is estimated as the spatial shift divided by the time period. This process assumes the direction of the velocity vector is known. Directional beamforming can also be used to estimate the direction. Spatial signals are then constructed in a number of directions. For each direction the correlation between directional signals from consecutive emissions is registered, and the direction of the highest correlation is assumed the direction of the velocity vector. These techniques are described in details and results from simulations and flow rig measurements are presented.

Finally relevant literature within synthetic aperture beamforming is discussed. An introduction is given to the two applications described in Chapter 3, and Chapter 4 applying synthetic aperture focusing.

2.1 BFT2, a Beamformation Toolbox

2.1.1 Introduction

The image quality and diagnostic capabilities in general of medical ultrasound imaging rely to a great extent on the beamformer, which is the primary signal processing task of an ultrasound system. The delay-and-sum beamformer (DASB) is the dominant type of beamformer and comprises computation and application of channel delays and apodization in both transmit mode and receive mode. Even though the principle of the DASB is quite simple the implementation can be complex. The evolution of ultrasound beamformers from analog into digital implementations have been described by Thomenius[1] and numerous variations exist and new and improved methods of beamforming continue to appear. The beamformer design is a consequence of the combination of desired application, image quality demands, array type, and the processing resources available for real-time implementation. Concurrently with the development within real-time processing technology, new types of beamformers, which can utilize this increase in resources, become an obvious subject of investigations.

Several commercial and non-commercial toolboxes have been developed for different purposes within array signal processing[6, 7, 8]. Section 2.1 is extracted from the paper in Appendix B.1, and is about a software toolbox dedicated for off-line beamformation of ultrasound array signals, written in C++ and with a MATLAB (*The MathWorks, Inc.*) program interface. The name of the toolbox is *BFT2* and the initial version was developed by Sara Gustavsson[5] and Svetoslav Nikolov in 2002 and has been under continuous development ever since. It is motivated by the potential in improving the image quality of ultrasound imaging by investigating novel beamforming methods, and by offering colleagues an opportunity not to implement a beamformer from scratch and, thus accelerating the research. The maturity level of the toolbox at present time is such that it is applicable to most state of the art beamforming applications and it is reliable due to the feedback from the intensive use in several projects at *Center for Fast Ultrasound Imaging*(CFU).

The purpose of the beamformation toolbox (BFT) is to serve as an applicable entry into receive beamforming (or focusing) of real RF signals or complex base band signals acquired from any given application and acquisition sequence. It performs dynamic receive focusing in any arbitrary direction in 3D space and offers a range of choices between static or dynamic apodization and various interpolation schemes. Such a toolbox improves the reliability and can ensure a consistency in the way beamforming is implemented and the numerous details involved in this process. The RF data can be of different types and can originate from either a simulation program such as Field II[9], from experimental equipment or from *in-vivo* experiments. Among the many applications of the toolbox are 3D imaging using 2D arrays or elevation focused 1D arrays. Also directional velocity vector estimation[10, 11, 12] in vascular imaging is an obvious candidate. Synthetic aperture (SA) imaging[13, 14, 15] and the many variations such as synthetic transmit aperture (STA)[16], synthetic receive aperture (SRA)[17, 18, 19] and hybrid combinations hereof are perhaps the most demanding beamforming tasks in medical ultrasound and can easily be explored.

Section 2.1 gives an insight into the software architecture of the toolbox and beamformer design principles and shares some of the many considerations in relation to beamformer development and implementation. Initially beamformer basics is described and the strategy for calculating the time-of-flight and the apodization for different applications is discussed. Some of the solutions for the implementation of the processing are briefly described. The discussion of the

software design and how the user can interact with the toolbox and control its parameters can be found in the paper in Appendix B.1. Finally an example of use is presented.

2.1.2 Beamforming Strategy

The general purpose of beamforming in terms of beam properties is to construct a narrow beam with a large range of depth. Beamforming in its simplest form is all about controlling the phase of a group of signals exploiting that the sum of these signals can be either constructive or destructive. In medical ultrasound beamforming is carried out during both transmit and receive and the type of beamforming varies first of all with the geometry of the applied transducer and the focal points. The main transducer categories are linear array, focused array, and phased array beside the 2D arrays, but can in principle be any kind of arbitrary array.

In transmit beamforming appropriate delays and possibly apodization are applied to the individual transducer elements to obtain a single focal point at which the emitted waves sum up constructively. Receive beamforming is similar since appropriate delays are applied to the signals received from the individual transducer elements and then a weighted sum is performed. The main difference is that in transmit only a single focal point can be created at each emission, since the delays are applied before the emission and the waves are summed physically in the focal point. In receive multiple focal points can be obtained, by applying a new set of delay values to the received signals for each focal point.

The BFT does off-line processing of the received signals and, thus, performs receive focusing. One of the challenges in receive focusing is the strategy for calculating the time-of-flight (TOF). TOF is the propagation time of the emitted wave in its path from the transmit origin, $\vec{r}_e$ to the point of receive focus (FP), $\vec{r}_{fp}$ and return to one of the elements of the receive aperture, $\vec{r}_r$ as illustrated in Fig. 2.1.

$$t_{tof} = \frac{|\vec{r}_{fp} - \vec{r}_e| + |\vec{r}_r - \vec{r}_{fp}|}{c} \,. \tag{2.1}$$

Calculating proper receive delays and, thus, the TOF requires that the characteristics of the transmit beamforming are known. The TOF can be split into the transmit time t_{tof_t} and the receive time t_{tof_r}. $t_{tof} = t_{tof_t} + t_{tof_r}$. Assuming the speed of sound, c is known the receive time is uniquely determined from the receive path which is simply the path from the FP to receive aperture elements. The transmit path though is not well defined because the emitted pressure wave does not necessarily emanate from a point source as illustrated in Fig. 2.1 but is a consequence of numerous waves emitted from different elements at different times. The transmit time must be approximated accordingly.

Fig. 2.2 and Fig. 2.3 are illustrations of different situations where the strategy for calculating the TOF are not the same. In Fig. 2.2 a focused transmission with a transmit focal point (TFP) located at $\vec{r}_{tfp}$ is applied and the FP is located off-axis. The transmit origin, $\vec{r}_e$ is defined as the center element of the transmit sub-aperture. In compliance with the concept of virtual sources[20, 21, 22, 23, 24], the transmit focal point can be considered as a point source emitting a spherical wave. By using this concept the transmit part t_{tof_t} of the TOF can be calculated unambiguously and the TOF becomes

$$t_{tof} = \frac{|\vec{r}_{tfp} - \vec{r}_e| \pm |\vec{r}_{fp} - \vec{r}_{tfp}| + |\vec{r}_r - \vec{r}_{fp}|}{c} \tag{2.2}$$

The $\pm$ in (2.2) refer to whether the FP is above or below the TFP. In Fig. 2.3 an unfocused plane wave is emitted and the transmit time t_{tof_t} in this case is simply proportional to the axial

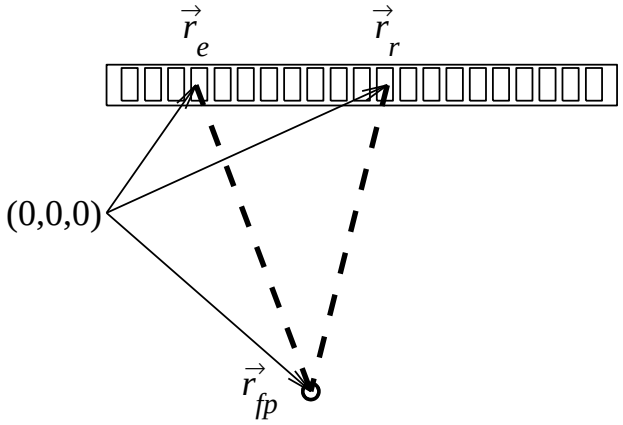

Figure 2.1: Wave propagation path (dotted line) for calculating the time-of-flight in receive focusing. The transmit origin, $\vec{r}_e$ and the receive point, $\vec{r}_r$ are illustrated as different elements of an array.

distance, $|z_{fp} - z_e|$ between the aperture and the FP and the TOF is then

$$t_{tof} = \frac{|z_{fp} - z_e| + |\vec{r}_r - \vec{r}_{fp}|}{c} \ . \tag{2.3}$$

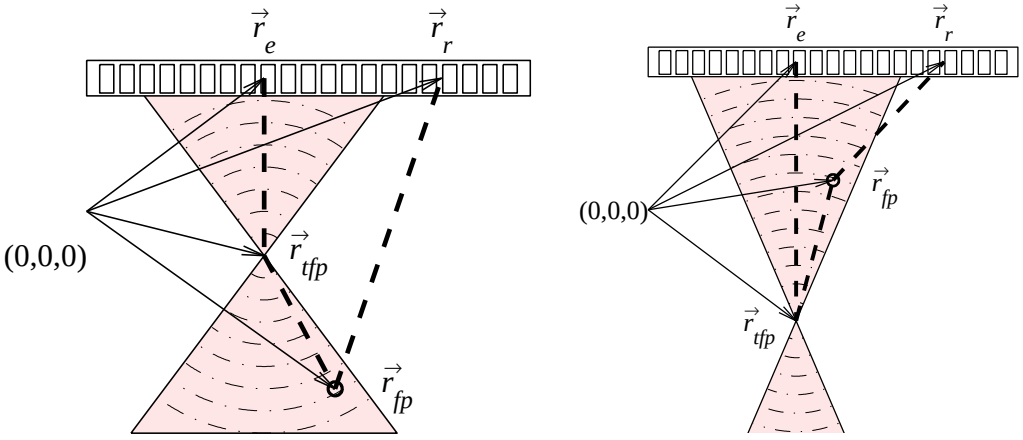

Figure 2.2: Wave propagation path (dotted line) for calculating the time-of-flight in receive focusing for a focused transmission. The transmit origin is perceived as the center element of the transmitting aperture. The TOF path is via the transmit focal point.

In DASB the strategy for beamforming a single point is to select one sample from each receive channel of the acquired data and then sum up a weighted set of these samples. By beamforming a group of points a scan line can be created. Different arrangements of scan lines are used for different applications. Examples of applications are illustrated in Fig. 2.4.

In general a beamformed image point, $I(\vec{r})$ at position, $\vec{r}_{fp}$ can be expressed as

$$I(\vec{r}_{fp}) = \sum_{e=1}^{N_e} \mathcal{A}_e(\vec{r}_{fp}) \sum_{r=1}^{N_r} \mathcal{A}_r(\vec{r}_{fp}) s_{e,r}(t_{tof}(\vec{r}_e, \vec{r}_{tfp}, \vec{r}_{fp}, \vec{r}_r)) \ , \tag{2.4}$$

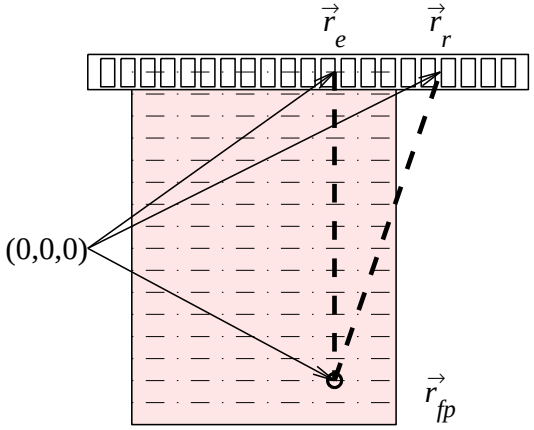

Figure 2.3: Wave propagation path (dotted line) for calculating the time-of-flight in receive focusing for a plane wave transmission. The transmit origin and the receive point are illustrated as different elements of an array. The transmit origin is assumed at the same lateral position as the receive point.

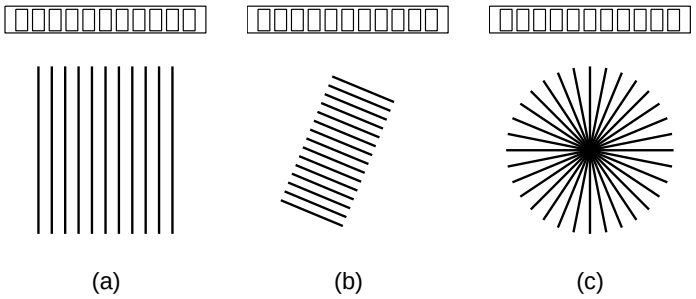

Figure 2.4: Receive points are located on straight lines. Different arrangements of lines are used for different applications. The examples shown illustrate B-mode imaging (a), directional beamforming for velocity estimation[10] (b) and directional beamforming for velocity vector angle estimation[11, 12] (c).

where N_r is the number of receiving elements, $\mathcal{A}$ is the dynamic apodization function in transmit and receive and $s_{e,r}(t)$ is the time-domain received echo signal at receiving element r after the e'th emission. N_e is the number of emissions used to construct the image point, where the origin of each emission is spatially different from the other as is the case in STA. E.g for a conventional B-mode image point, $N_e = 1$.

As already stated the samples to select are determined by the TOF. Due to the continuous nature of the TOF the sample index will not necessarily coincide with the discrete time indices of the sampled channel data. A nearest neighbor approach or some form of inter-sample interpolation is needed. This has a influences on the image quality and the hardware complexity for implementation. This is discussed further in Section 2.2.

With an aperture of finite size edge waves will affect the beam pattern by increasing the side lobes. Apodization is often applied in both transmit and receive to suppress the side lobes with a trade-off in lateral resolution, since the aperture width is inversely proportional to the main lobe width of the beam pattern. Receive apodization can take the form of a fixed tapering

of channel signals, a step-wise depth dependent function or a fully dynamic function. The latter offers an opportunity to introduce an expanding and contracting aperture and maintain a constant preferred F-number and uniform beam pattern[25] until the entire aperture is applied.

Toolbox Software Design.

The software design of the toolbox is described in more detail in the paper in Appendix B.1. The toolbox is written in C++ and since it has a MATLAB (MathWorks Inc.) user interface MATLAB MEX-files are used to link between the C++ source code and the MATLAB environment. MEX-files are dynamically linked routines, which can be invoked from MATLAB just as a general built-in function[26, 27]. The toolbox is designed for parallelization on a multi-processor cluster but can just as well run on a single processor system with a Windows or a Linux operating system. This part of the design is called *Parlib*[28].

One of the processing tasks of the toolbox is the apodization calculation. The apodization can be defined in two distinct ways. One option is completely flexible in the sense that arbitrary apodization values can be defined for an arbitrary number of depth intervals. With this option a simple and fixed tapering can be applied for FP's at all depth or extraordinary apodization functions e.g. the functions investigated by Jensen and Munk for vector velocity estimation[29] can easily be implemented.

A dynamic apodization function with an expanding aperture can also be implemented with this option. This is done by supplying a table of the desired apodization values and manually calculating the depth intervals in which the different apodization values should be applied. This can be slightly cumbersome and for the purpose of creating a dynamic apodization function with a preferred F-number another option exist. Here a pre-defined analytical window function e.g. a Hamming or a Tukey is given as a text string along with a desired F-number. The toolbox then calculates the width of the active sub-aperture and the apodization values. If the width of the active sub-aperture exceeds the aperture width already defined elsewhere in the toolbox, then only the central part of the calculated values are applied as illustrated in Fig. 2.5. For a given FP the analytical calculation of the apodization value for aperture element, i, if e.g. a Hanning window is applied, is

$$\mathcal{A}(\gamma) = \begin{cases} 0.5(1-\cos(\pi\gamma+\pi)) & \text{for} \quad \gamma \leq 1 \\ 0 & \text{for} \quad \gamma > 1 \end{cases} \tag{2.5}$$

where γ is a normalized index which depends on the distance, D between the FP and a reference point on the aperture, the desired F-number, F and on the position of the element, $\vec{r}_i$ for which the apodization value is calculated relative to the center position of the aperture, $\vec{r}_c$

$$\gamma(r_i) = |(\vec{r}_i - \vec{r}_c)|2F/D \; . \tag{2.6}$$

The BFT is primarily designed to beamform FP's located on straight lines in any arbitrary direction as illustrated in Fig. 2.4. Equidistant points on a line can be characterized by an origin, $\vec{r}_0$, a direction, $\boldsymbol{\zeta}$, a length, L and the distance between consecutive points, Δr as illustrated in Fig. 2.6. The coordinate of the i'th point, $\vec{r}_i = (x,y,z)$ on the line is

$$\vec{r}_i = \vec{r}_0 + i\Delta r\boldsymbol{\zeta} \; . \tag{2.7}$$

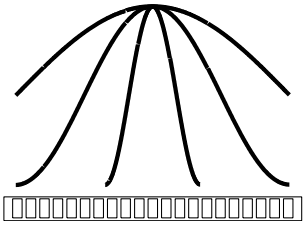

Figure 2.5: Dynamic apodization with expanding aperture.

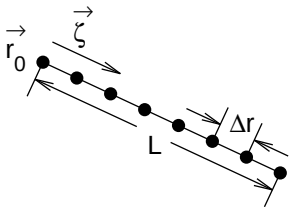

Figure 2.6: Line of equidistant receive focus points.

The method for calculating the TOF consists of nested loops going through lines, FP's, and finally transducer elements. This facilitates that the TOF can be calculated for all permutations of FP's, transmit aperture elements, and receive aperture elements. The TOF calculation in (2.1) and (2.2) involves a square root operation which is a computational heavy task to implement i hardware[30]. An alternative to calculating the TOF for each individual FP has been studied by Nikolov et al[31, 32].

2.1.3 Example of use

An example of use is presented next. As stressed previously in Section 2.1.2 the strategy for calculating the TOF is of great significance in respect to phase coherent summation of channel data. An example of a Field II[9] simulation is given in Fig. 2.7. Here a single point target (PT) located at $\vec{r}_{pt} = (5, 0, 12)$ mm has been beamformed according to (2.3) and (2.2) respectively. The beamformed FP's are located on the axial line intersecting the PT. The simulated application is a focused transmission using a linear array aperture of 128 elements, a 2-cycle sinusoid excitation and a transmit focal point at $\vec{r}_{tfp} = (0, 0, 5)$ mm. The beamformed pre-sum data are shown for all the receiving channels (columns). It appears that the beamformed channels are more coherent in phase around the PT when beamformed according to (2.2). This is in agreement with the strategy that the receive beamforming must comply with the transmit beamforming.

The BFT has been used in several occasions and for many different applications. Some examples of use are SA B-mode imaging[33],SA flow[34, 35], directional beamforming for velocity estimation[10], directional beamforming for velocity vector angle estimation[11, 12], plane wave color flow imaging[36], and coded SA[37, 38].

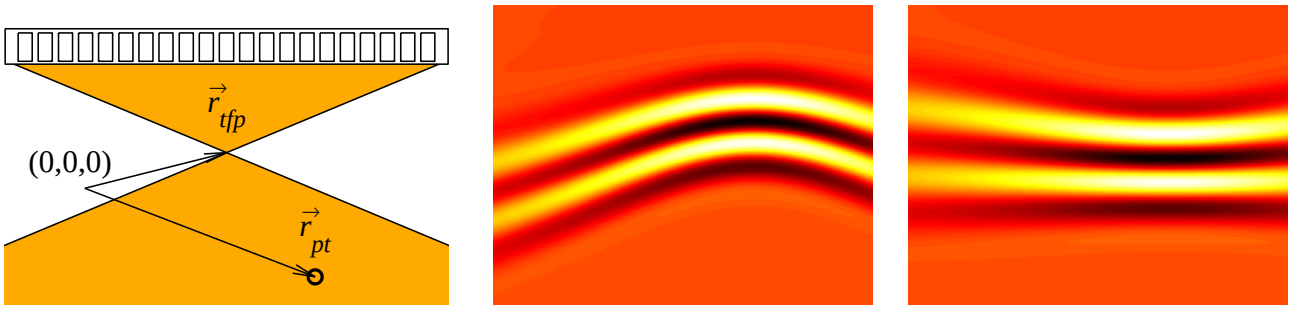

Figure 2.7: The response from a point target is simulated in Field II[9] with a focused transmission. The data are beamformed with two different strategies for calculating the TOF, (2.3) (left) and (2.2) (right). The beamformed data is shown for all the receiving channels (columns).

2.1.4 Conclusion

A software toolbox for off-line dynamic receive focusing of scan lines in any arbitrary direction in 3D space has been developed. It offers a choice between different methods for calculating time-delays, various inter-sample interpolation schemes, and apodization can be any preferred window function of fixed size or it can be fully dynamic with an expanding and contracting aperture to obtain a preferred F-number. Some of the beamformer design principles and some of the many considerations in relation to beamformer development and implementation are shared.

2.2 Interpolation

2.2.1 Introduction

In medical ultrasound receive focusing is a core signal processing element used for reconstruction of image points from the received transducer signals in both conventional and synthetic aperture imaging. In the delay-and-sum beamformer a sample is selected from each of the receive channels corresponding to the echo of the image point target. The sample index is based on the total transmit-receive time-of-flight. Due to the continuous nature of the time-of-flight, it will not necessarily lie at the discrete time indices of the sampled channel data. Thus, some form of interpolation is needed and this heavily influences the image quality and the hardware complexity for implementation. By using a proper interpolation scheme it is possible to reduce the sampling frequency or to improve performance.

Section 2.2 is extracted from the paper in Appendix B.2. The investigation is based on the work of Henrik Andresen [39] and quantifies the change in performance as a function of interpolation type applied by means of ultrasound simulations of point scatterers in Field II [9]. The beamformation toolbox, BFT2 which was described in Section 2.1 is used in the investigation. It performs dynamic receive focusing and offers choices between static or dynamic apodization and various interpolation schemes. The interpolation schemes investigated include linear, polynomial, and up-sampling and FIR filtering. Various order polynomials and FIR filters are investigated.

2.2.2 Description

The investigation on the influence of the choice of interpolation scheme includes conventional B-mode imaging and synthetic aperture imaging (SAI). The ultrasound RF signals for the investigation is created using Field II and the beamforming is performed with BFT2. From a reference data set an evaluation data set is created, which is used for the evaluation. For the evaluation the point-spread function, PSF is useful when observing the characteristics of different imaging modalities. It is highly affected by the type of transmit-receive focusing used, and is, thus, also affected by the interpolation in receive beamforming. The lateral part of the PSF is especially interesting in terms of spatial distribution and amplitude of the side-lobe energy, which again directly affects the image contrast. The evaluation and comparison of interpolation schemes is done by partly observing the lateral PSF and quantizing the main-lobe and side-lobe energy distribution in terms of the full-width-half-maximum, FWHM and the side-lobe-main-lobe-ratio, SLMLR and partly by the noise power of the interpolation error. The FWHM and the SLMLR are calculated in the horizontal plane at the depth of each of the point scatterers and compared to the case where the reference data is used.

Simulation setup

The ultrasound RF signals for the investigation is created using Field II with a 192-element, 7 MHz linear array transducer with λ pitch as Simulation Model and a 3-cycle sinusoid as excitation. The simulation is based on point scatterers placed at a depth of 10 mm to 80 mm with 5 mm between each, placed along the center of the transducer. A reference RF data set has been created using a sampling frequency of 1 GHz and linear interpolation and the evaluation RF data set is created by decimating the reference data (picking out samples) to a sampling frequency of 40 MHz. Two data sets are created. One by using conventional B-mode imaging, and one by using SAI. The conventional B-mode imaging with a sliding aperture of 64 elements applies dynamic receive focus and dynamic Hanning apodization with an F-number of two. In transmit an F-number of two is applied which gives a single transmit focus at 26.6 mm close to the geometrical focal point of the transducer at 25 mm. In SAI each element will transmit a pulse in sequence, and all elements are used in receive and a Hanning apodization is applied over the entire aperture. The points selected for beamforming are along the center of the active aperture, creating a total of 129 lines for both imaging modalities, where the points along each line will be spaced 0.1 mm apart.

Linear, polynomial and upsampling and filtering are the interpolation schemes applied. The polynomial interpolation estimates the value between samples by fitting a polynomial of order M to the M+1 nearest points, and the algorithm for implementation in BFT2 is taken from [40]. Polynomials of order two to five are examined. Instead of fitting a function type to the measured data, simply upsampling and low-pass filtering the data is another option [41]. The upsampling is set to a factor of eight and the low-pass filtering will be performed by an equiripple FIR-filter designed with Matlab's *Filter Design and Analysis Tool* with a pass band between 0 and $\frac{1}{16}$ relative to the upsampled Nyquist rate. The stop band is defined from $\frac{3}{16}$ to 1. The design parameters of the filters used can be seen in Table 2.1.

Filter setup	Pass band ripple, dB	Stop band amplitude, dB	Filter order
1	±0.1	-30	30
2	±0.1	-40	34
3	±0.1	-50	38
4	±0.1	-70	48

Table 2.1: Filter design parameters

2.2.3 Simulation Results

The observation of main-lobe and side-lobe levels is part of the evaluation. The investigation shows that the main-lobe is practically the same for the reference data and the decimated data, hence the full width at half maximum (FWHM) does not vary significantly with the interpolation schemes. The FWHM is the lateral distance between the two points on the lateral PSF where the amplitude is -6 dB relative to the maximum of the PSF. However the side-lobe level does vary with the interpolation type and the SLMLR of the different interpolation schemes at the depth of each of the point scatterers is calculated and quantized into the difference between the mean SLMLR over all depths of the interpolated data and the reference data, $\Delta SLMLR$

$$\Delta SLMLR = \frac{1}{D}\sum_{i=1}^{D}\frac{E_{i_{SL}}}{E_{i_{ML}}} - \frac{1}{D}\sum_{i=1}^{D}\frac{E^{ref}_{i_{SL}}}{E^{ref}_{i_{ML}}}. \tag{2.8}$$

D is the number of depths and E_i denotes the energy of the lateral part of the PSF at depth index i. The side-lobes are not necessarily distinct peaks in the lateral PSF. Side-lobes are here defined as whenever the lateral distance from the point scatterer is larger than 5 mm. Another quantitative measure is the signal-to-noise ratio, SNR which is a measure of how much the interpolated signal differ from the reference signal, $SNR = 10\log(\frac{\mu^2}{(\widehat{\mu}-\mu)^2})$, where μ is the reference signal and $\widehat{\mu}$ is the interpolated signal.

All results are found in the paper in Appendix B.2.

2.2.4 Conclusion

The main-lobe of the lateral point-spread function is practically the same, when using the reference data and the linear interpolated data. Hence, the FWHM in this investigation is not affected by the type of interpolation. When using conventional B-mode imaging and linear interpolation, the difference in mean SLMLR is 6.2 dB. With polynomial interpolation the difference is in the range 6.2 dB to 0.3 dB using 2nd to 5th order polynomials, and with FIR interpolation the difference is reduced from 5.8 dB to 0.1 dB depending on the filter design. The SNR is between 21 dB and 45 dB with the polynomial interpolation and between 37 dB and 43 dB with FIR filtering. The order of the FIR-filters can be decreased by reducing the demands on the pass band. The result of this is a decrease in the SNR, but the SLMLR is practically unchanged compared to the higher order filters. Thus, in B-mode imaging, the decimated data in combination with 4th order polynomial interpolation or a FIR filter of order 28 will yield a performance very near to the performance of using the reference data.

In the synthetic aperture imaging modality the influence of the type of interpolation applied is even higher. Here the difference in mean SLMLR ranges from 14 dB to 33 dB and 6 dB to

31 dB for the polynomial and FIR filtering schemes respectively. The SNR is similar to the case of conventional B-mode imaging. By using a proper interpolation scheme it is possible to reduce the sampling frequency and avoid a decrease in performance. When replacing linear interpolation with a more advanced interpolation scheme it is possible to obtain a reduction in SLMLR of 18 dB and 33 dB in the B-mode and SA imaging, respectively, and an improvement in SNR of 24 dB.

2.3 Directional Beamforming

2.3.1 Introduction

Modern ultrasound systems can estimate the blood velocity in-vivo in real time [42, 43]. This is done by acquiring ultrasound signals from the same direction a number of times, and then correlate the signals. The shift in phase as a function of time can be determined using an autocorrelation estimator and this yields the velocity [2]. A second approach is to determine the shift in position using the cross-correlation function and dividing with the time between emissions [3, 4] gives the velocity. Both approaches only find the shift along the ultrasound beam direction, and only the projected velocity along this direction is, thus, found. Velocities transverse to the beam are not detected, and velocities in different directions are not depicted correctly. There is, thus, a need for methods that can detect the correct velocity magnitude and direction as a function of spatial position.

Several authors have devised methods for estimating the correct velocity. Fox [44] suggested using two crossing beams to have two independent measurements. This, however, necessitates the use of a large aperture to get a sufficient angle between the beams to ensure a precise determination of the transverse component. Trahey and co-workers [45] suggested using speckle tracking over a region of the image to track the motion in any direction. This necessitates the use of fast beamformer to generate the large amounts of data. It has also been suggested to introduce a lateral oscillation, so that the phase shift in the lateral directions also can be found using a modified autocorrelation method [29, 46]. Several other methods have been suggested [47, 48], but none have so far yielded a satisfactory performance to be commercially implemented.

Section 2.3 is extracted from the paper in Appendix B.3, and suggests a method for estimating the velocity vector, and especially the direction of the vector. The velocity magnitude is determined by focusing signals along the direction of the flow as suggested in [10, 49]. This can be done, if the correct direction is known. In current commercial scanners this is found by inspecting the B-mode image, and then use this angle in the beamforming. This is cumbersome and difficult to use, if the beam-to-flow angle changes throughout the image. An angle estimation approach based on directional beamforming is suggested here in Section 2.3. The approach is founded on the idea from [11]. Directional signals for a number of directions are beamformed, and the peak normalized correlation value is found. The direction with the highest correlation is then chosen as the angle estimate. The basics of the velocity estimation scheme is briefly described in Section 2.3.2, and the angle estimation method is introduced in Section 2.3.3. The results of the simulations and the measurements are found in the paper in Appendix B.3. Further results can be found in the co-authored papers in Appendix C.1 and Appendix C.2.

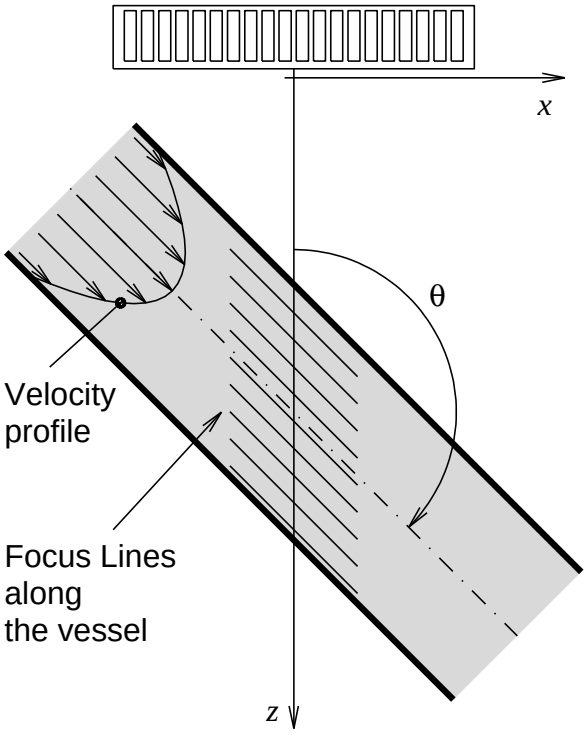

Figure 2.8: Focus-lines for constructing spatial directional signals.

2.3.2 Directional Velocity Estimation

This section gives a brief introduction to the principles from [10] of directional velocity estimation using focusing along the flow direction. The concept of spatial directional signals is introduced, and it is shown how the velocity can be estimated from these.

As described the conventional cross-correlation method can only estimate the velocity component projected onto the direction of the ultrasound propagation, since the beamforming is done along this direction. In directional velocity estimation the beamforming is done along the flow direction, and the correct velocity amplitude can, thus, be found, also for a purely transverse direction.

The basic principle is to focus the responses received by the transducer along focus-lines in the flow direction, which is referred to as *directional signals* in the spatial domain. In Fig. 2.8 a blood vessel and examples of focus-lines are shown. The spatial signals for two consecutive emissions are then cross-correlated and the shift between them is found. This is a shift in spatial position of the scatterers, and dividing by the time between emissions, thus, directly gives the velocity magnitude. Just as for the conventional systems the angle between the propagating direction of the emitted beam and the flow direction must be known before the beamforming can be done.

The directional signals are denoted $g(x')$, where x' is the x-coordinate in a rotated coordinate system aligned along the flow rather than along the ultrasound beam direction as shown in Fig. 2.9. Here the x'-axis of the new coordinate system is parallel to the flow direction, and the origin of the coordinate system is placed at the center of the vessel at depth Z_{ves}. The original coordinate system, (x,z) has origin at the center of the transducer, the x-axis is parallel with the transducer, and the z-axis represents the depth. The y-axis represents the elevation plane,

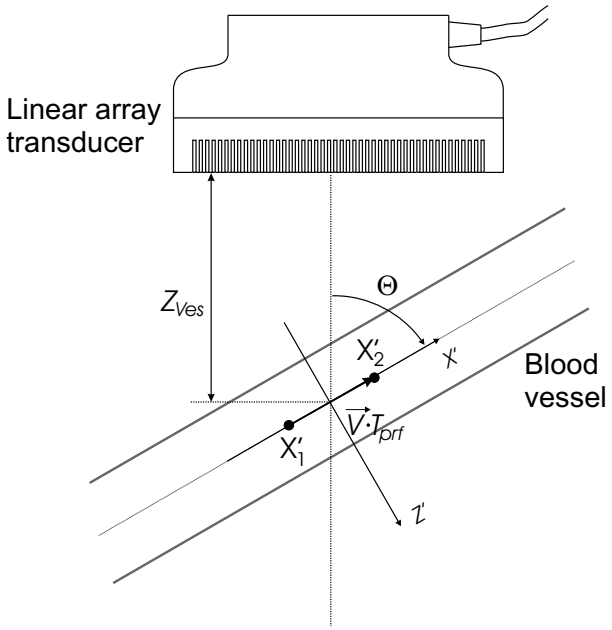

Figure 2.9: Rotated coordinate system (x', z') oriented along the flow direction, and with origin at the center of the vessel at a distance Z_{ves} from the transducer.

and this is the same for both coordinate systems. The relation between the rotated coordinate systems and the original coordinate system is given by

$$\begin{aligned} x &= \sin(\theta)\cdot x' + \cos(\theta)\cdot z' \\ y &= y' \\ z &= -\cos(\theta)\cdot x' + \sin(\theta)\cdot z' + Z_{ves}\,, \end{aligned} \tag{2.9}$$

or given in matrix notation

$$\begin{bmatrix} x \\ z \end{bmatrix} = \mathbf{R_{xz}} \cdot \begin{bmatrix} x' \\ z' \end{bmatrix} + \begin{bmatrix} 0 \\ Z_{ves} \end{bmatrix}, \tag{2.10}$$

where $\mathbf{R_{xz}}$ is the rotation matrix given by

$$\mathbf{R_{xz}} = \begin{bmatrix} \sin(\theta) & \cos(\theta) \\ -\cos(\theta) & \sin(\theta) \end{bmatrix}. \tag{2.11}$$

The angle θ is defined in Fig. 2.9. In the new coordinate system the velocity vector is $\vec{v} = (v_{x'}, 0, 0)$, which has only one non-zero component, $v_{x'} = |\vec{v}|$ provided the correct angle is used. The position of the scatterers can now be expressed through a scalar, where the first position is x'_1, and the position after T_{prf} seconds is $x'_2 = x'_1 + v_{x'}T_{prf}$. The directional signals are used to find the velocity. The first signal is given by $g_1(x')$, and the second obtained T_{prf} seconds later is $g_2(x')$. The two signals are related by

$$g_2(x') = g_1(x' - v_{x'}T_{prf}). \tag{2.12}$$

Cross-correlating the two signals gives

$$R_{12}(\xi_{x'}) = \int_X g_1(x')g_2(x' + \xi_{x'})dx'\,, \tag{2.13}$$

where X is the length of the directional signals. Using (2.12) the cross-correlation can be rewritten as

$$R_{12}(\xi_{x'}) = \int_X g_1(x')g_1(x' - v_{x'}T_{prf} + \xi_{x'})dx' = R_{11}(\xi_{x'} - v_{x'}T_{prf}), \tag{2.14}$$

which is the shifted auto-correlation $R_{11}(\xi_{x'})$ of $g_1(x')$, which has a global maximum at $\xi_{x'} = v_{x'}T_{prf}$. The maximum of the cross-correlation function

$$\xi_{x'_{max}} = \arg\max_{\xi_{x'}} \{R_{12}(\xi_{x'})\}, \tag{2.15}$$

is, thus, the shift in spatial position of the scatterers over the time interval T_{prf}. This makes it possible to calculate the velocity estimate along the flow direction, given by

$$\hat{v}_{x'} = \frac{\xi_{x'_{max}}}{T_{prf}}. \tag{2.16}$$

The cross-correlation can be improved by averaging over several estimates of R_{12} under the assumption, that the velocity of the scatterers can be considered constant for several pulses. A number of cross-correlations, N_{xc} can, thus, be used in the estimation. When applying averaging, $R_{12}(\xi_{x'})$ in Eq. (2.13) and Eq. (2.15) is substituted with

$$R_{12}(\xi_{x'}) = \sum_{i=1}^{N_{xc}} \mathcal{R}\left\{g_i(x',z'), g_{i+1}(x',z')\right\}, \tag{2.17}$$

where $\mathcal{R}$ is the cross-correlation operator. The correct flow angle must be determined, for this to work, and this is the topic of Section 2.3.3.

Beamforming of directional signals is performed as described in [10, 49]. The discrete directional signals are obtained by focusing signals received by the transducer elements in a set of points. These points are located on a straight line in any arbitrary direction and e.g. aligned along the flow direction for velocity estimation. The focusing of any of these points, is based on the total transmit-receive time-of-flight and a sample of the directional signal corresponding to the point $\mathbf{r_x}$ is calculated as

$$g(\mathbf{r_x}) = \sum_{j=1}^{N_E} s_j(t_{\mathbf{r_x}}) = \sum_{j=1}^{N_E} s_j\left(\frac{|\mathbf{r_t} - \mathbf{r_x}| + |\mathbf{r_x} - \mathbf{r_j}|}{c}\right), \tag{2.18}$$

where N_E is the number of transducer elements, $s_j(t)$ is the received signal from transducer element j, $t_{\mathbf{r_x}}$ is the time instance at which to select a value from the signal $s_j(t)$, $\mathbf{r_t}$ is the position of the transmit source and $\mathbf{r_j}$ is the position of the j'th transducer element.

2.3.3 Angle Estimation

Conventional velocity estimation systems relies on knowledge of the angle between the flow vector and the direction of the emitted ultrasound beam, and traditionally this knowledge comes from the B-mode image. In the ideal situation the vessel is rigid and straight without sudden geometric changes within the range of the B-mode image, or at least within the velocity estimation range. In this case the beam-to-flow angle could be determined with satisfactory results from the B-mode image. Unfortunately, this is not a realistic case. The blood vessels are branching

and curving and typically no unique direction can be found for the whole image. This leads to a wrong correction value for the projected velocity component, and the consequence is an increase in bias and standard deviation. The approach also fails for angles close to 90°. This motivates the investigations of an automatic approach to angle estimation.

The spatial directional signals are obtained by focusing the received responses in points along the flow direction. Directional signals obtained from two consecutive acquired responses properly aligned with the flow direction have a high correlation. The primary contribution to the de-correlation between the signals is the spatial shift due to the movement of the scatterers. Another minor contribution is due to new scatterers entering the directional signal at one end and others leaving at the other end. Now consider the case where the directional signals are not aligned along the flow direction. The distribution of the scatterers for the second directional signal is no longer just a shift in position of the previous scatterer distribution. The relative positions between the scatterers have changed, due to the different velocities for the different scatterers. The consequence is that the correlation between the two directional signals is reduced compared to the case of focusing along the flow direction. This change in correlation is the property used for the angle estimation. The method is, thus to obtain directional signals in a number of directions, and quantify the correlation between signals in each direction. From this procedure a *correlation-function* is constructed showing the normalized correlation as a function of search angle. The maximum of this function indicates the direction with the highest correlation between consecutive signals; hence the flow direction.

The cross-correlation is an obvious choice for the correlation-function. The cross-correlation peak amplitude is though not directly a valid measure. The cross-correlation output values are dependent on the amplitudes of the directional signals, and the amplitudes will differ due to different scatterer distributions at the focal points, and due to the spatial energy distribution of the transmitted ultrasound beam. Instead the correlation peak should be found from the normalized cross-correlation. The normalization factor could be the power of the signal, and this approach is formulated as

$$\begin{aligned} R_{12_n}(l,\phi) &= \frac{R_{12}(l,\phi)}{P_{12}(\phi)} \\ R_{12_{max}}(\phi) &= \max\left(R_{12_n}(l,\phi)\right) \\ \widehat{\theta}_k &= \arg\max_{\phi}\left\{R_{12_{max}}(\phi)\right\}, \end{aligned} \tag{2.19}$$

where $R_{12_n}(l,\phi)$ is the normalized cross-correlation estimate between directional signals, $g_1(x',\phi)$ and $g_2(x',\phi)$ and

$$P_{12}(\phi) = \sqrt{R_{11}(0,\phi)\cdot R_{22}(0,\phi)} = \sqrt{\sum_{x'} g_1(x',\phi)^2 \cdot \sum_{x'} g_2(x',\phi)^2} \tag{2.20}$$

represents the power of the signals. ϕ denotes the angle of the directional signal. $R_{12_{max}}(\phi)$ is the maximum value of the normalized cross-correlation estimate as a function of beam-angle. The discrete angle estimate, $\widehat{\theta}_k$, is found where $R_{12_{max}}(\phi)$ has its peak value.

The discrete cross-correlation estimates can yield erroneous peaks, when a limited amount of data is used, and if noise is present in the data. This has been investigated in [10] and the influence of noise on the angle estimation is expected to be similar. The cross-correlation estimate can be improved by averaging over several directional signals. If averaging is used,

$R_{12_n}(l,\phi)$ in Eq. (2.19) can be rewritten as

$$R_{12_n}(l,\phi) = \sum_i \frac{R_{i,i+1}(l,\phi)}{P_{i,i+1}(\phi)}, \tag{2.21}$$

where, i, represent the pulse-echo lines, and the final correlation-function from Eq. (2.19) is, thus, formulated as

$$R_{12_{max}}(\phi) = \max\left(\sum_i \frac{R_{i,i+1}(l,\phi)}{P_{i,i+1}(\phi)}\right). \tag{2.22}$$

The quantization of the cross-correlation is determined from the spatial sampling frequency, when constructing the directional signals. If the spatial sampling interval is sparse, the performance can be improved by interpolation around the peak value of $R_{12_n}(l,\phi)$. Fitting a second order polynomial to the samples around the peak, $R_{12}(l_p,\phi)$, where l_p denotes the lag at which the peak occurs, will give a more precise maximum value [3], hence a more precise angle estimation.

The correlation between the directional signals can also be described using the *correlation coefficient* ρ. Correlation is the degree to which two or more components are linearly associated and the statistical term is the covariance

$$\mathrm{cov}(x_1,x_2) = \langle (x_1-\bar{x}_1)(x_2-\bar{x}_2)\rangle, \tag{2.23}$$

between components, x_1 and x_2, and where $\langle\rangle$ is the expectation operator. The correlation coefficient is simply the covariance normalized with the product of the standard deviations of the two components, and is defined as

$$\rho = \frac{\mathrm{cov}(x_1,x_2)}{\sigma_{x_1}\sigma_{x_2}}, \tag{2.24}$$

where $\rho \in [-1,1]$ and $\rho = 1$, corresponds to perfect linear relation or full correlation.

The strategy for the angle estimation involves two steps, when the correlation coefficient is used for the correlation-function. Before calculating the correlation coefficient the two directional signals, for which the correlation coefficient is needed, are aligned. Otherwise the correlation coefficient will be small even at the true angle due to the spatial shift from the movement of the scatterers. The alignment is determined from the discrete lag at the cross-correlation peak, l_p. To increase accuracy a 2$^{\text{nd}}$ order polynomial is fitted around the peak [3] to find a new interpolated lag value, l_p^{int} :

$$l_p^{int} = l_p - \frac{R_{12_n}(l_p+1) - R_{12_n}(l_p-1)}{2\left(R_{12_n}(l_p+1) - 2R_{12_n}(l_p) + R_{12_n}(l_p-1)\right)}. \tag{2.25}$$

Due to the new continuous lag the alignment operation involves a first order linear interpolation or a higher order interpolation scheme between the samples in one of the signals g_1 or g_2. The correlation-function using the correlation coefficient is, thus, defined as

$$\rho(\phi) = \sum_i \frac{\mathrm{cov}\left(g_i(x',\phi), g_{i+1}(x'+l_p^{int},\phi)\right)}{\sigma_{g_i(x',\phi)}\sigma_{g_{i+1}(x'+l_p^{int},\phi)}}, \tag{2.26}$$

and the final angle estimation using this function is

$$\widehat{\theta}_k = \arg\max_{\phi}\{\rho(\phi)\}, \tag{2.27}$$

where the estimate has been improved by averaging over several estimates of ρ using several pulse-echo lines i.

If the expectation operator is approximated by the temporal average and assuming $\bar{x}_1 = \bar{x}_2 = 0$ then the correlation coefficient of Eq. (2.24) can be written as

$$\rho = \frac{\sum x_1 x_2}{\sqrt{\sum x_1^2}\sqrt{\sum x_2^2}}, \tag{2.28}$$

and the correlation-function can be calculated by rewriting (2.26) into

$$\rho(\phi) = \sum_i \frac{\sum_{x'} g_i(x',\phi) \cdot g_{i+1}(x' + l_p^{int},\phi)}{\sqrt{\sum_{x'} g_i(x',\phi)^2 \cdot \sum_{x'} g_{i+1}(x' + l_p^{int},\phi)^2}}, \tag{2.29}$$

or written in terms of the cross-correlation

$$\rho(\phi) = \sum_i \frac{R^*_{i,i+1}(0,\phi)}{P^*_{i,i+1}(\phi)}, \tag{2.30}$$

where * denotes operation on the aligned signals.

The two approaches to calculating the correlation-function in Eq. (2.22) and Eq. (2.29) (or Eq. (2.30)) respectively are closely related but there are some differences. The quantifier in Eq. (2.29) benefits from the directional signals being accurately aligned before multiplication and summing contrary to the quantifier in Eq. (2.22). Here the summing of cross-correlation functions will suffer from a sparse spatial sampling and they will not sum fully coherently. The quantifier in Eq. (2.29) though requires additional computation due to the interpolation involved in the alignment. The influence of the choice of quantifier on the angle estimation performance is discussed in the paper in Appendix B.3.

The directional lines are placed with an angular distance, $\Delta\phi$, and the estimates are, thus, initially restricted to be discrete estimates, $\widehat{\theta}_k$ with the same resolution. Continuous estimates, $\widehat{\theta}$ can be obtained by employing interpolation similar to (2.25) around the peak of the correlation-function to find a continuous index for the peak and then use linear interpolation between the neighboring discrete angles. This will reduce the number of directions to beamform signals in. Prior knowledge of the actual flow angle can also be used in confining the angle search range with the purpose of limiting the computational task. Iterative schemes could be used, where a temporary estimate based on interpolation between results from a few search angles is used. A new search, in a new confined search range around this temporary estimate, can now be made with an increased search resolution. This process continues until the desired precision is obtained or until the limit on the accuracy of the method has been reached.

In the angle and velocity estimator the correlation is traditionally calculated based on consecutive directional signals. Considering the velocity estimator, for low velocities or high pulse repetition frequencies, the shift between signals is low yielding a value of $\xi_{x'_{max}}$ from Eq. (2.16) close to zero. This will make the relative estimation variance high since noise will dominate the estimate. It can be an advantage to correlate signals, where the time between acquisitions is higher. The directional signals used for the cross-correlations are then selected with a time interval, $T_{cc} = k_{tprf} \cdot T_{prf}$ between the correlated signals. T_{cc} is referred to as the *correlation-time* and the proportionality, k_{tprf} is referred to as the *correlation-time-factor*. The correlation-time-factor is, thus, a representation of how many directional signals that are bypassed before the

correlation is performed. All indices equal to $i+1$ in all previous equations for both velocity and angle estimation must then be substituted by $i+k_{tprf}$, and, e.g. Eq. (2.13), is then written as

$$R_i(\xi_{x'}) = \int_X g_i(x')\, g_{i+k_{tprf}}(x'+\xi_{x'})dx', \quad i = 1 \ldots N_{xc}\,, \tag{2.31}$$

where g_i is the i'th directional signal. Considering the angle estimator, the same dependency on the choice of k_{tprf} applies, and it appears to be an important parameter, which affects performance radically, and the optimal value varies with the flow angle. This will be discussed in more detail in the paper in Appendix B.3.

The consequence of using a wrong beam-to-flow angle is different in conventional velocity estimation [43, 42] than with the directional beamforming approach proposed in this paper. With the conventional velocity estimation approach the estimate available is the velocity projected along the ultrasound beam direction, and this estimate must, thus, be compensated with the beam-to-flow angle to obtain the correct velocity amplitude along the flow. If the angle estimate is not correct a bias will occur in the velocity estimate. The bias will increase for the same absolute angle estimation error as the true flow angle increases toward 90°. This can be seen from the expression of the relative change in velocity estimate

$$\frac{\Delta v}{v} = \frac{\cos(\phi)}{\cos\left(\widehat{\phi}\right)} - 1\,. \tag{2.32}$$

With the velocity estimation approach suggested in this paper the beam-to-flow angle estimate is used for beamforming the focus lines, and the consequence on the velocity bias is only related to the cosine-relation between the true angle and the estimated angle. In Fig. 2.10 the relative change in velocity estimate is shown as a function of beam-to-flow estimation error for both velocity estimation approaches with angle errors of $\pm 10°$ assuming velocity projection. For the conventional approach the relative change is shown for $\theta = 45°$ and $\theta = 60°$.

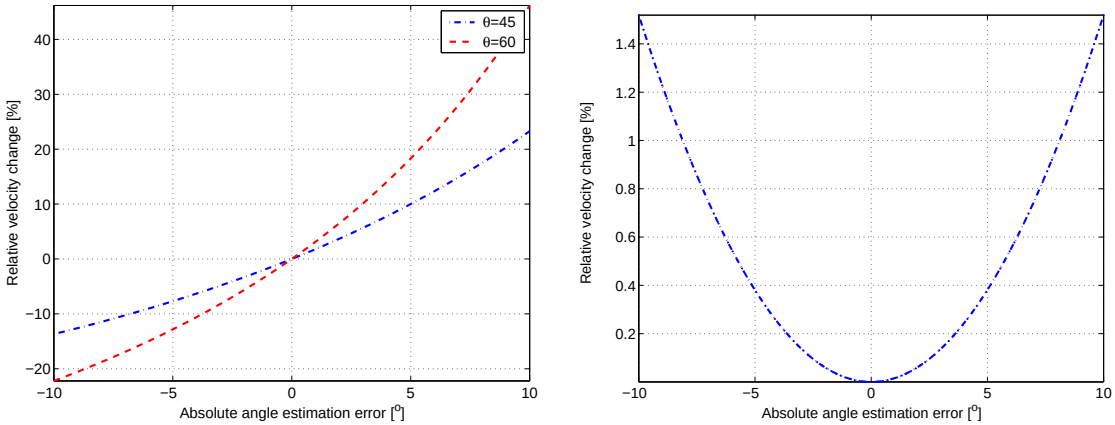

Figure 2.10: Velocity estimation error due to a wrong beam-to-flow angle estimate. Conventional velocity estimation approach for two different flow directions (Left). Directional velocity estimation approach (Right).

All results are found in the paper in Appendix B.3.

2.3.4 Conclusion

When using focusing along the velocity direction for velocity estimation the velocity profile estimates from simulations have relative mean standard deviations between 0.7% and 7.7% for flow between 45° and 90°. The simulation study and measurement study both showed that angle estimation by directional beamforming can be estimated with a high precision and potentially yielding velocity estimates with a better accuracy.

The angle estimation performance is strongly influenced by the choice of correlation-time, and a proper choice varies with flow angle and will vary with flow velocity amplitude though the latter is not shown in this paper. Flow angles of $\theta = \{45^\circ, 60^\circ, 75^\circ\}$ requires a high value of the correlation-time whereas for $\theta = 90^\circ$ a low value is required. By using the optimal choice of correlation-time for the different flow angles based on a parameter study the potential of the method has been revealed. With these favorable conditions the simulations produced 100% valid estimates (no outliers) and a bias and standard deviation below 2° for all flow angles.

Using the measurements more than 96% valid estimates were produced for the flow angles $\theta = \{60^\circ, 75^\circ, 90^\circ\}$ and with a bias below 2° and a standard deviation below 5°. The techniques used are based on an assumption of a laminar flow. A a turbulent flow will evidently complicate matters of angle estimation and can be a topic of future investigations.

2.4 Synthetic Aperture Focusing

Inspired by synthetic aperture (SA) radar techniques[50, 51, 25], SA ultrasound imaging has been investigated thoroughly for many years. In synthetic transmit aperture (STA) imaging[52, 53] a single element is used to transmit a spherical wave that occupies the entire region of interest. The backscattered signals are registered using a multi-element receive aperture and RF-samples from all channels are stored. Delay-and-sum (DAS) beamforming can be applied to these data to construct a low-resolution image (LRI), hence an image constructed from a single emission. Several emissions from single elements across the aperture will synthesize a larger aperture and the LRI's from these emissions can be added into a single high-resolution image (HRI). The HRI is dynamically focused in both transmit and receive yielding an improvement in resolution[54]. This has been confirmed with side-by-side comparisons with conventional ultrasound imaging in pre-clinical trials by Pedersen et. al[55]. This imaging technique sets high demands on processing capabilities, data transport, and storage and makes implementation of a full SA system very challenging and costly. The method investigated in this paper is yet another variation on SA processing. The objective is to reduce the demands on the system making it a more realistic task to implement, while still preserving benefits in imaging performance.

Synthetic aperture imaging and principles have been studied in other Ph.D. theses[14, 15]. Many variations of synthetic aperture focusing (SAF) and examples of implementation have been reported with improvements in both frame rate, penetration, and lateral resolution. A simple real-time single channel system with a multiplexer for array imaging was described by Peterson and Kino[56] back in 1984. In the mono-static approach[54] the same element serves as a transmitter and a receiver. A SA technique suitable for a hand held system using a multi-element transmit and receive aperture was described by Karaman et al.[52]. Lockwood and Hazard described a sparse SA beamforming technique for three-dimensional ultrasound imaging using a few transmit pulses for each image[13, 16]. A SA method for a circular

aperture was investigated by O'Donnell and Thomas[57].

The concept of using the transmit focal point as a virtual source (VS) or a virtual aperture was introduced by Passmann and Ermert[21]. Virtual sources in SAF was further investigated by Frazier and O´Brien[22], Nikolov and Jensen [23, 58], and Bae and Jeong[59]. It was shown that the virtual source coincides with the focal point of the transducer, and that a depth independent resolution can be achieved.

In this thesis synthetic aperture focusing is applied in two different applications in Chapter 3 and in Chapter 4. In Chapter 3 synthetic aperture techniques are applied to 2-dimensional imaging with a single rotating mechanically focused concave element. It is proposed to apply mono-static synthetic aperture focusing (SAF) on data acquired with such a transducer. The focal point of the transducer element is considered a virtual source. Virtual sources from several emissions form a virtual aperture and data from these emissions are used to construct the final image. A simulation study is carried out with the objective of improving lateral resolution and signal-to-noise ratio (SNR).

In Chapter 4 a similar technique is applied, but to linear array imaging. Here the synthesized aperture consists of virtual sources created from a sub-aperture. The position and the opening angle of the VS are determined by the electronic focusing instead of a concave element. The technique is realized using two beamformers. In the first beamformer the receive focusing is a simple fixed focusing with receive focal point in the transmit focal point. The focused beamformed lines from the first beamformer are transferred to a 2nd beamformer just as the one applied with the rotating transducer. This technique is investigated by simulations and by processing data acquired with a commercial scanner.

CHAPTER

THREE

Synthetic Aperture Focusing using a Rotating Single Element Transducer

In this chapter synthetic aperture focusing is applied to data acquired with a rotating single element transducer. Literature within synthetic aperture imaging relevant for the technique presented in this section was given in Section 2.4. The concept and application to a rotating single element transducer is introduced in Section 3.1, and further described in Section 3.2. The vast majority of the content of this chapter is also found in the conference paper *Synthetic aperture focusing using a rotating single element transducer* in Appendix B.5.

3.1 Introduction

This chapter applies the concept of virtual sources and synthetic aperture techniques to 2-dimensional imaging with a single rotating mechanically focused concave element. Such an imaging system can e.g. be found in an anorectal ultrasound transducer. With such a transducer emission and reception are done while the transducer element continuously rotates and the received RF signals are stored. It is proposed to apply mono-static synthetic aperture focusing (SAF) on these data with the objective of improving lateral resolution and signal-to-noise ratio (SNR). This is investigated using simulations in Field II[60, 61] and SAF is carried out using the Beamformation Toolbox, *BFT2*[62]. Images of point targets are created and the radial and angular resolution in the polar coordinate system are extracted. The potential improvement in SNR is also evaluated. The SAF method is described in Section 3.2. The simulation setup and simulation results are found in Section 3.3, and the investigation is concluded in Section 3.4.

3.2 Method

In the mono-static case of linear array SAF, a single element is used in both transmit and receive. The transmitting element can be considered a point source emitting a spherical wave. The wave traverses all image points and an entire LRI can be formed after each emission. Several emissions from across the aperture can be used to construct a HRI. The HRI has a better resolution than the LRI, since the multiple emissions synthesize an effective aperture of a certain lateral width.

This focusing scheme can not directly be applied to imaging with a rotating mechanically focused element. To begin with the lateral translation of the transmit source is smaller for the

rotating system than for the linear array making the synthesized width of the aperture smaller. Secondly the concave rotating element can not be considered a point source because of the physical extent of the element and the geometrical focusing due to the concave shape. Instead the geometrical focal point can be considered as a point source emitting a spherical wave in a limited angular region. The focal depth of the transducer element or more exact the focusing $F\#$ determines the opening angle, hence the width of the wave field and the point spread function (PSF). An illustration of propagating waves from 3 different emissions is shown in Fig. 3.1 for a transducer element with a focal depth of 5 mm.

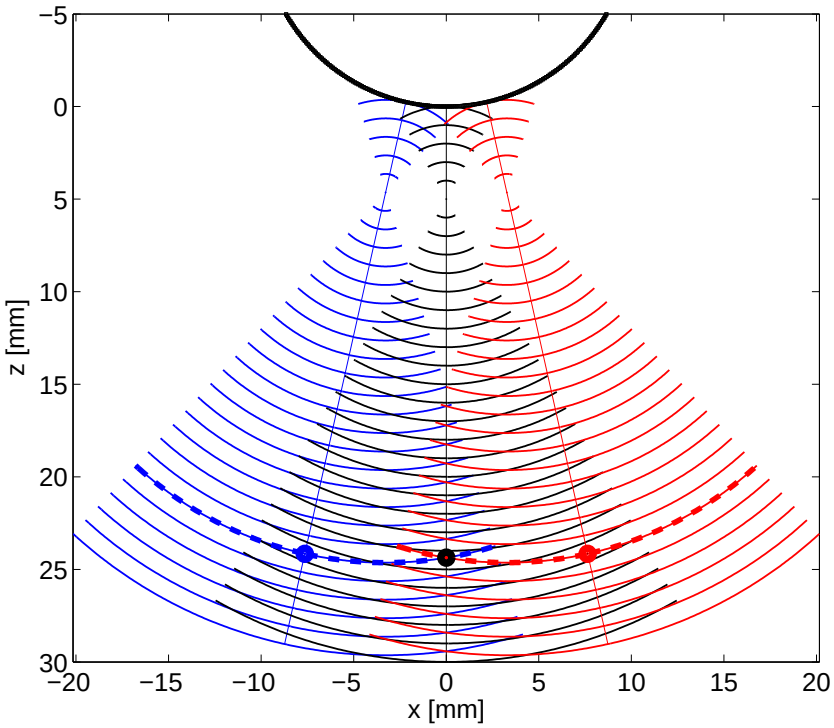

Figure 3.1: An illustration of propagating waves from 3 different emissions for a transducer element with a focal depth of 5 mm. A single sample of the image line from the center emission is indicated with a dot. Samples from the off-center image lines which share the same phase-information are also indicated. These samples are added in the beamformer.

A LRI of the entire imaging area can not be formed after each emission due to the spatially limited wave propagation. Instead, for each image point in a high resolution image line (HRL) it must be determined which emissions that have a wave field that encompasses the image point. These emissions contribute to the HRL, and samples from each of them are selected according to the SAF delays, and added together. This is also illustrated in Fig. 3.1. In other words a single HRL is composed of the sum of a number of low resolution lines (LRL). A single LRL is, thus, the contribution from a given emission to a HRL. The term LRL is used for an RF-line which have been processed using SAF and which contains at least one non-zero sample which carries information of one of the image points of the HRL.

The SAF can be formulated as a sum over LRL. A single sample of the HRL, representing the image point at the location $\vec{r}_{ip}$ with angular coordinate ϕ and radial coordinate r becomes

$$h(\phi, r) = \sum_{\theta} \mathcal{A}(\theta, r) l_{\theta}(r)\,, \tag{3.1}$$

where $h(\phi, r)$ is the HRL sample, and $l_\theta(r)$ is the LRL sample from the emission with propagation direction θ. Both with radial coordinate r. The variable $\mathcal{A}$ is an apodization function which controls the weighting of the contribution from each of the LRL. It is a function a the radial coordinate, since the number of contributing emissions increases with range. The synthesized aperture increases with range resulting in a less range dependent lateral resolution. The LRL can be formulated using the RF-line, $s_\theta(r')$

$$l_\theta(r) = s_\theta(r')\,. \tag{3.2}$$

r' is the radial coordinate at which to select a sample from the RF-line and is not the same radial coordinate as in the HRL. r' can be found from the distance function, $r' = d(\vec{r}_{v_\theta}, \vec{r}_{ip})$ which calculates the transmit-receive time-of-flight for the SAF, and thus the sample index for the RF-line, $s_\theta(r')$. The transducer element at the position $\vec{r}_{t_\theta}$ is physically focused at the VS at the position $\vec{r}_{v_\theta}$ with a focal distance of d_v from the element. The element is focused in both transmit and receive and the distance function becomes a sum of transmit and receive travel paths

$$\begin{aligned} d(\vec{r}_{v_\theta}, \vec{r}_{ip}) = & \quad |\vec{r}_{v_\theta} - \vec{r}_{t_\theta}| \pm |\vec{r}_{ip} - \vec{r}_{v_\theta}| \\ & \pm |\vec{r}_{v_\theta} - \vec{r}_{ip}| + |\vec{r}_{t_\theta} - \vec{r}_{v_\theta}| \\ = & \quad 2|\vec{r}_{v_\theta} - \vec{r}_{t_\theta}| \pm 2|\vec{r}_{ip} - \vec{r}_{v_\theta}| \\ = & \quad 2d_v \pm 2|\vec{r}_{ip} - \vec{r}_{v_\theta}| \end{aligned} \tag{3.3}$$

The $\pm$ in (3.3) refer to whether the image point is above or below the VS. A single sample of the HRL can thus be formulated using (3.1) and (3.2)

$$h(\phi, r) = \sum_\theta \mathcal{A}(\theta, r) s_\theta(d(\vec{r}_{v_\theta}, \vec{r}_{ip}))\,. \tag{3.4}$$

A single element of limited extent can be considered as a wave source emitting a spherical wave, which will cover the entire image area. With complete overlap between the covered image areas all emission can be utilized to create a HRI. Having a physically focused transducer element the VS is conceived as the wave source. With a transducer element of fixed size the focal depth determines the opening angle, α and the confined image area covered by the wave field. The consequence is that not all emissions can be utilized to create a HRI. Having a rotating element instead of a translating element even further limits the number of applicable emissions. From geometrical observation the opening angle can be expressed as

$$\alpha = 2 \arctan \frac{1}{2F\#}\,, \tag{3.5}$$

which is a valid approximation[35]. The confined image area covered by the wave field is, thus, a function of the $F\#$. With a higher $F\#$ the point spread function becomes narrower improving the resolution for the single RF-line. This portrays a conflict between using a low $F\#$ and adding a large number of LRL, and using a high $F\#$ and reducing the number of applied LRL. Performance results for these different configurations are presented in Section 3.3.

3.3 Simulation Results

The SAF scheme is investigated using Field II[60, 61]. The simulations are based on moving a single concave element of radius 2.5 mm along a circle of radius 10 mm. Elements with

different concave curvatures are used to obtain geometrical focusing depths at 10 mm, 15 mm, and 20 mm. The scattering media consists of point targets (PT) in the range from 5 mm to 65 mm with a distance of 10 mm. The transducer element is rotated with a fixed angle of 0.63° corresponding to moving the element $\lambda/2$ between each acquisition. It is assumed that the transducer element is not moving during emission and reception. The 7 MHz pulse, and the one-way impulse response are weighted single-cycle sinusoids.

3.3.1 Resolution

The envelope HRI's are shown in this section. The radial and angular resolution are extracted at -6 dB and -40 dB. For each PT the resolution is calculated as the width at which the envelope amplitude has decreased to the specified level relative to the maximum level at that given PT. For the lateral resolution the envelope amplitude is taken as the maximum amplitude within a radial range of $\pm$ 3 mm around the PT. Likewise for the radial resolution the envelope amplitude is taken as the maximum amplitude across the entire angular range of the image.

The variable $\mathcal{A}$ from (3.4) controls the weighting of the contribution from each of the LRL and is a function a the radial coordinate. The actual number of contributing LRL is shown in Fig. 3.2 for the transducer elements with focusing depths at 10 mm, 15 mm, and 20 mm. As the focal depth increases, and the opening angle decreases, the number of contributing LRL's decreases.

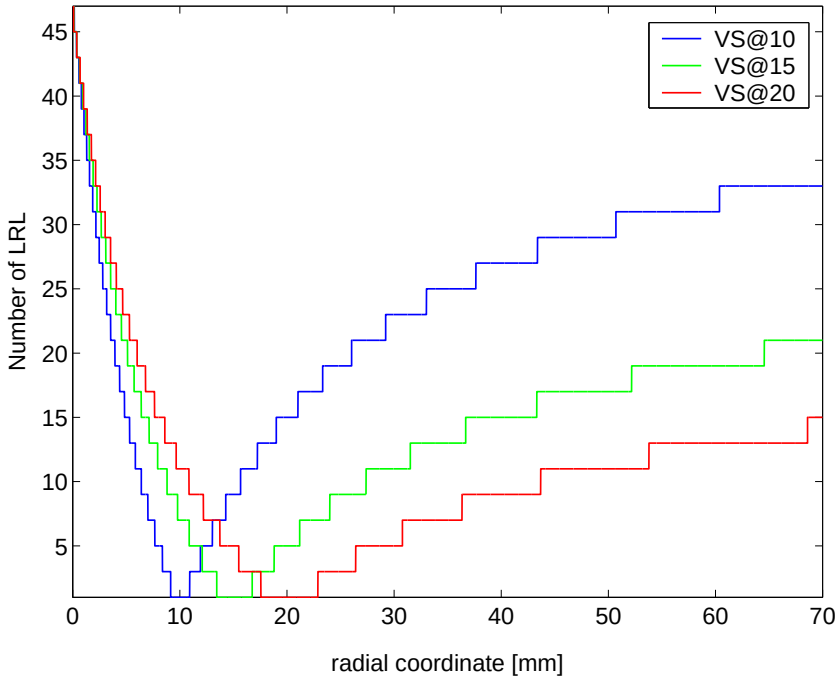

Figure 3.2: The number of contributing LRL's for the transducer elements with focusing depths at 10 mm, 15 mm, and 20 mm.

Images with different setups are shown in Fig. 3.3. In the first three images the focusing depths of the element are 10 mm, 15 mm, and 20 mm, respectively and SAF has been applied. In the last image the element has a focusing depths of 20 mm and SAF is not applied. The differences between the images are better demonstrated in Fig. 3.4 where the radial and angular resolution are extracted. The performance of the setup with a VS at 20 mm is superior to the other setups.

This reflects the conflict stated earlier between using a low $F\#$ and adding a large number of LRL's, and using a high $F\#$ and reducing the number of LRL's. Due to the rotation the synthesized aperture only experiences a moderate expansion even for the setup with a focal depth of 10 mm. The modest expansion is not sufficient to reduce the extent of the wide point spread function of a single emission. At least not to a level which is competitive to the relatively narrow PSF of the setup with focal depth at 20 mm. The effect of SAF with focal depth at 20 mm is negligible. This is also caused by the small number of LRL's. Only 15 LRL's are used at a range of 70 mm as shown in Fig. 3.2.

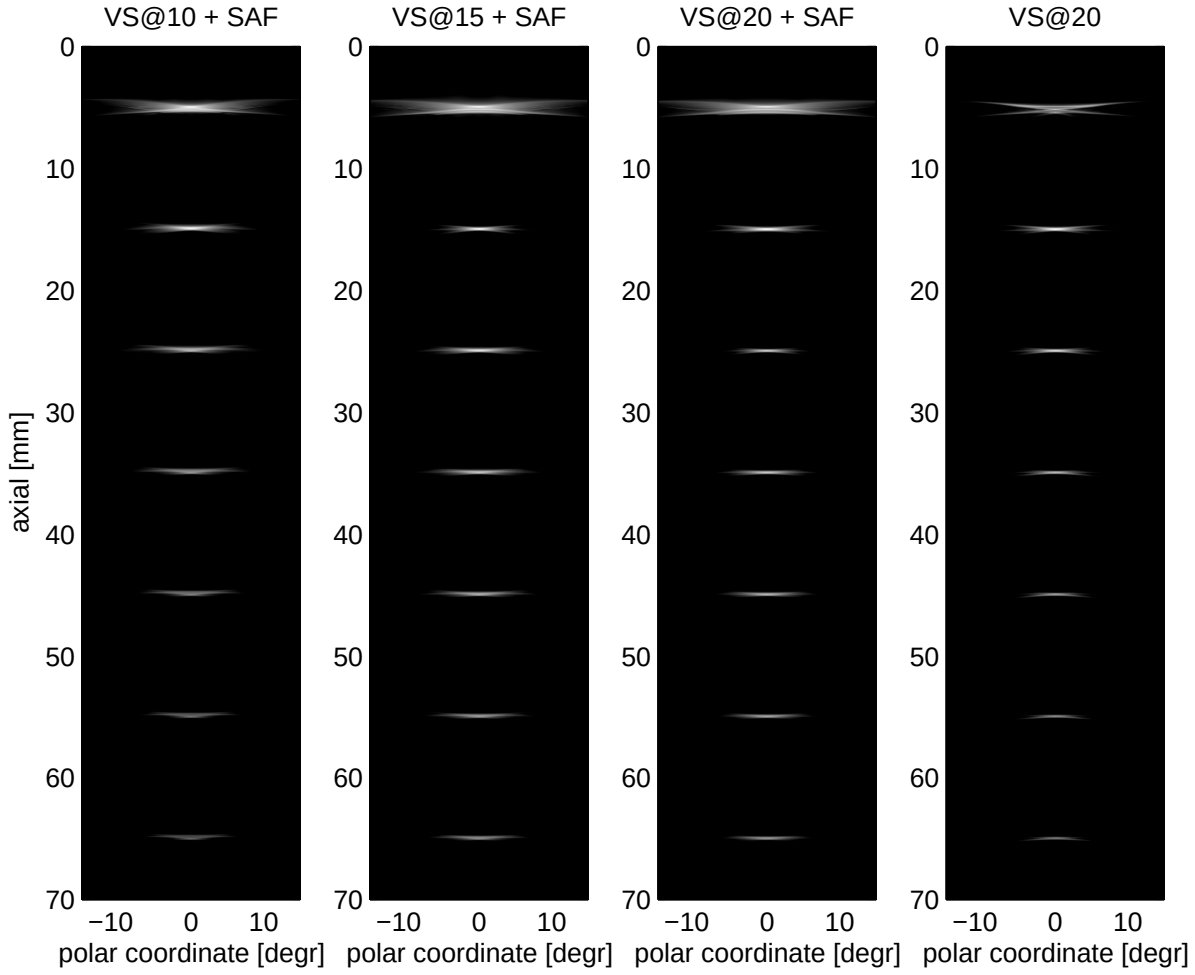

Figure 3.3: Images from 4 different setups. In the first three images the focusing depths of the elements are 10 mm, 15 mm, and 20 mm respectively and SAF has been applied. In the last image the element has a focusing depths of 20 mm and SAF is not applied.

The SAF technique rely on phase coherent addition of the LRL's. The LRL's composing the HRL around the PT at 35 mm and the envelope of the HRL are plotted in Fig. 3.5. The log-compressed and envelope detected LRL's are shown in Fig. 3.6. The setup is with an element with focal depth of 10 mm. It is apparent that the LRL's in some degree are phase aligned and add up constructively.

In the remainder of this section the setup with focal depth at 10 mm is investigated further. The spatial variant pulse-echo response has been simulated in Field II and shown in Fig. 3.7 at different depths. The pulse-echo response is calculated at the positions, $\vec{r_p} = (0, 0, r_{p_z})$ where

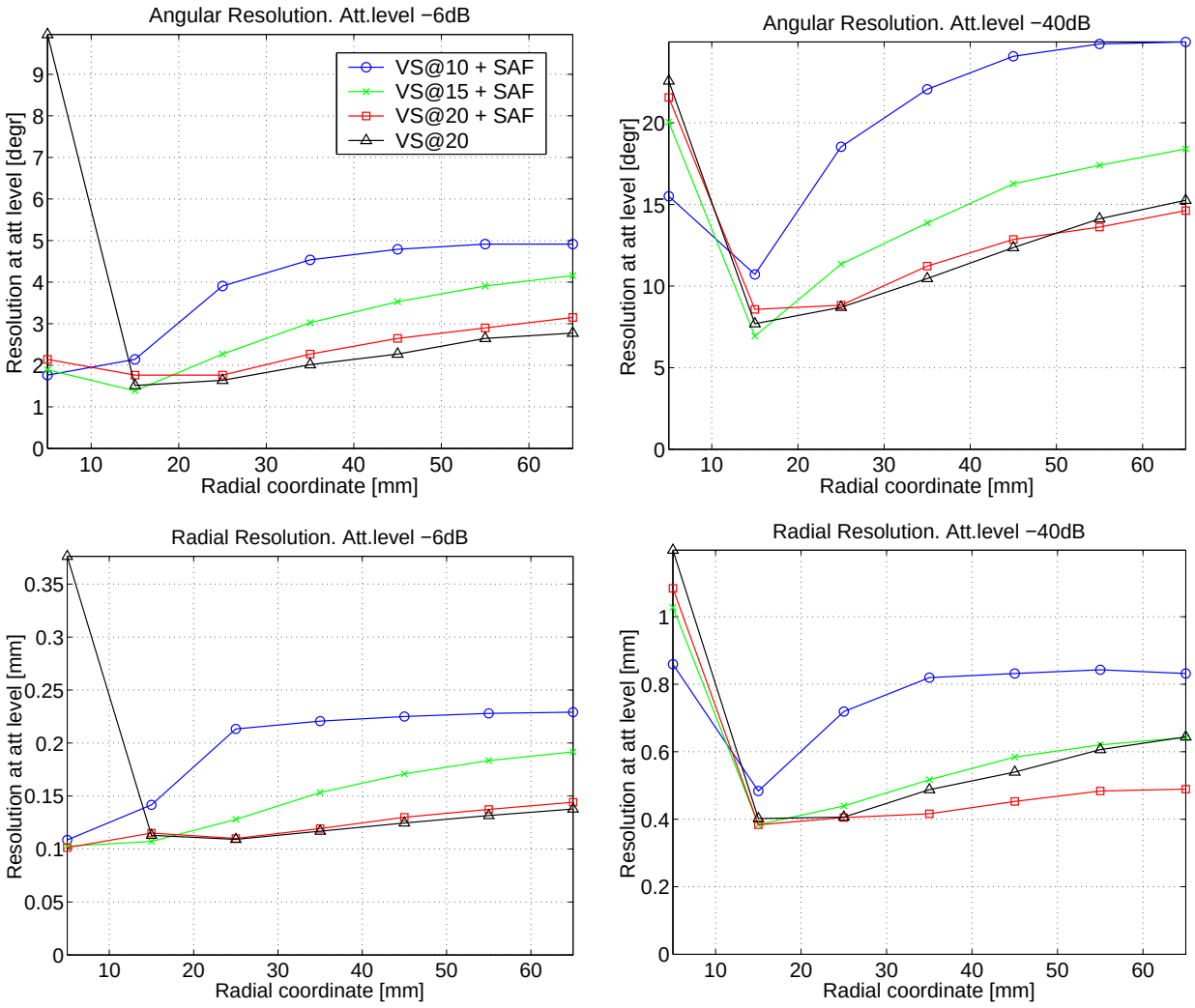

Figure 3.4: Angular resolution (top) and radial resolution (bottom) at -6 dB (left) and -40 dB (right).

r_{p_z} is 15, 25, 35, and 65 mm. The HRL is constituted from the sum of a number of LRL's. In the beamforming process it is assumed that the wave field can be considered spherical and propagating as if it was emitted from the virtual point source. Provided the assumption is true the LRL's constituting the HRL at the PT will be almost identical, and the HRL thus almost identical to the system pulse-echo response at the position of the PT. The HRL at the PT's at the same positions as $\vec{r_p}$ is also shown in Fig. 3.7. The simulated pulse-echo response and the HRL have been aligned by means of a cross-correlation and shown without the spatial axis solely to illustrate the resemblance between the waveforms.

The coherence between the HRL and the pulse-echo response at $r_{p_z} = 15$ mm is evident but they are not equal. As r_{p_z} increases the coherence decreases. The spatial variant pulse-echo response, h_{pe} is found from the convolution between the spatial pulse-echo impulse response, $h_{s_{pe}}$ and the electro-mechanical two-way response, h_{em}.

$$h_{pe}(\vec{r_p},t) = h_{s_{pe}}(\vec{r_p},t) * h_{em}(t)\,. \tag{3.6}$$

The electro-mechanical response is constituted from the transducer transfer function and the excitation signal and is not spatially dependent. It is also shown in Fig. 3.7. Notice that the

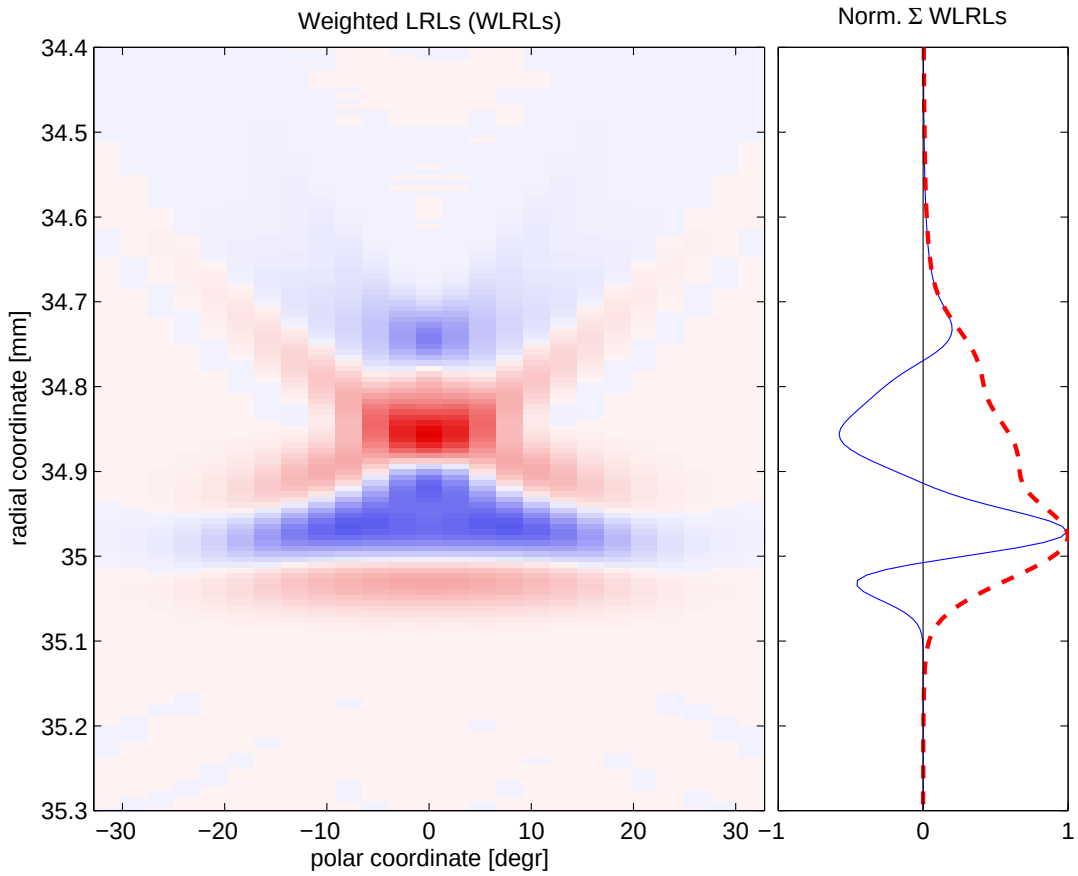

Figure 3.5: A single HRL is composed of the sum of a number of weighted low resolution lines. Here the LRL's and the envelope detected LRL's composing the HRL around the PT at 35 mm are shown. The setup is with a focal depth of 10 mm.

electro-mechanical response, h_{em}, and the pulse-echo response, h_{pe} for a given point in space is a function of time. Here the time-axis has been converted to a spatial pulse-echo axis for a convenient comparison to the HRL.

There is some coherence between the electro-mechanical response and the pulse-echo response at $r_{p_z} = 15$ mm. This is demonstrating that the pulse-echo response is not limited by the bandwidth of the spatial pulse-echo impulse response. As r_{p_z} increases the resemblance between h_{pe} and h_{em} disappears demonstrating a spatial pulse-echo impulse response which varies considerably.

The assumption of a spherical wave field propagating from a virtual point source in the focal point is apparently not entirely valid. The coherence between the HRL and the pulse-echo response is not impressive at greater depths. It was shown that the pulse-echo response varied with depth. The variation over the angular dimension is presented in Fig. 3.8, and Fig. 3.9. The response is simulated in a number of different positions, $\vec{r}_p = r_p \angle \phi_p$ and compared. r_p is the radial distance from the focal point to the point of investigation. Four studies of the variation are performed where the distance to the focal point is $r_p = -5$ mm, $r_p = 5$ mm, $r_p = 25$ mm, and $r_p = 55$ mm respectively. A negative value of r_p indicates that the points of investigation are above the focal point. In each study all responses are normalized to a maximum value of 1, and plotted with a small offset in between each of them. This will form an illusion of the pulse-echo wave front. The positions of the points of investigation span over twice the opening

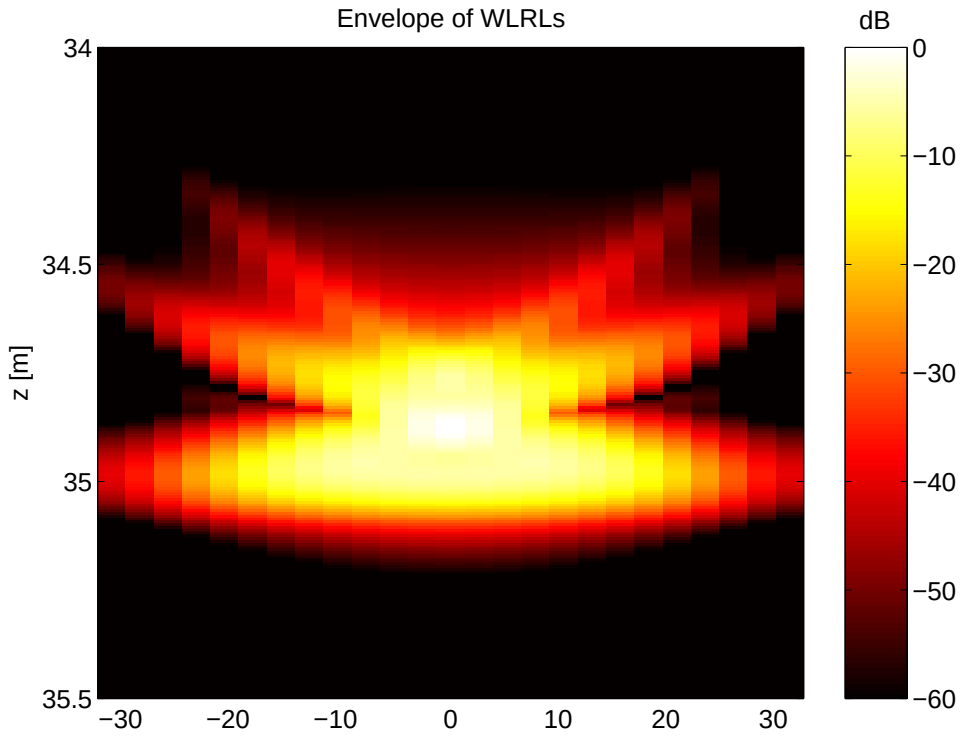

Figure 3.6: The log-compressed and envelope detected LRL's from Fig. 3.5.

angle, $-\alpha \leq \phi_p \leq \alpha$. The positions of the four studies are indicated in Fig. 3.10.

The presentation of the responses in Fig. 3.8, and Fig. 3.9 witness that the pulse-echo signal is not constant across the wave field and the wave front is not spherical. This is most prominent at greater depths. This supports the observation from Fig. 3.7, where the coherence between the HRL and the pulse-echo response is diminished at greater depths. Especially at the center of the wave field there are great aberrations from the spherical wave front. No apodization of the transducer element is applied and effects from the transducer edges does have an influence. The normalized envelopes of the responses in Fig. 3.8, and Fig. 3.9 are shown in Fig. 3.11, and Fig. 3.12. Here it is even more clear that the peaks of the envelopes do not form a straight line. The pulse-echo wave field can not be assumed spherical and originating from the focal point. The responses also show that the estimate of the opening angle from (3.5) seems to be a valid estimate. The wave front was supposed to take form of a straight line within the opening angle and deviate from this beyond the opening angle. It is not easy to conclude though since the wave front is only an approximate straight line.

3.3.2 Signal-to-Noise-Ratio

Provided that the image object does not move in between acquisitions and assuming uncorrelated electronic noise at the receivers the SNR improvement using SAF is

$$\Delta SNR(r) = 10\log_{10}(N_{r_v}(r))\,. \tag{3.7}$$

$N_{r_v}(r)$ is the number of emissions which contributes to the HRL for a transducer element with a VS at radius r_v as shown in Fig. 3.2. With a VS at 20 mm $N_{r_v}(r) = 13$ at radius, $r = 60$ mm. This yields a SAF SNR improvement of $\Delta SNR = 11$ dB. With a lower $F\#$ the number of

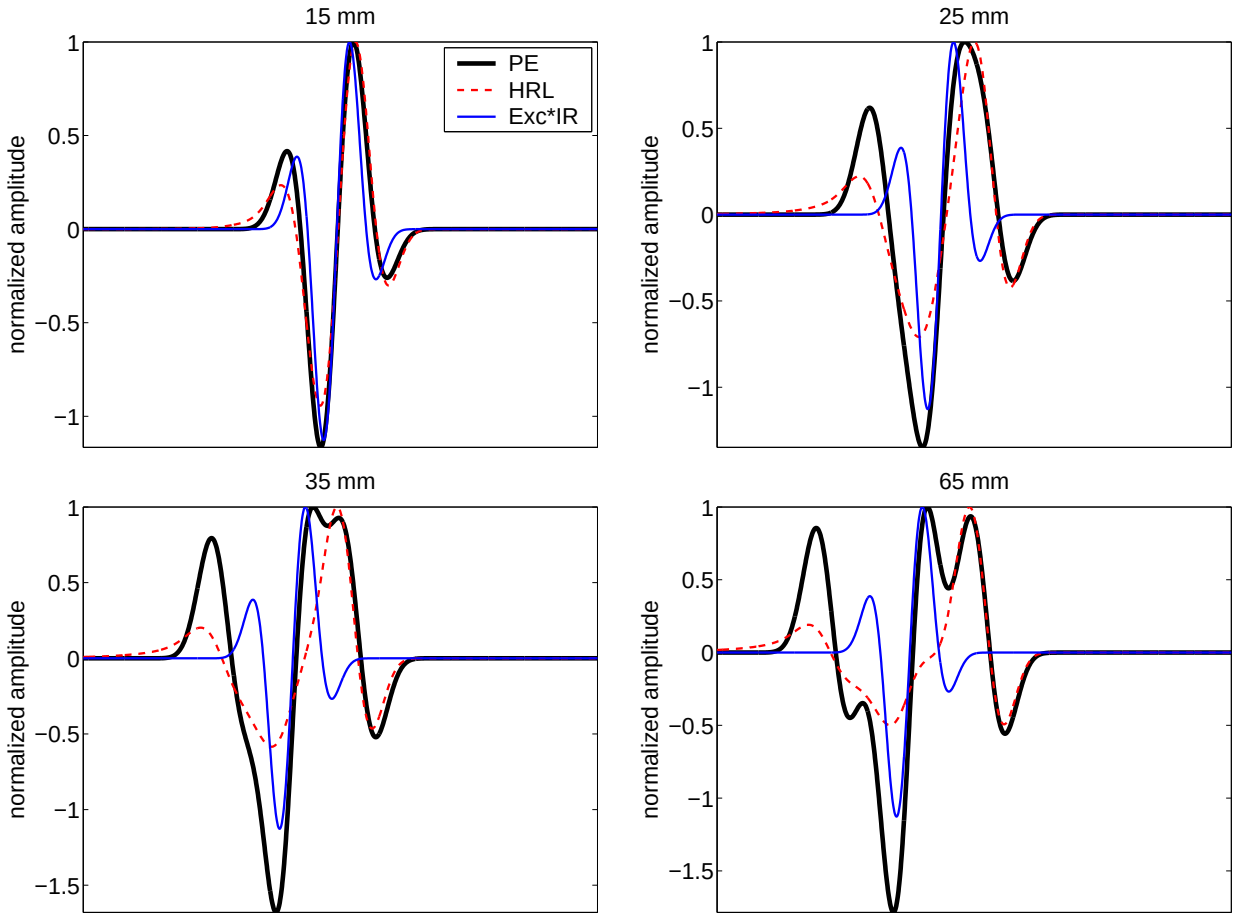

Figure 3.7: The spatial pulse-echo response at the positions, $\vec{r_p} = (0,0,r_{p_z})$ where r_{p_z} is 15, 25, 35, and 65 mm. The electro-mechanical two-way response and the HRL are also shown.

contributing emissions increases, but the width of the wave field does also increase. Provided that the transmitted power is equally distributed over the width of the field, the SAF SNR improvement of a setup with a VS at radius r_v over conventional imaging with a VS at 20 mm can be expressed as

$$\Delta SNR_{r_v}(r) = 10\log_{10}\left(N_{r_v}(r)\frac{W_{r_{20}}(r)}{W_{r_v}(r)}\right). \tag{3.8}$$

$W_{r_{20}}$ and W_{r_v} are the -6 dB widths of the wave fields measured in whole wave lengths for the elements with VS's at radius 20 mm and at radius r_v, respectively. The widths are calculated using the opening angle, α. The width-ratio and the SNR improvement are shown in Fig. 3.13 for elements with VS's at radius $r_v = 10$ mm, $r_v = 15$ mm, and $r_v = 20$ mm. At greater range the width-ratio is 2.5, and 1.5 with elements having VS's at radius $r_v = 10$ mm, $r_v = 15$ mm respectively, while $N_{r_v}(r)$ is 33 and 21. This results in an improvement in SNR of 11 dB in both cases just as the improvement of using SAF on the setup with the VS at radius 20 mm. The SNR improvement can be converted directly to an increase in penetration or an increase in emitted frequency yielding a higher resolution.

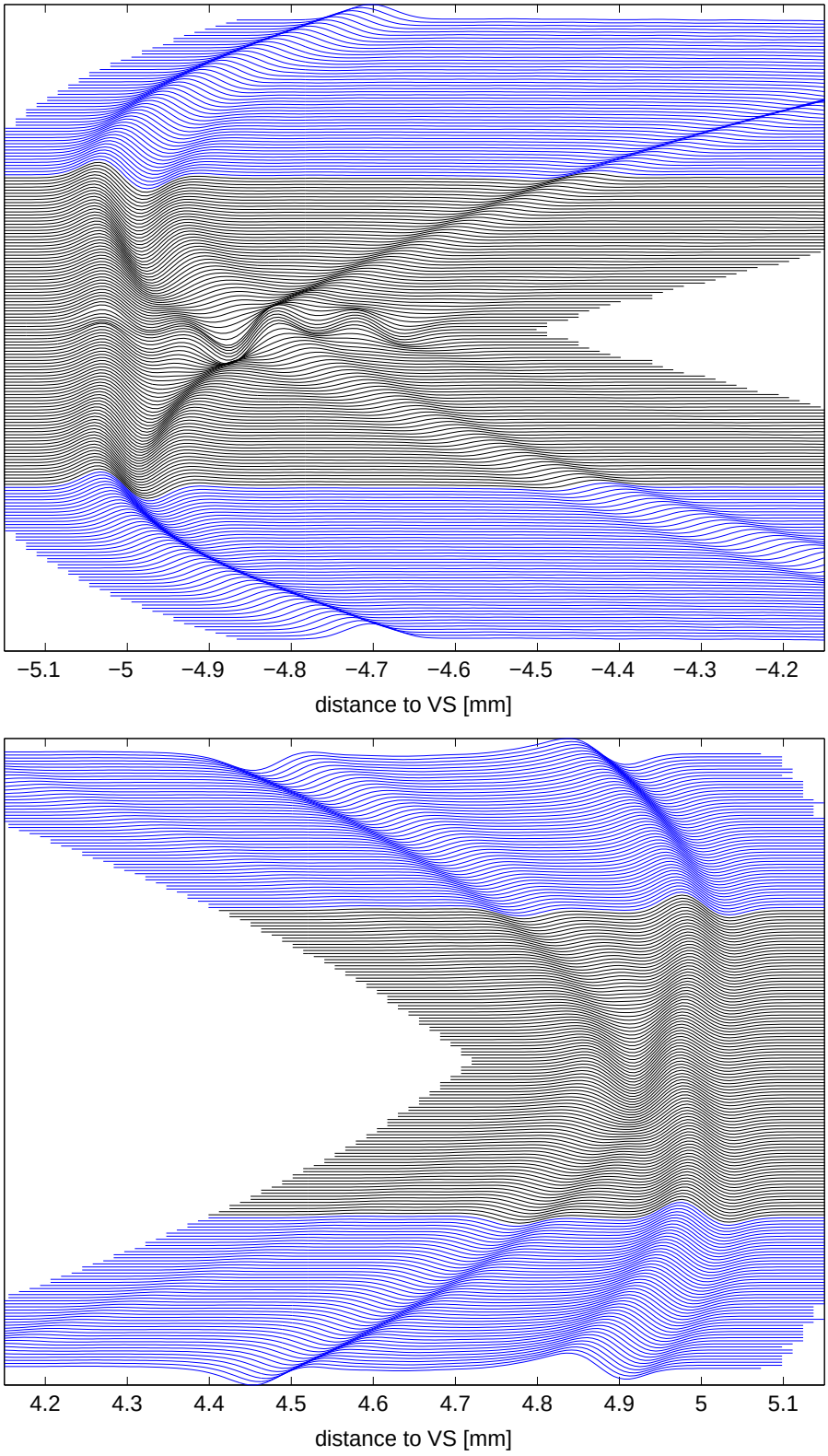

Figure 3.8: A number of pulse-echo responses in different positions are compared. All positions have the same distance to the focal point. The positions are indicated in Fig. 3.10. The distance is 5 mm above the VS (top), and 5 mm below the VS (bottom). The positions span over twice the opening angle, $-\alpha \leq \phi_p \leq \alpha$. Responses from positions within the opening angle are plotted with a different color than for those beyond the opening angle.

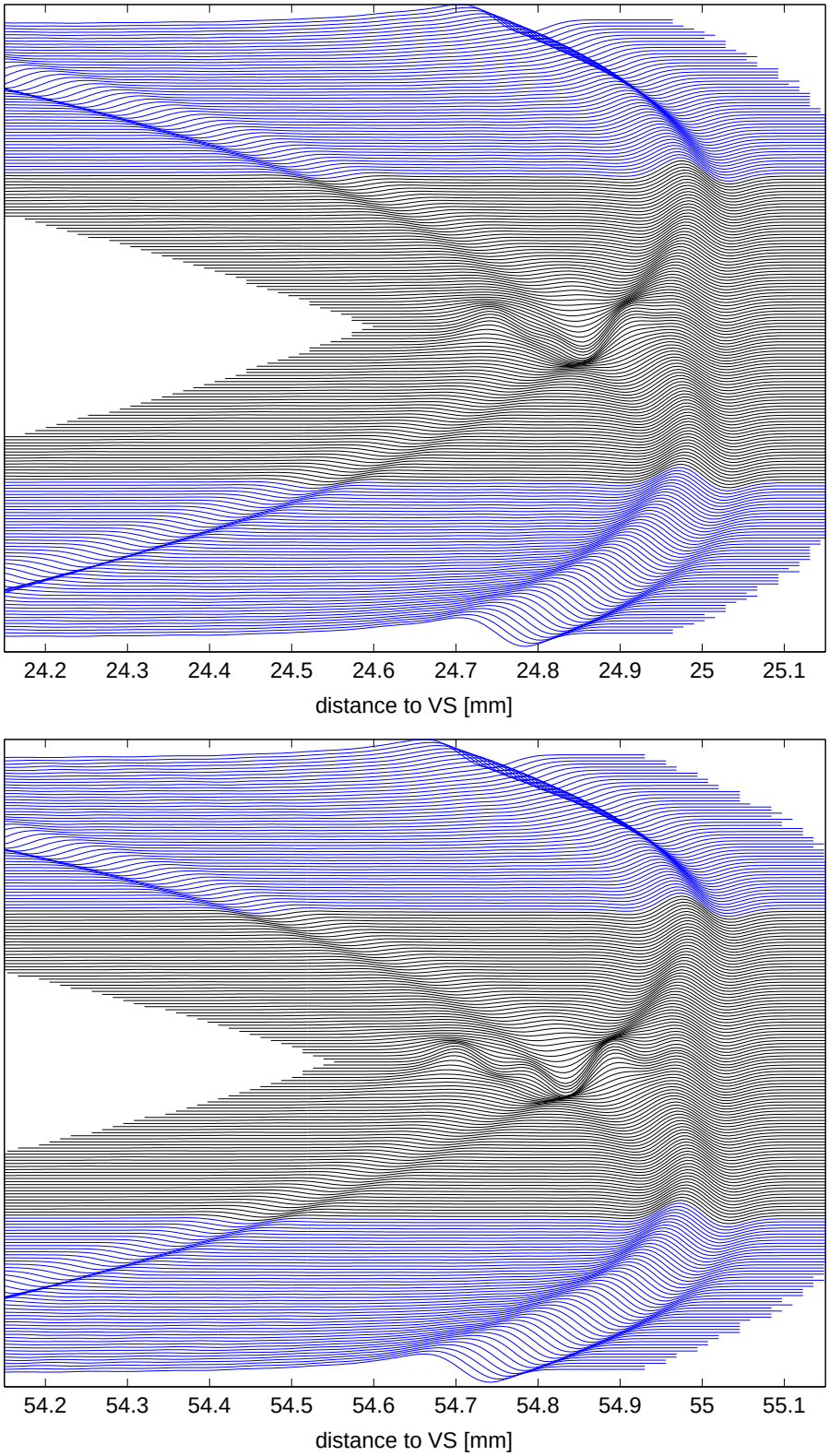

Figure 3.9: A number of pulse-echo responses in different positions are compared. All positions have the same distance to the focal point. The positions are indicated in Fig. 3.10. The distance is 25 mm (top), and 55 mm (bottom). The positions span over twice the opening angle, $-\alpha \leq \phi_p \leq \alpha$. Responses from positions within the opening angle are plotted with a different color than for those beyond the opening angle.

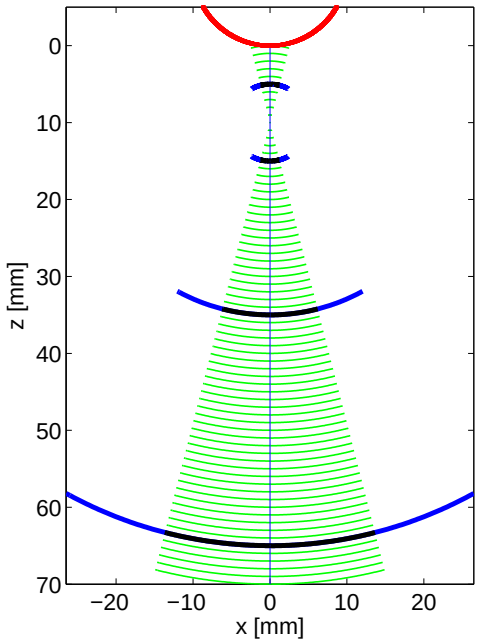

Figure 3.10: Positions at which the spatial pulse-echo responses shown in Fig. 3.8 and Fig. 3.9 are calculated. The positions span over twice the opening angle $-\alpha \leq \phi_p \leq \alpha$.

3.4 Conclusion

Through simulations in Field II mono-static synthetic aperture focusing of pulse-echo data from a rotating concave element has been investigated. The radial and angular resolution have been extracted using transducer elements with a focal depth of 10 mm, 15 mm, and 20 mm. Due to the rotation, the synthesized aperture only experiences a moderate expansion. This is not sufficient to reduce the extent of the wide point spread function of a single emission. At least not to a level which is competitive to the relatively narrow PSF of the setup with focal depth at 20 mm. The effect of SAF with focal depth at 20 mm is also negligible due to the small number of LRL added.

The advantage of the SAF is the increase in SNR. For the setup with focal depth at 20 mm the SAF SNR gain is 11 dB. The SNR gain of a setup with a VS at radius 10 mm or 15 mm over conventional imaging with a VS at 20 mm is also 11 dB. The SNR improvement can be converted directly to an increase in penetration or an increase in emitted frequency yielding a higher resolution.

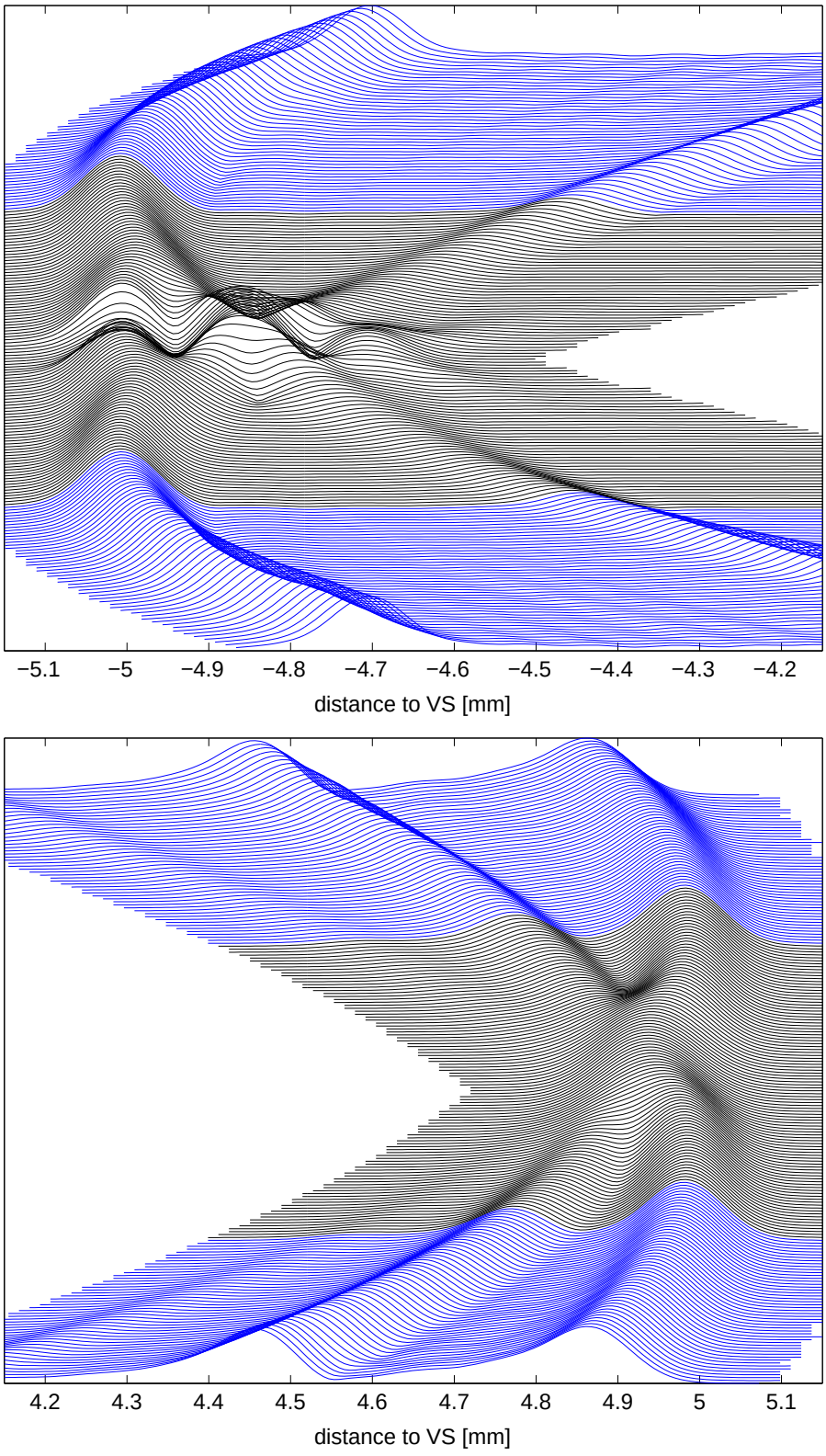

Figure 3.11: The envelopes of the pulse-echo responses from Fig. 3.8.

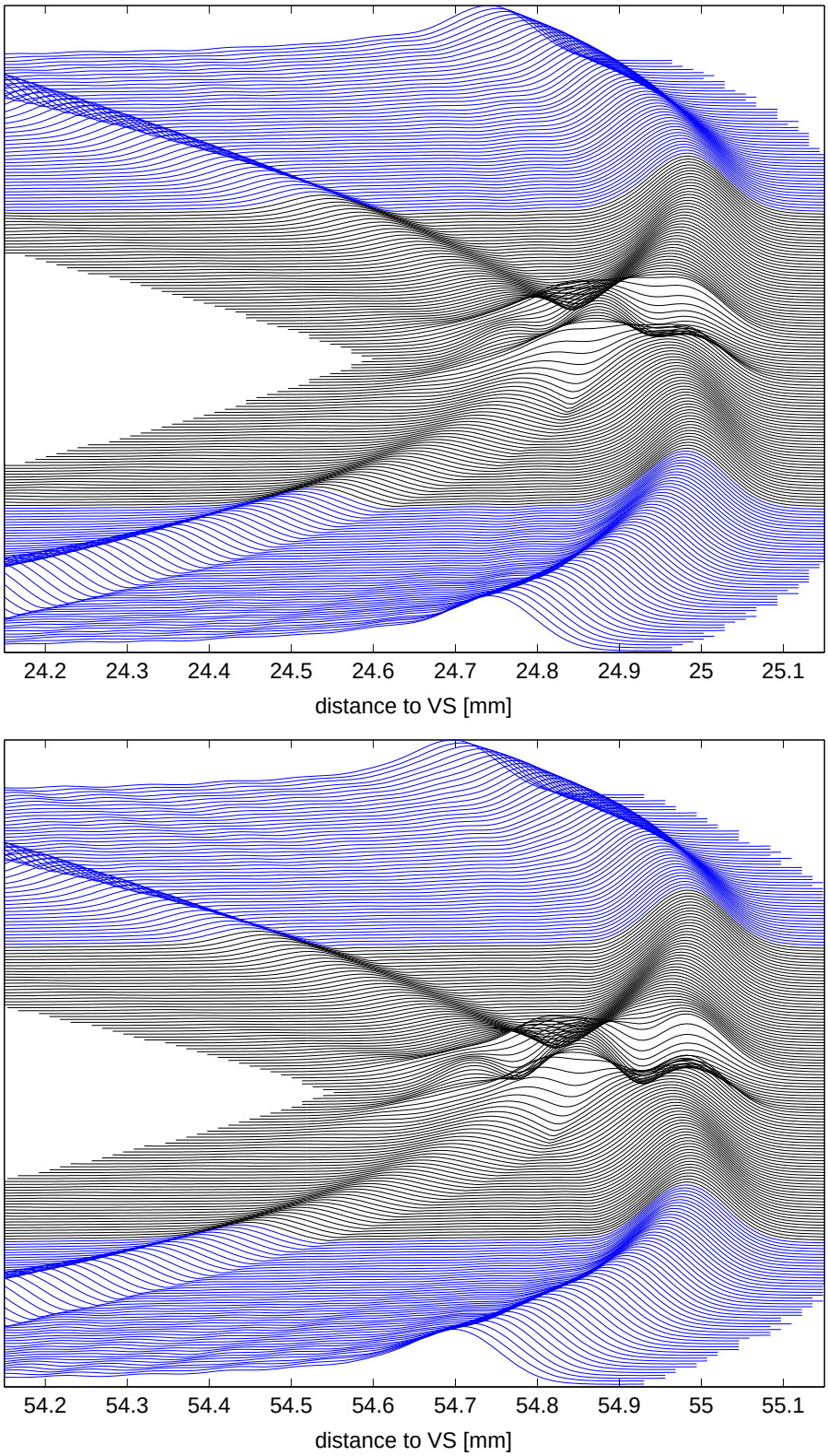

Figure 3.12: The envelopes of the pulse-echo responses from Fig. 3.9.

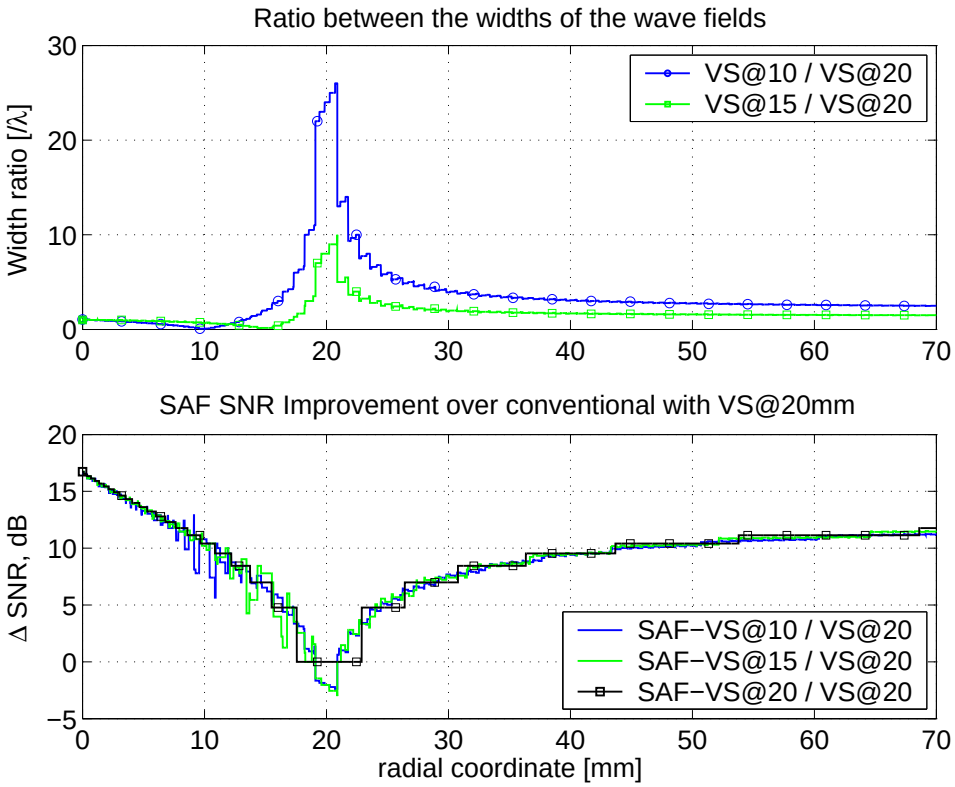

Figure 3.13: The ratio between the width of different wave fields (top) and SAF SNR improvement over conventional imaging with a VS at radius 20 mm (bottom).

CHAPTER

FOUR

Synthetic Aperture Sequential Beamforming

The concept of synthetic aperture sequential beamforming (SASB) is described in the journal paper *Synthetic Aperture Sequential Beamforming* in Appendix B.6. A patent investigation is ongoing at present time and for this reason the paper is not submitted. The vast majority of the content of this chapter is also found in the paper.

Literature within synthetic aperture imaging relevant for the technique presented in this section was given in Section 2.4. An introduction to SASB is given in Section 4.1, and the method is described in more detail in Section 4.2 with a short discussion of issues related to practical implementation of the method. Section 4.3 presents results from the Field II[60, 61] simulation study. A parameter study shows the performance and artifacts of the method for a number of different configurations. This study covers an analysis of grating lobes, the influence of the impulse response of the transducer, and the influence of transmit apodization. The preferred embodiment of the method is discussed and the performance is compared with conventional dynamic receive focusing (DRF). Section 4.4 presents imaging examples and signal-to-noise ratio (SNR) calculations with data acquired from phantom measurements with a commercial scanner.

4.1 Introduction

Mono-static SA focusing applied to imaging with a single rotating mechanically focused concave element was described in Chapter 3 and published by Kortbek et al.[63]. Such an imaging system can e.g. be found in an anorectal ultrasound transducer. One objective of this study was to improve lateral resolution. This was done by storing the RF-lines from every emission and feeding these to a SA beamformer. Due to the small radius of rotation, the synthesized aperture only experiences a moderate lateral expansion. This was not sufficient to reduce the wide extent of the point spread function of a single emission, thus, improvement in lateral resolution was not significant.

The same SAF technique is applied in this chapter, but to linear array imaging. Here the synthesized aperture becomes considerable larger with a lateral translation of the VS than with a rotation. Instead of having a VS created from a single concave element physically focused in both transmit and receive the VS is now created from a sub-aperture - a group of elements. This offers more flexibility since the position and the opening angle of the VS are determined by the electronic focusing instead of the physical concave shape of the single element transducer. The

receive focusing is a simple fixed focusing with receive focal point in the transmit focal point. This first beamformer, thus, mimics the focusing that is a consequence of the concave single element transducer. The focused RF-lines from every emission are stored and transferred to a SA beamformer just as the one applied with the rotating transducer. Two beamformers are, thus, applied sequentially - a simple fixed focus beamformer and a SA beamformer denoted Synthetic Aperture Sequential Beamforming (SASB).

One objective of SASB is to improve the penetration depth. The primary objective though is to improve lateral resolution and obtain a more range independent resolution compared to conventional ultrasound imaging. The improvement is naturally not as great as with a full SA setup. Contrary to a full SA setup only a single RF-line is beamformed and stored for each emission. This reduces the system requirements significantly. For simplicity the method is investigated using a linear array, but it might as well apply to other types of imaging. The investigation comprises performance evaluation at a large imaging range. This is done without consideration for the typical use of the specific transducer but as a mean to demonstrate the properties of the method.

4.2 Method

Synthetic aperture sequential beamforming (SASB) is a two-stage procedure which can be applied to B-mode imaging with any array transducer. The initial step is to construct and store a set of B-mode image lines using a conventional sliding sub-aperture. These 1st stage lines are obtained with a single focal point near the transducer in both transmit and receive. The second stage consist of an additional beamformer using the focused image-lines from the first stage as input data. The concept of virtual sources and means of calculating the focusing delays are briefly discussed in Section 4.2.1 before presenting the SASB in more detail in Section 4.2.2.

4.2.1 Virtual Sources and Focusing Delays

In delay-and-sum receive focusing appropriate delays are applied to the responses of the individual transducer elements originating from the focusing point and coherently adding these responses. The delays are found from the round trip time-of-flight (TOF), which is the propagation time of the emitted wave in its path from the transmit origin to the focusing point (FP), and return to one of the elements of the receive aperture. Different ways of calculating TOF was discussed in Section 2.1.

The transmit origin is not necessarily well defined, if the emitted pressure wave does not emanate from a single element point source. In multi-element synthetic aperture imaging[52] a multi-element transmit sub-aperture is introduced as an alternative to mono-static SAF to ensure sufficient transmitted energy. Here the pressure wave is the result of numerous waves emitted from a multiple elements. With a focused transmission the focal point is introduced as a virtual source, since a spherical wave emanates from this point in a limited angular region. With a known position of the source this allows for the SAF delays to be calculated.

Applying a VS instead of a single element source has a consequence for the calculations of SA focusing delays. In dynamic receive beamforming a new set of delay values is calculated for each focusing point (FP). Assuming the speed of sound c is known, the delay value, t_d for the

receiving element with position $\vec{r}_r$ is calculated in accordance with Fig. 4.1 (left)

$$t_{d_{fp}}(\vec{r}_r) = \frac{|\vec{r}_{tfp} - \vec{r}_e| \pm |\vec{r}_{fp} - \vec{r}_{tfp}|}{c} + \frac{|\vec{r}_r - \vec{r}_{fp}|}{c} \tag{4.1}$$

The transmit origin, $\vec{r}_e$ is the center element of the transmit sub-aperture. $\vec{r}_{tfp}$ and $\vec{r}_{fp}$ is the position of the transmit focal point and the receive focusing point respectively. The $\pm$ in (4.1) refer to whether the FP is above or below the VS.

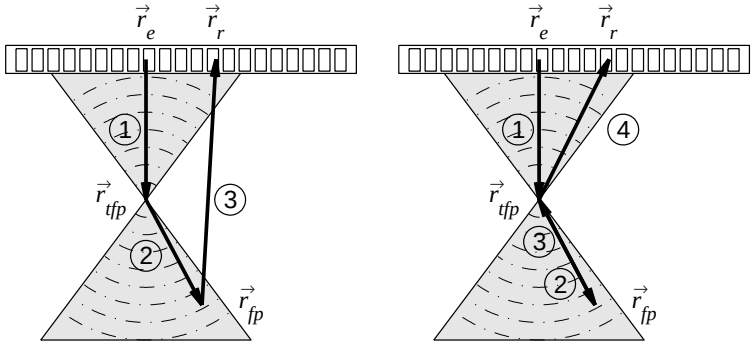

Figure 4.1: Wave propagation path (solid line) for calculating the receive focusing time delays for a focused transmission. The transmit origin is perceived as the center element of the transmitting aperture. Dynamic receive focusing (left) and fixed receive focusing (right).

With SASB the first stage beamformer has a fixed receive focus and the delay values, t_d are calculated in accordance with Fig. 4.1 (right)

$$\begin{aligned} t_{d_{fp}}(z_v) = & \quad \frac{1}{c}\Big(|\vec{r}_{tfp} - \vec{r}_e| \pm |\vec{r}_{fp} - \vec{r}_{tfp}| \\ & \pm |\vec{r}_{tfp} - \vec{r}_{fp}| + |\vec{r}_r - \vec{r}_{tfp}|\Big) \\ = & \quad \frac{1}{c}\Big(2z_v \pm 2|\vec{r}_{tfp} - \vec{r}_{fp}|\Big) \end{aligned} \tag{4.2}$$

z_v is the distance from the aperture to the VS. With dynamic receive beamforming the differences between the individual channel delays changes with the position of the focusing point due to the term $|\vec{r}_r - \vec{r}_{fp}|$ in (4.1). A new set of delay values are, thus, calculated for each focusing point. With fixed receive focusing as in (4.2) only a single set of delay values is calculated and for each focusing point a constant is added. This is an important issue in respect to the complexity of the beamformer. With dynamic focusing the delay calculations involve among others the computational costly square root operation.

4.2.2 Two Stage Beamforming

The 1st stage RF-lines, which are the output from the first beamformer, are obtained with a single focal point near the transducer in both transmit and receive. This focal point is considered as a VS emitting a spherical wave front spatially confined by the opening angle. Each point in the focused image line contains information from a set of spatial positions. These are defined by the arc of a circle limited by the opening angle that crosses the image point and has a center in the focal point as illustrated in Fig. 4.2. A single image point is therefore represented in multiple 1st stage lines obtained from multiple emissions. This is exploited in the second

stage. Each HRI consists of a number of high resolution image lines - the output lines from the 2nd stage beamformer. In this chapter, N denotes the number of emissions, which is the same as the number of 1st stage lines and also the number of high resolution lines. Each sample in a high resolution line (HRL) is constructed in the second beamformer by selecting a sample from each of those 1st stage lines, which contain information from the spatial position of the image point and summing a weighted set of these samples.

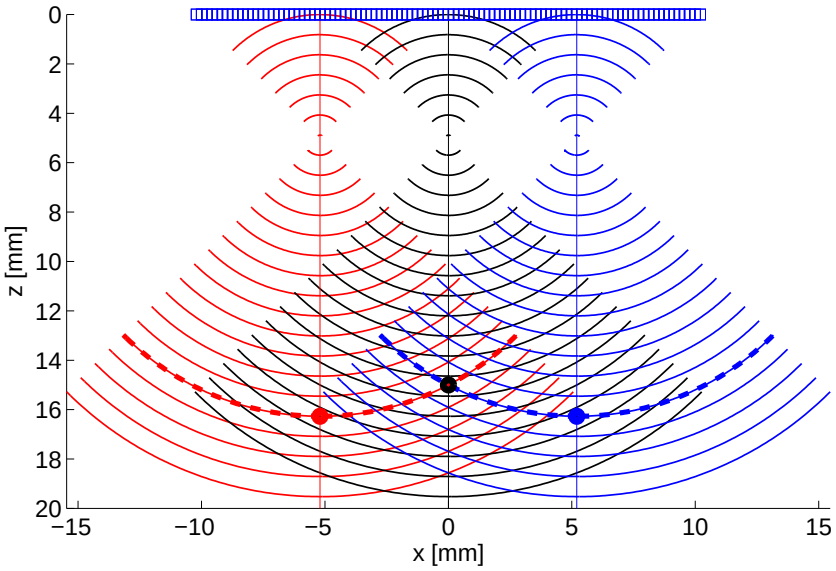

Figure 4.2: Example of wave propagation and 1st stage image lines from 3 different emissions. Each point on the image lines contains information from the spatial positions which are indicated by the arc of a circle intersecting the point. A single high resolution image point of the SASB method is obtained by extracting information from all of those 1st stage image lines which contain information about that point.

The number of elements in the transmit sub-aperture, the depth of the focal point and, thus, the $F\#$ determines the opening angle, hence the width of the transmitted wave field and the point spread function (PSF). A LRI of the entire imaging area can not be formed after each emission due to the spatially limited wave propagation. Instead, for each image point in a HRL it must be determined which emissions that have a wave field encompassing the image point. These emissions contribute to the HRL, and samples from each of them are selected according to the SAF delays, and added together. In other words a single HRL is composed of the sum of a number of low resolution lines. A single low resolution line (LRL) is, thus, the contribution from a given emission to a HRL. The term LRL is used for an RF-line, which has been processed using SAF and which contains at least one non-zero sample that carries information from one of the image points of the HRL.

The SAF can be formulated as a sum over LRL's. A single sample of the HRL, representing the image point at the location $\vec{r}_{ip}$ with lateral coordinate x and axial coordinate z, can be expressed as

$$h(x,z) = \sum_{k}^{K(z)} \mathcal{W}(x_k,z) l_{x_k}(z)\,. \tag{4.3}$$

$h(x,z)$ is the HRL sample, and $l_{x_k}(z)$ is the LRL sample from the emission with lateral position x_k. The variable $\mathcal{W}$ is an apodization function with $K(z)$ values, which controls the weighting of the contribution from each of the LRL's. It is a function of the axial position of the image

point, since the number of contributing emissions, $K(z)$ increases with range. K determines the number of VS's applied for a given HRI point and is a measure of the size of the synthesized aperture. $K(z)$ can be calculated directly from the geometry shown in Fig. 4.3 as

$$K(z) = \frac{L(z)}{\Delta} = \frac{2(z - z_v)\tan(\alpha/2)}{\Delta} \tag{4.4}$$

showing that K increases linearly with range. This facilitates a range independent lateral resolution. $L(z)$ is the lateral width of the wave field at a depth, z, and Δ is the distance between the VS's of two consecutive emissions. α is the opening angle of the VS. It is the angular span for which the phase of the wave field can be considered constant. The opening angle can be expressed as

$$\alpha = 2\arctan\frac{1}{2F\#}, \tag{4.5}$$

which is a valid approximation[35]. With L_A denoting the size of the sub-aperture $F\# = z_v/L_A$.

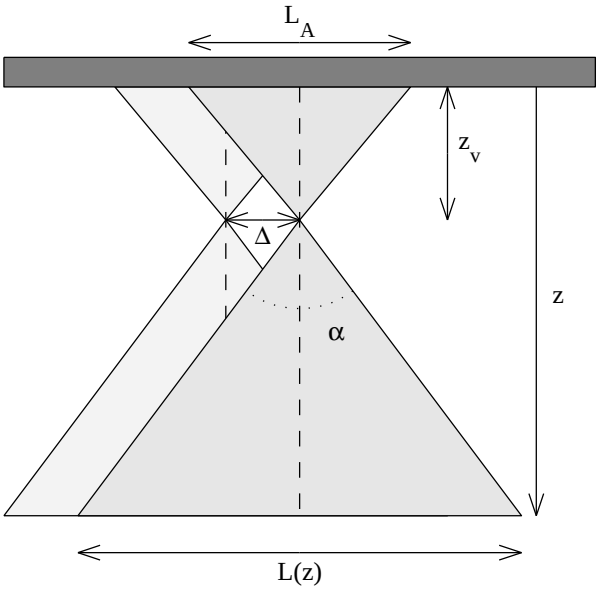

Figure 4.3: Geometry model of the emitted wave fields from two consecutive emissions. The lateral width, $L(z)$ of the wave field at a depth, z determines the number of LRL's which can be added in the 2nd stage beamformer for an image point at depth, z.

The LRL can be formulated using the RF-line, $s_{x_k}(z')$

$$l_{x_k}(z) = s_{x_k}(z'). \tag{4.6}$$

z' is the axial position at which to select a sample from the RF-line and is not the same axial position as in the HRL. z' can be found from the distance function, $z' = d(\vec{r}_{v_{x_k}}, \vec{r}_{ip})$ which calculates the transmit-receive round trip travel path for the SAF, and thus the sample index for the RF-line, $s_{x_k}(z')$. The transducer elements are electronically focused at the VS at the position $\vec{r}_{v_{x_k}}$ with a focal distance of z_v from the aperture. The aperture is focused in both transmit and receive and the distance function becomes a sum of transmit and receive travel paths

$$d(\vec{r}_{v_{x_k}}, \vec{r}_{ip}) = 2z_v \pm 2|\vec{r}_{ip} - \vec{r}_{v_{x_k}}| \tag{4.7}$$

The $\pm$ in (4.7) refer to whether the image point is above or below the VS. A single sample of the HRL can thus be formulated using (4.3) and (4.6)

$$h(x,z) = \sum_{x_k}^{K(z)} \mathcal{W}(x_k,r) s_{x_k}(d(\vec{r}_{v_{x_k}},\vec{r}_{ip})) \,. \tag{4.8}$$

The formulation of the method in this section assumes an aperture with an infinite number of elements. This becomes apparent when observing (4.4). At greater depth $K(z)$ will exceed the number of available 1st stage lines, N. At depths beyond the point where $K(z) = N$ the synthesized aperture will no longer increase with depth. The $F\#$ will increase and the lateral resolution will no longer be range independent beyond that depth. Another consequence of a limited element count is that the opening angle of the VS decreases as the position of the VS approaches the transducer edges as indicted in Fig. 4.4. The synthesized aperture decreases for the HRL's near the edges, since K decreases. The lateral resolution is, thus, laterally dependent. The apodization function $\mathcal{W}$ is also laterally dependent with a finite aperture. The

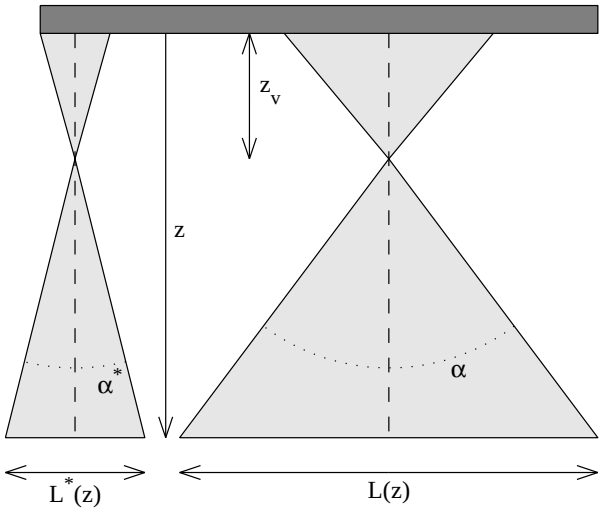

Figure 4.4: Geometry model of the emitted wave fields from two emissions. The opening angle of the VS decreases as the position of the VS approaches the transducer edges. This has an influence on the calculation of $K(z)$ and makes the lateral resolution laterally dependent.

HRI is composed of a sum of LRI's from multiple transmissions as formulated in (4.8). The formulation assumes that the image object is stationary during all transmission, which is not the case in-vivo. Tissue motion and motion artifacts are nevertheless not completely destructive to SA imaging. The susceptibility to motion of SA imaging has been investigated by several authors[18, 19, 64, 65, 66, 67, 68, 69, 70], and techniques to address the problems with tissue motion have been demonstrated.

4.2.3 Implementation

In SAF data from multiple emissions are applied. This could essentially decrease the image frame rate if a full set of emissions is needed to construct a HRI. Nikolov and Jensen proposed SA recursive imaging[71] to be able to construct a new frame after each emission. In SASB acquisition of a full set of N emissions is also a necessity before a HRI can be constructed. By

storing the N most recent 1st stage lines a new HRL can be constructed after each emission. This is feasible by having a temporal offset between the reconstructed HRL and the acquired RF-line corresponding to $N/2$ emissions. The RF-lines across the aperture are denoted $j = 1,2,\ldots N$ and the HRL's are denoted $J = 1,2,\ldots N$. The HRL $J = n$ can be constructed while acquiring the RF-line, j

$$j = \begin{cases} n+N/2 & \text{for} \quad 1 \leq n \leq N/2 \\ n-N/2 & \text{for} \quad N/2 < n \leq N \end{cases}$$

Following this scheme the 1st stage lines which potentially can contribute to a given HRL, is always available.

A view on implementation of the SASB at a block function level demonstrates a requirement for two beamformers and memory for storage of the 1st stage image lines to feed the 2nd stage beamformer. The 1st stage beamformer is simple since the receive delay-profiles are the same for all image points except for a depth dependant additive constant. It only requires calculation of a single profile or a look up table (LUT) with a single entry. It could easily be analog and thereby save many ADC's. The 2nd stage beamformer has the complexity of a general dynamic receive focusing beamformer. For each depth a separate entry in a LUT for a profile is required or the delay profile must be calculated. Apodization is also a desirable requirement for the 2nd stage beamformer to suppress off-axis energy lobes. Since $K(z)$ increases linearly with depth the apodization is dynamic. The apodization is also a function of the lateral position of the HRL due to the finite aperture and it can profitably be calculated as a parametric function. The number of channels in the 2nd stage beamformer is determined by the number of acquired 1st stage lines and a combination of the demand for penetration and resolution.

4.3 Simulation Results

In this section the method is investigated using simulations in Field II[60, 61] and SAF is carried out using the Beamformation Toolbox, *BFT2*[62]. Images of point targets using different realizations of SASB are created. The axial and lateral resolution are extracted and compared to conventional B-mode imaging. The simulations are made with a model of a linear array 7 MHz transducer with properties similar to a commercial transducer.

4.3.1 Setup

The parameters which are the most decisive for the performance of the SASB imaging method are the depth z_v (the focal depth), and the $F\#$ of the VS. A parameter study is done by varying z_v with values of $5, 10, 15, 20$ mm and the $F\#$ with values in the range 0.5 to 2.5. The study is done with a fixed set of transducer parameters and processing parameters shown in Table 4.1.

In the main parameter study the value of $N_e = 401$ has been set to exclude the effects of a finite aperture to demonstrate the ability of the method to generate a range independent resolution. The number of 1st stage image lines and also 2nd stage image lines is the same as the number of transducer elements. Only LRL's symmetric around the HRL are valid candidates for the 2nd stage processing. The apodization function for a given depth $\mathcal{W}(z)$ may differ between two neighboring HRL's if the number of symmetric LRL's is different.

In this study a single cycle sinusoid with frequency, f_0 is used as excitation. A weighted double cycle sinusoid with frequency, f_0 is used to simulate the transducer impulse response. Another

Parameter		Value
Various		
Sampling frequency	f_s	120 MHz, (20 MHz)
Transducer		
Pitch	Δ	0.208 mm
Center frequency	f_0	7 MHz, (5 MHz)
Bandwidth, relative	B	0.6
Elevation Focus	z_{ele}	25 mm
Number of elements	N	401, (191)
Excitation		1, (2) cycles
Impulse response		1-cycle, (measured IR)
1st stage processing		
Focusing		fixed, (xmt/rcv)
Number of channels, xmt/rcv	N_{1st}	63/63
Transmit Sub-aperture		Symmetric only
Transmit apodization	$\mathcal{A}_{xmt}$	Hamming, (Boxcar)
Focal depth (virtual source)	z_v	$5, 10, 15, 20$ mm
Receive Apodization	$\mathcal{A}_{rcv}$	Hamming
Receive Sub-aperture		same as transmit
Number of image lines	N	401, (191)
Distance between lines	Δ	0.208 mm
2nd stage processing		
Focusing		Synthetic aperture
Number of channels	N_{2nd}	401, (191, 127, 63)
SA Weighting	$\mathcal{W}$	Hamming
Number of image lines	N	401, (191)
Distance between lines	Δ	0.208 mm
Applied 1st stage lines		Symmetric only

Table 4.1: Applied values for the simulation parameter study. Values in brackets are applied for various performance illustrations. If nothing else is noticed the value without brackets are applied.

less extensive study is performed with more practical realizable parameters. The number of elements is $N = 191$. A double cycle sinusoid forms the excitation, and the measured impulse response of the applied transducer type is used. The scattering media consists of stationary point targets (PT) placed in the center of the image in the range from 5 mm to 95 mm with a distance of 10 mm.

4.3.2 Resolution Study

Different realizations of SASB are simulated to evaluate performance and limitations. The position of the VS and the opening angle determines the image area covered by a single emission. If the covered area increases, the number of 1st stage lines which can be used for the 2nd stage beamforming, also increases, yielding a larger synthesized aperture. This explicitly sets demands on the size of the array and the number of required 2nd stage beamformer channels if a range independent resolution is the objective. The study will show that other complications

exist with the combination of a shallow focal depth and a large opening angle.

The envelope HRI's are shown in this section. The axial and lateral resolution are extracted at the image center for several depths. The resolution is quantified at -6 dB, the Full Width at Half Maximum (FWHM), and at -40 dB. For each PT the resolution is calculated as the width at which the envelope amplitude has decreased to the specified level relative to the maximum level at that given PT. For the lateral resolution the envelope amplitude is taken as the maximum amplitude within a axial range of $\pm$ 3 mm around the PT. Likewise for the axial resolution the envelope amplitude is taken as the maximum amplitude across the entire lateral range of the image. A poor lateral resolution is the consequence of having a PSF with a wide main lobe and/or high side-lobe levels. The illustrations of the quantified lateral resolution reflects this by also showing the main-lobe resolution as a dotted line, but only if the lateral PSF has a distinct main-lobe and side-lobe distribution. That is if the lateral PSF drops below the -40 dB level and rises above this level again at a wider lateral position.

The PSF at the output of the 1st stage beamformer has a large extent because of the fixed receive focusing. The curvature is determined by the distance between the VS's and the point of the PSF. Consider the point at position $\vec{r}_p = (x,z) = (0,z_p)$. The curvature, $z_c(x)$ is

$$z_c(n) = z_p + \sqrt{(z_p - z_v)^2 + (|n|\,\Delta)^2}\,. \tag{4.9}$$

The variable x has been substituted by $n\Delta$, where $-N/2 \leq n \leq N/2$ is the VS number counting from the VS at $x = 0$. The contour plot of the PSF is shown in Fig. 4.5 with a VS at 5 mm and with $F\# = 0.5$, and $F\# = 2$. The shape of the PSF is the same in both cases, but the width of the PSF differs due to the different opening angles. $z_c(n)$ from (4.9) has been plotted on top of the contour plot to illustrate the coherence. A PT is placed at $z = 65$ mm and z_c has been plotted for two points at $z_p = 64$ mm and $z_p = 66$ mm, respectively. The curvatures of these plots are the same as for the PSF.

The envelope images after 2nd stage processing of these data sets are shown in Fig. 4.6 with a 60 dB dynamic range. The images are constructed with $N = 401$ which equals an image width of approximately 83 mm, but the displayed images have been cropped to a width of 40 mm. If the dominant side-lobes are discounted to begin with the resolution seems range independent. The lateral resolution decreases as the $F\#$ increases as expected because of the decrease in the width of the synthesized aperture.

The number of applied 1st stage lines in the 2nd stage beamformer at a given depth determines the width of the synthesized aperture. This is expressed by $K(z)$ from (4.4). This was for the image-center line only, and assumed an infinite aperture. The theoretical required number of lines, and the actual number of applied lines for the center HRL is shown in Fig. 4.7 for the different setups represented in Fig. 4.6. The linear dependence on depth is only a reality until a certain depth. At this depth the required number of applied VS's approaches a level where the VS's near the transducer edges are included. The opening angles of these VS's decrease due to the limited aperture and the slope of $K(z)$ drops off. This drop-off occurs at 42 mm and 84 mm for $F\# = 0.5$ and $F\# = 1$ respectively. For $F\# = 1.5$ and $F\# = 2$ the linearity is maintained through range.

The lateral PSF's at the different PT's are shown i Fig. 4.8. As the $F\#$ increases the beam width increases and the off-axis energy lobes decreases. The massive off-axis energy lobes for low values of $F\#$ is discussed in Section 4.3.2. For a fixed $F\#$ the profiles are very similar within a dynamic range of approximately 40 dB. This is an indication of a fairly range independent resolution. This is also demonstrated in Fig. 4.9, where the quantified resolution is shown.

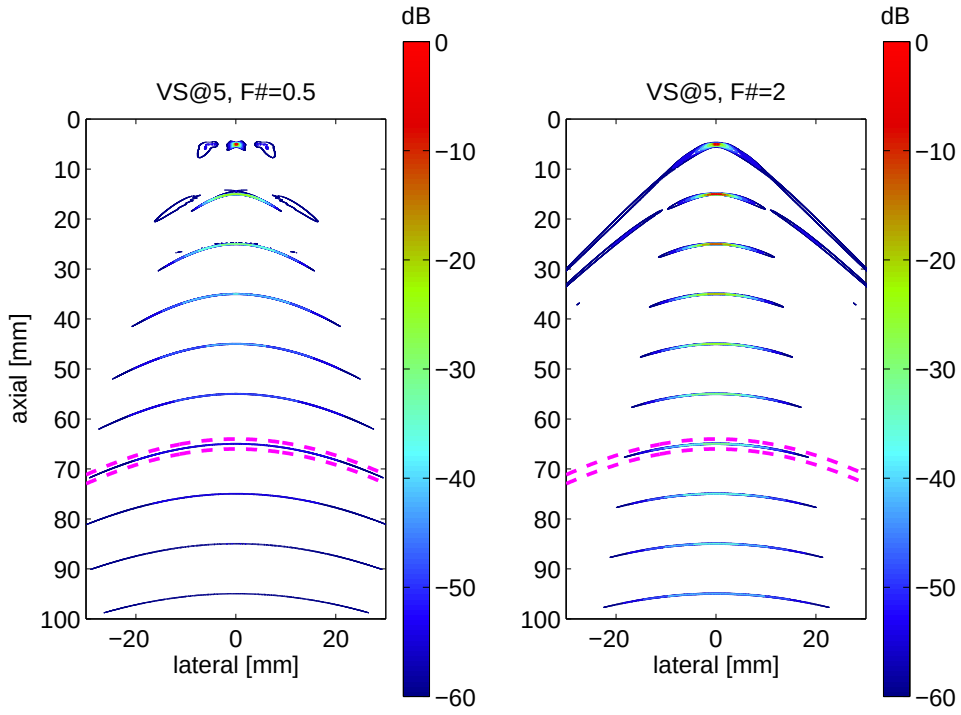

Figure 4.5: Contour plots of the envelope of the output from the 1st stage beamformer. $F\# = 0.5$ (left), and $F\# = 2$ (right). The VS is at 5 mm. The curvature of the PSF is determined by the distance between the VS's and the point of the PSF. This is calculated analytically and shown as dotted lines for two points just above and below the PT at $z = 65$ mm.

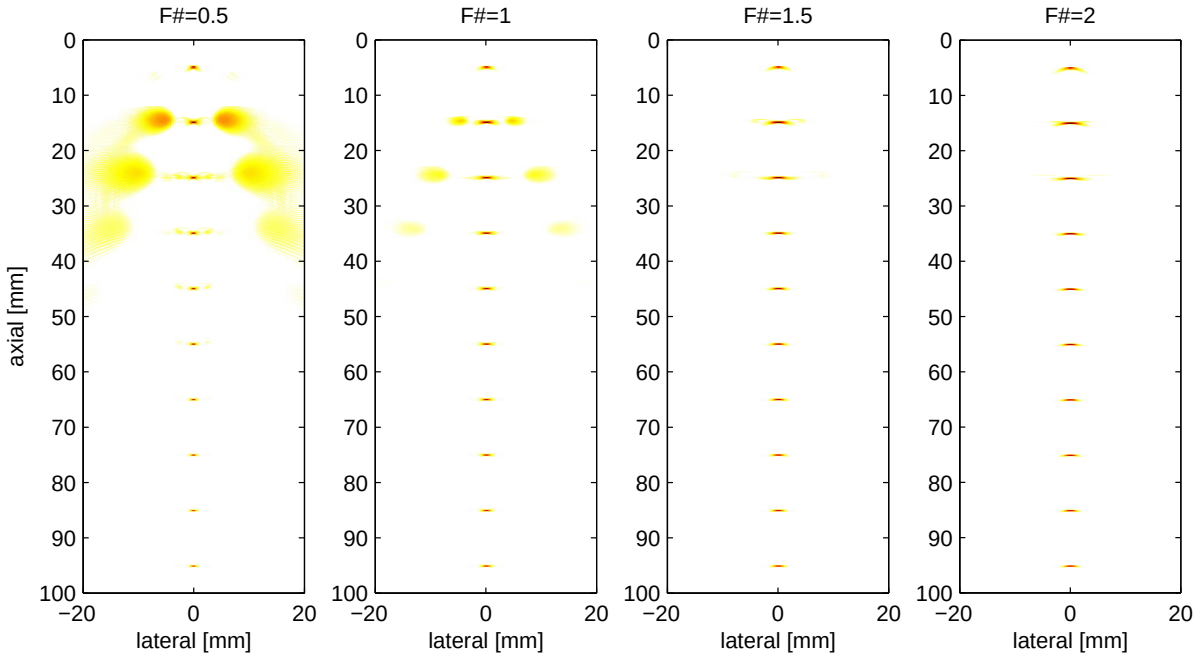

Figure 4.6: Envelope Images with the VS at 5 mm and with different values of $F\#$. Dynamic Range is 60 dB.

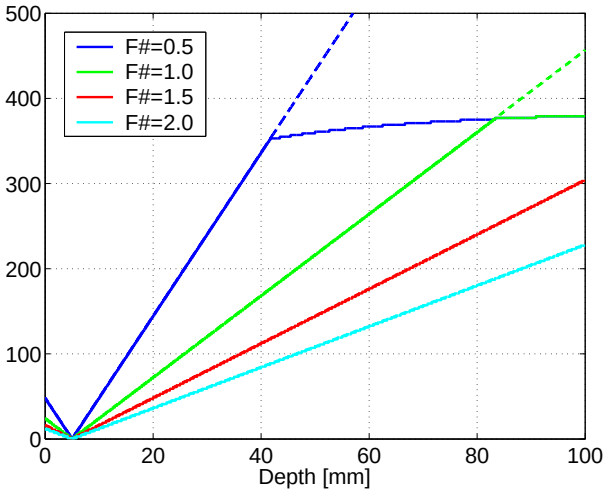

Figure 4.7: The number of applied 1st stage lines in the 2nd stage beamformer for the center HRL. Shown for the four different setups represented in Fig. 4.6. Required number to obtain range independent resolution (dotted lines). Actual number of applied lines (solid lines).

The resolution is practically constant at -6 dB and -40 dB through range for all values of $F\#$, with a few exceptions. As stated previously the linear relation between depth and $K(z)$ is only valid until $z = 42$ mm and $z = 84$ mm for $F\# = 0.5$ and $F\# = 1$ respectively. This has a direct consequence on the FWHM and can be read from Fig. 4.9 directly. The resolution ceases to be constant at these depths and starts to increase linearly.

Another exception from the constant and range independent resolution is for those PT's in near proximity to the VS when $F\# = 0.5$. Here the off-axis lobe level is very dominant. A single lateral profile is shown in Fig. 4.10 for the PT at 15 mm to illustrate this. The points on the profile at which the lateral resolution, and the main-lobe resolution is quantified for the -40 dB level are also shown.

Side-lobes are also noticeable for $F\# = 1$ when looking at the HRI in Fig. 4.6. They are below the -40 dB level though and do not show in Fig. 4.9. They do show when looking at the -50 dB level in Fig. 4.11. Again the main-lobe resolution (dotted line) is practically constant but the difference between the main-lobe resolution and the resolution including the side-lobes (solid line) is significant.

Additional performance results are shown in Appendix A for a number of different configurations.

Investigating grating-lobes

The off-axis energy-lobes in Fig. 4.6 for $F\# = 0.5$ are dominant. Taking a closer look at the phase of those LRL's which are summed in the 2nd stage beamformer can disclose the origin of this artifact. The part of the image containing the PT at 15 mm is shown in Fig. 4.12. Three different HRL's are investigated. They are marked with dotted lines in Fig. 4.12. SASB relies on phase coherent addition of the LRL's as expressed in (4.3). The LRL's composing the center HRL are plotted in Fig. 4.13. It is apparent that the LRL's are completely phase aligned and add up constructively as expected. The figure shows the LRL's before and after the weighting function. It also shows the HRL, hence the summation of the LRL's and the corresponding

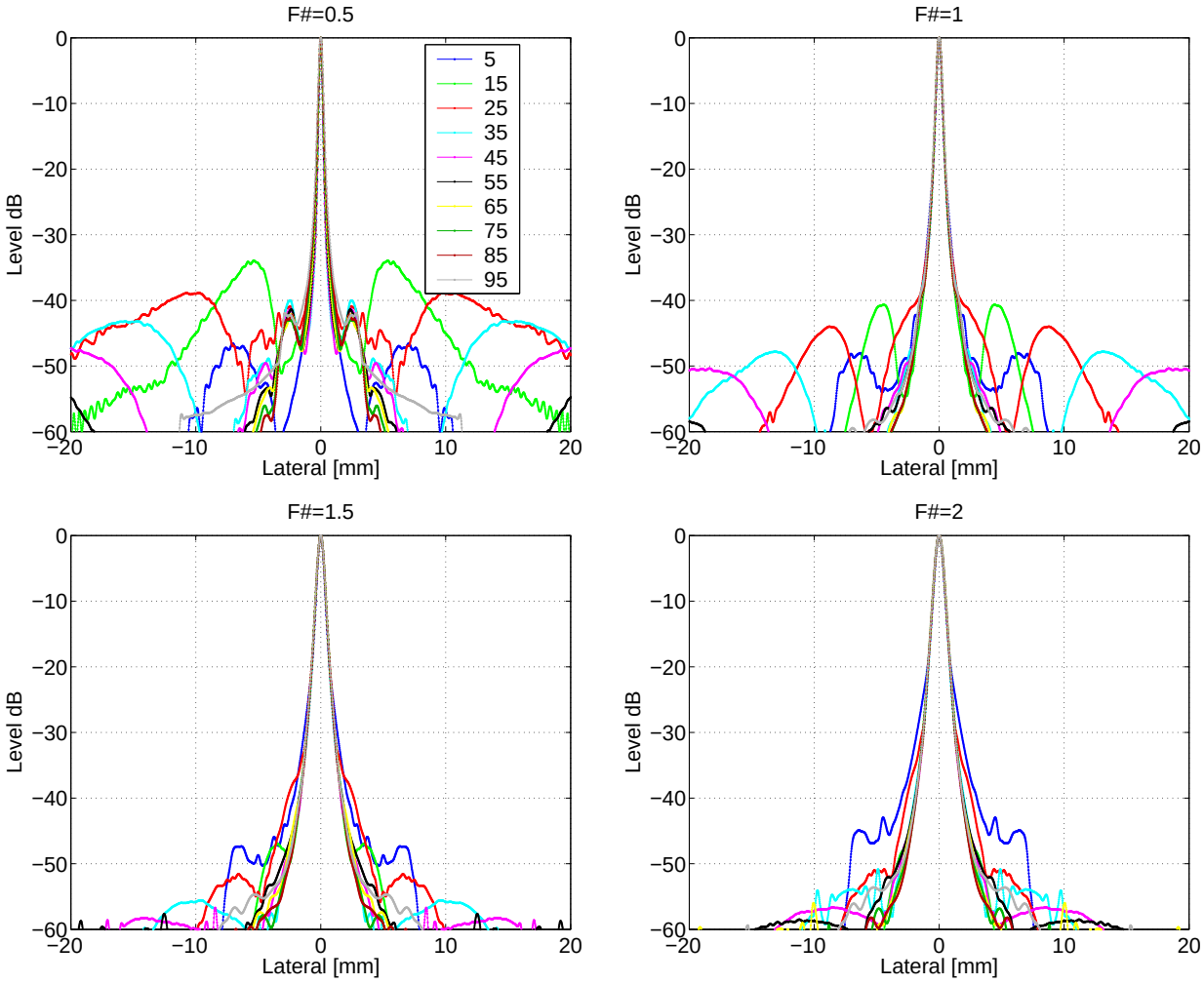

Figure 4.8: Lateral PSF's at different depths are stacked up for the four different setups represented in Fig. 4.6.

envelope. Finally the envelope of the weighted HRL is shown relative to the maximum of the HRI in Fig. 4.12.

The LRL's composing the HRL at $x = 3.1$ mm are plotted in Fig. 4.14. The LRL's are shown before the weighting and a zoom in on a few of the LRL's after the weighting function is shown. The phase shift between consecutive LRL's is close to half a pulse-echo wave length and this destructive summation yields an envelope level near -60 dB.

The LRL's composing the HRL at $x = 6.7$ mm are plotted in Fig. 4.15. The phase shift between consecutive LRL's has increased to almost an entire pulse-echo wave length and the LRL's add up constructively to an envelope level above -40 dB. In this simulated setup the pulse-echo signal consists of only a few periods, hence only a few non-zero contributions are included in the summation of the LRL's. If the pulse-echo signal contains several periods several non-zero LRL's will be present in the sum, yielding an even higher envelope level.

The artifacts shown are best described as grating lobes, since they arise due to lateral spatial under-sampling. Consider having a setup with a phased array transducer with a $\lambda/2$ pitch and, thus, twice the lateral density of VS's. The illustration of LRL's prior to summation equivalent to the one shown in Fig. 4.15 will contain LRL's with a phase shift between consecutive LRL's

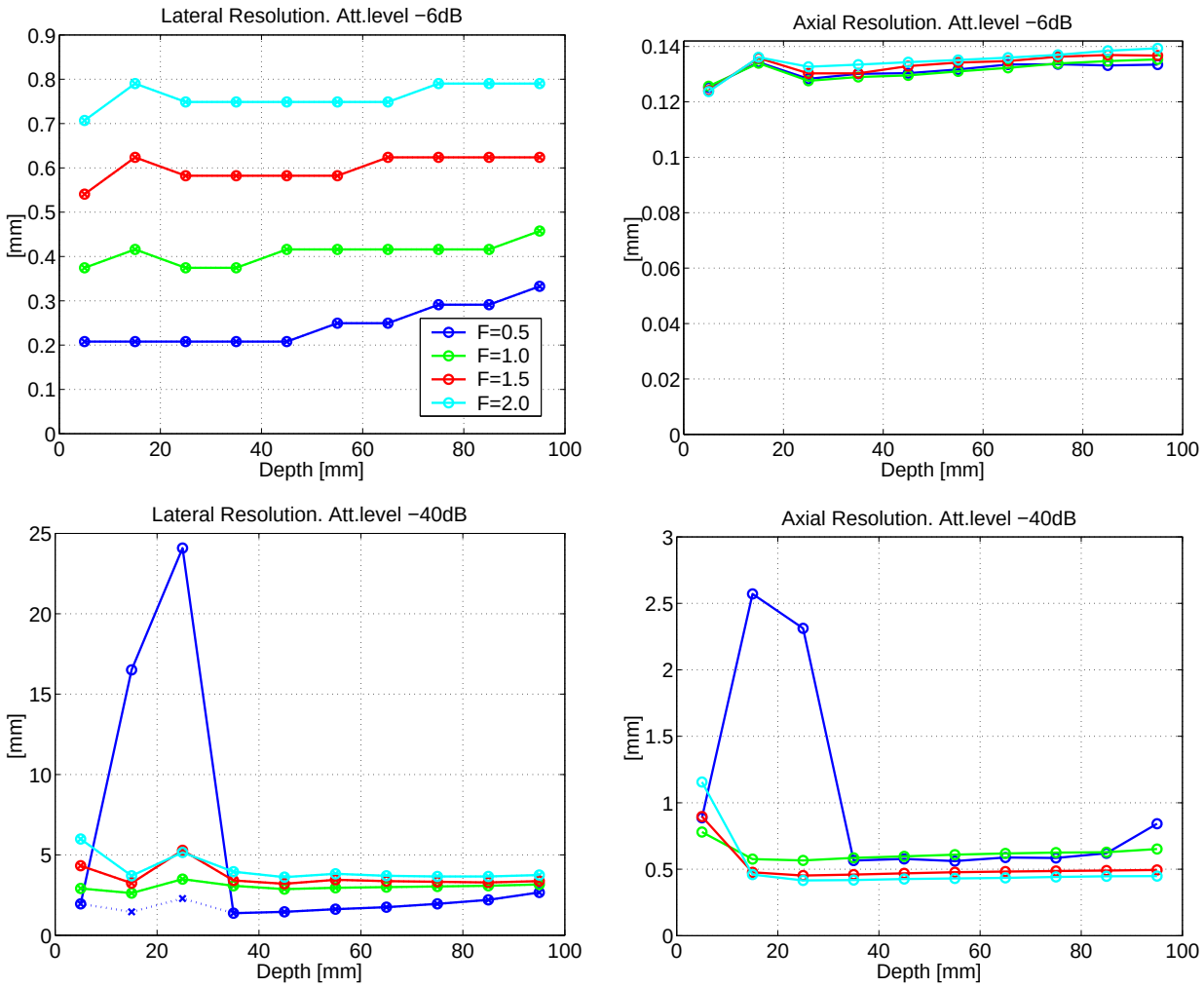

Figure 4.9: Resolution as function of depth at -6 dB (top) and -40 dB (bottom). Lateral resolution (left) and axial resolution (right). If the lateral PSF has a distinct main-lobe and side-lobe distribution, the main-lobe resolution is shown as a dotted line. Shown for the four different setups represented in Fig. 4.6.

of only half a wave length. Every second LRL will be equal to the ones shown in Fig. 4.15 but every other LRL will have a phase which is in between the two. The result is destructive summation instead of unintentional constructive summation, and the massive grating lobes are avoided. This is exemplified in Fig. 4.16. Two HRI's are constructed using a linear array with λ-pitch and a linear phased array with $\lambda/2$-pitch respectively. Both having 401 elements, a VS at 5 mm, and with $F\# = 0.75$. The linear array is, thus, twice the width of the phased array, but the image has been cropped to the same width as the phased array image. The difference between the images is striking, since the grating lobes are avoided by increasing the lateral spatial sampling in the 1st stage processing. With a phased array the linear relation between depth and $K(z)$ is valid for only half the range of a linear array with the same element count.

The VS's can be conceived as elements in a virtual array. In SASB the wave fields from several emissions are sampled by the virtual array and coherently added. Grating lobes arise at a combination of a sparse spatial sampling by the virtual array and wave fields with incident angles beyond a certain limit. Both of these parameters can be controlled in SASB to prevent grating lobes. For a given array and a fixed distance between the VS's the range of incident

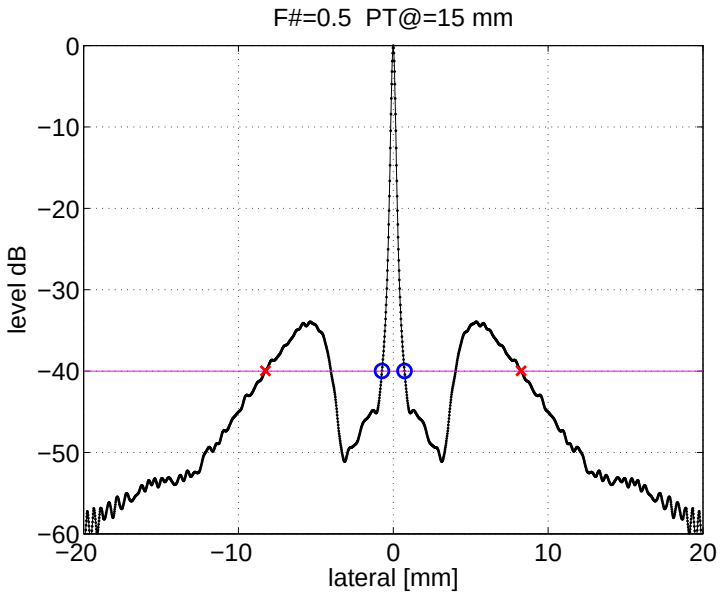

Figure 4.10: A single lateral beam profile for the PT at 15 mm, from setup in Fig. 4.6 with $F\# = 0.5$. The points on the profile at which the lateral resolution, and the main-lobe resolution is quantified for the -40 dB level are also shown.

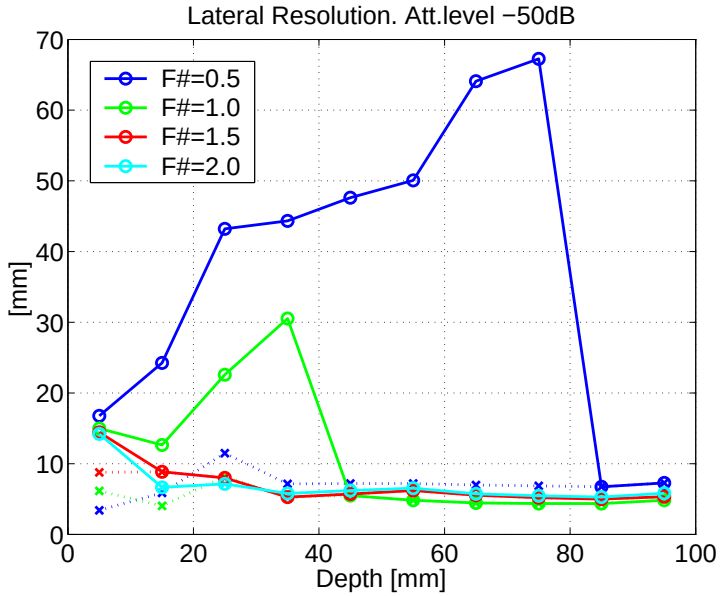

Figure 4.11: Lateral Resolution as function of depth at -50 dB. The main-lobe resolution (dotted line), and the resolution including the side-lobes (solid line). Shown for the four different setups represented in Fig. 4.6.

angles must be restricted. This is possible by putting a limit to the opening angle of the VS.

The restriction on the opening angle to avoid grating lobes can be determined from an analysis of the LRL's constituting the off-center HRL's. The appearance of these LRL's can be predetermined to some extent. In Fig.4.15 the LRL's constituting the center HRL at the lateral position $x_h = 0$ are phase-coherently aligned. They are aligned at the depth, $z_p = 15$ mm, where a PT at $\vec{r}_p = (x,y) = (0,z_p)$ is placed. The line of phase equality is perpendicular to the line with

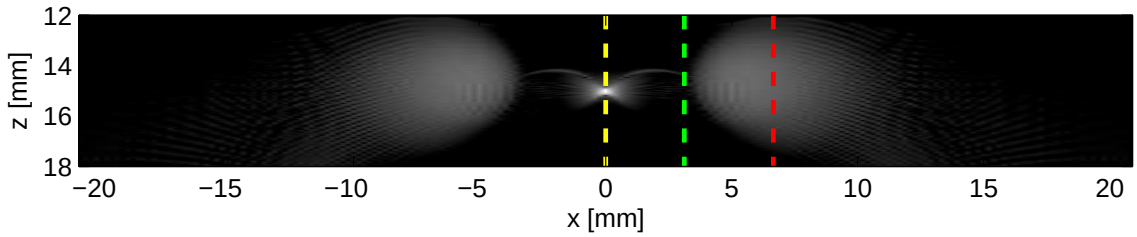

Figure 4.12: A zoom in on the HRI shown in Fig. 4.6 for $F\# = 0.5$. Three different HRL's are marked with dotted lines. The LRL's composing these HRL's are shown in Fig. 4.13, Fig. 4.14, and Fig. 4.15.

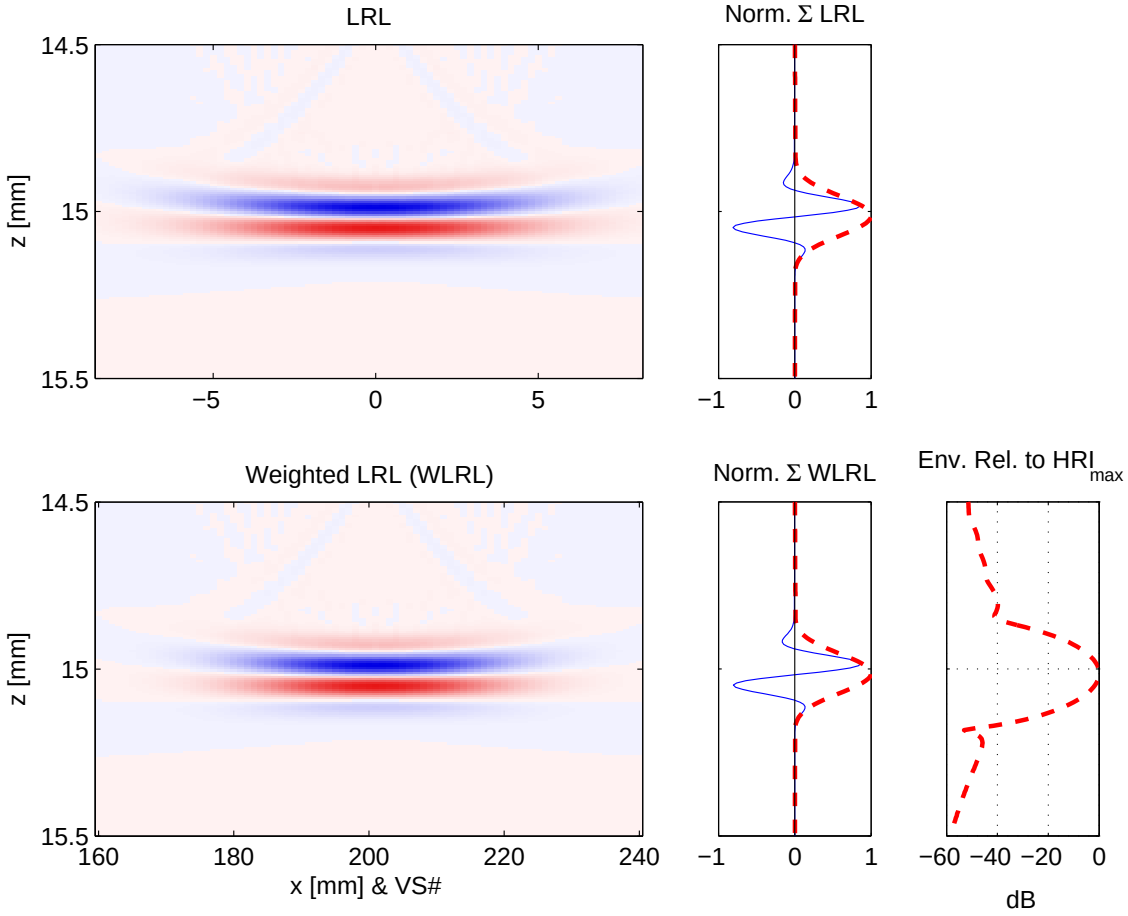

Figure 4.13: The LRL's composing the center HRL of the HRI shown in Fig. 4.12. The LRL's are shown before and after the weighting function. The summation of the LRL's and the corresponding envelope are also shown.

origin in the VS of the center HRL and going to $\vec{r}_p$. This line has a length $z_r = z_p - z_v$, where z_v is the depth of the VS. In Fig.4.15 the LRL's constituting an off-center HRL at the lateral position x_h are no longer aligned phase-coherently. As a simple approximation these LRL's can be found by a rotation of the aligned LRL's. They are rotated such that the line of phase equality is perpendicular to the line with origin in the VS of the off-center HRL and again with length z_r. The angle of this line is

$$\theta_r = \arcsin\left(\frac{x_h}{z_r}\right). \tag{4.10}$$

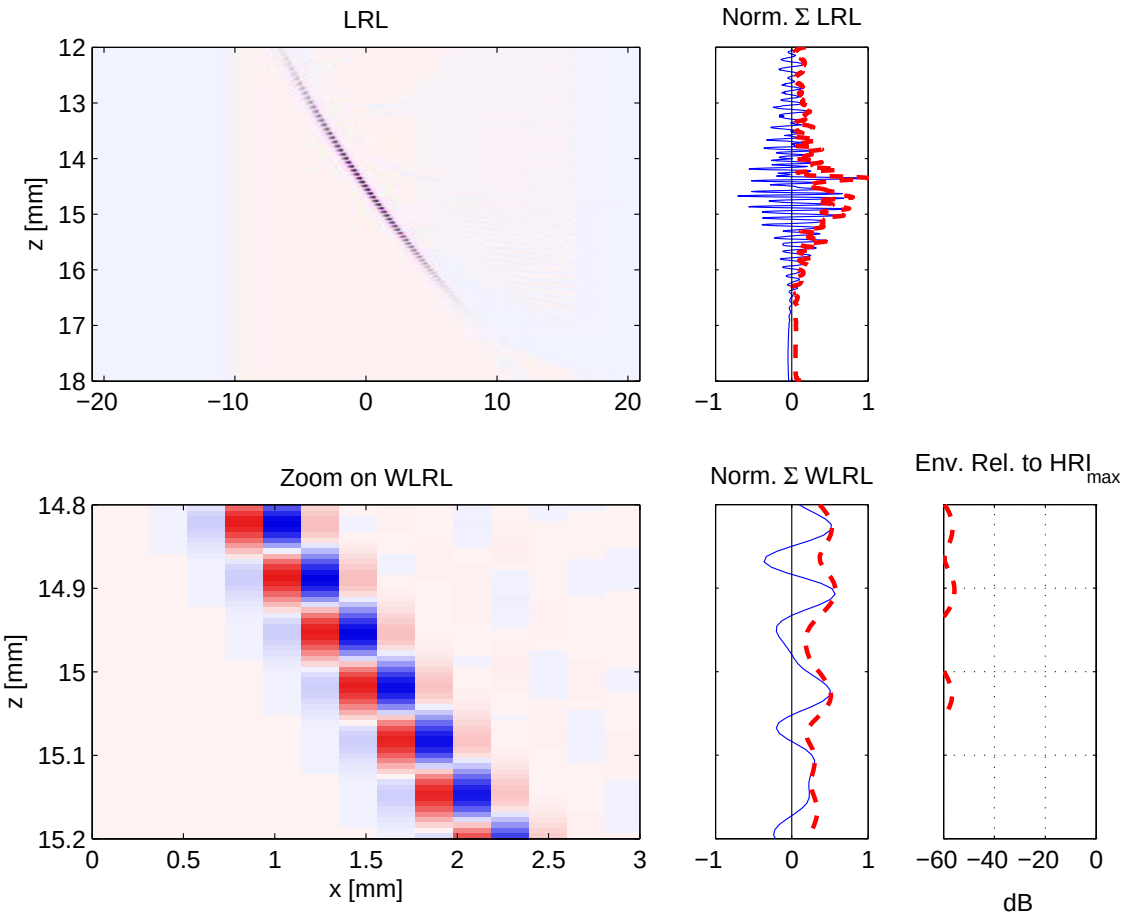

Figure 4.14: The LRL's composing the off-center HRL at the lateral position $x = 3.1$ of the HRI shown in Fig. 4.12. A zoom in on a few of the weighted LRL's is shown to visualize destructive summation of the LRL's.

This geometry is illustrated in Fig. 4.17 superimposed on the log-compressed envelope of a set of LRL's. The LRL's constitutes the HRL's at $x_h = 1$ mm and $x_h = 4$ mm in the range 12-18 mm. Beyond this range the envelope image is cropped. It seems reasonable, that the line of phase equality is perpendicular to the line originating at the VS.

The rotation of the aligned LRL's is only an approximation, which is valid in the proximity of $x = 0$. The positions of phase equality is not a straight line entirely. The curvature increases for LRL's with increasing distance to the HRL when the distance between the FP and the VS decreases. This would be the case if VS's with large opening angles are applied. The consequence of having a curvature that deviates considerably from the straight line approximation is that the axial shift between consecutive LRL's is greater than estimated for the outermost LRL's. This indicates a requirement for a limited opening angle. It is also an argument for using apodization in the 2nd stage beamformer, which will reduce the influence of the LRL's with increasing distance to the HRL.

The exact positions are also indicated in Fig. 4.17 for $x_h = 4$ mm as a dashed line cutting through the path of constant phase. The exact positions are determined by observing the focusing indices of each channel in the 2nd stage beamforming, and the indices representing the PT at $\vec{r}_p$ in each channel. These indices are shown in Fig. 4.18 for the same setup as in Fig. 4.17 and for a few FP's all placed in the same off-center HRL. For each FP it is registered at which LRL's

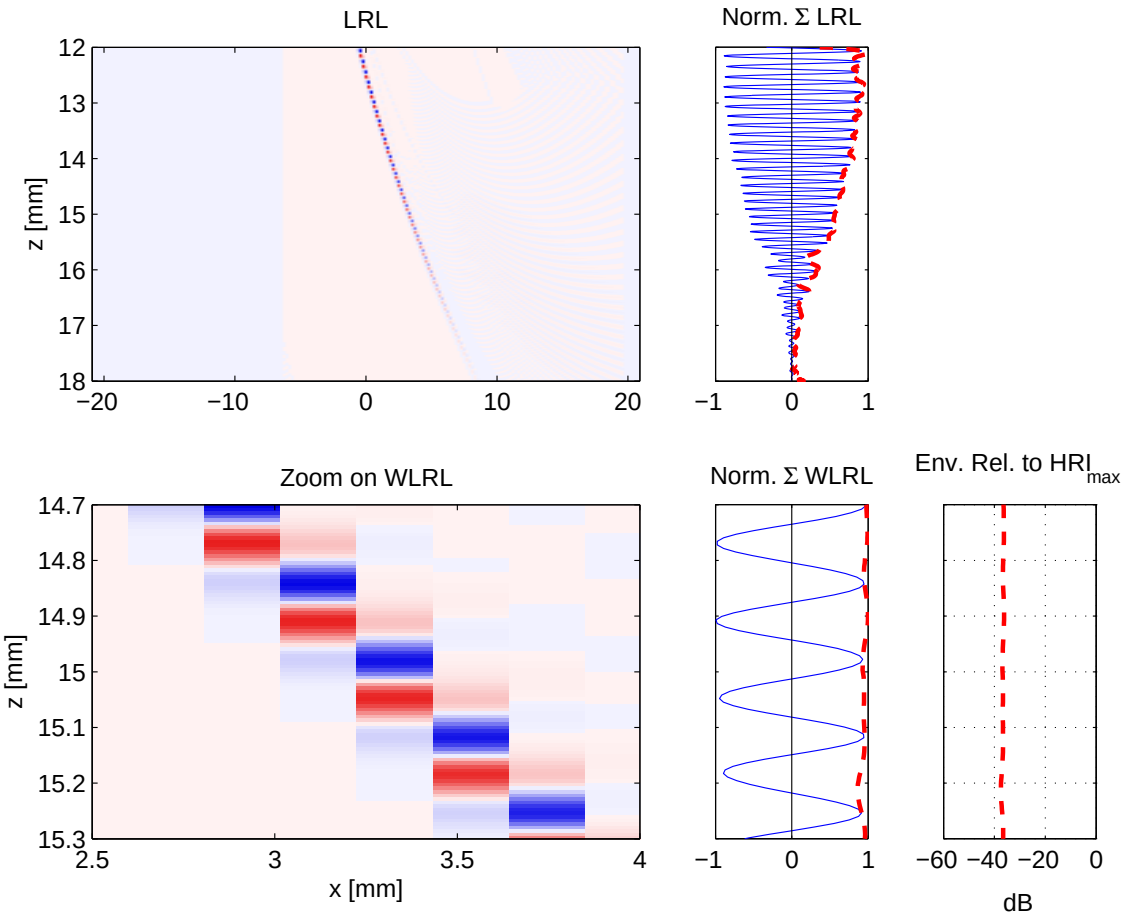

Figure 4.15: The LRL's composing the off-center HRL at the lateral position $x = 6.7$ of the HRI shown in Fig. 4.12. A zoom in on a few of the weighted LRL's is shown to visualize a phase-shift of almost an entire pulse-echo wave length, yielding constructive summation, and an envelope level above -40 dB.

the intersection between the FP-index and the PT-index takes place. In the reverse process the depth of the intersection between the FP-index and the PT-index is registered for each LRL. This is also shown in Fig. 4.18, and it is the same way the exact positions of phase equality is indicated in Fig. 4.17.

By applying the approximation about the rotated LRL's it is possible to estimate the phase shift between consecutive LRL's with a simple expression. The axial shift between consecutive LRL's is

$$x = \tan\theta_r \Delta . \tag{4.11}$$

Substituting θ_r with half the opening angle, $\alpha' = \alpha/2$ the axial shift can be expressed as

$$x = \tan(\alpha')\Delta = \frac{\Delta}{2F\#} . \tag{4.12}$$

If the spatial shift does not exceed half the wavelength of the pulse-echo signal, $\lambda_{pe} = \lambda/2 = c/f_0/2$ grating lobes are avoided. This condition can be used to put restrictions on the $F\#$ of the VS

$$F\# \geq \frac{\Delta}{\lambda/2} \quad \text{for } x \leq \lambda/4 . \tag{4.13}$$

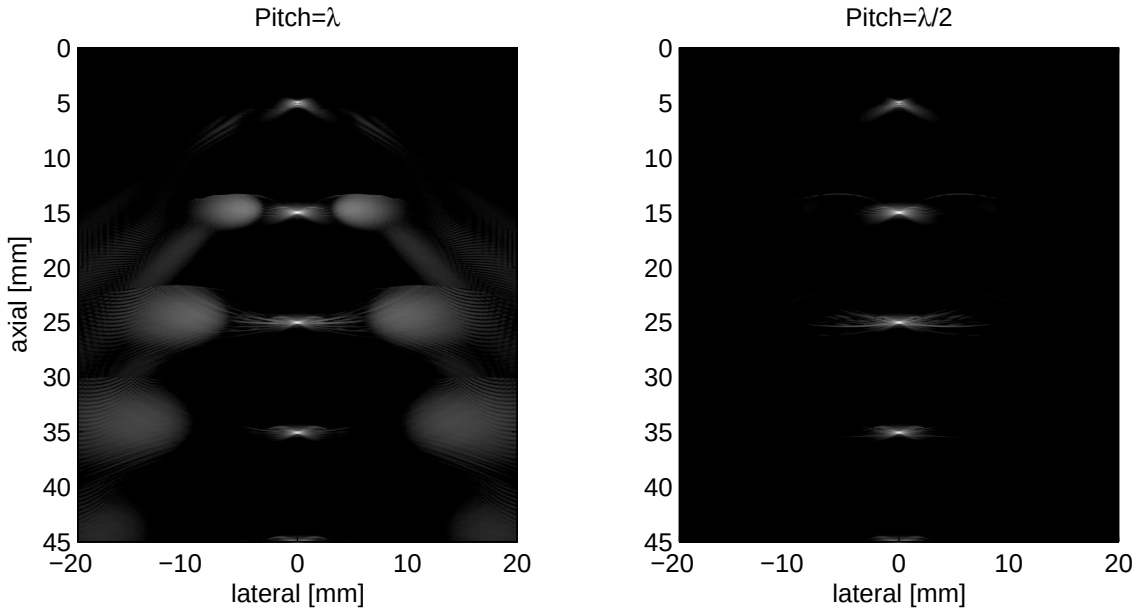

Figure 4.16: Two SASB images are constructed using a linear array (left) and a linear phased array (right). Both having 401 elements, a VS at 5 mm, and with $F\# = 0.75$. The linear array is twice the width of the phased array, but the image has been cropped to the same width as the phased array image. Dynamic range is 70 dB.

The opening angle of the VS limits the range of angles of the wave field. If a transducer with $\Delta = \lambda$ are used in SASB grating lobes are avoided if $F\# \geq 2$.

An approximation of the actual pulse-echo response and the spatial frequency content is extracted from the center LRL, and shown in Fig. 4.19. It is shown for the setup with VS at 5 mm and $F\# = 0.5$ and for the PT at 15 mm, but the spatial frequency content does not differ noticeably from the other setups and depths. The dominant spatial pulse-echo wavelength is $\lambda_{pe} = 0.15$ mm. With $\Delta = 0.208$ mm the VS must be designed with $F\# \geq 1.39$ with the restriction of (4.13). For $F\# = 0.5$, $F\# = 1$, $F\# = 1.5$, and $F\# = 2$ the spatial shift between consecutive LRL's measured in units of λ_{pe} is 1.39, 0.70, 0.46, and 0.35 respectively according to (4.12). The criterion for avoiding grating lobes is obeyed for $F\# = 1.5$, and $F\# = 2$ only. This is also reflected in Fig. 4.6, and Fig. 4.11, where the grating lobes evidently are attenuated for $F\# = 1.5$ and $F\# = 2$ compared to the setup where $F\# = 0.5$, and $F\# = 1$. In Fig. 4.16 a phased array with $\Delta = 0.104$ is applied. In this setup the VS must be designed with $F\# \geq 0.70$ with the restriction of (4.13). In Fig. 4.16 this criterion is obeyed with $F\# = 0.75$, and the grating lobes are avoided.

$K(z)$ from (4.4) determines the number of VS's applied and the size of the synthesized aperture. It is a function of the position of the VS and the opening angle and, thus, the $F\#$. It was shown previously that the grating lobes were appropriately attenuated for the linear array with $F\# = 1.5$ when the VS was at 5 mm. The lateral resolution with $F\# = 1.5$ and different positions of the VS is shown in Fig. 4.20, and $K(z)$ is shown in Fig. 4.21. The resolution functions are very similar but not the same in the four different setups because of the different number of applied VS's.

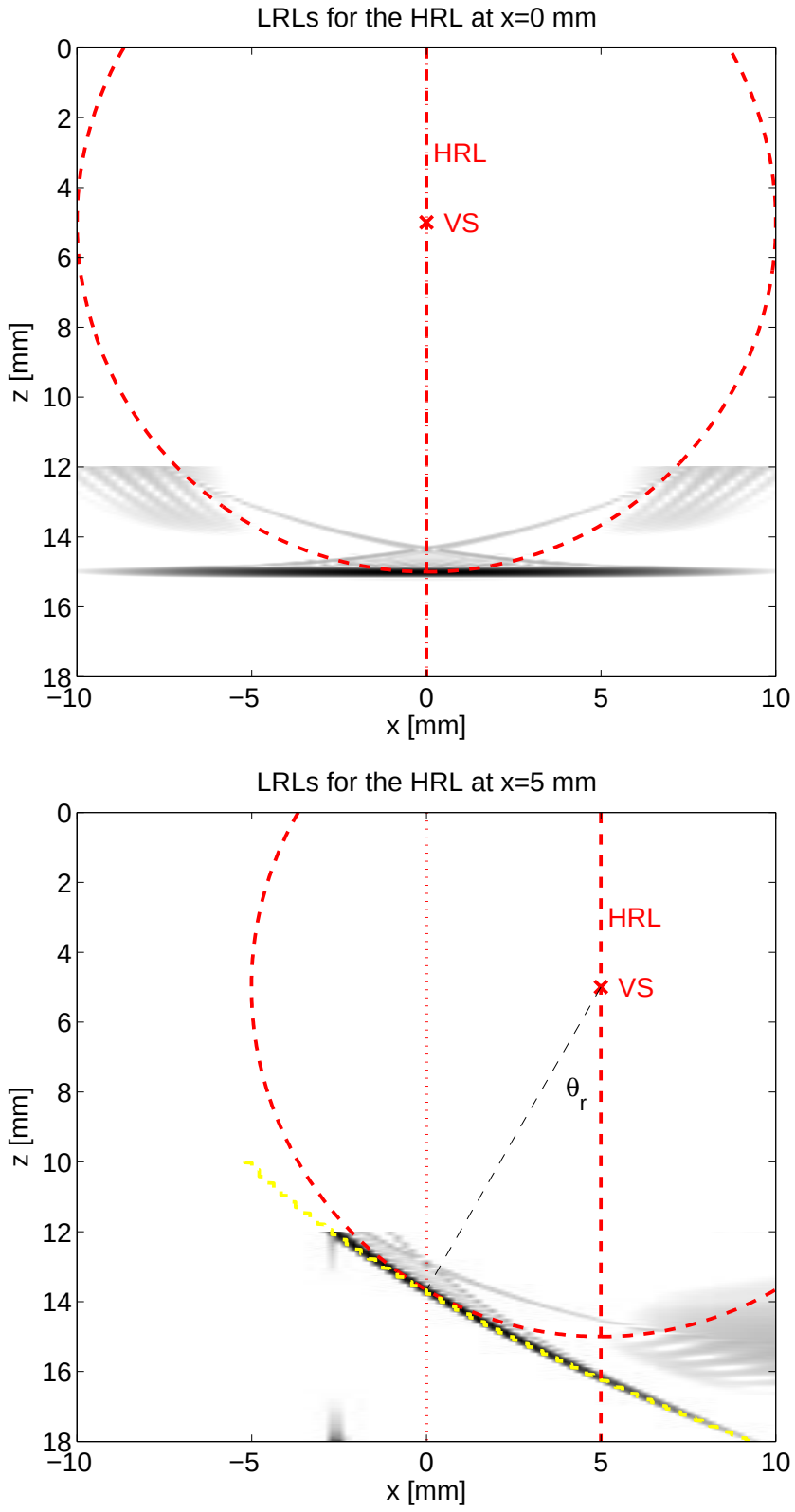

Figure 4.17: The log-compressed envelope of the LRL's constituting the HRL's at $x_h = 0$ mm (top) and $x_h = 4$ mm (bottom) is shown in the range 12-18 mm with a dynamic range of 50 dB. The VS is at the depth $z_v = 5$ mm and $F\# = 0.5$. A PT is positioned at the point $\vec{r}_p = (x,y) = (0,z_p)$ with depth, $z_p = 15$ mm. The appearance of the LRL's for the off-center HRL can be approximated by a rotation of the LRL's of the center HRL. The center of rotation is the VS of the off-center HRL, and the rotation radius is $z_r = z_p - z_v$. The angle of rotation $\theta_r = \arcsin(x_h/z_r)$ is also indicated.

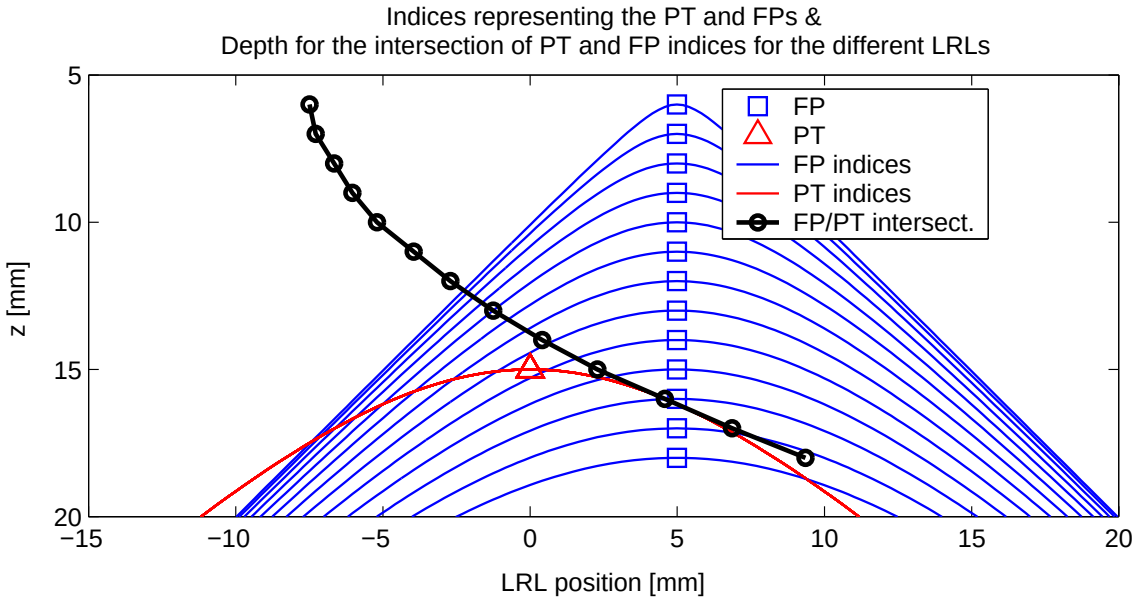

Figure 4.18: Focusing indices of each channel in the 2nd stage beamforming for a few FP's ranging from 6 mm to 18 mm from an off-center HRL. Indices representing the PT in each channel. For each LRL the depth of the intersection between the FP-index and the PT-index is shown.

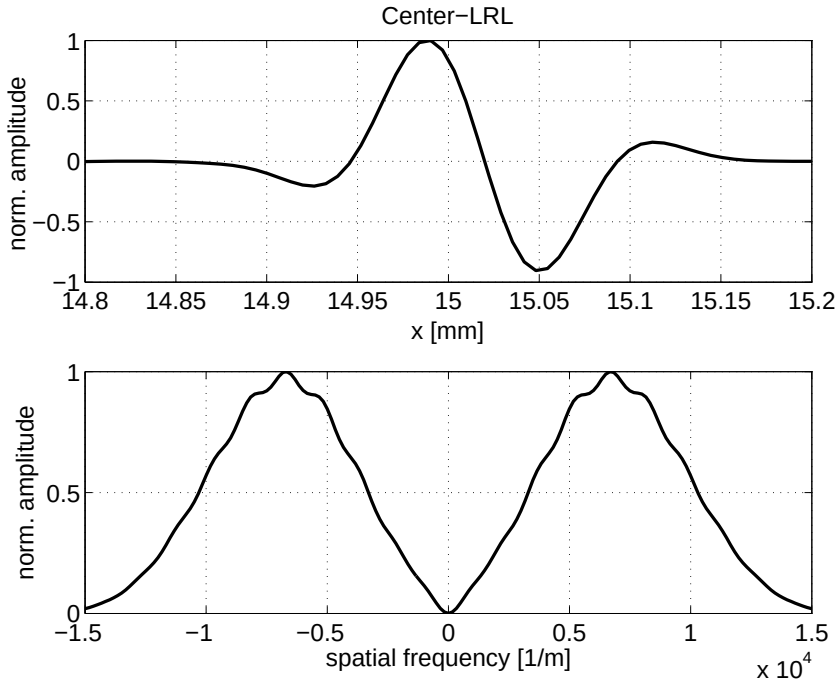

Figure 4.19: Center LRL with the VS at 5 mm and $F\# = 0.5$. Shown in a limited range near the PT at 15 mm (top). The spatial frequency content (bottom).

Influence of transducer impulse response.

The performance results presented in the previous sections were based on a transducer with $N = 401$, a short excitation signal, and a simple impulse response. The performance using

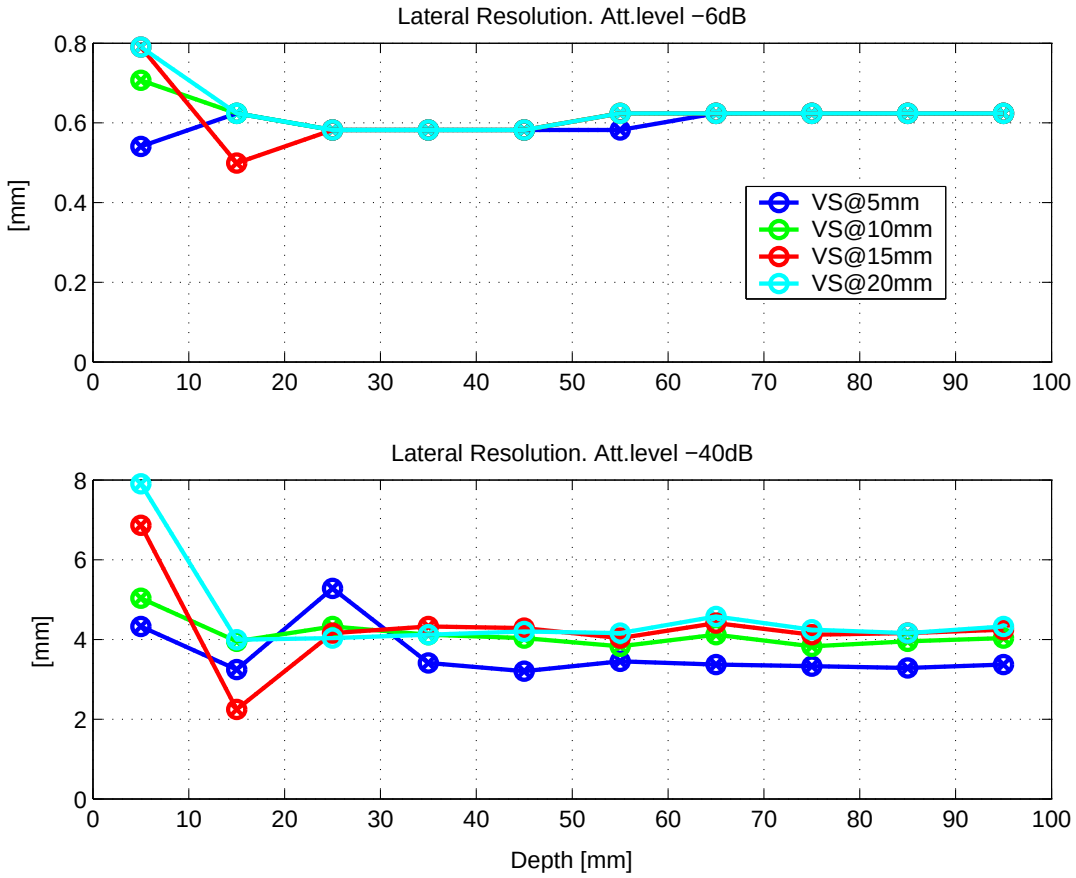

Figure 4.20: Lateral resolution with $F\# = 1.5$ as a function of depth at -6 dB (top) and -40 dB (bottom).

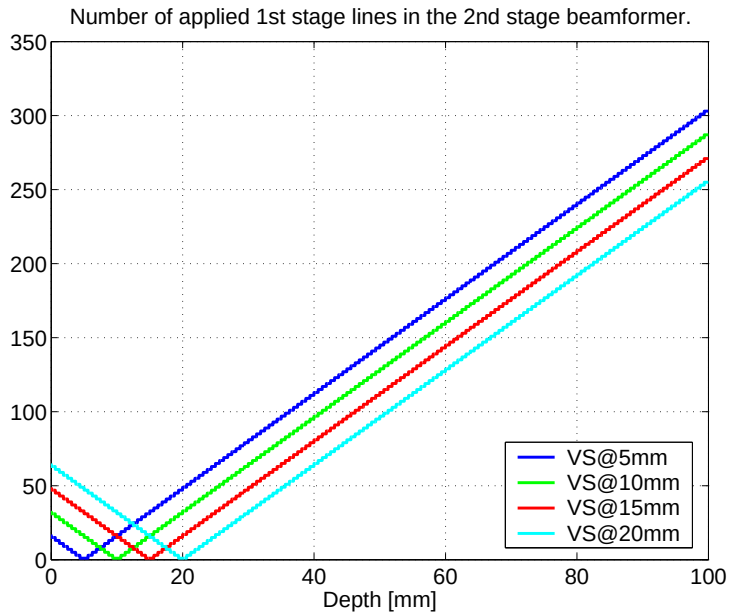

Figure 4.21: The number of applied 1st stage lines in the 2nd stage beamformer for the center HRL when $F\# = 1.5$.

a more realistic transducer Simulation Model is presented in this section and a comparison between the two is made. Envelope images with the VS at 20 mm, $F\# = 2$, and with the two different Simulation Models are shown in Fig. 4.22. The new Simulation Model has $N = 191$. The excitation signal has two periods. The transducer impulse response applied in the model is the measured response of a transducer with parameters similar to the model. In total yielding a longer system pulse-echo (PE) response.

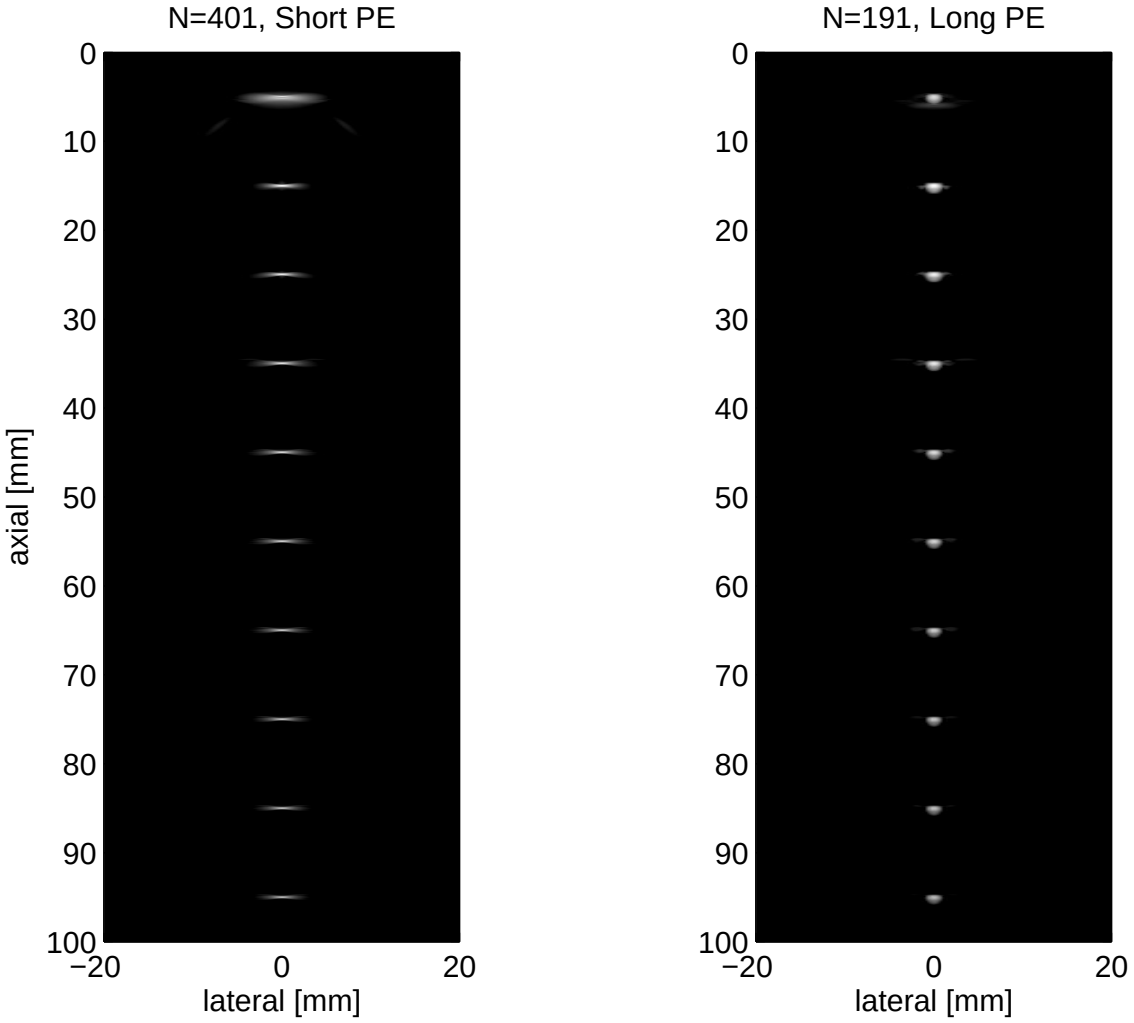

Figure 4.22: Envelope images with the VS at 20 mm and with $F\# = 2$. Two different Simulation Models are used. $N = 401$, and a short pulse-echo (PE) response (left). $N = 191$, and a long pulse-echo response (right). The image using $N = 401$ has been cropped to the same width as the image using $N = 191$. Dynamic Range is 60 dB.

The difference between the two images in Fig. 4.22 is significant. The axial resolution has decreased as a consequence of the extended PE response. The lateral resolution has improved in the entire range also beyond depths of 80 mm, where $K(z)$ ceases to increase linearly. The axial and lateral resolution are extracted, and shown in Fig. 4.23. The improvement in lateral resolution at -40 dB is at least a factor of 2.

The system pulse-echo response of the realistic transducer Simulation Model has been simulated in Field II and shown in Fig. 4.24 at different depths. The pulse-echo response is spatially variant because of the spatial pulse-echo impulse response, $h_{s_{pe}}(\vec{r}_p, t)$. It is the received

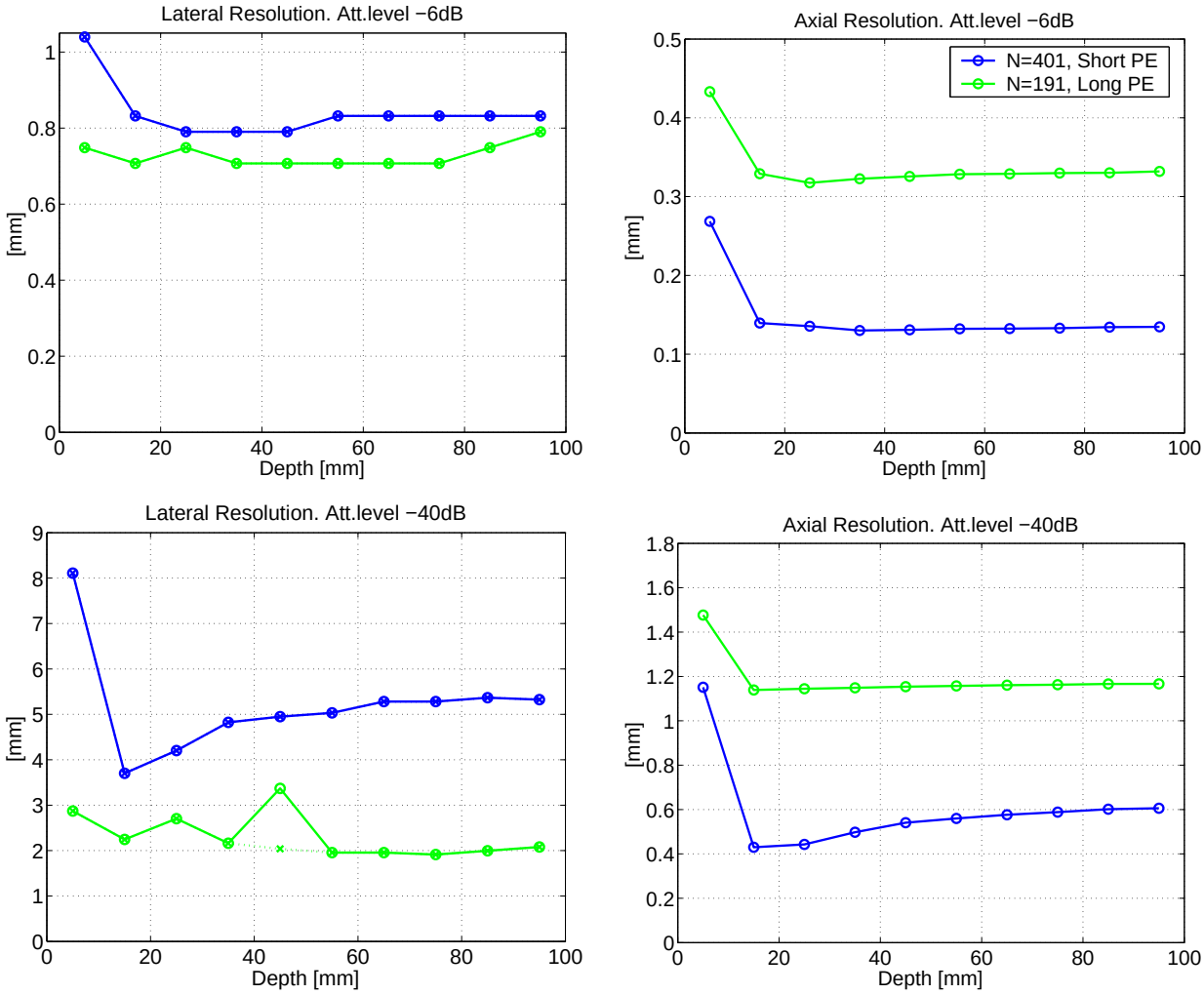

Figure 4.23: Resolution as function of depth at -6 dB (top) and -40 dB (bottom). Lateral resolution (left) and axial resolution (right). If the lateral PSF has a distinct main-lobe, and side-lobe distribution, the main-lobe resolution is shown as a dotted line. The resolution is extracted from the HRI's in Fig. 4.22.

response when an excitation signal, $e(t)$ is applied to a transducer with the two-way electro-mechanical impulse response, $h_t(t)$ if a PT is placed at the position $\vec{r_p}$. The pulse-echo response is found from the convolution[72, 73]

$$h_{pe}(\vec{r_p},t) = e(t) * h_{s_{pe}}(\vec{r_p},t) * h_t(t)\,. \tag{4.14}$$

The pulse-echo response in Fig. 4.24 is calculated at the positions, $\vec{r_p} = (0,0,r_{p_z})$ where r_{p_z} is 15, 25, 55, and 95 mm.

In the beamforming process it is assumed that the wave field can be considered spherical and propagating as if it was emitted from the virtual point source, as already discussed in Section 3.3.2. If the assumption is valid and the beamforming process is performed properly the LRL's constituting the HRL at the PT will be almost identical. The HRL at the PT thus equals the system pulse-echo response at the position of the PT. The HRL at the PT's at the same positions as $\vec{r_p}$ is also shown in Fig. 4.24 together with the convolution of the electro-mechanical impulse response and the excitation signal. A considerable coherence between the signals is

found at all depths, though small deviations are present near the VS. All signals in Fig. 4.24 have been aligned by means of cross-correlation and shown without the spatial axis solely to illustrate the resemblance between the waveforms.

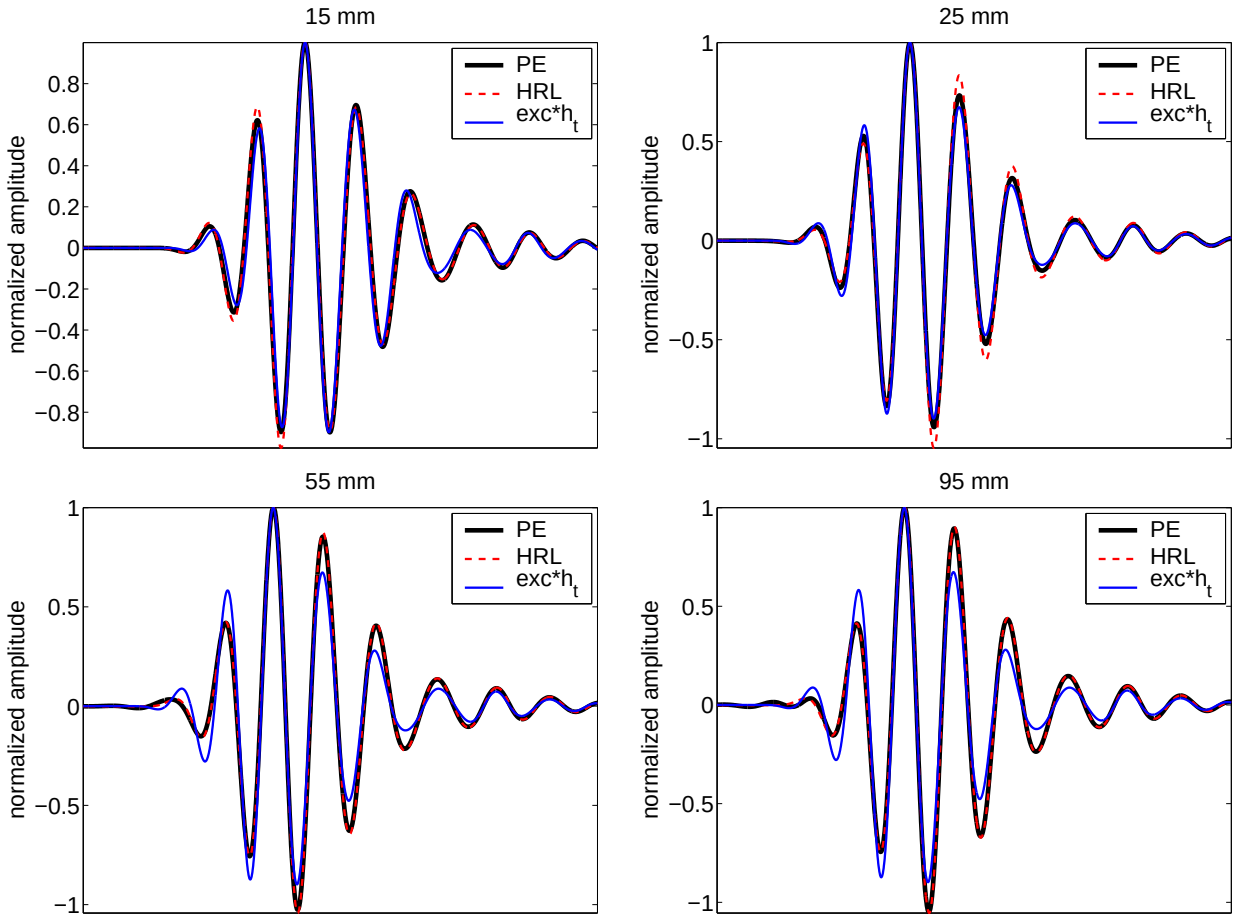

Figure 4.24: The spatial pulse-echo response at the positions, $\vec{r}_p = (0, 0, r_{p_z})$ where r_{p_z} is 15, 25, 55, and 95 mm. The center HRL at the PT's at the same positions (dotted line). The convolution of the electro-mechanical impulse response and the excitation signal is also shown.

The great resemblance between the waveforms in Fig. 4.24 demonstrates a successful beamforming. This can be only be a result of having a spherical wave field originating from the virtual source. This is studied in Fig. 4.25 to Fig. 4.28 where the variation of the pulse-echo response over the angular dimension is presented. This study is similar to the one presented in Section 3.3.2. The responses are simulated in a number of different positions, $\vec{r}_p = r_p \angle \phi_p$ and compared. r_p is the radial distance from the focal point to the point of investigation. Four studies are performed where the distance to the focal point is $r_p = -5$ mm, $r_p = 5$ mm, $r_p = 35$ mm, and $r_p = 75$ mm respectively. A negative value of r_p indicates that the points of investigation are above the focal point. In each study all responses and the envelope of the responses are normalized to a maximum value of 1, and plotted with a small offset in between each of them. This will form an illusion of the pulse-echo wave front at a given depth as a function of time. The positions of the points of investigation span over twice the opening angle, $-\alpha \leq \phi_p \leq \alpha$. The positions of the four studies are indicated in Fig. 4.29. The illustrations of the pulse-echo responses in Fig. 4.25 to Fig. 4.28 support the assumption of having a spherical wave field originating from the virtual source. The pulse-echo responses are not entirely equal

nor entirely aligned at depths near the VS as also concluded for the signals in Fig. 4.24. The envelopes though form an almost completely straight line. This is a demonstration of a pulse-echo wave field with a spherical wave front. This is the precondition for a successful 2nd stage beamforming.

The difference between the images in Fig. 4.22 is significant. The cause of the difference between the two Simulation Models are investigated by taking a closer look at the LRL's composing the HRL's. The investigation concerns only the range from 53 mm to 57 mm which include a single PT at a depth of 55 mm. The HRI's in this range are shown in fig 4.30, superimposed with vertical dashed lines indicating those HRL's for which the LRL's are shown.

The LRL's for the center HRL are shown in Fig. 4.31. The LRL's for the off-center HRL are shown in Fig. 4.32. In these figures the LRL's after LRL-weighting are shown. They also show the summation of the LRL's and the corresponding envelope. Finally the envelope of the weighted HRL is shown relative to the maximum of the HRI's in Fig. 4.30. The LRL's sum completely constructive for the center HRL in both setups.

For the off-center HRL's the LRL's sum destructively toward zero level. With a short pulse-echo response the off-center HRL is composed of the sum of a only a few positive and negative half-periods. The amplitudes of these half-periods varies with range and lateral position. The amplitude of the HRL, thus, varies with range. The variation over range is considerable due to the sparse number of cycles in the sum.

With a longer pulse-echo response the off-center HRL is composed of the sum of several positive and negative half-periods. The amplitudes of these half-periods decay smoothly over range and lateral position and on average sum destructively to a zero level. The HRL is of oscillating nature with the same center frequency as the pulse-echo response, which is not the case for the setup with the short PE response.

Additional performance results using the longer pulse-echo response are shown in Appendix A for a number of different configurations.

Transmit Apodization

Transmit apodization has been applied in all simulations. The consequence on performance of the SASB of omitting apodization is shown in Fig. 4.33 and Fig. 4.34. By using apodization the lateral FWHM degrades with approximately 0.1 mm. On the other hand the side-lobes are attenuated yielding an improvement in the -40 dB lateral resolution with a factor of 4 (6 mm) at greater depths.

Comparison to dynamic receive focusing.

The performance of SASB is among others a function of VS position and $F\#$. These parameters also determine the number of elements used during transmission. This has an influences on the emitted energy and the signal to noise ratio. It was shown in Section 4.3.2 that the grating lobes were appropriately attenuated for $F\# = 1.5$ and $F\# = 2$. The number of elements used as a function of VS position and $F\#$ is shown in Table 4.2

The choice of configuration for comparison with DRF is based on the results presented in Fig. 4.35. Here the lateral resolution for a number of configurations is shown. In all configurations the results are based on the realistic transducer Simulation Model introduced in

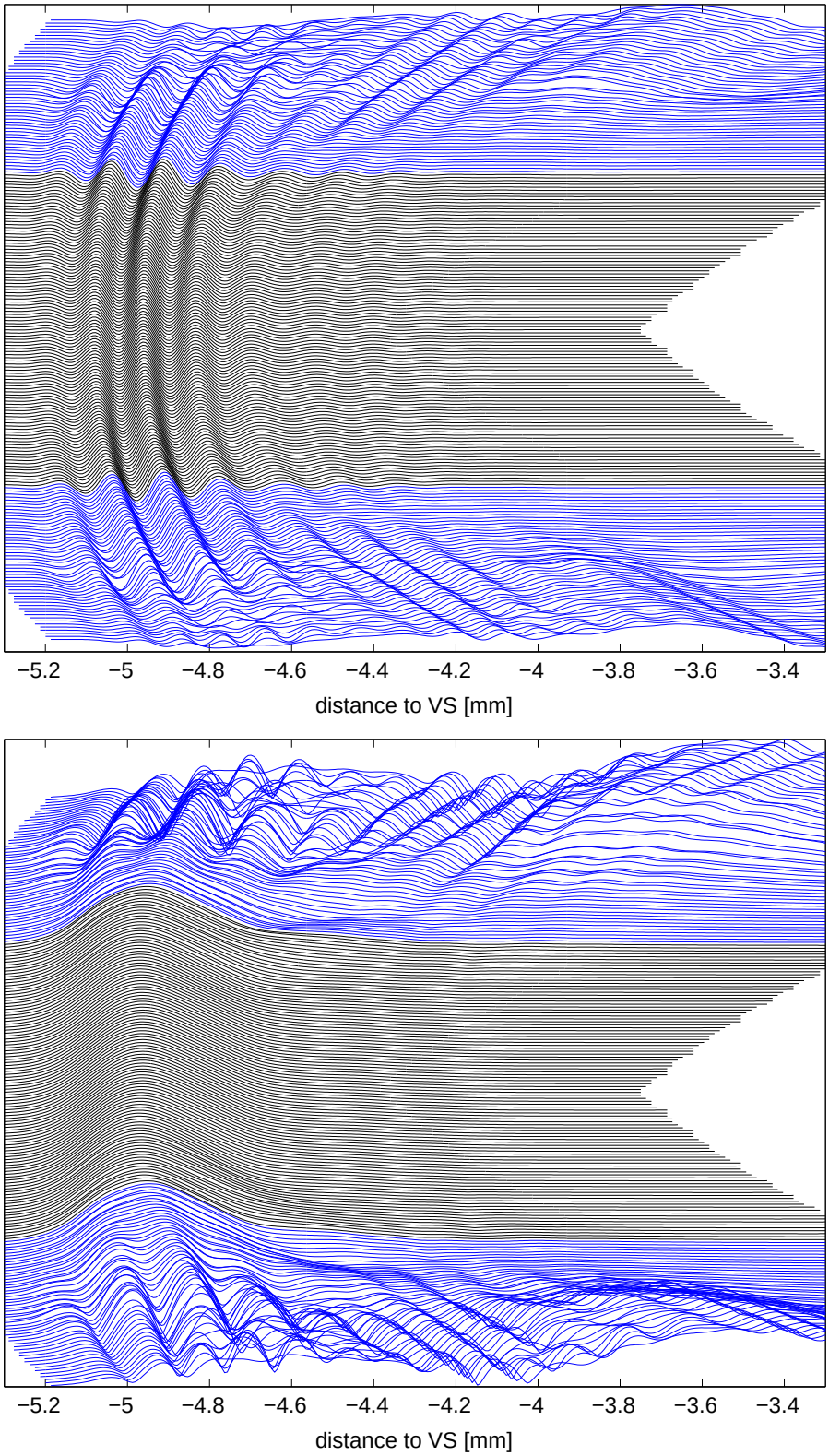

Figure 4.25: A number of pulse-echo responses (top) and their envelopes (bottom) in different positions are compared. All positions are above the focal point and the distance to the focal point is 5 mm. The positions are indicated in Fig. 4.29. The positions span over twice the opening angle, $-\alpha \leq \phi_p \leq \alpha$. Responses from positions within the opening angle are plotted with a different color than for those beyond the opening angle.

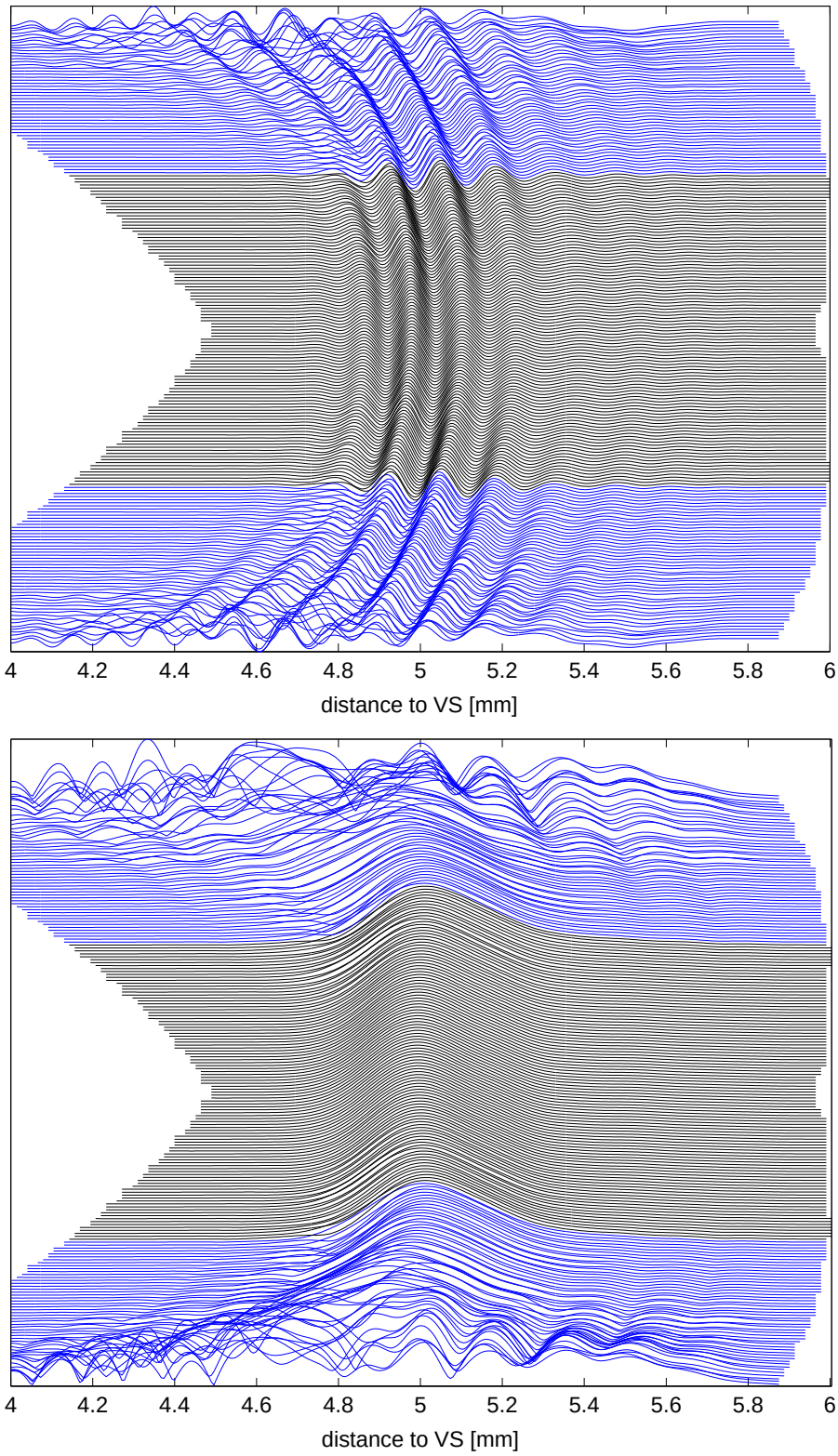

Figure 4.26: A number of pulse-echo responses (top) and their envelopes (bottom) in different positions are compared. All positions are below the focal point and the distance to the focal point is 5 mm. The positions are indicated in Fig. 4.29. The positions span over twice the opening angle, $-\alpha \leq \phi_p \leq \alpha$. Responses from positions within the opening angle are plotted with a different color than for those beyond the opening angle.

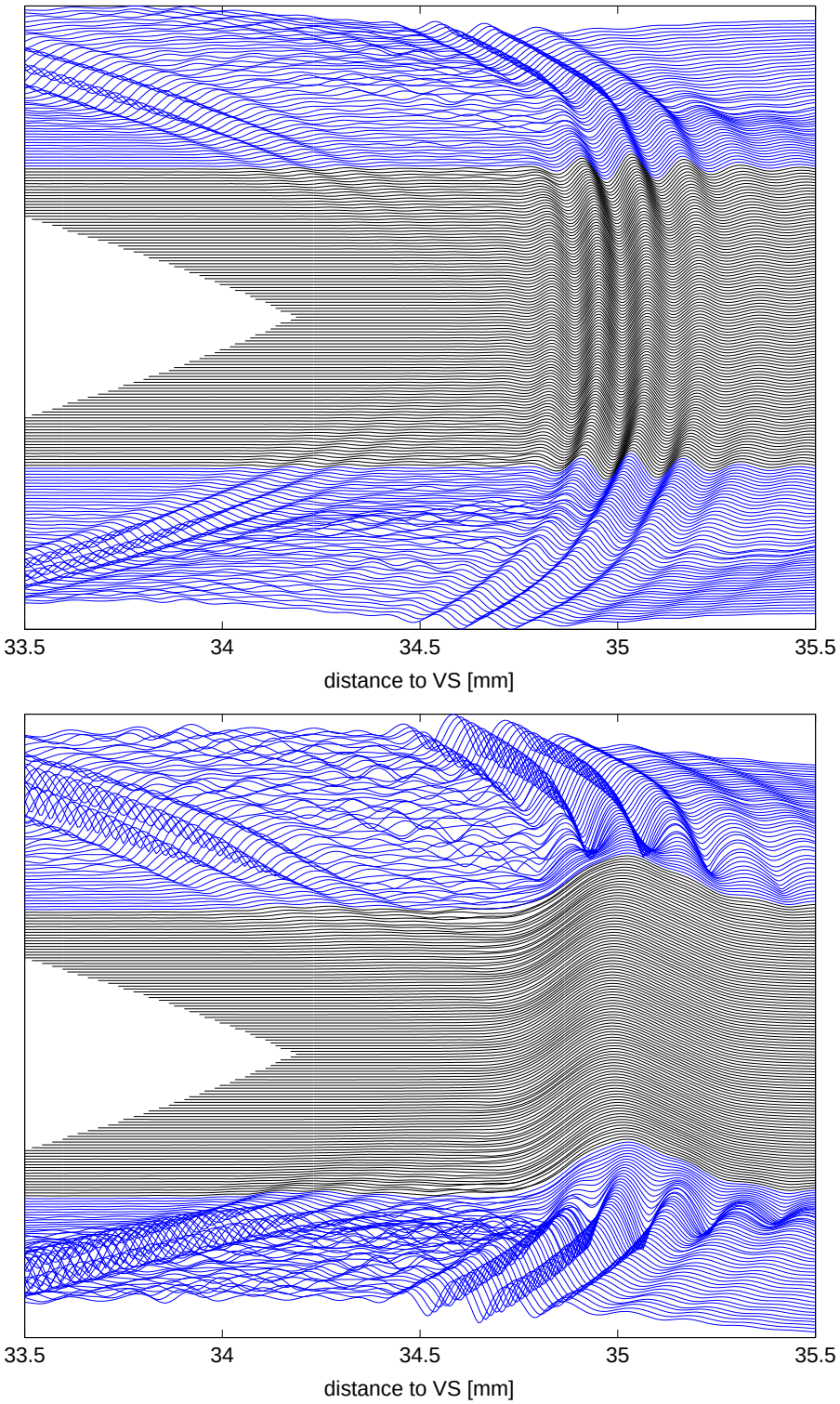

Figure 4.27: A number of pulse-echo responses (top) and their envelopes (bottom) in different positions are compared. All positions have a distance to the focal point of 35 mm. The positions are indicated in Fig. 4.29. The positions span over twice the opening angle, $-\alpha \leq \phi_p \leq \alpha$. Responses from positions within the opening angle are plotted with a different color than for those beyond the opening angle.

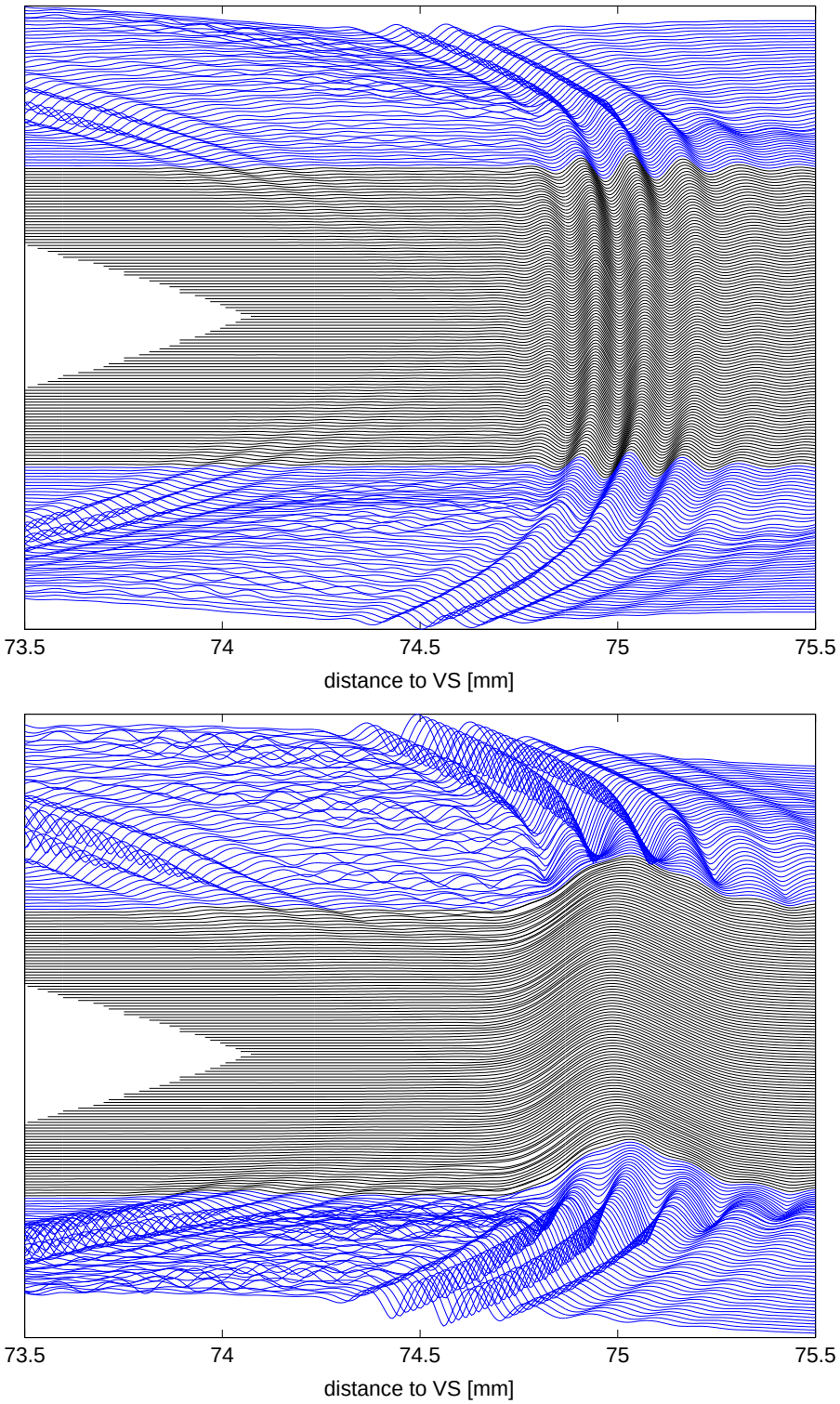

Figure 4.28: A number of pulse-echo responses (top) and their envelopes (bottom) in different positions are compared. All positions have a distance to the focal point of 75 mm. The positions are indicated in Fig. 4.29. The positions span over twice the opening angle, $-\alpha \leq \phi_p \leq \alpha$. Responses from positions within the opening angle are plotted with a different color than for those beyond the opening angle.

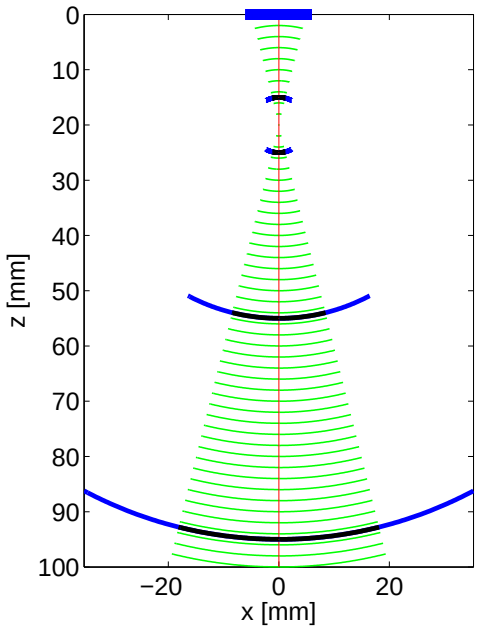

Figure 4.29: Positions at which the spatial pulse-echo responses shown in Fig. 4.25 to Fig. 4.28 are calculated. The positions span over twice the opening angle $-\alpha \leq \phi_p \leq \alpha$.

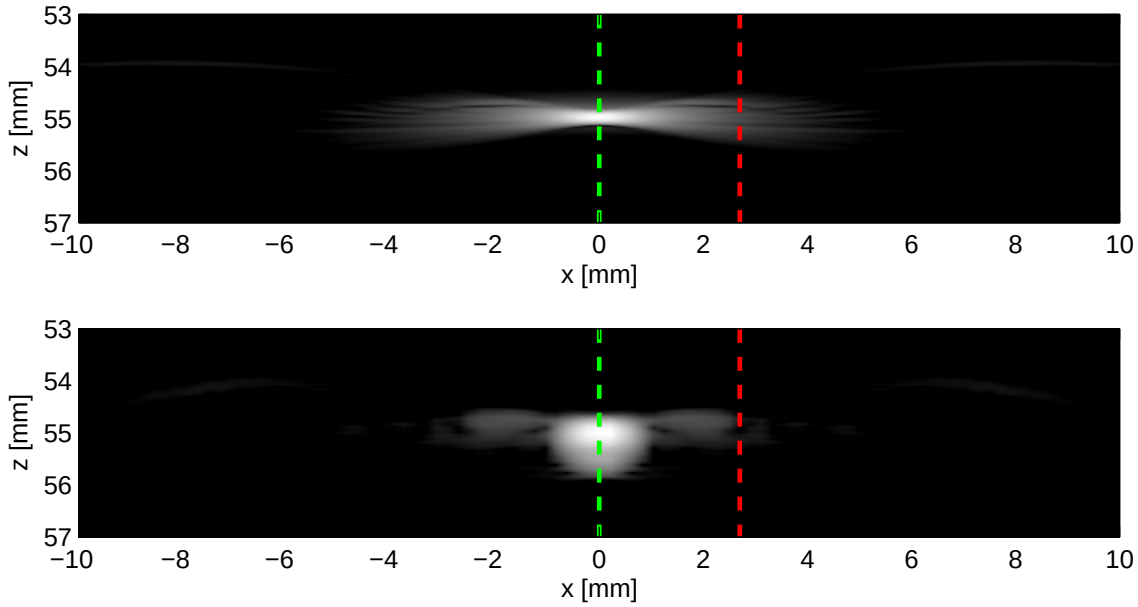

Figure 4.30: Envelope images with the VS at 10 mm, and with $F\# = 2$ from Fig. 4.22. Short PE response (top), and long PE response (bottom). Shown in the range from 53 mm to 57 mm, and superimposed with vertical dashed lines indicating those HRL's for which the LRL's are shown. The LRL's are shown in Fig. 4.31 and Fig. 4.32.

Section 4.3.2. The performance with the VS at 20 mm and $F\# = 1.5$ is superior to the other configurations in almost the entire range. It is thus a rational choice for a good performance and a comparison with DRF.

Fig. 4.36 show images with DRF and SASB side by side, and Fig. 4.37 show the quantified lateral resolution for different configurations. The quantified axial resolution does not differ

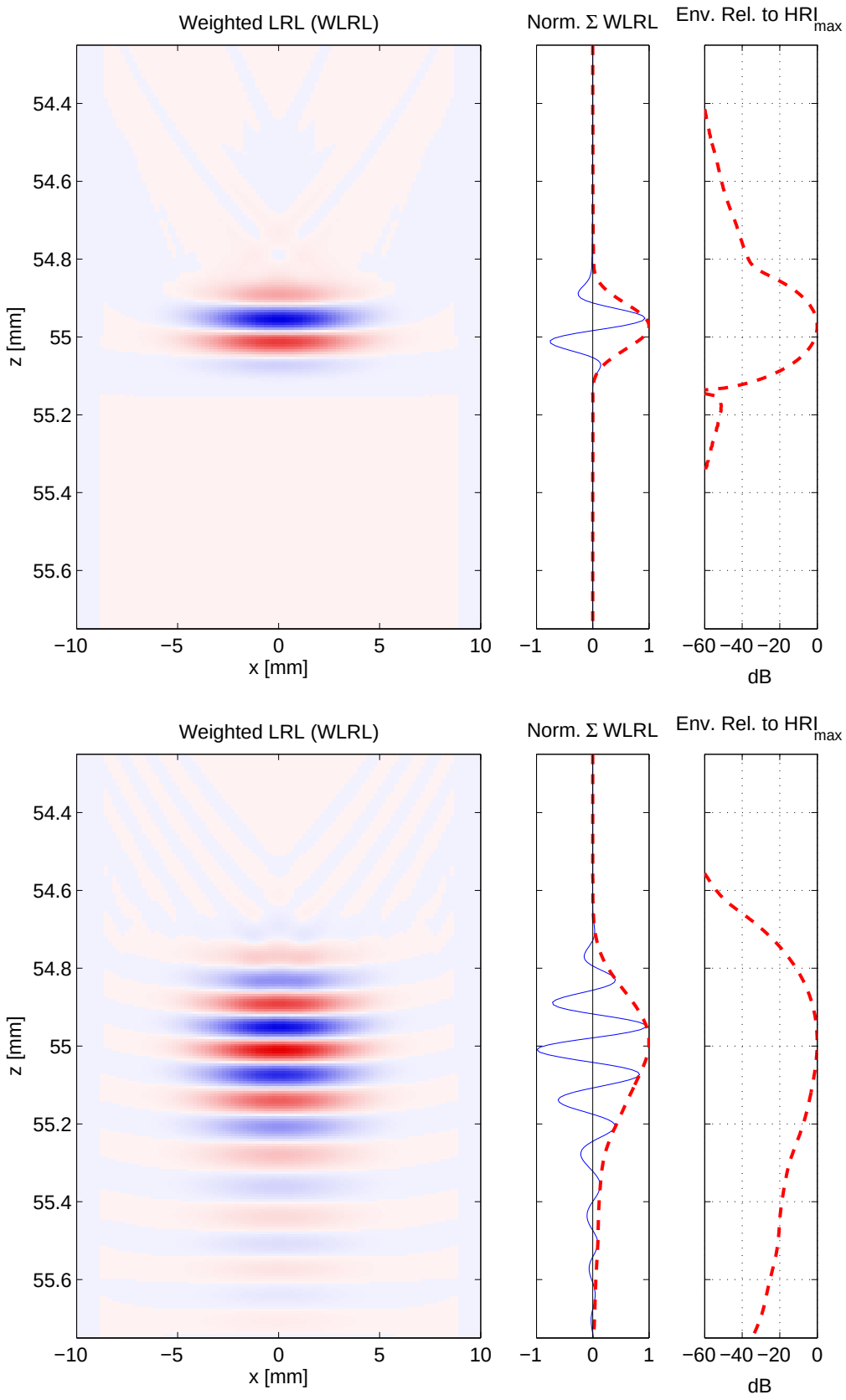

Figure 4.31: The LRL's composing the center HRL of the two HRI's shown in Fig. 4.30. The LRL's are shown after the weighting function. The summation of the LRL's and the corresponding envelope are also shown.

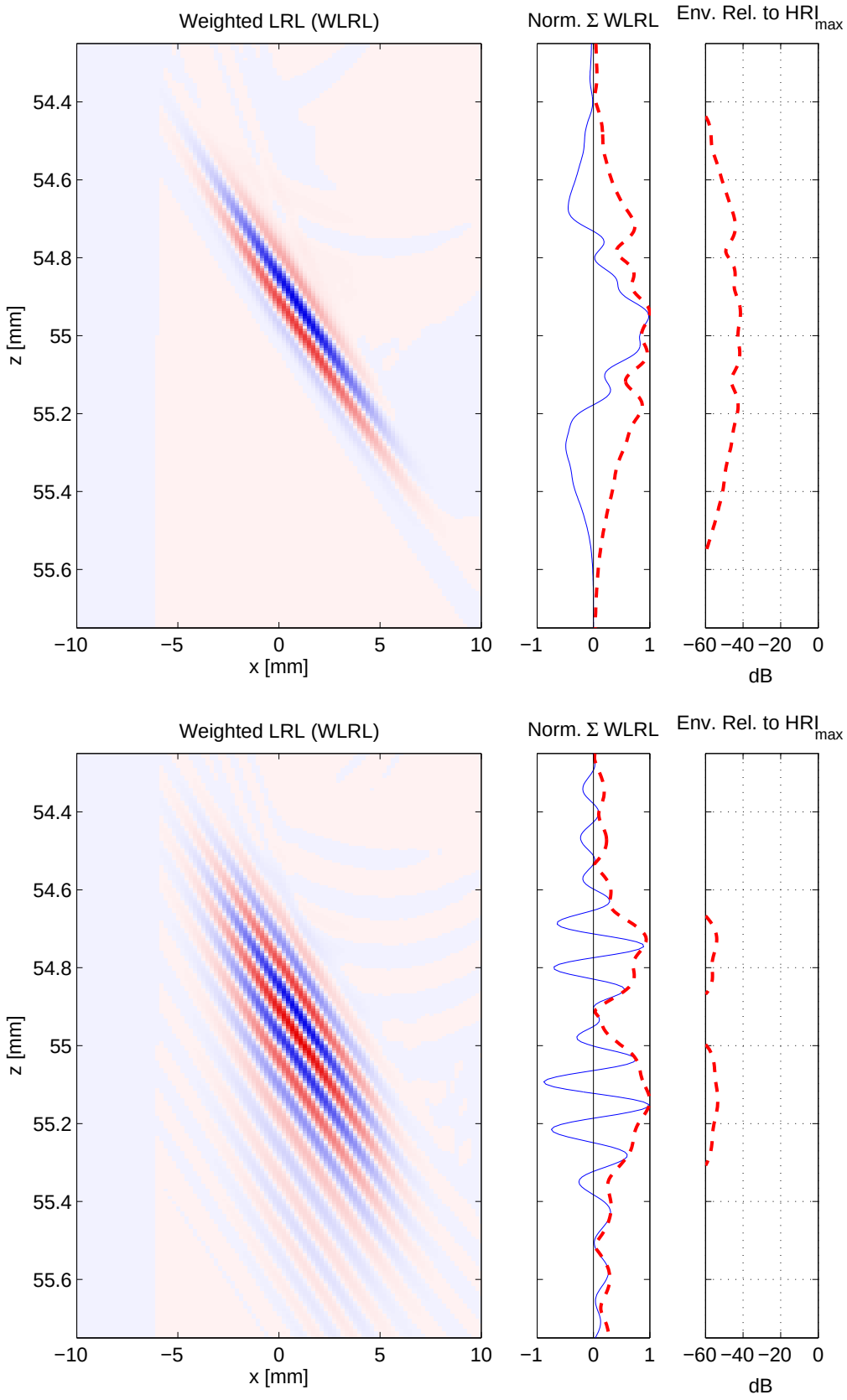

Figure 4.32: The LRL's composing the off-center HRL of the two HRI's shown in Fig. 4.30. The LRL's are shown after the weighting function. The summation of the LRL's and the corresponding envelope are also shown.

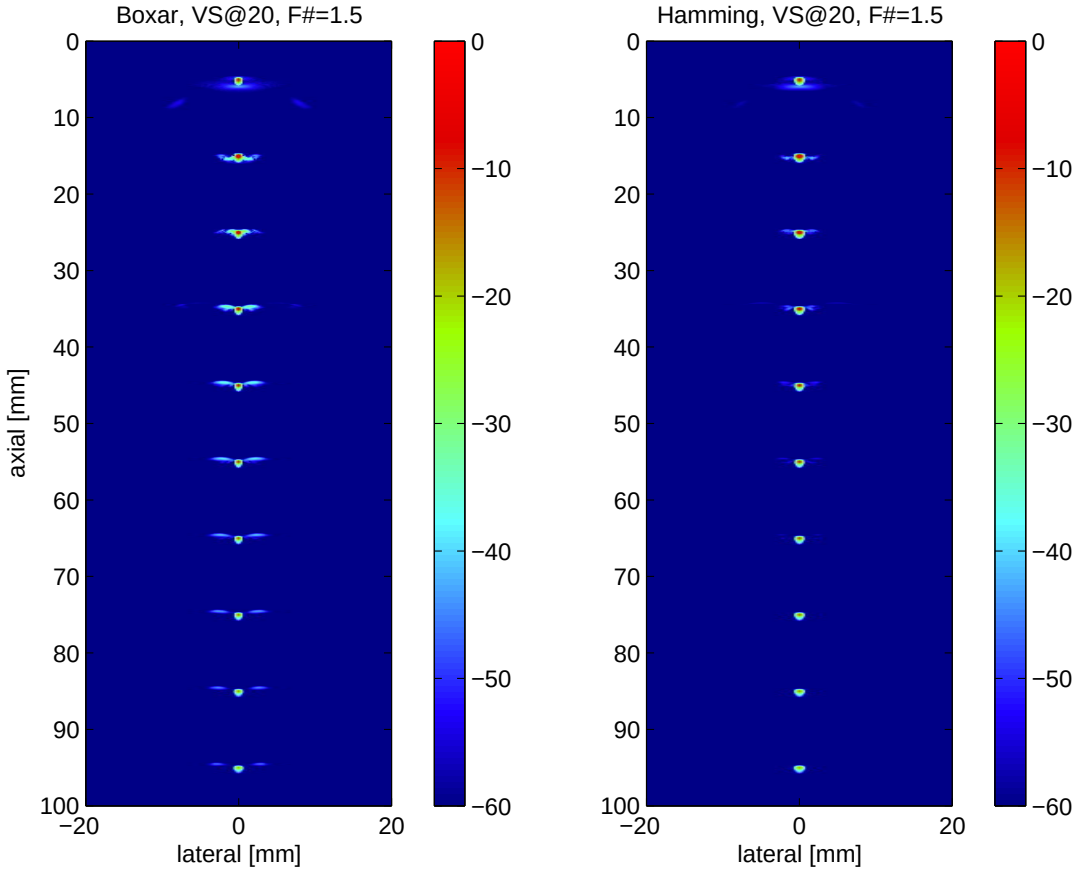

Figure 4.33: SASB with Boxcar transmit apodization (left) and Hamming (right). The VS is at 20 mm, $F\# = 1.5$, and the realistic transducer Simulation Model from Section 4.3.2 is used. The dynamic range is 60 dB.

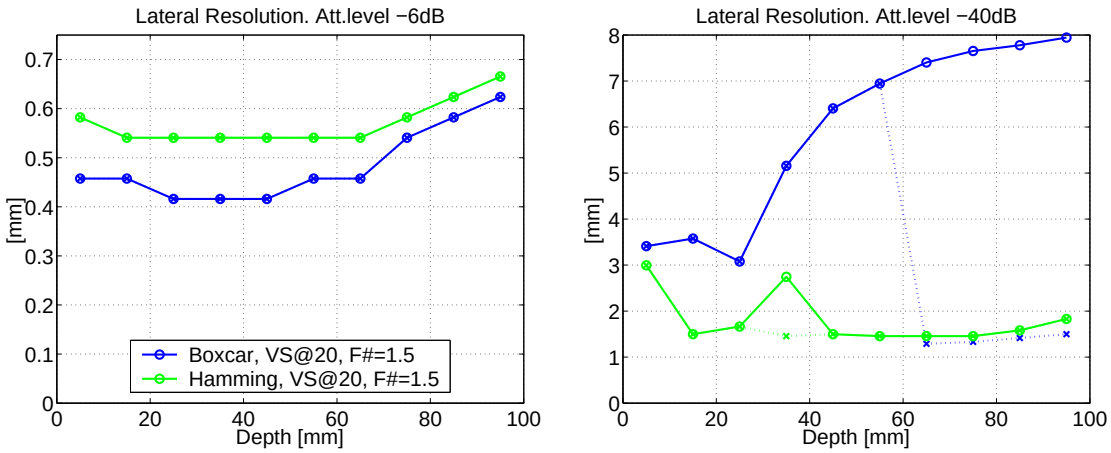

Figure 4.34: Lateral resolution at -6 dB (left) and -40 dB (right) with and without transmit apodization. Extracted from the images in Fig. 4.33. The dashed curve is the resolution for the main-lobe only. The solid curve includes the side-lobes as well.

between the different configurations and is not shown. Different positions of the transmit focal point in DRF has been applied for a fair comparison of the quantified resolution. The VS is at 20 mm and $F\# = 1.5$ for all cases of SASB. In Fig. 4.36, and in the previous sections the number

VS depth	$F\# = 1.5$	$F\# = 2$
5 mm	17	13
10 mm	33	25
15 mm	49	37
20 mm	65	49

Table 4.2: The number of array elements used during transmission as a function of VS position and $F\#$.

of channels in the 2nd stage beamformer is unlimited, so that $N_{2nd} = N$. In Fig. 4.37 additional SASB results are presented where the number of channels has been limited to $N_{2nd} = 127$, and $N_{2nd} = 63$.

There is an substantial improvement in resolution using SASB compared to DRF. It accounts for both the FWHM and the resolution at -40 dB. The improvement in FWHM is at least a factor of 2 and the improvement at -40 dB is at least a factor of 3. The improvement of SASB over DRF is a reality except for a few exceptions. At depths until 20 mm the FWHM is superior with DRF. With SASB the resolution is almost constant throughout the range. For DRF the FWHM increases almost linearly with range and the resolution at -40 dB is fluctuating with range.

The opening angles of the VS's decrease toward the transducer edges due to a limited number of transducer elements. As a consequence the number of valid 1st stage lines to potentially include in the sum deviates from the required linear increase accordingly as range increases as already shown in Fig. 4.7. This deviation from the linear increase will affect the performance of the lateral resolution. Deliberately limiting the number of channels in the 2nd stage beamformer to reduce system complexity has the same effect. The number of applied channels as a function of depth is shown in Fig. 4.38 when the number of available channels is limited to $N_{2nd} = 63$, $N_{2nd} = 127$, and $N_{2nd} = 191$.

Contour plots of the PSF with restricted channel counts of $N_{2nd} = 63$, and $N_{2nd} = 191$ are shown in Fig. 4.39. The contours are only shown for the PT beyond 50 mm since this is where they differentiate. The quantified resolution is included in Fig. 4.37. The performance degradation when reducing the number of channels from $N_{2nd} = 191$ to $N_{2nd} = 127$ is noticeable but not very significant. This is reasonable since in practice it is only a reduction from using a maximum of 150 channels to using 127 channels. Limiting the number of channels to $N_{2nd} = 63$ does on the other hand degrade performance significantly. When the number of channels is restricted to $N_{2nd} = 63$, and $N_{2nd} = 127$ the depths at which $K(z)$ ceases to increase linearly is at 40 mm and 61 mm respectively. This is also apparent when observing the resolution in Fig. 4.37, where both the FWHM and the resolution at -40 dB are no longer constant beyond these depths. Even when the number of channels is restricted to $N_{2nd} = 63$ the performance of SASB is superior to DRF.

4.4 Measurement Results

A commercial scanner and a linear array transducer with parameters similar to the ones in Table 4.1 have been used to acquire data. A tissue phantom with wire targets and 0.5 dB/MHz/cm attenuation is used as imaging object. RF-data using DRF and 1st stage SASB is acquired with a 5 MHz center frequency and stored. 2nd stage SASB processing, envelope detection, and logarithmic compression is done off-line for both DRF and SASB. An envelope image of the

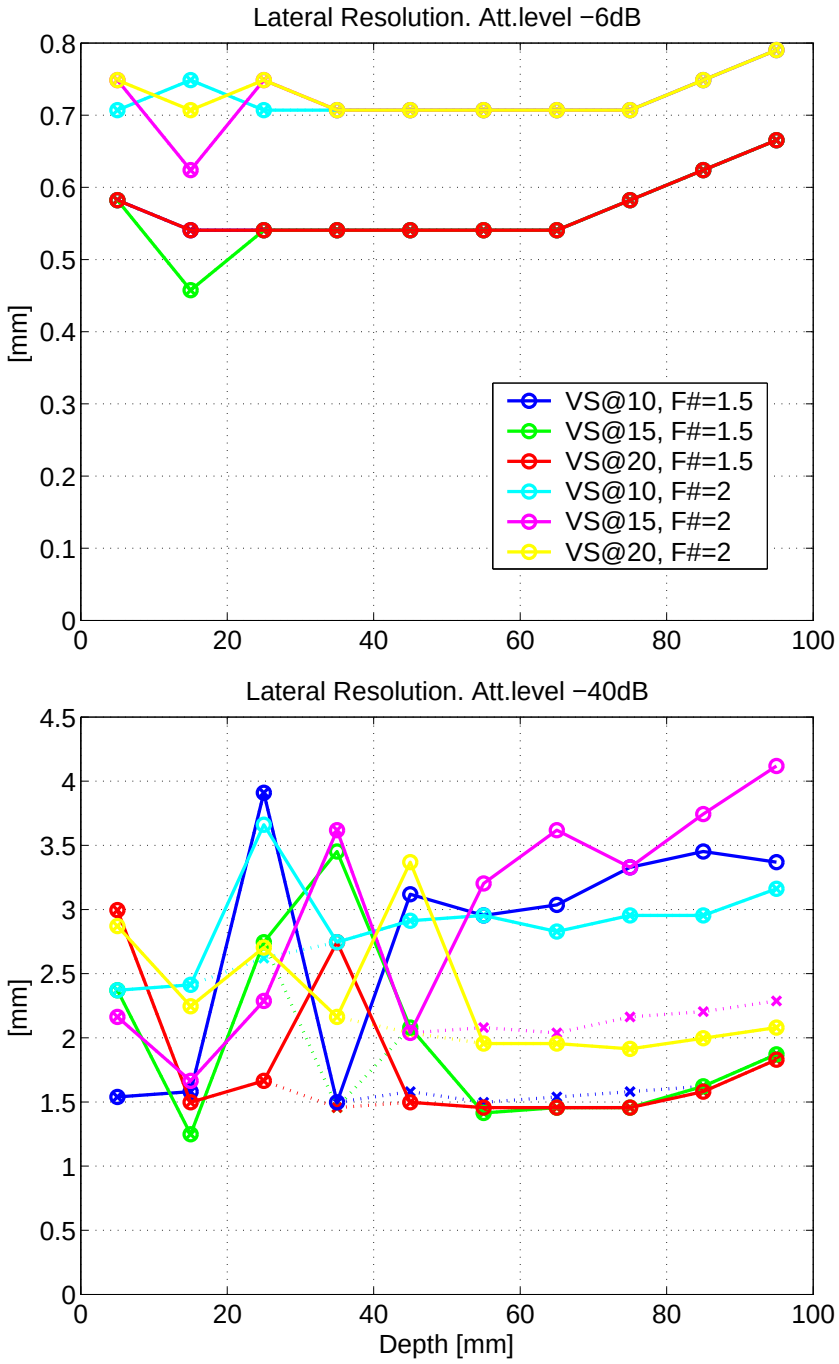

Figure 4.35: Lateral resolution of SASB as function of depth at -6 dB (top) and -40 dB (bottom). If the lateral PSF has a distinct main-lobe, and side-lobe distribution, the main-lobe resolution is shown as a dotted line. In all configurations the results are based on the realistic transducer Simulation Model introduced in Section 4.3.2.

acquired 1st stage SASB data is shown in Fig. 4.40. It resembles the shape of the contours shown in Fig. 4.5 as expected. Notice the arcs are turned upside down before and after the focal point at 20 mm. A side by side comparison between the DRF image and the SASB image is also shown in Fig. 4.40. With DRF the transmit focal point is at 65 mm, and with SASB the VS is at 20 mm $F\# = 2$.

The images based on measured data confirms the results from the simulations. At the center

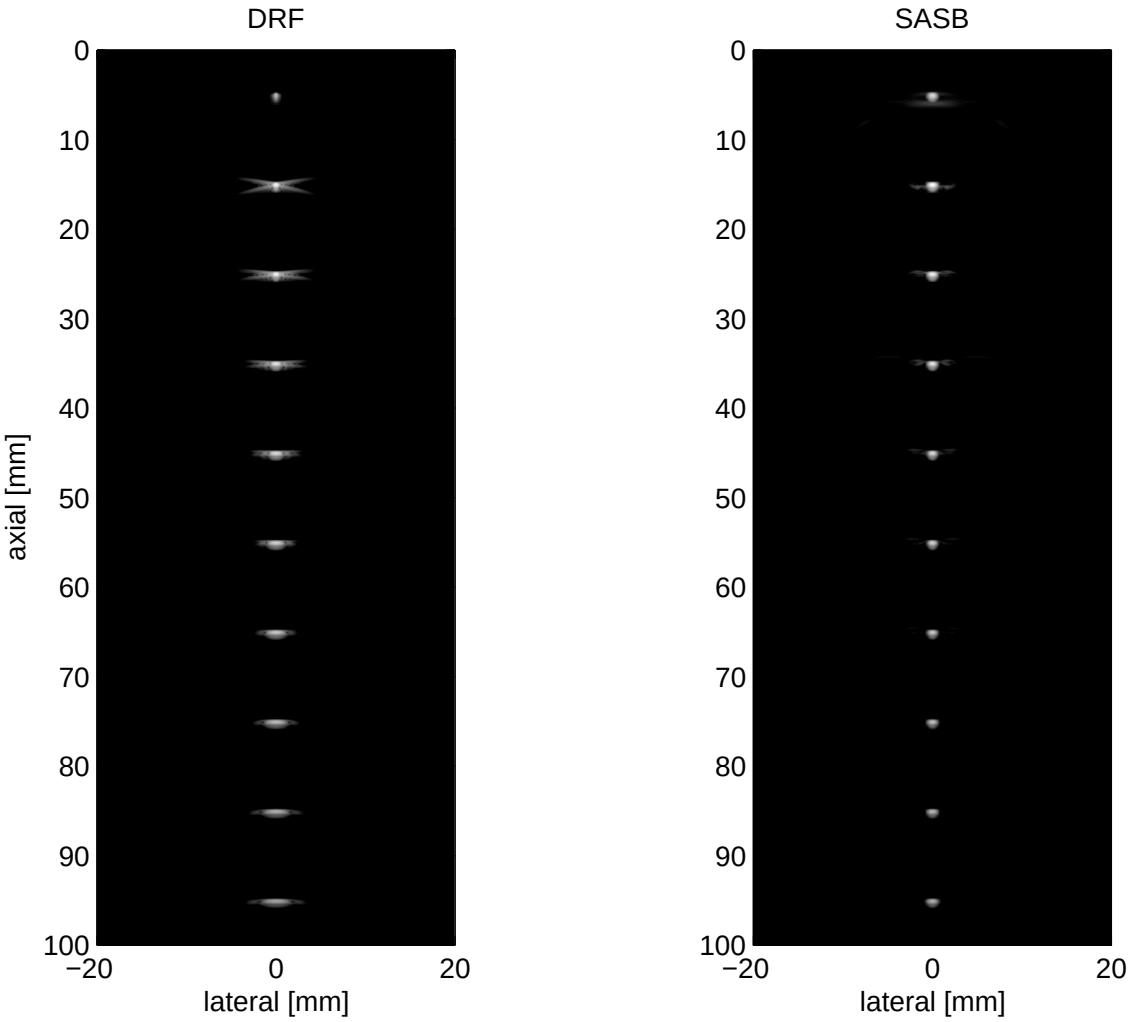

Figure 4.36: Envelope images using DRF (left) and SASB (right). For DRF the transmit focal point is at 70 mm. For SASB the VS is at 20 mm and $F\# = 1.5$. Dynamic Range is 60 dB.

of the image the resolution of SASB is superior to DRF and is practically range independent. A zoom in on the PT at 69 mm for the DRF and SASB images from Fig. 4.40 is shown in Fig. 4.41. Here the difference in resolution is prominent. The resolution in the near field is slightly better for DRF as stated in Section 4.3.2 and in Fig. 4.37.

Artifacts at the transducer edges occur for both DRF and SASB but are more profound for SASB and especially at greater depths. As stated in Section 4.2.2 the lateral resolution is laterally dependent since the number of applied LRL's decreases as the HRL approaches the edges of the transducer. This is illustrated in Fig. 4.42, where the number of applied LRL's as a function of depth and lateral position of the HRL is shown as an image for the configurations with VS at 20 mm, and $F\# = 1.5$. The number of applied LRL's as a function lateral position for a few depths is also shown. At greater depth the synthesized aperture, hence the resolution, decreases linearly as the HRL moves toward the transducer edge.

The speckle pattern is present at a greater range in the SASB image compared to the DRF image indicating greater penetration. At greater depths the emitted wave field in SASB is wide compared to DRF. The intensity is lower and so is the SNR of the 1st stage SASB-data. The SNR increases because of the summation of a number of LRL's. Provided that the image

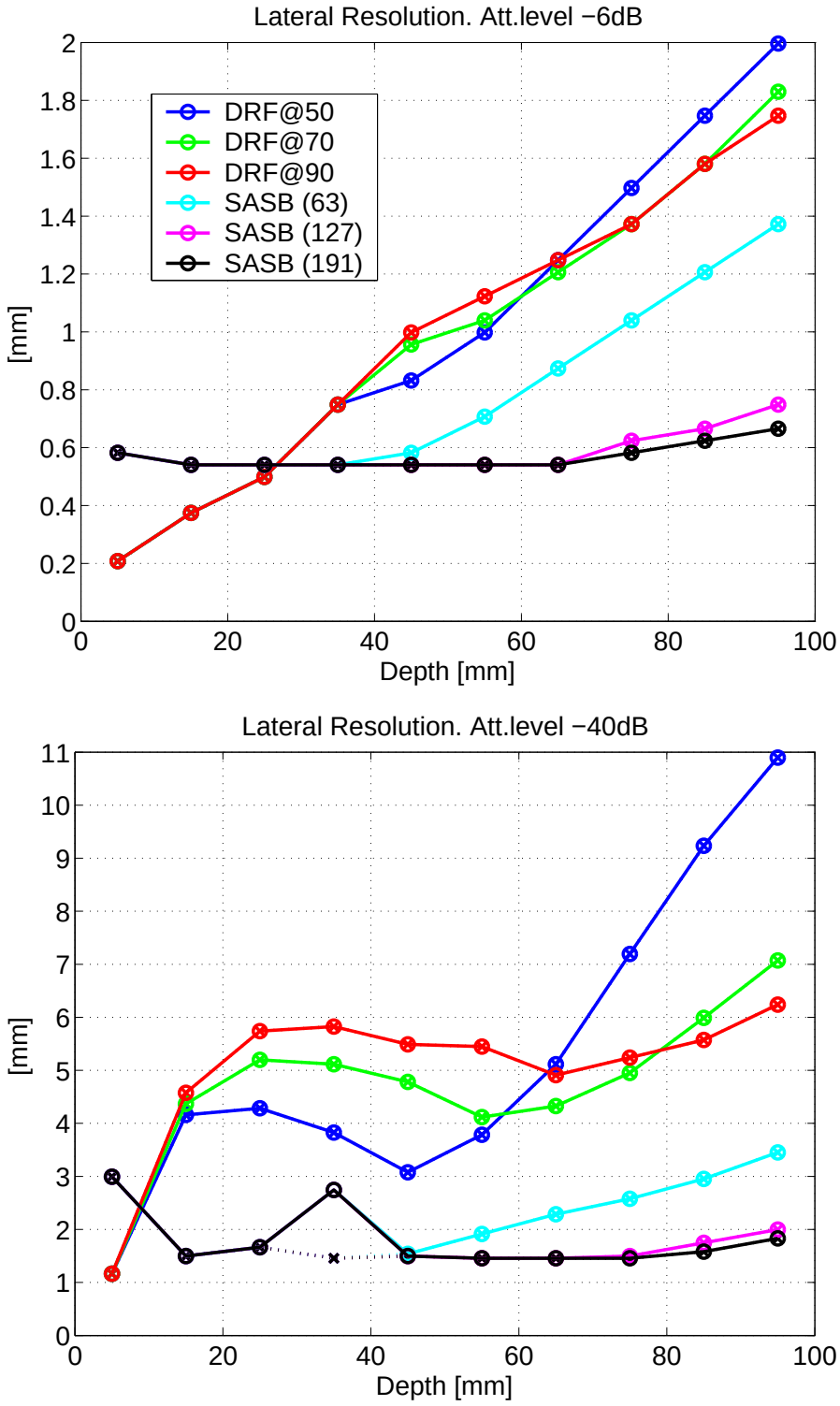

Figure 4.37: Lateral resolution of DRF and SASB as function of depth at -6 dB (top) and -40 dB (bottom). If the lateral PSF has a distinct main-lobe, and side-lobe distribution, the main-lobe resolution is shown as a dotted line. In all configurations the results are based on the realistic transducer Simulation Model introduced in Section 4.3.2. For DRF the transmit focal point is at 50 mm, 70 mm, and 90 mm. For SASB the VS is at 20 mm and $F\# = 1.5$. SASB results are presented using a different number of available 2nd stage beamformer channels. $N_{2nd} = 63$, $N_{2nd} = 127$, and $N_{2nd} = 191$.

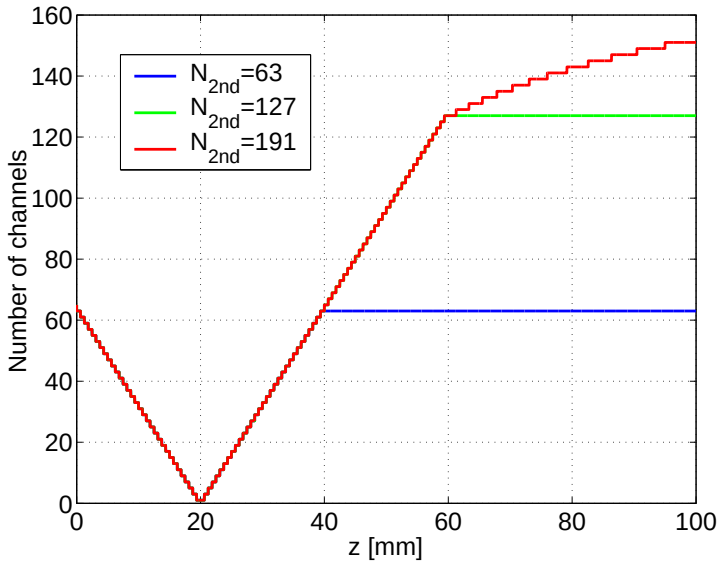

Figure 4.38: The number of applied 1st stage lines in the 2nd stage beamformer for the center HRL, when the number of available channels is limited to $N_{2nd} = 63$, $N_{2nd} = 127$, and $N_{2nd} = 191$.

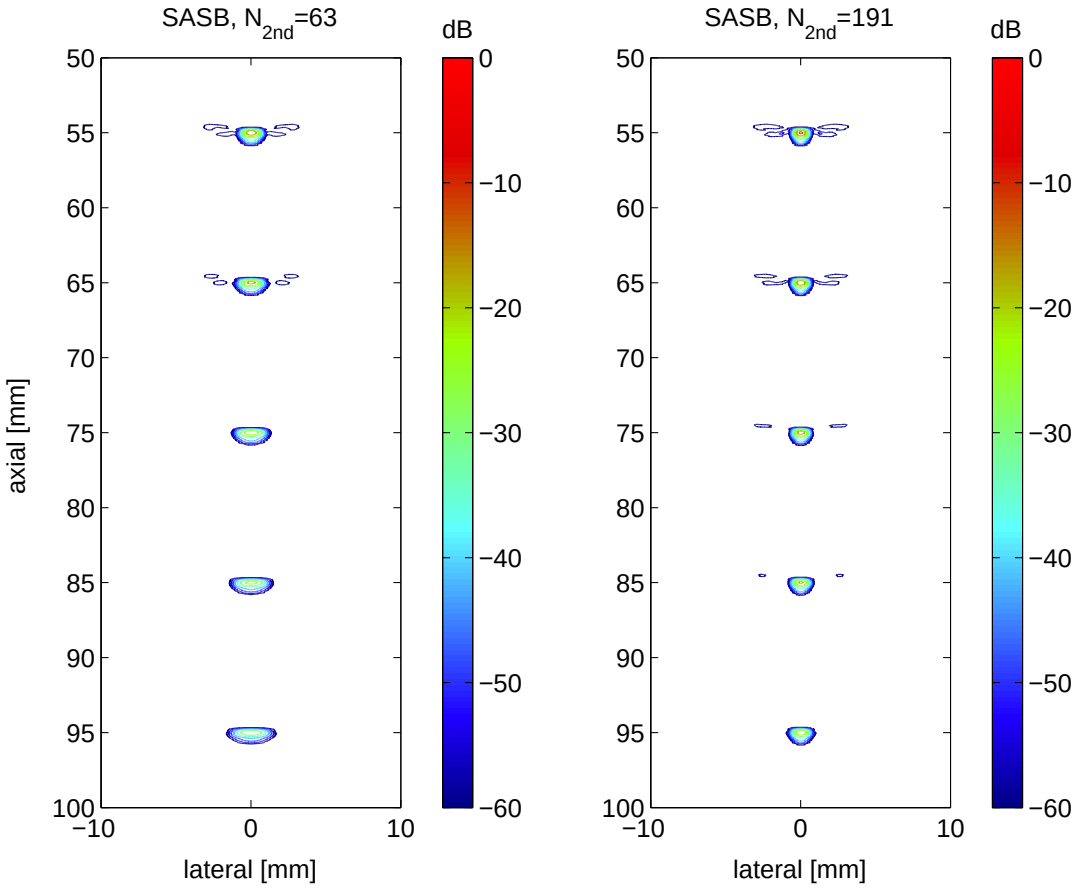

Figure 4.39: Contour plots of the PSF with restricted channel counts of $N_{2nd} = 63$, and $N_{2nd} = 191$. The VS is at 20 mm and $F\# = 1.5$

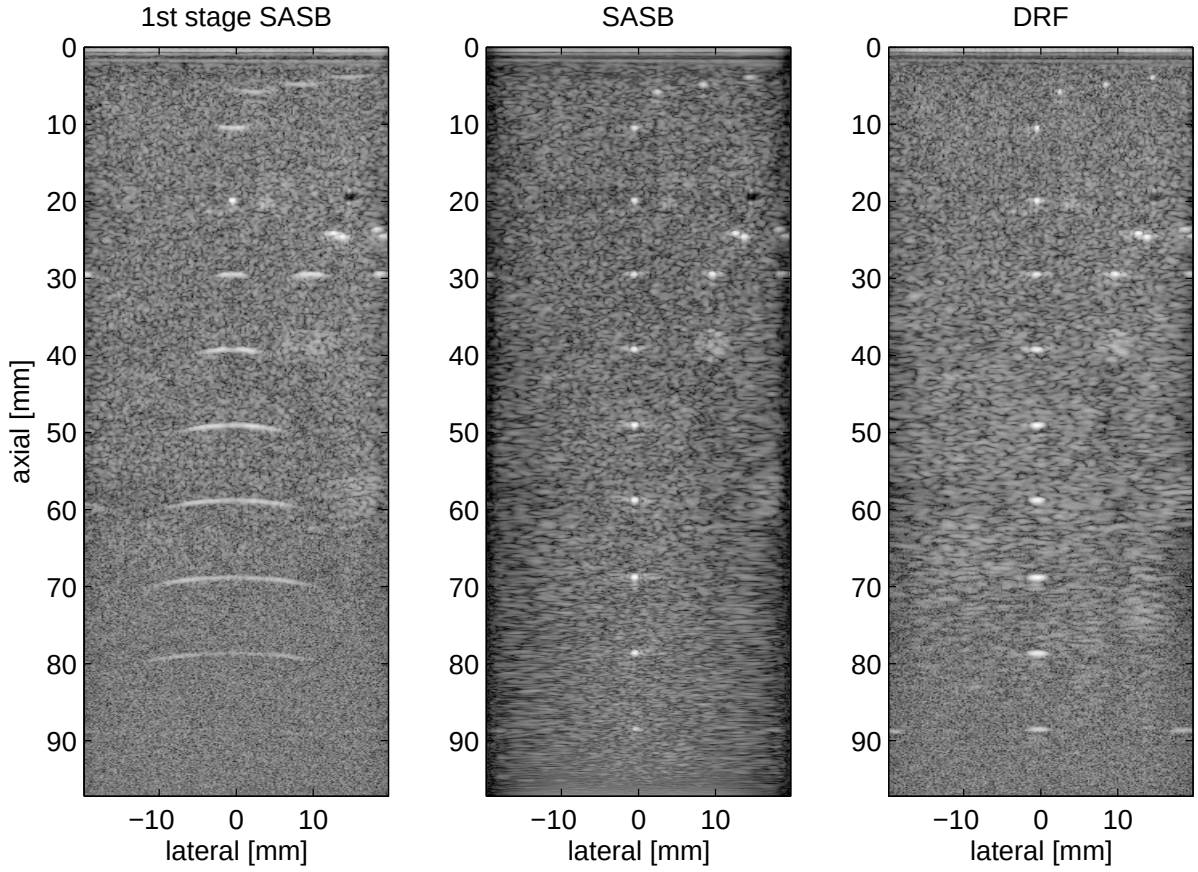

Figure 4.40: Envelope images using 1st stage SASB (left), SASB (center), and DRF (right). RF-data is acquired using a commercial scanner, and processing is done off-line. For DRF the transmit focal point is at 65 mm. For SASB the VS is at 20 mm and $F\# = 2$. Dynamic Range is 60 dB.

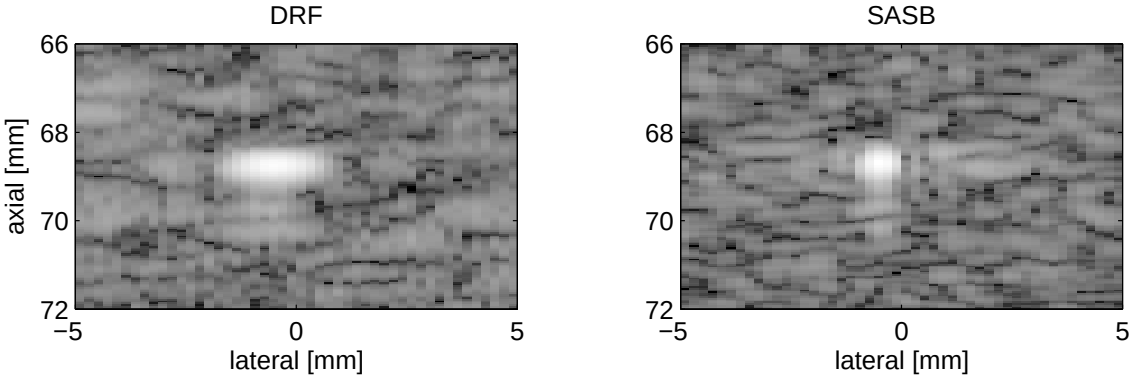

Figure 4.41: A zoom in on the DRF and SASB images from Fig. 4.40.

object does not move in between acquisitions and assuming uncorrelated electronic noise at the receivers the potential SNR improvement at the center HRL compared to 1st stage RF-data is

$$\Delta SNR(z) = 10\log_{10}\left(\sum_{k}^{K(z)} \mathcal{W}(x_k, z)\right). \tag{4.15}$$

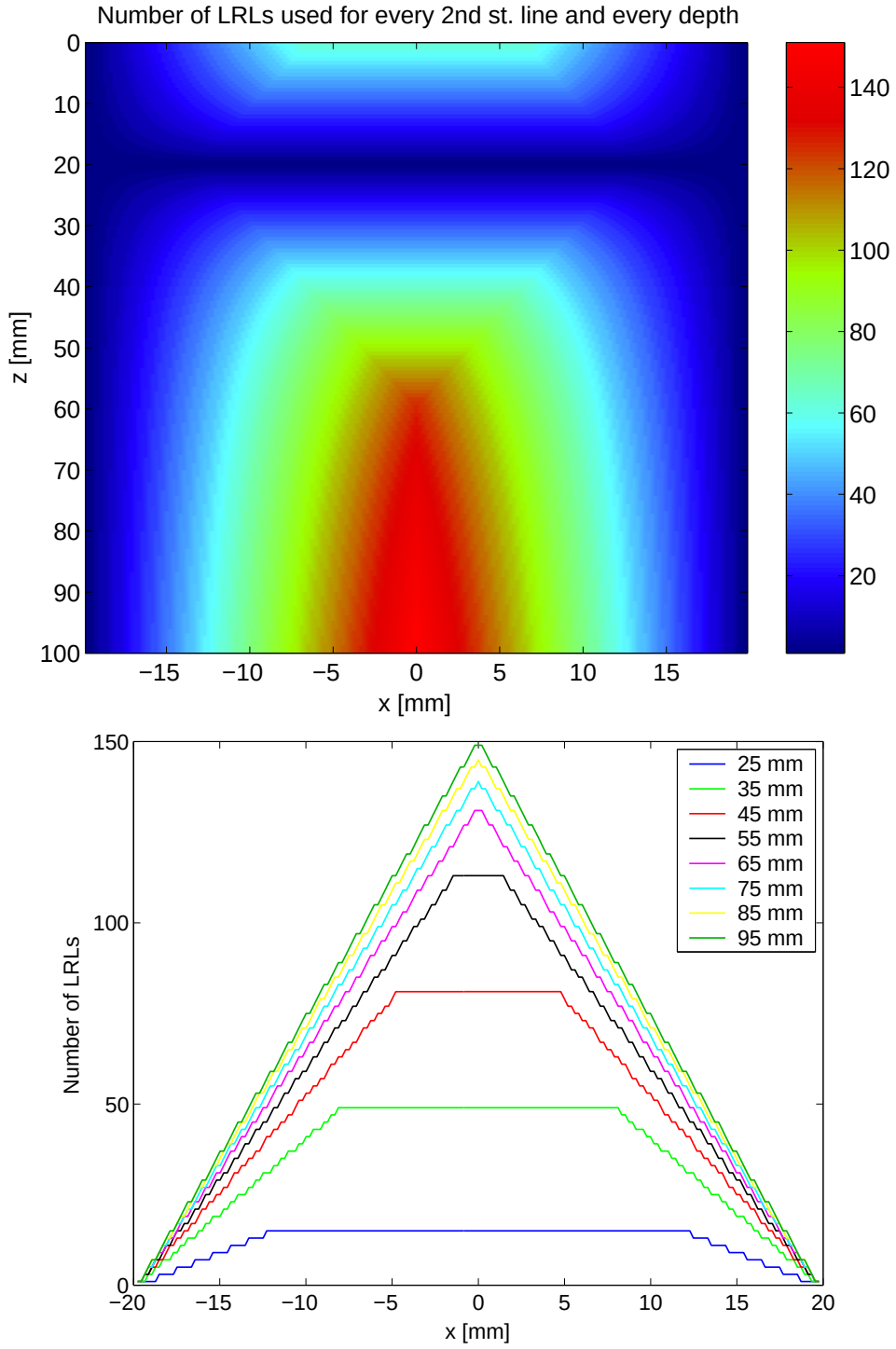

Figure 4.42: Number of applied LRL's as a function of depth and lateral position of the HRL (Top). The VS is at 20 mm and $F\# = 1.5$. Shown as a function of lateral position only for different depths (bottom).

The signal to noise ratio as a function of depth for a set of acquired DRF-data and a set of 1st stage SASB-data has been estimated, and is shown in Fig. 4.43. For DRF the transmit focus is at 45 mm and for SASB the VS is at 20 mm with $F\# = 2$. 20 data sets have been acquired for both DRF and SASB using a tissue phantom with an attenuation of 0.5 dB/[MHz cm]. The signal part is estimated by averaging the measured signals. A set of noise signals is estimated

by subtracting the estimated signal part from the measured signals. The SNR is

$$\begin{aligned} SNR(z) &= \frac{\mathcal{E}\{Y(z)\}^2}{\mathcal{E}\left\{[Y(z)-\mathcal{E}\{Y(z)\}]\right\}^2} \\ &\simeq \frac{\left(\frac{1}{M}\sum_{m=1}^{M} y_m(z)\right)^2}{\frac{1}{M}\sum_{m=1}^{M}\left[y_m(z)-\frac{1}{M}\sum_{m=1}^{M} y_m(z)\right]^2}. \end{aligned} \tag{4.16}$$

$\mathcal{E}$ is the expectation operator. $Y(z)$ denotes the M number of measured data sets, and $y_m(z)$ is the m'th data set. The theoretical potential improvement in SNR, $\Delta SNR(z)$ from (4.15) is also shown in Fig. 4.43 with a boxcar and a Hamming window as SA weighting. For $z = 80$ mm the value of $\Delta SNR(z)$ can be calculated using (4.5) and (4.4) and is 19 dB. The potential SNR of the SASB is superior to DRF at the entire range and an improvement of 8 dB is realized at a depth of 80 mm.

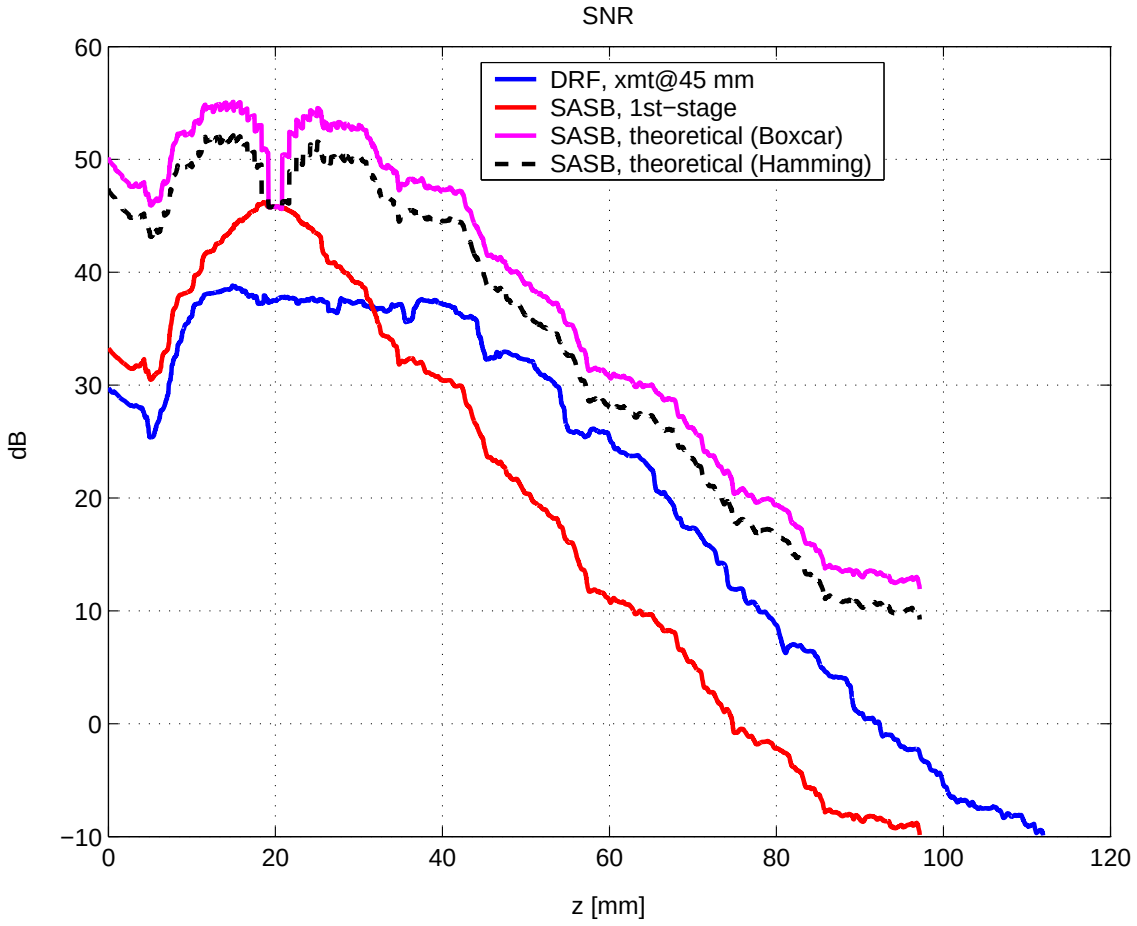

Figure 4.43: Estimated SNR as a function of depth. Data sets are acquired with a commercial scanner and a tissue phantom for both DRF (blue) and 1 stage SASB (red). The theoretical SNR of the 2nd stage SASB is also shown with and without the SA-weighting (black and magenta).

4.5 Conclusion

The main motivation for SASB is to apply synthetic aperture techniques with a restricted system complexity. The objective is to improve lateral resolution and obtain a more range independent

resolution compared to conventional ultrasound imaging.

The SASB method has been investigated using simulations in Field II and by off-line processing of data acquired with a commercial scanner. The parameters which are the most decisive for the performance are the depth of the VS (the focal depth), and the $F\#$ of the VS. The lateral resolution increases with a decreasing $F\#$, but grating lobes arise at a combination of a sparse spatial sampling by the virtual array and wave fields with incident angles beyond a certain limit. It is possible to restrict the range of incident angles by putting a limit to the opening angle of the VS. For a transducer with a pitch of $\Delta = \lambda$ grating lobes are avoided if $F\# \geq 2$. For a phased array transducer with $\Delta = \lambda/2$ grating lobes are avoided if $F\# \geq 1$.

Simulations have been done with two different pulse-echo responses having different bandwidths. The performance difference between the two Simulation Models is significant. The lateral resolution is significantly better for the Simulation Model with the longer pulse-echo response and the improvement is at least a factor of 2 at -40 dB. With a longer pulse-echo response the off-center HRL is composed of the sum of several positive and negative half-periods of the LRL's and on average sum destructively to a zero level. This is not the case for a short pulse-echo response. Here the off-center HRL is composed of the sum of a only a few positive and negative half-periods and, thus, sum less destructively.

The performance of SASB with the VS at 20 mm and $F\# = 1.5$ is compared with conventional dynamic receive focusing (DRF). The axial resolution is the same for the two methods. There is an substantial improvement in lateral resolution using SASB compared to DRF. It accounts for both the FWHM and the resolution at -40 dB. The improvement in FWHM is at least a factor of 2 and the improvement at -40 dB is at least a factor of 3. The improvement of SASB over DRF is a reality except for a few exceptions. At depths until 20 mm the FWHM is superior with DRF. With SASB the resolution is almost constant throughout the range. For DRF the FWHM increases almost linearly with range and the resolution at -40 dB is fluctuating with range. By putting restrictions on the number of 2nd stage beamformer channels the system complexity is reduced. It will have a negative consequence on resolution, since the synthesized aperture decreases, but even when the number of channels is restricted to $N_{2nd} = 63$ the performance of SASB is still superior to DRF.

SASB has been applied to data acquired with a commercial scanner and a tissue phantom with wire targets. The images confirms the results from the simulations. At the center of the image the resolution of SASB is superior to DRF and is practically range independent. The resolution in the near field is slightly better for DRF. A feasible solution could be to construct the final image by applying DRF above the VS and SASB beyond the VS.

A decrease in performance at the transducer edges occur for both DRF and SASB. They are more profound for SASB and especially at greater depths it is obvious that the lateral resolution is laterally dependent. A solution could be to apply DRF at the edges as a supplement to SASB.

The speckle pattern is present at a greater range in the SASB image compared to the DRF image indicating greater penetration. The signal to noise ratio as a function of depth for a set of acquired DRF-data and a set of 1st stage SASB-data has been estimated. The theoretical potential improvement in SNR of SASB over DRF has been estimated based on the measured SNR data and an assumption of a stationary image object, and a correct phase-alignment in the 2nd stage beamformer. The improvement is attained at the entire range and at a depth of 80 mm the improvement is 8 dB.

CHAPTER

FIVE

Conclusion

Several subjects have been addressed during this PhD project, and all of them are related to beamforming.

Many aspects of delay-and-sum beamforming have been investigated. A part of the project has been to take part in the development of a software toolbox for off-line dynamic receive focusing of scan lines in any arbitrary direction in 3D space. It offers a choice between different methods for calculating time-delays, and various inter-sample interpolation schemes. Apodization can be any preferred window function of fixed size or it can be fully dynamic with an expanding and contracting aperture to obtain a preferred F-number. Some of the beamformer design principles and some of the many considerations in relation to beamformer development and implementation have been shared.

Directional beamforming has been applied for a velocity vector estimator. The simulation study and measurement study both showed that angle estimation by directional beamforming can be estimated with a high precision. Using the measurements more than 96% valid estimates were produced for the flow angles $\theta = \{60^\circ, 75^\circ, 90^\circ\}$ and with a bias below 2° and a standard deviation below 5°. The angle estimation performance is strongly influenced by the choice of correlation-time, and the computational task is heavy.

Through simulations in Field II mono-static synthetic aperture focusing of pulse-echo data from a rotating concave element has been investigated. The radial and angular resolution have been extracted using transducer elements with a focal depth of 10 mm, 15 mm, and 20 mm. Due to the rotation, the synthesized aperture only experiences a moderate expansion. This is not sufficient to reduce the extent of the wide point spread function of a single emission. At least not to a level which is competitive to the relatively narrow PSF of the setup with focal depth at 20 mm. The effect of SAF with focal depth at 20 mm is also negligible due to the small number of LRL's added. The advantage of SAF is the increase in SNR. For the setup with focal depth at 20 mm the SAF SNR gain is 11 dB. The SNR gain of a setup with a VS at radius 10 mm or 15 mm over conventional imaging with a VS at 20 mm is also 11 dB. The SNR improvement can be converted directly to an increase in penetration or an increase in emitted frequency yielding a higher resolution.

The SASB method has been investigated using simulations in Field II and by off-line processing of data acquired with a commercial scanner. The parameters which are the most decisive for the performance are the depth of the VS (the focal depth), and the $F\#$ of the VS. The lateral resolution increases with a decreasing $F\#$, but the effects of grating lobes become increasingly more dominant. For a transducer with a pitch of $\Delta = \lambda$ grating lobes are avoided if $F\# \geq 2$. For a phased array transducer with $\Delta = \lambda/2$ grating lobes are avoided if $F\# \geq 1$.

The performance of SASB with the VS at 20 mm and $F\# = 1.5$ is compared with conventional dynamic receive focusing (DRF). The axial resolution is the same for the two methods. There is an substantial improvement in lateral resolution using SASB compared to DRF. It accounts for both the FWHM and the resolution at -40 dB. The improvement in FWHM is at least a factor of 2 and the improvement at -40 dB is at least a factor of 3. The improvement of SASB over DRF is a reality except for a few exceptions. At depths until 20 mm the FWHM is superior with DRF. With SASB the resolution is almost constant throughout the range. For DRF the FWHM increases almost linearly with range and the resolution at -40 dB is fluctuating with range. By putting restrictions on the number of 2nd stage beamformer channels the system complexity is reduced. It will have a negative consequence on resolution, since the synthesized aperture decreases, but even when the number of channels is restricted to $N_{2nd} = 63$ the performance of SASB is still superior to DRF.

SASB has been applied to data acquired with a commercial scanner and a tissue phantom with wire targets. The images confirm the results from the simulations. At the center of the image the resolution of SASB is superior to DRF and is practically range independent. The resolution in the near field is slightly better for DRF. A feasible solution could be to construct the final image by applying DRF above the VS and SASB beyond the VS.

A decrease in performance at the transducer edges occur for both DRF and SASB. They are more profound for SASB and especially at greater depths it is obvious that the lateral resolution is laterally dependent. A solution could be to apply DRF at the edges as a supplement to SASB.

The speckle pattern is present at a greater range in the SASB image compared to the DRF image indicating greater penetration. The signal to noise ratio as a function of depth for a set of acquired DRF-data and a set of 1st stage SASB-data has been estimated. The theoretical potential improvement in SNR of SASB over DRF has been estimated based on the measured SNR data and an assumption of a stationary image object, and a correct phase-alignment in the 2nd stage beamformer. The improvement is attained at the entire range and at a depth of 80 mm the improvement is 8 dB.

Bibliography

[1] K. E. Thomenius, “Evolution of ultrasound beamformers,” in *Proc. IEEE Ultrason. Symp.*, vol. 2, 1996, pp. 1615–1621.

[2] C. Kasai, K. Namekawa, A. Koyano, and R. Omoto, “Real-time two-dimensional blood flow imaging using an autocorrelation technique,” *IEEE Trans. Son. Ultrason.*, vol. 32, pp. 458–463, 1985.

[3] S. G. Foster, “A pulsed ultrasonic flowmeter employing time domain methods,” Ph.D. dissertation, Dept. Elec. Eng., University of Illinois, Urbana, Ill., 1985.

[4] O. Bonnefous and P. Pesqué, “Time domain formulation of pulse-Doppler ultrasound and blood velocity estimation by cross correlation,” *Ultrason. Imaging*, vol. 8, pp. 73–85, 1986.

[5] S. Gustavsson, “Parallel algorithms for ultrasound beamformation,” Master’s thesis, Ørsted•DTU, Technical University of Denmark, Lyngby, Denmark, 2002.

[6] T. Pham and T. Whipps, “Acoustic signal processing toolbox for array processing,” *Proceedings of SPIE - The International Society for Optical Engineering*, vol. 5096, pp. 597–606, 2003.

[7] S. Bjorklund and D. Rejdemyhr, “A matlab toolbox for radar array processing,” *Signal Processing and Its Applications, 1999. ISSPA ’99*, vol. 2, pp. 547–550, 1999.

[8] R. Hansen, T. Saebo, H. Callow, P. Hagen, and E. Hammerstad, “Synthetic aperture sonar processing for the hugin auvoceans 2005 - europe,” *Oceans 2005 - Europe, IEEE*, vol. 2, pp. 1090–1094, 2005.

[9] J. A. Jensen, “Users’ guide for the Field II program, version 2.70 of may 26, 1999,” Department of Information Technology, DTU, Tech. Rep., 1999.

[10] ——, “Directional velocity estimation using focusing along the flow direction: I: Theory and simulation,” *IEEE Trans. Ultrason., Ferroelec., Freq. Contr.*, pp. 857–872, 2003.

[11] ——, “Velocity vector estimation in synthetic aperture flow and B-mode imaging,” in *IEEE International Symposium on Biomedical imaging from nano to macro*, 2004, pp. 32–35.

[12] J. Kortbek and J. A. Jensen, “Estimation of velocity vector angles using the directional cross-correlation method,” *IEEE Trans. Ultrason., Ferroelec., Freq. Contr.*, vol. 53, pp. 2036–2049, 2006.

[13] G. R. Lockwood, J. R. Talman, and S. S. Brunke, “Real-time 3-D ultrasound imaging using sparse synthetic aperture beamforming,” *IEEE Trans. Ultrason., Ferroelec., Freq. Contr.*, vol. 45, pp. 980–988, 1998.

[14] S. I. Nikolov, “Synthetic aperture tissue and flow ultrasound imaging,” Ph.D. dissertation, Ørsted•DTU, Technical University of Denmark, 2800, Lyngby, Denmark, 2001.

[15] K. Gammelmark, “Improving the image quality of synthetic transmit aperture ultrasound images,” Ph.D. dissertation, Ørsted•DTU, Technical University of Denmark, 2800, Lyngby, Denmark, 2004.

[16] C. R. Hazard and G. R. Lockwood, “Theoretical assessment of a synthetic aperture beamformer for real-time 3-D imaging,” *IEEE Trans. Ultrason., Ferroelec., Freq. Contr.*, vol. 46, pp. 972–980, 1999.

[17] L. F. Nock and G. E. Trahey, “Synthetic aperture imaging in medical ultrasound with correction for motion artifacts,” in *Proc. IEEE Ultrason. Symp.*, 1990, pp. 1597–1601.

[18] ——, “Synthetic receive aperture imaging with phase correction for motion and for tissue inhomogenities - part I: basic principles,” *IEEE Trans. Ultrason., Ferroelec., Freq. Contr.*, vol. 39, pp. 489–495, 1992.

[19] G. E. Trahey and L. F. Nock, “Synthetic receive aperture imaging with phase correction for motion and for tissue inhomogenities - part II: effects of and correction for motion,” *IEEE Trans. Ultrason., Ferroelec., Freq. Contr.*, vol. 39, pp. 496–501, 1992.

[20] C. Passmann and H. Ermert, “Adaptive 150 MHz ultasound imaging of the skin and the eye using an optimal combination of short pulse mode and pulse compression mode,” in *Proc. IEEE Ultrason. Symp.*, 1995, pp. 1291–1294.

[21] ——, “A 100-MHz ultrasound imaging system for dermatologic and ophthalmologic diagnostics,” *IEEE Trans. Ultrason., Ferroelec., Freq. Contr.*, vol. 43, pp. 545–552, 1996.

[22] C. H. Frazier and W. D. O’Brien, “Synthetic aperture techniques with a virtual source element,” *IEEE Trans. Ultrason., Ferroelec., Freq. Contr.*, vol. 45, pp. 196–207, 1998.

[23] S. I. Nikolov and J. A. Jensen, “Virtual ultrasound sources in high-resolution ultrasound imaging,” in *Proc. SPIE - Progress in biomedical optics and imaging*, vol. 3, 2002, pp. 395–405.

[24] ——, “Comparison between different encoding schemes for synthetic aperture imaging,” in *Proc. SPIE - Progress in biomedical optics and imaging*, vol. 3, 2002, pp. 1–12.

[25] J. C. Curlander and R. N. McDonough, *Synthetic Aperture Radar: Systems and Signal Processing*. John Wiley & Sons, Inc., 1991.

[26] The MathWorks Inc., *MATLAB Application Program Interface Guide*. The MathWorks Inc., 1998.

[27] ——, *External Interfaces/API*. The MathWorks Inc., 2002.

[28] A. Melchiorsen, "A library for parallel computations in Matlab," Master's thesis, Ørsted•DTU, Technical University of Denmark, Lyngby, Denmark, 2002.

[29] J. A. Jensen and P. Munk, "A new method for estimation of velocity vectors," *IEEE Trans. Ultrason., Ferroelec., Freq. Contr.*, vol. 45, pp. 837–851, 1998.

[30] P. Montuschi, "Survey of square rooting algorithms," *IEEE Proceedings, Pt. E, No.1*, vol. 137, 1990.

[31] S. I. Nikolov, J. A. Jensen, and B. G. Tomov, "Recursive delay calculation unit for parametric beamformer," in *Proc. SPIE - Progress in biomedical optics and imaging*, vol. 6147-13, 2006, pp. 1–12.

[32] S. I. Nikolov, B. G. Tomov, and J. A. Jensen, "Parametric beamformer for synthetic aperture ultrasound imaging," in *Proc. IEEE Ultrason. Symp.*, 2006, pp. 2172–2176.

[33] H. Andresen, S. Nikolov, C. Hassager, J. Kjærgaard, and J. A. Jensen, "Cardiac in-vivo measurements using synthetic transmit aperture ultrasound," in *Proc. IEEE Ultrason. Symp.*, 2006, pp. 1115–1118.

[34] N. Oddershede and J. A. Jensen, "Motion compensated beamforming in synthetic aperture vector flow imaging," in *Proc. IEEE Ultrason. Symp.*, 2006, pp. 2027–2031.

[35] ——, "Effects influencing focusing in synthetic aperture vector flow imaging," *IEEE Trans. Ultrason., Ferroelec., Freq. Contr.*, vol. 54, no. 9, pp. 1811–1825, September 2007.

[36] I. Bolic, J. Udesen, F. Gran, and J. A. Jensen, "Plane wave fast color flow mode imaging: parameter study," in *Proc. SPIE - Progress in biomedical optics and imaging*, vol. 6417-30, 2006, pp. 1–11.

[37] F. Gran and J. A. Jensen, "Directional velocity estimation using a spatio-temporal encoding technique based on frequency division for synthetic transmit aperture ultrasound," *IEEE Trans. Ultrason., Ferroelec., Freq. Contr.*, vol. 53(7), pp. 1289–1299, 2006.

[38] ——, "Frequency division transmission and synthetic aperture reconstruction," *IEEE Trans. Ultrason., Ferroelec., Freq. Contr.*, vol. 53(5), pp. 900–911, 2006.

[39] H. Andresen, *Beamformation Interpolation Schemes using Field II*. Special Course Report. Ørsted•DTU, Technical University of Denmark, 2005.

[40] W. H Press et. Al, *Numerical Recipes in C*. Cambridge University Press, 1992.

[41] R. E. Crochiere and L. R. Rabiner, *Multirate digital signal processing*. Prentice-Hall, Englewood Cliffs, NJ, 1983.

[42] D. H. Evans, W. N. McDicken, R. Skidmore, and J. P. Woodcock, *Doppler Ultrasound, Physics, Instrumentation, and Clinical Applications*. New York: John Wiley & Sons, 1989.

[43] J. A. Jensen, *Estimation of Blood Velocities Using Ultrasound: A Signal Processing Approach*. New York: Cambridge University Press, 1996.

[44] M. D. Fox, "Multiple crossed-beam ultrasound Doppler velocimetry," *IEEE Trans. Son. Ultrason.*, vol. SU-25, pp. 281–286, 1978.

[45] G. E. Trahey, J. W. Allison, and O. T. von Ramm, "Angle independent ultrasonic detection of blood flow," *IEEE Trans. Biomed. Eng.*, vol. BME-34, pp. 965–967, 1987.

[46] M. E. Anderson, "Multi-dimensional velocity estimation with ultrasound using spatial quadrature," *IEEE Trans. Ultrason., Ferroelec., Freq. Contr.*, vol. 45, pp. 852–861, 1998.

[47] H. F. Routh, T. L. Pusateri, and D. D. Waters, "Preliminary studies into high velocity transverse blood flow measurement," in *Proc. IEEE Ultrason. Symp.*, 1990, pp. 1523–1526.

[48] V. L. Newhouse, D. Censor, T. Vontz, J. A. Cisneros, and B. B. Goldberg, "Ultrasound Doppler probing of flows transverse with respect to beam axis," *IEEE Trans. Biomed. Eng.*, vol. BME-34, pp. 779–788, 1987.

[49] J. A. Jensen and R. Bjerngaard, "Directional velocity estimation using focusing along the flow direction: II: Experimental investigation," *IEEE Trans. Ultrason., Ferroelec., Freq. Contr.*, pp. 873–880, 2003.

[50] L. J. Cutrona, W. E. Vivian, E. N. Leith, and G. O. Hall, "A high resolution radar combat-surveillance system," *IRE Trans. Mil. Elect.*, vol. MIL-5, no. 2, pp. 127–131, 1961.

[51] C. W. Sherwin, J. P. Ruina, and D. Rawcliffe, "Some early developements in synthetic aperture radar systems," *IRE Trans. Mil. Elect.*, vol. MIL-6, no. 2, pp. 111–115, 1962.

[52] M. Karaman, P. C. Li, and M. O'Donnell, "Synthetic aperture imaging for small scale systems," *IEEE Trans. Ultrason., Ferroelec., Freq. Contr.*, vol. 42, pp. 429–442, 1995.

[53] R. Y. Chiao, L. J. Thomas, and S. D. Silverstein, "Sparse array imaging with spatially-encoded transmits," in *Proc. IEEE Ultrason. Symp.*, 1997, pp. 1679–1682.

[54] J. T. Ylitalo and H. Ermert, "Ultrasound synthetic aperture imaging: monostatic approach," *IEEE Trans. Ultrason., Ferroelec., Freq. Contr.*, vol. 41, pp. 333–339, 1994.

[55] M. H. Pedersen, K. L. Gammelmark, and J. A. Jensen, "In-vivo evaluation of convex array synthetic aperture imaging," *Ultrasound Med. Biol.*, vol. 33, pp. 37–47, 2007.

[56] D. K. Peterson and G. S. Kino, "Real-time digital image reconstruction: A description of imaging hardware and an analysis of quantization errors," *IEEE Trans. Son. Ultrason.*, vol. 31, pp. 337–351, 1984.

[57] M. O'Donnell and L. J. Thomas, "Efficient synthetic aperture imaging from a circular aperture with possible application to catheter-based imaging," *IEEE Trans. Ultrason., Ferroelec., Freq. Contr.*, vol. 39, pp. 366–380, 1992.

[58] S. I. Nikolov and J. A. Jensen, "3D synthetic aperture imaging using a virtual source element in the elevation plane," in *Proc. IEEE Ultrason. Symp.*, vol. 2, 2000, pp. 1743–1747.

[59] M. H. Bae and M. K. Jeong, "A study of synthetic-aperture imaging with virtual source elements in B-mode ultrasound imaging systems," in *IEEE Trans. Ultrason., Ferroelec., Freq. Contr.*, vol. 47, 2000, pp. 1510–1519.

[60] J. A. Jensen and N. B. Svendsen, “Calculation of pressure fields from arbitrarily shaped, apodized, and excited ultrasound transducers,” *IEEE Trans. Ultrason., Ferroelec., Freq. Contr.*, vol. 39, pp. 262–267, 1992.

[61] J. A. Jensen, “Field: A program for simulating ultrasound systems,” *Med. Biol. Eng. Comp.*, vol. 10th Nordic-Baltic Conference on Biomedical Imaging, Vol. 4, Supplement 1, Part 1, pp. 351–353, 1996b.

[62] J. Kortbek, S. I. Nikolov, and J. A. Jensen, “Effective and Versatile software Beamformation Toolbox,” in *Proc. SPIE - Medical Imaging - Ultrasonic Imaging and Signal Processsing*, 2007, pp. 651 319,1–10.

[63] J. Kortbek, J. A. Jensen, and K. L. Gammelmark, “Synthetic Aperture Focusing Applied to Imaging Using a Rotating Single Element Transducer,” in *Proc. IEEE Ultrason. Symp.*, Oct. 2007 (Accepted).

[64] H. Ş. Bilge, M. Karaman, and M. O’Donnell, “Motion estimation using common spatial frequencies in synthetic aperture imaging,” in *Proc. IEEE Ultrason. Symp.*, 1996, pp. 1551–1554.

[65] M. Karaman, H. Ş. Bilge, and M. O’Donnell, “Adaptive multi-element synthetic aperture imaging with motion and phase aberation correction,” *IEEE Trans. Ultrason., Ferroelec., Freq. Contr.*, vol. 42, pp. 1077–1087, 1998.

[66] C. R. Hazard and G. R. Lockwood, “Effects of motion artifacts on a synthetic aperture beamformer for real-time 3D ultrasound,” in *Proc. IEEE Ultrason. Symp.*, 1999, pp. 1221–1224.

[67] J. S. Jeong, J. S. Hwang, M. H. Bae, and T. K. Song, “Effects and limitations of motion compensation in synthetic aperture techniques,” in *Proc. IEEE Ultrason. Symp.*, 2000, pp. 1759 –1762.

[68] S. I. Nikolov and J. A. Jensen, “K-space model of motion artifacts in synthetic transmit aperture ultrasound imaging,” in *Proc. IEEE Ultrason. Symp.*, 2003, pp. 1824–1828.

[69] K. L. Gammelmark and J. A. Jensen, “Multielement synthetic transmit aperture imaging using temporal encoding,” *IEEE Trans. Med. Imag.*, vol. 22, no. 4, pp. 552–563, 2003.

[70] ——, “Duplex synthetic aperture imaging with tissue motion compensation,” in *Proc. IEEE Ultrason. Symp.*, 2003, pp. 1569–1573.

[71] S. I. Nikolov, K. Gammelmark, and J. A. Jensen, “Recursive ultrasound imaging,” in *Proc. IEEE Ultrason. Symp.*, vol. 2, 1999, pp. 1621–1625.

[72] P. R. Stepanishen, “Pulsed transmit/receive response of ultrasonic piezoelectric transducers,” *J. Acoust. Soc. Am.*, vol. 69, pp. 1815–1827, 1981.

[73] J. A. Jensen, “A model for the propagation and scattering of ultrasound in tissue,” *J. Acoust. Soc. Am.*, vol. 89, pp. 182–191, 1991a.

APPENDIX

A

Synthetic Aperture Sequential Beamforming - Additional Results

This chapter contains additional results from the parameter study of synthetic aperture sequential beamforming. They include plots of the number of applied LRL's, log-compressed envelope images with a dynamic range of 60 dB, and plots of lateral point spread functions. The axial and lateral FWHM, and lateral resolution at levels of -40 dB and -50 dB are also shown. The simulation study described in Section 4.3 made use of two different Simulation Models. Both Simulation Models are applied for the results presented in this chapter. The two models are described in Section 4.3.1. They are denoted Simulation Model *I* and Simulation Model *II*. Parameters common for both models are shown in Table 4.1, and the differences are highlighted in Table A.1. The image width using Simulation Model *I* is greater than with Simulation Model *II*. All results in this chapter are shown for an image width of 40 mm only. The results are presented in sections with the following section titles

- VS at 5 mm, Simulation Model *I*
- VS at 10 mm, Simulation Model *I*
- VS at 15 mm, Simulation Model *I*
- VS at 20 mm, Simulation Model *I*
- VS at 10 mm, Simulation Model *II*
- VS at 15 mm, Simulation Model *II*
- VS at 20 mm, Simulation Model *II*

Parameter	*I*	*II*
Transducer		
Number of elements	401	191
Excitation	1 cycle (f_0)	2 cycles (f_0)
Impulse response	2-cycle (f_0)	measured

Table A.1: Differences between Simulation Model *I* and Simulation Model *II*. The other values common for both models are found in Table 4.1.

A.1 VS at 5 mm, Simulation Model *I*

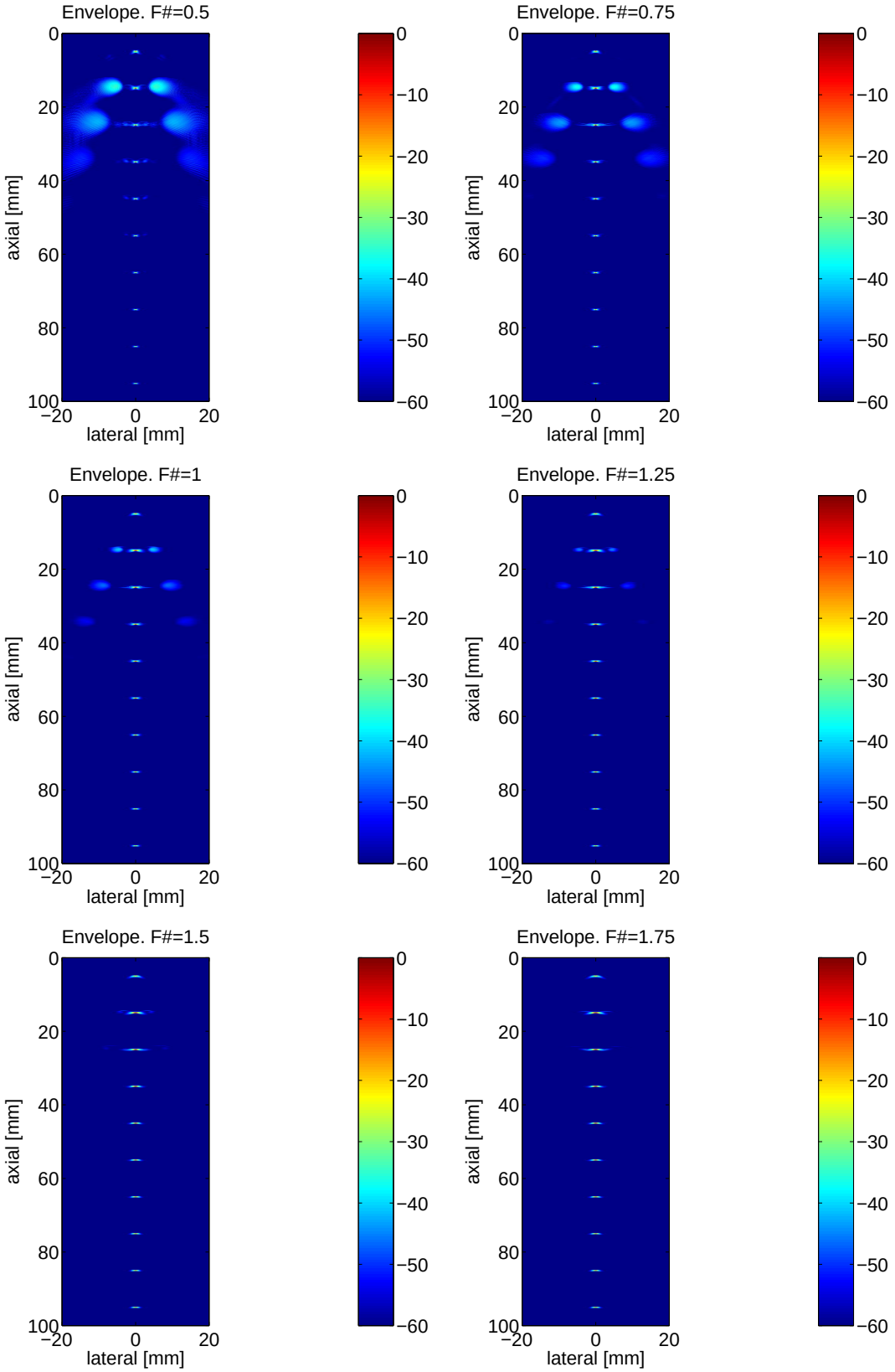

Figure A.1: Envelope detected and log-compressed images for different values of $F\#$ and with a dynamic range of 60 dB. VS at 5 mm, Simulation Model *I*.

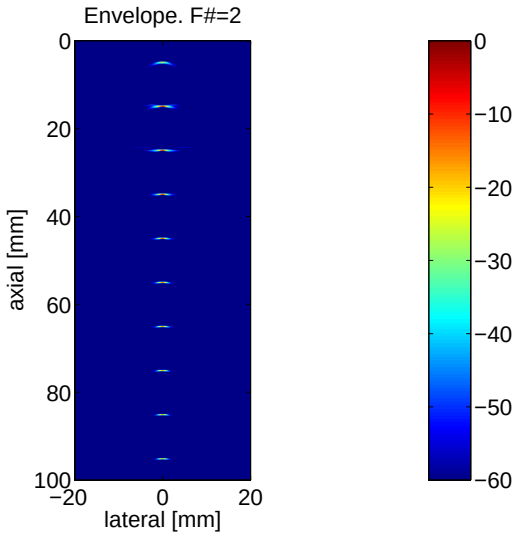

Figure A.2: Envelope detected and log-compressed image for $F\# = 2$ with a dynamic range of 60 dB. VS at 5 mm, Simulation Model *I*.

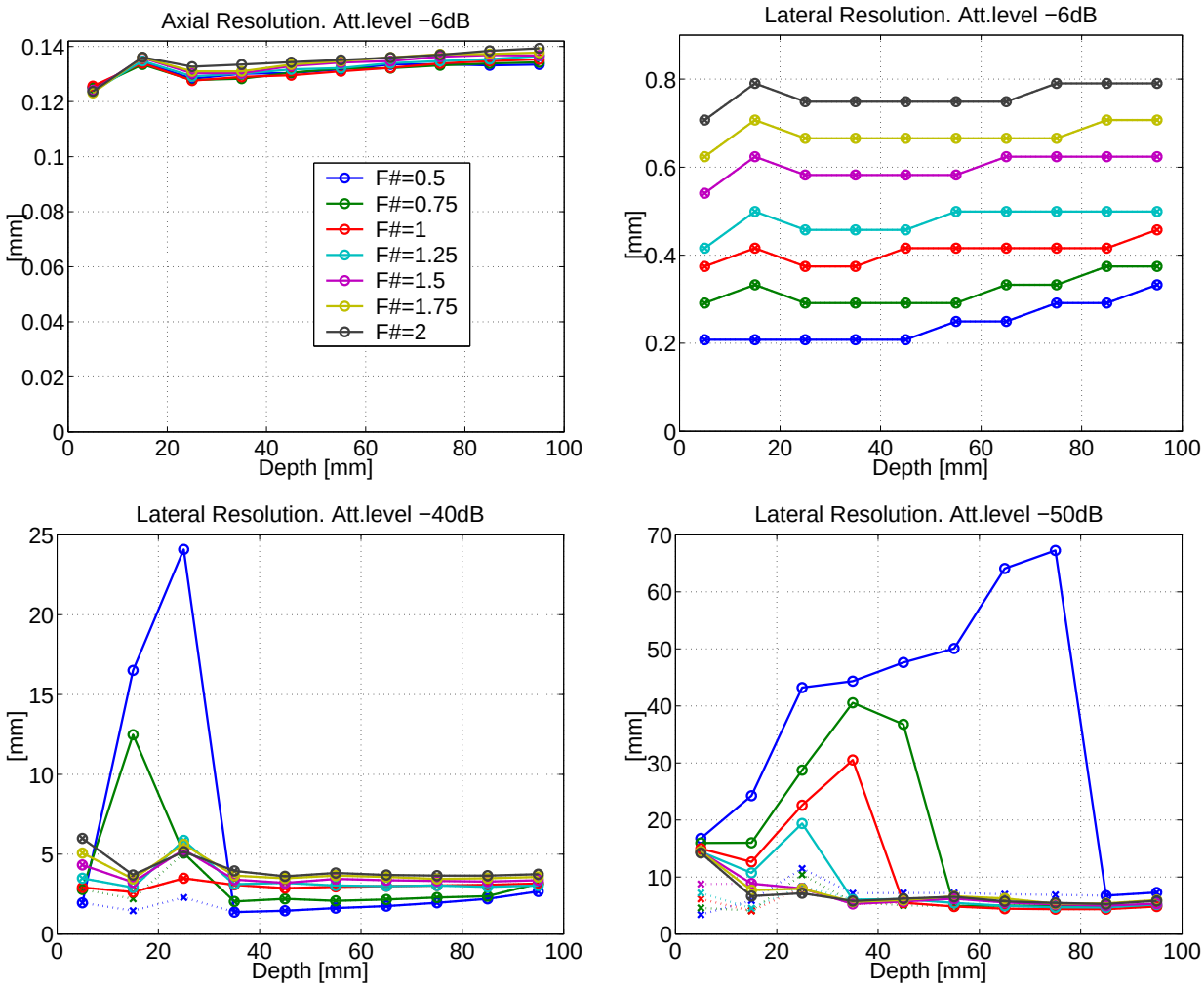

Figure A.3: Axial and lateral resolution as function of depth at levels of -6 dB, -40 dB, and -50 dB. If the lateral PSF has a distinct main-lobe and side-lobe distribution, the main-lobe resolution is shown as a dotted line. VS at 5 mm, Simulation Model *I*.

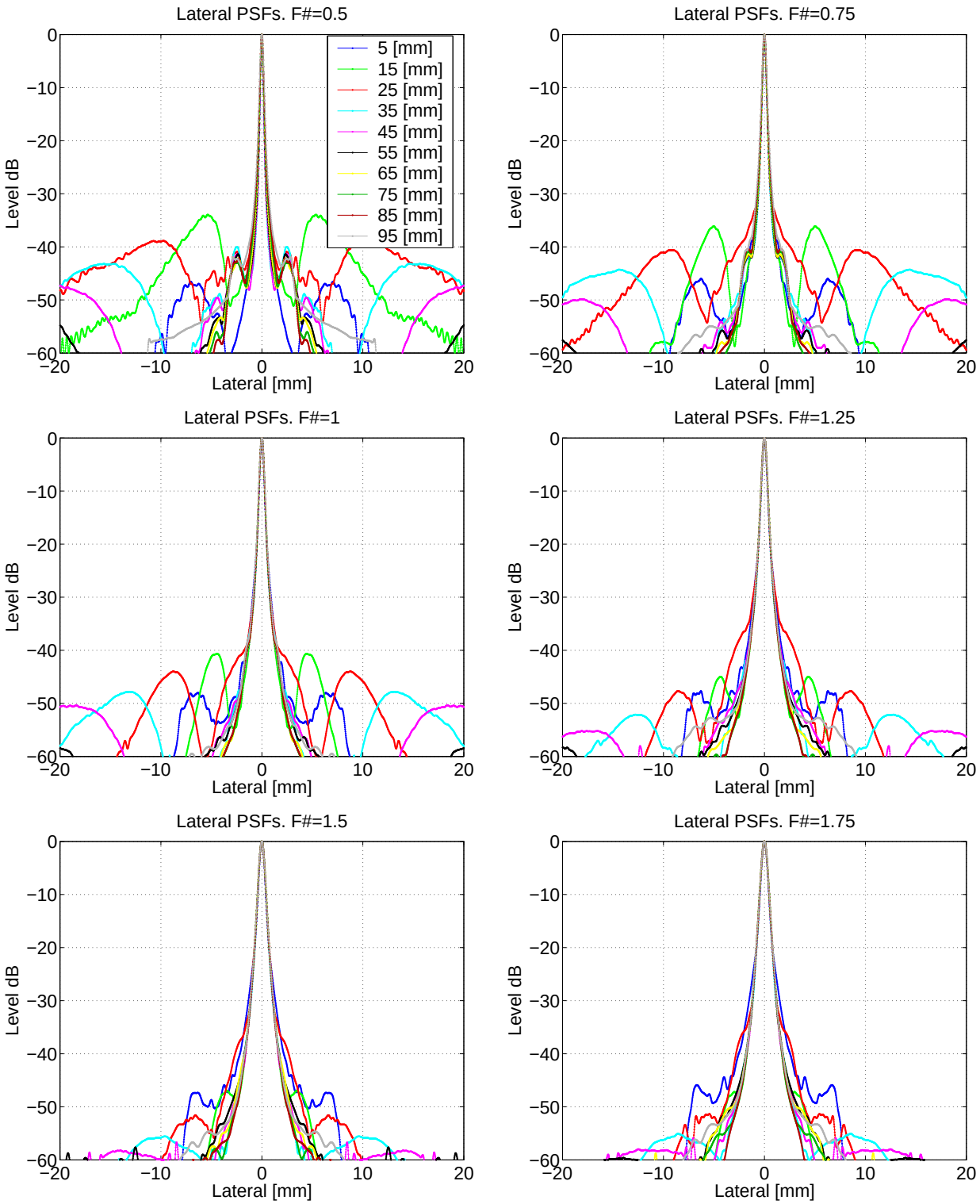

Figure A.4: Lateral PSF's at different depths are stacked up for different values of *F#*. VS at 5 mm, Simulation Model *I*.

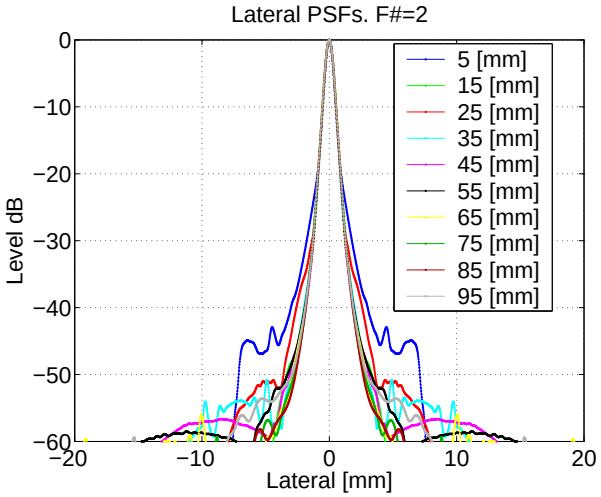

Figure A.5: Lateral PSF's at different depths are stacked up for $F\# = 2$. VS at 5 mm, Simulation Model *I*.

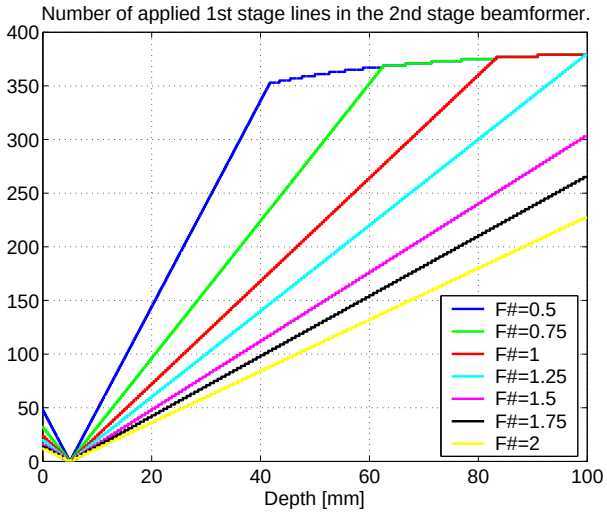

Figure A.6: The number of applied 1st stage lines in the 2nd stage beamformer for the center HRL. VS at 5 mm, Simulation Model *I*.

A.2 VS at 10 mm, Simulation Model *I*

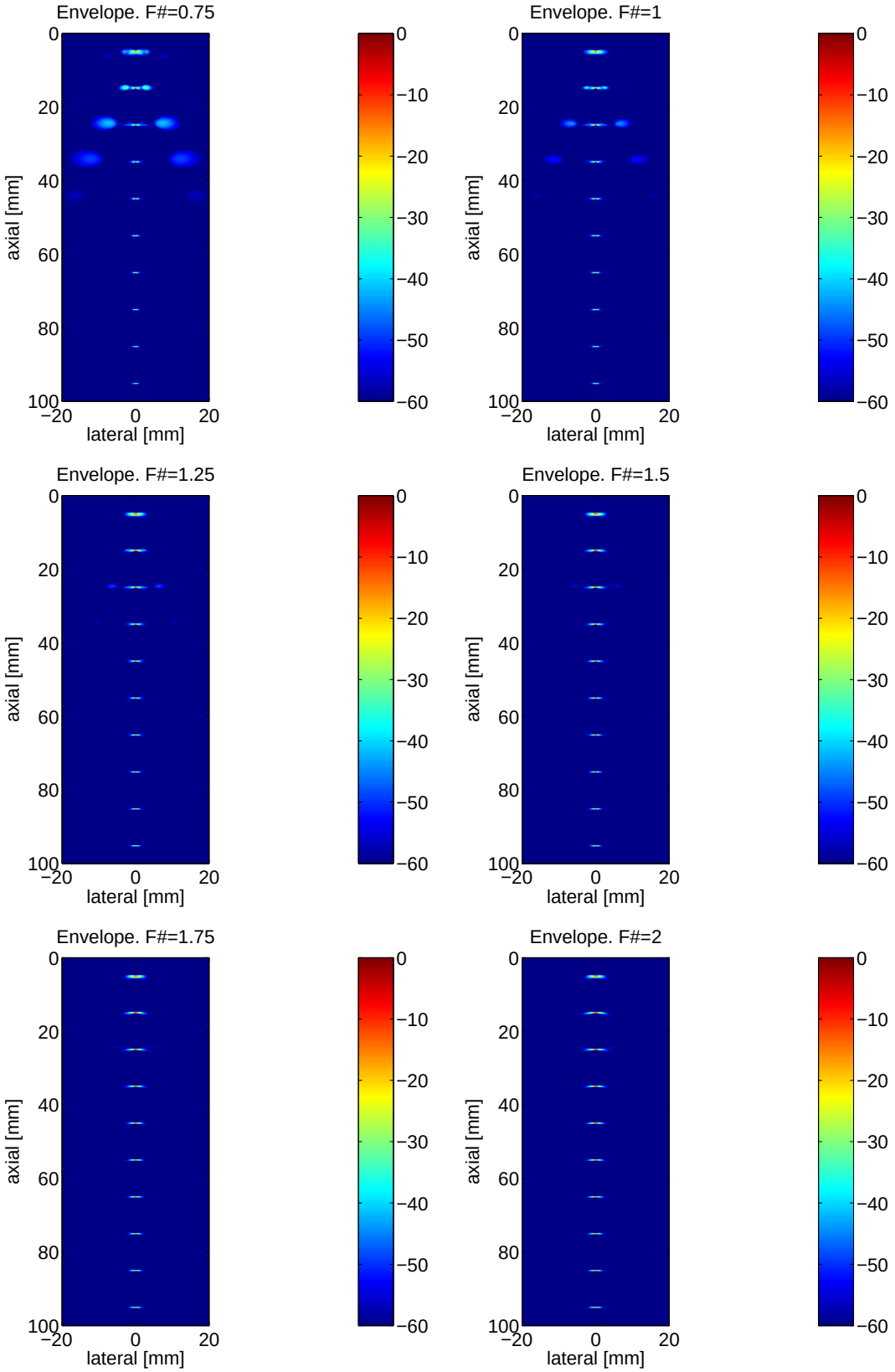

Figure A.7: Envelope detected and log-compressed images for different values of $F\#$ and with a dynamic range of 60 dB. VS at 10 mm, Simulation Model *I*.

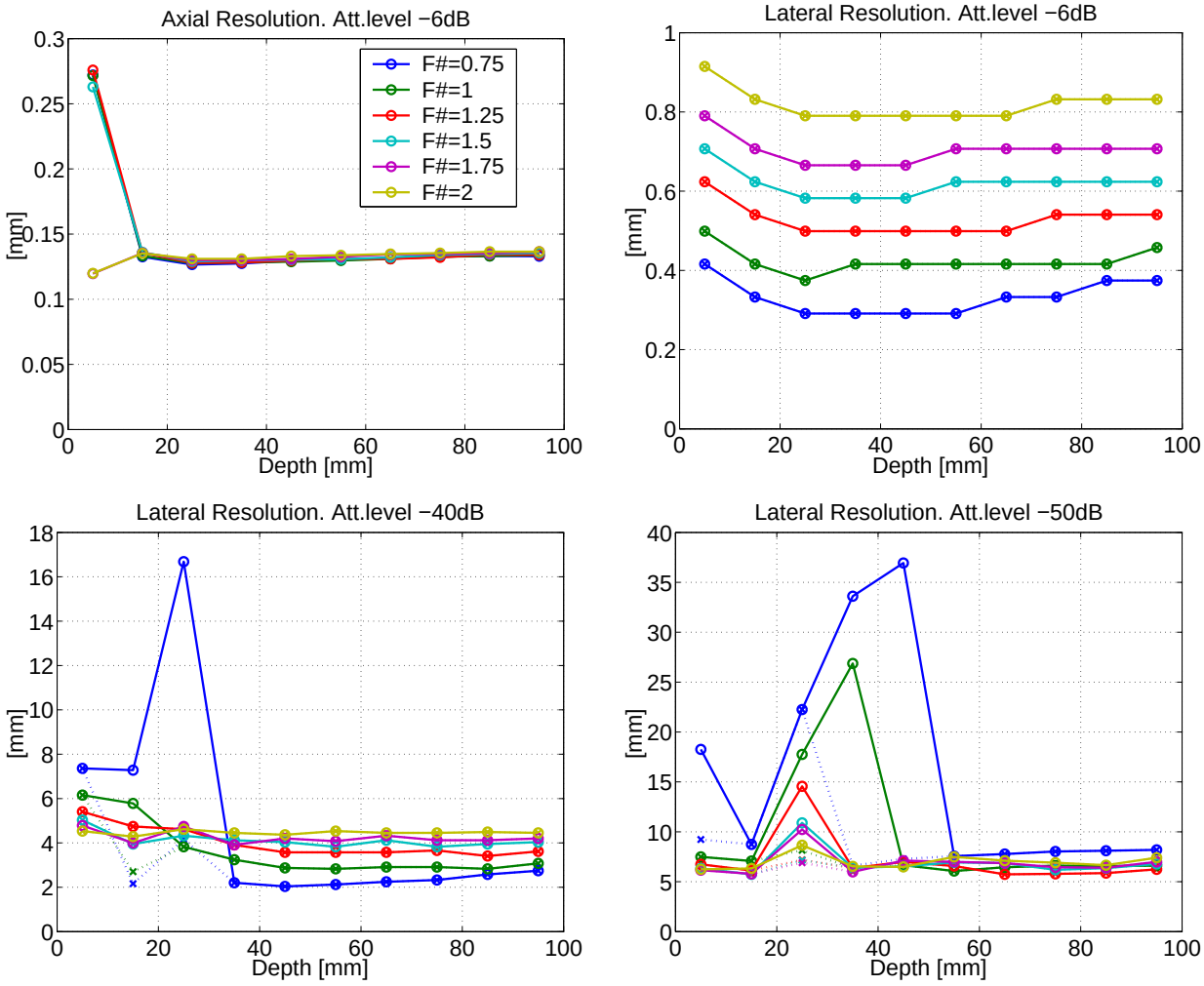

Figure A.8: Axial and lateral resolution as function of depth at levels of -6 dB, -40 dB, and -50 dB. If the lateral PSF has a distinct main-lobe and side-lobe distribution, the main-lobe resolution is shown as a dotted line. VS at 10 mm, Simulation Model *I*.

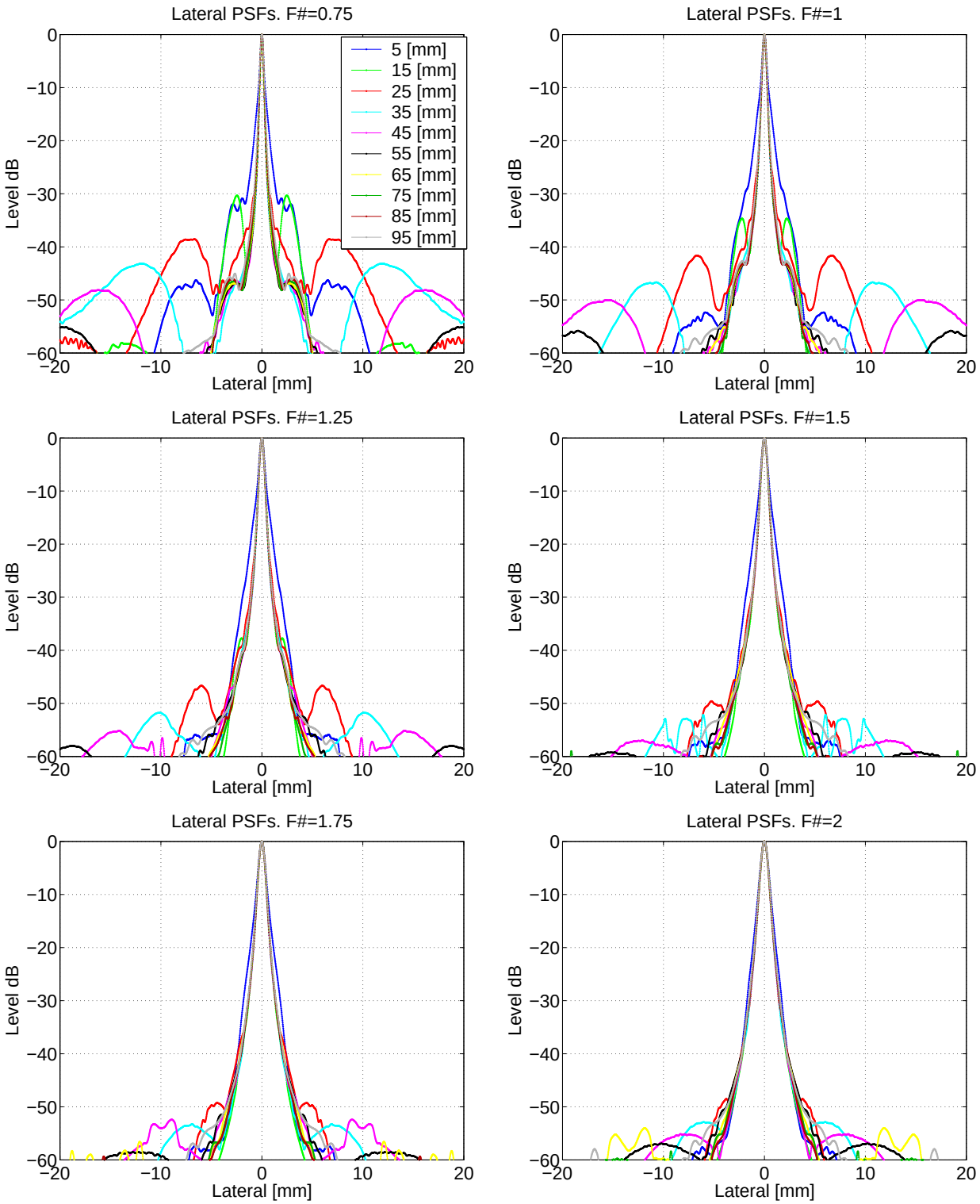

Figure A.9: Lateral PSF's at different depths are stacked up for different values of $F\#$. VS at 10 mm, Simulation Model *I*.

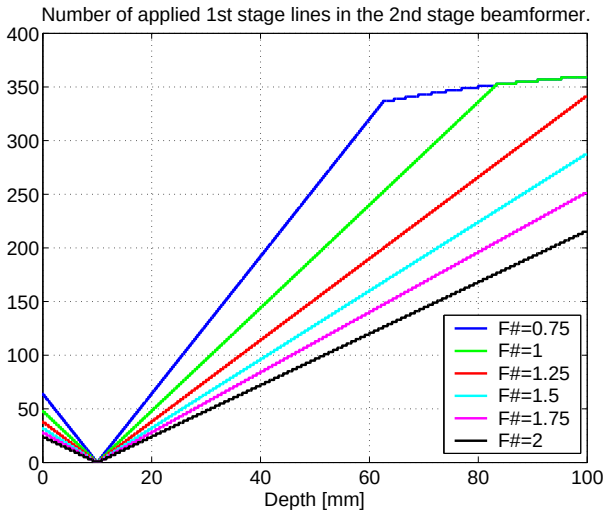

Figure A.10: The number of applied 1st stage lines in the 2nd stage beamformer for the center HRL. VS at 10 mm, Simulation Model *I*.

A.3 VS at 15 mm, Simulation Model *I*

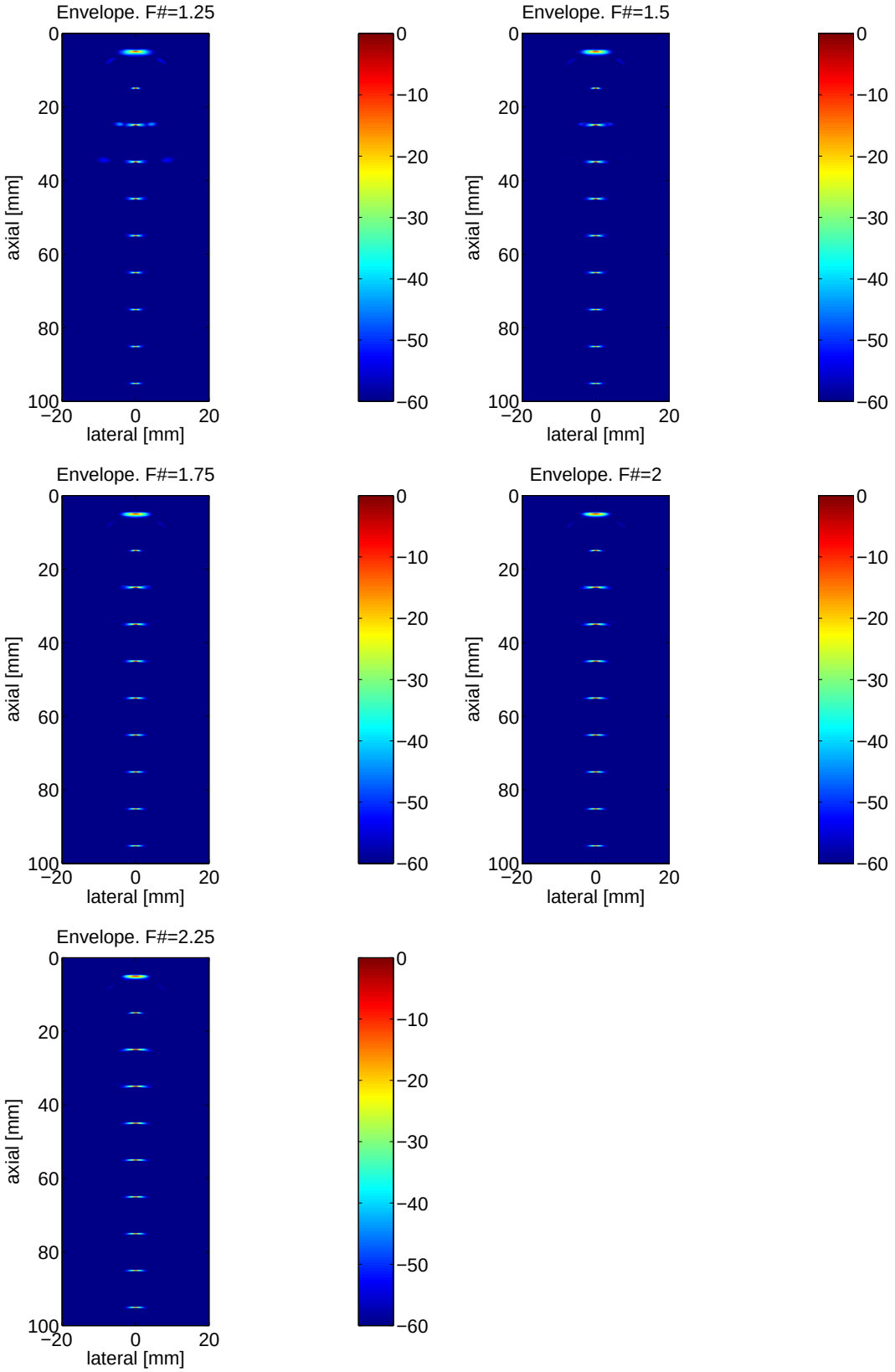

Figure A.11: Envelope detected and log-compressed images for different values of $F\#$ and with a dynamic range of 60 dB. VS at 15 mm, Simulation Model *I*.

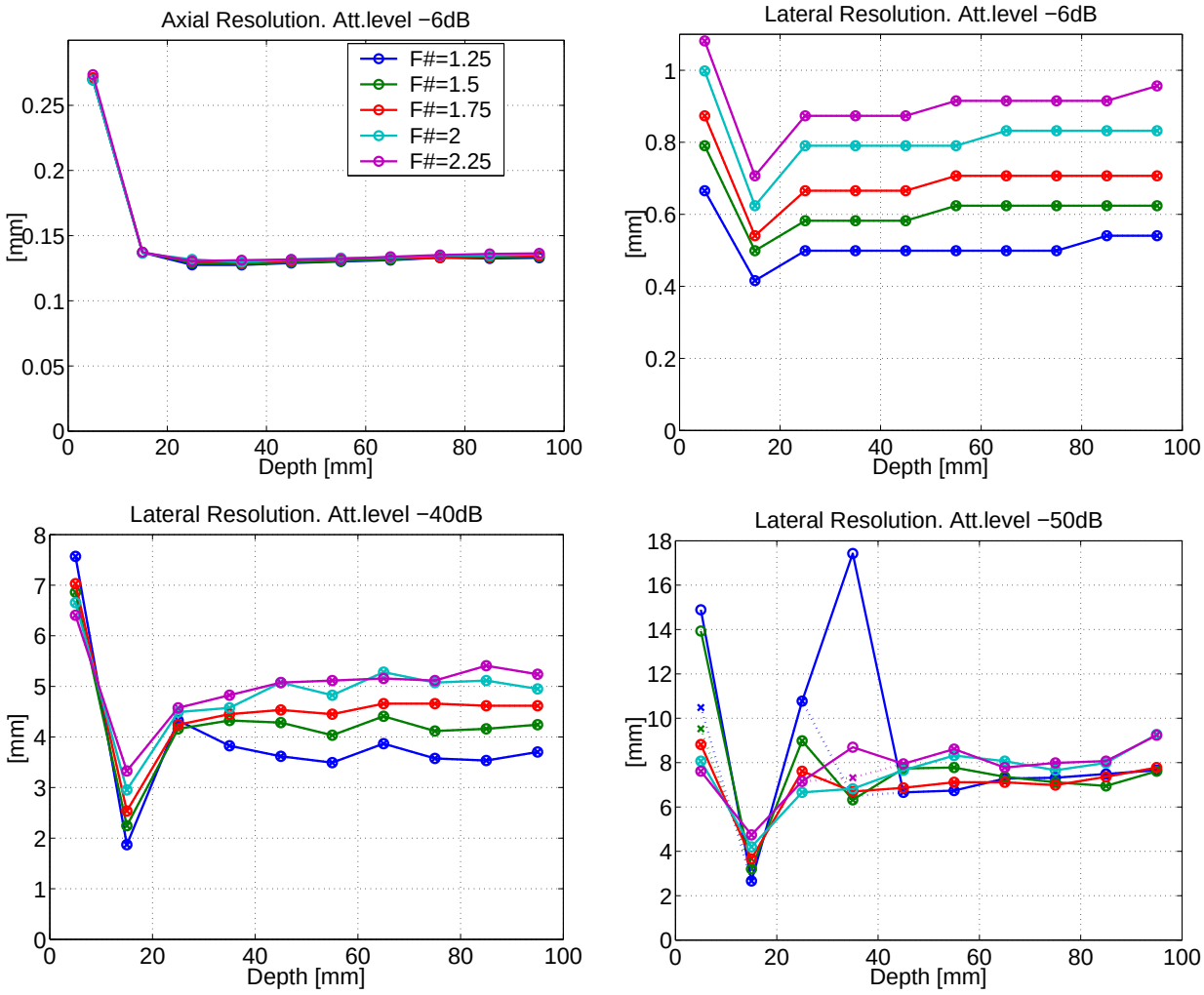

Figure A.12: Axial and lateral resolution as function of depth at levels of -6 dB, -40 dB, and -50 dB. If the lateral PSF has a distinct main-lobe and side-lobe distribution, the main-lobe resolution is shown as a dotted line. VS at 15 mm, Simulation Model *I*.

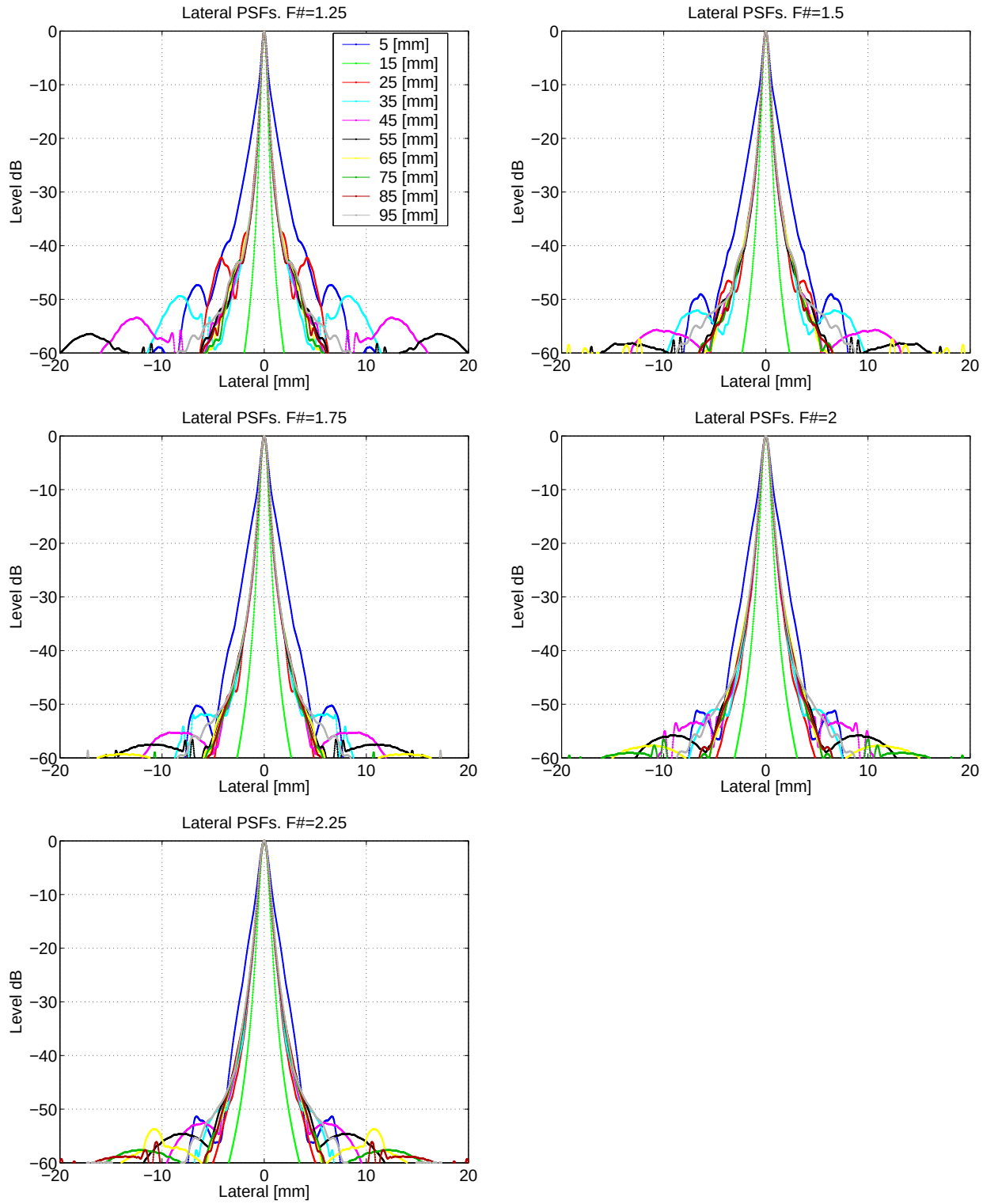

Figure A.13: Lateral PSF's at different depths are stacked up for different values of *F#*. VS at 15 mm, Simulation Model *I*.

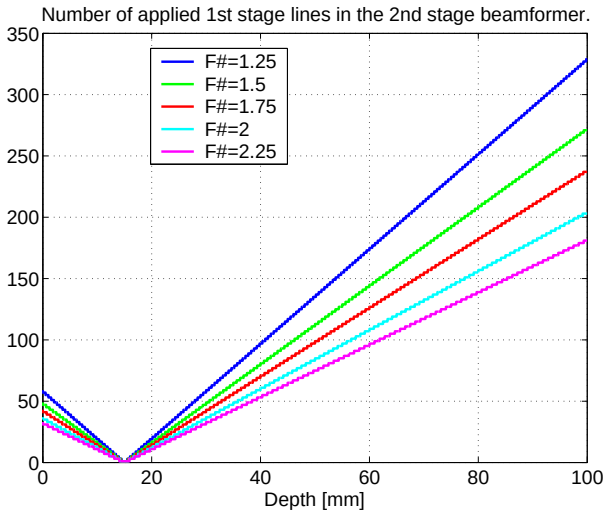

Figure A.14: The number of applied 1st stage lines in the 2nd stage beamformer for the center HRL. VS at 15 mm, Simulation Model *I*.

A.4 VS at 20 mm, Simulation Model *I*

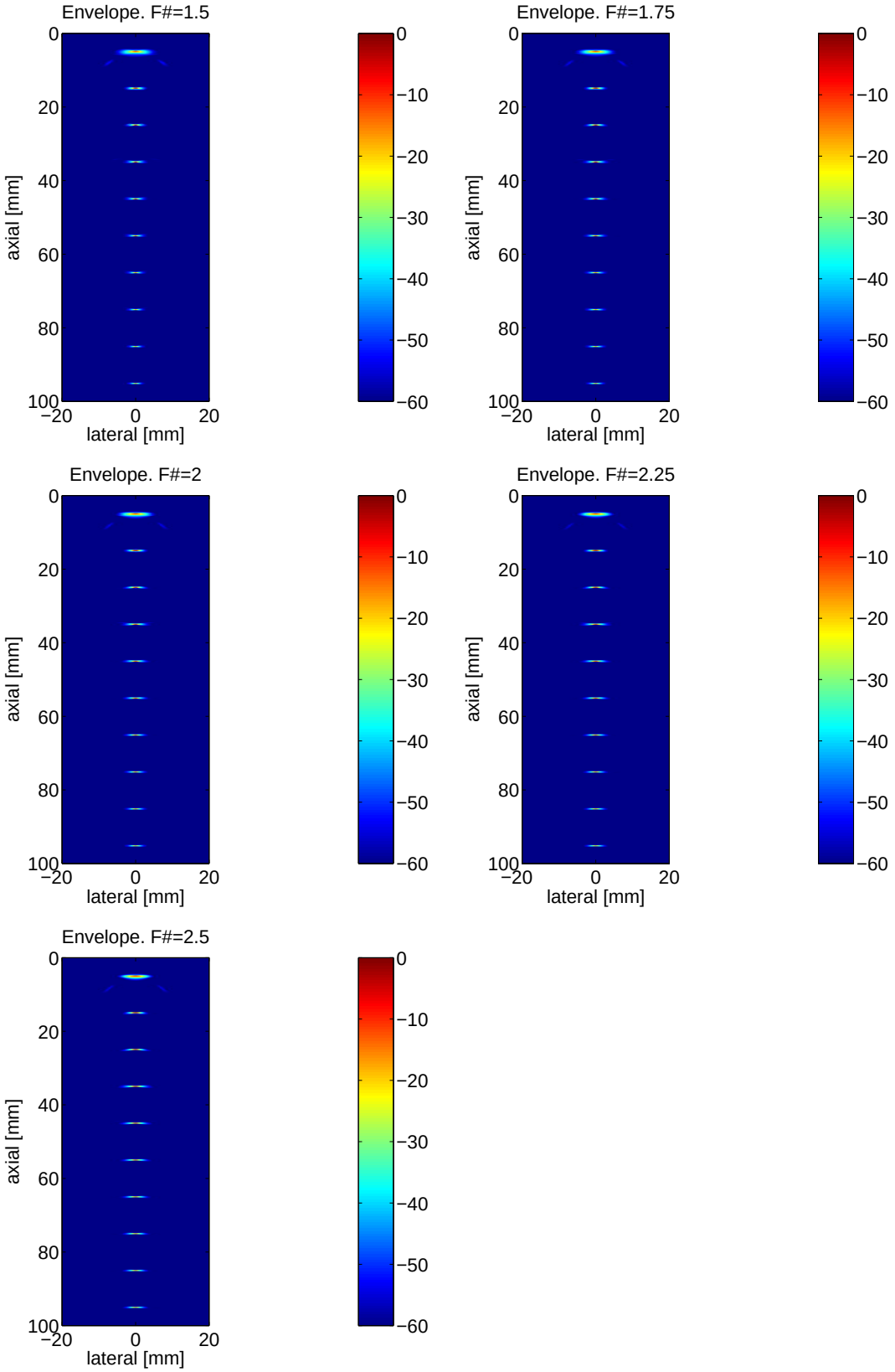

Figure A.15: Envelope detected and log-compressed images for different values of $F\#$ and with a dynamic range of 60 dB. VS at 20 mm, Simulation Model *I*.

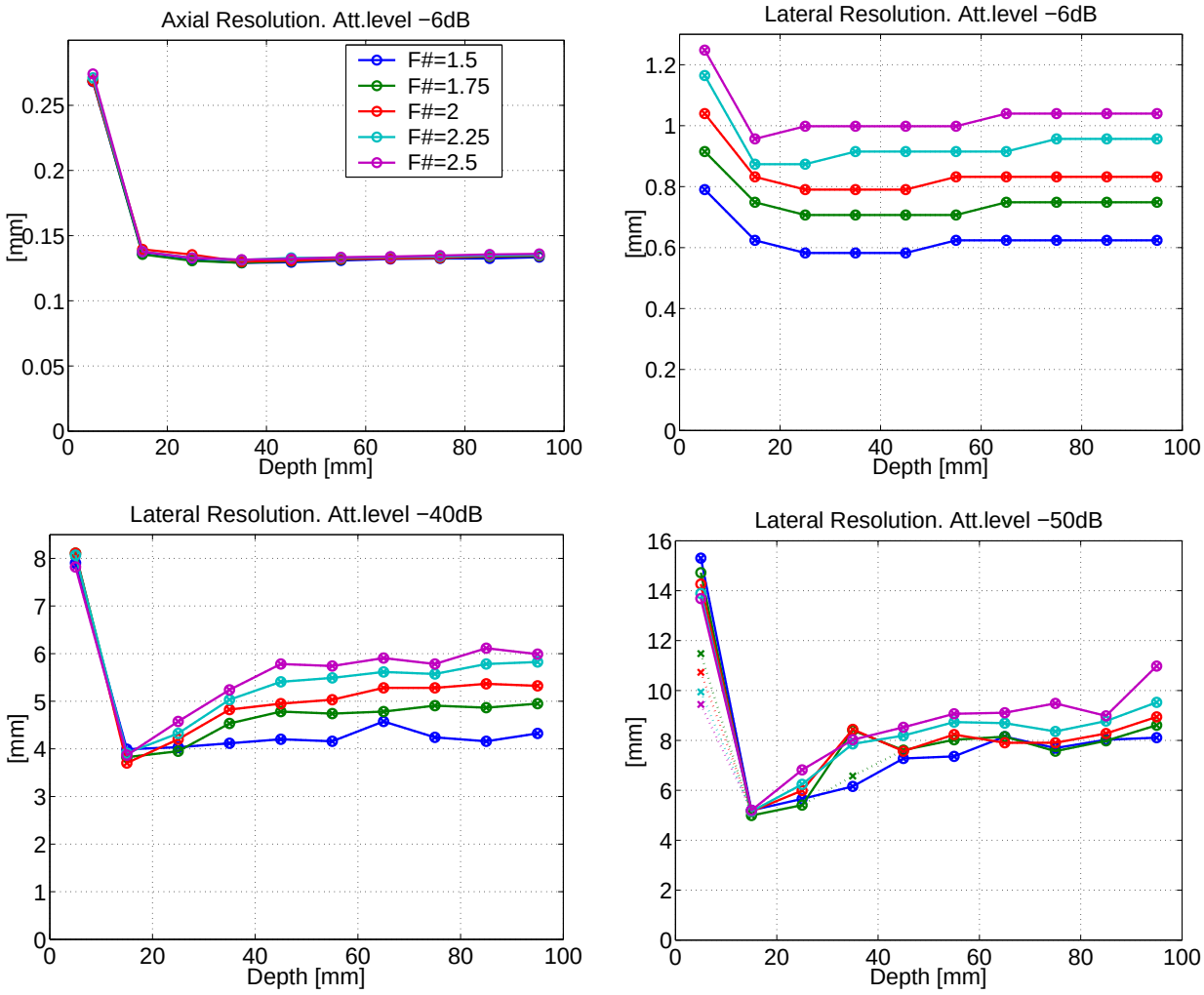

Figure A.16: Axial and lateral resolution as function of depth at levels of -6 dB, -40 dB, and -50 dB. If the lateral PSF has a distinct main-lobe and side-lobe distribution, the main-lobe resolution is shown as a dotted line. VS at 20 mm, Simulation Model *I*.

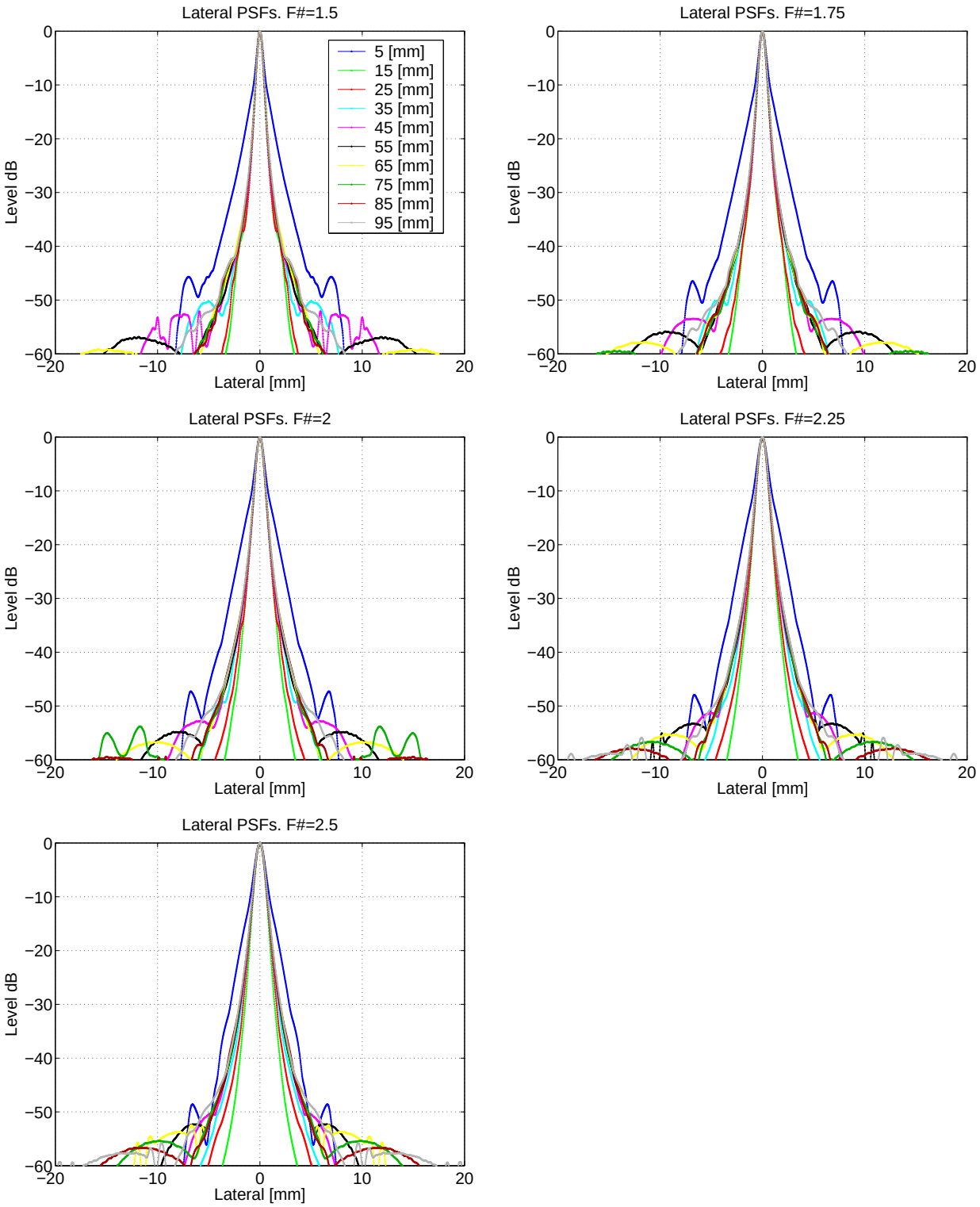

Figure A.17: Lateral PSF's at different depths are stacked up for different values of *F#*. VS at 20 mm, Simulation Model *I*.

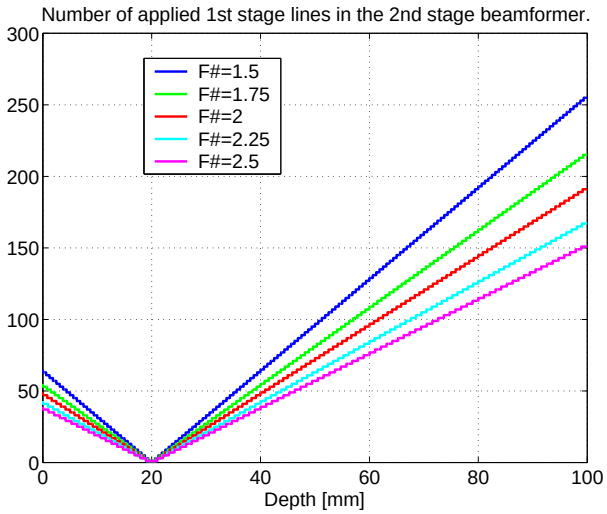

Figure A.18: The number of applied 1st stage lines in the 2nd stage beamformer for the center HRL. VS at 20 mm, Simulation Model *I*.

A.5 VS at 10 mm, Simulation Model *II*

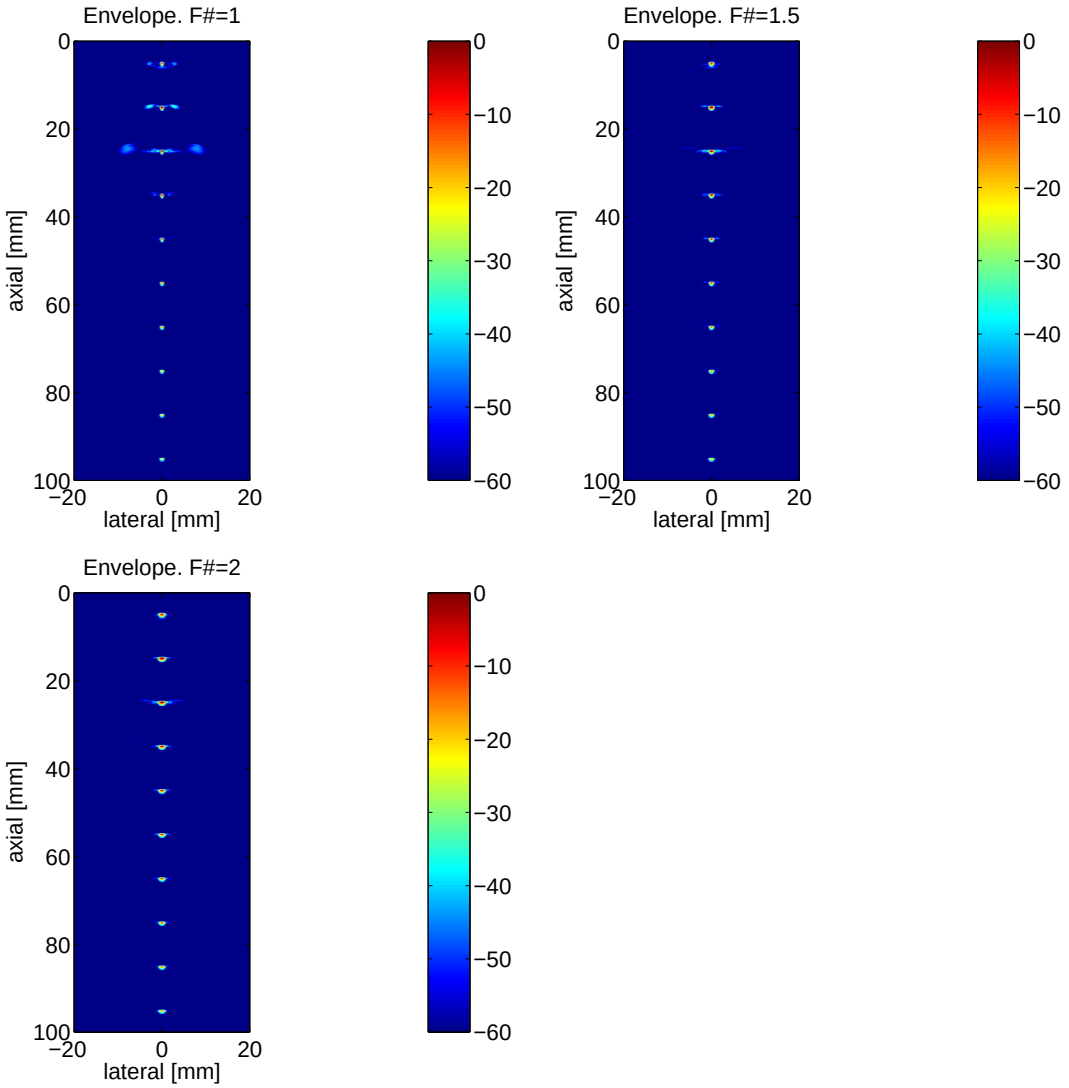

Figure A.19: Envelope detected and log-compressed images for different values of *F#* and with a dynamic range of 60 dB. VS at 10 mm, Simulation Model *II*.

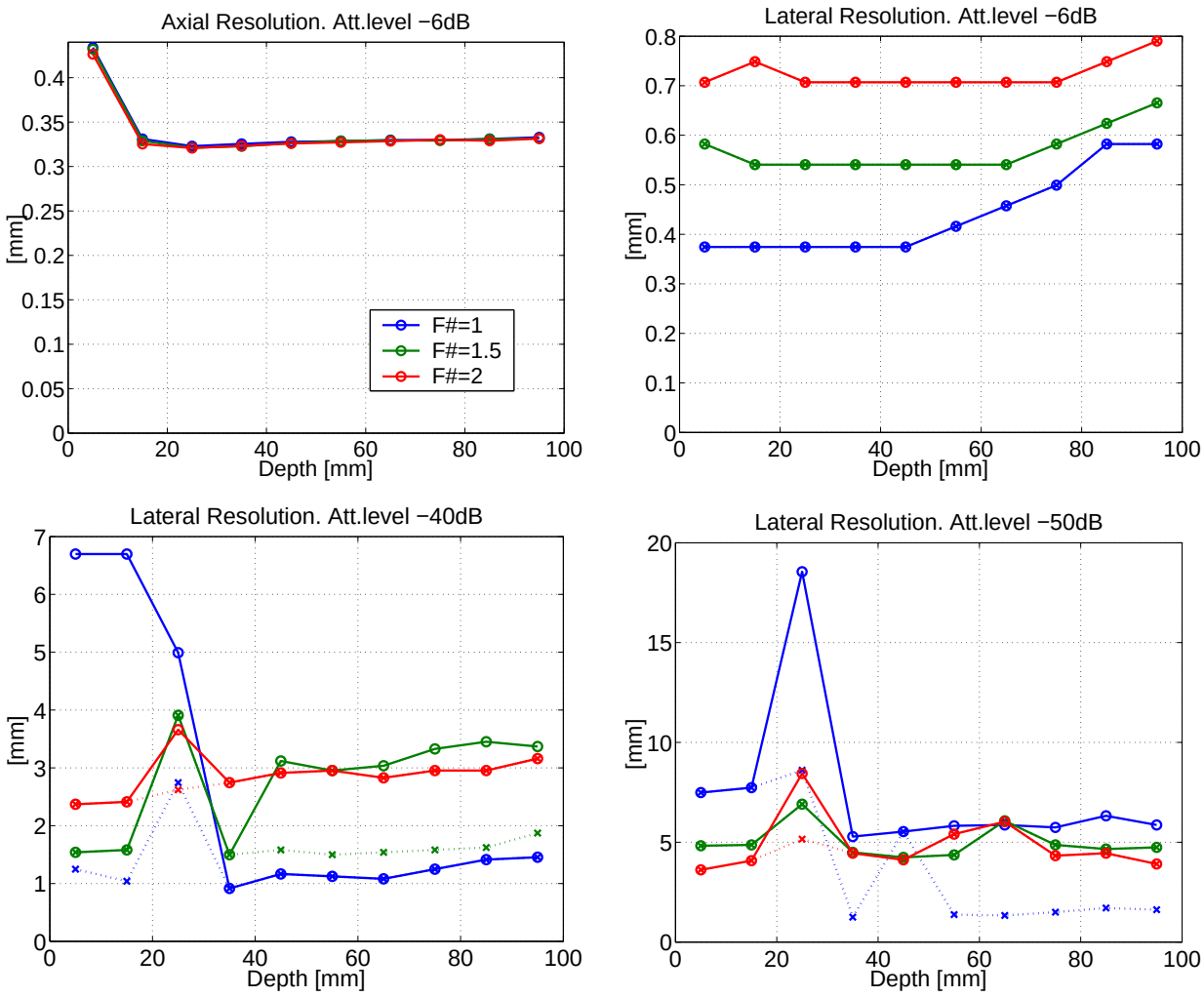

Figure A.20: Axial and lateral resolution as function of depth at levels of -6 dB, -40 dB, and -50 dB. If the lateral PSF has a distinct main-lobe and side-lobe distribution, the main-lobe resolution is shown as a dotted line. VS at 10 mm, Simulation Model *II*.

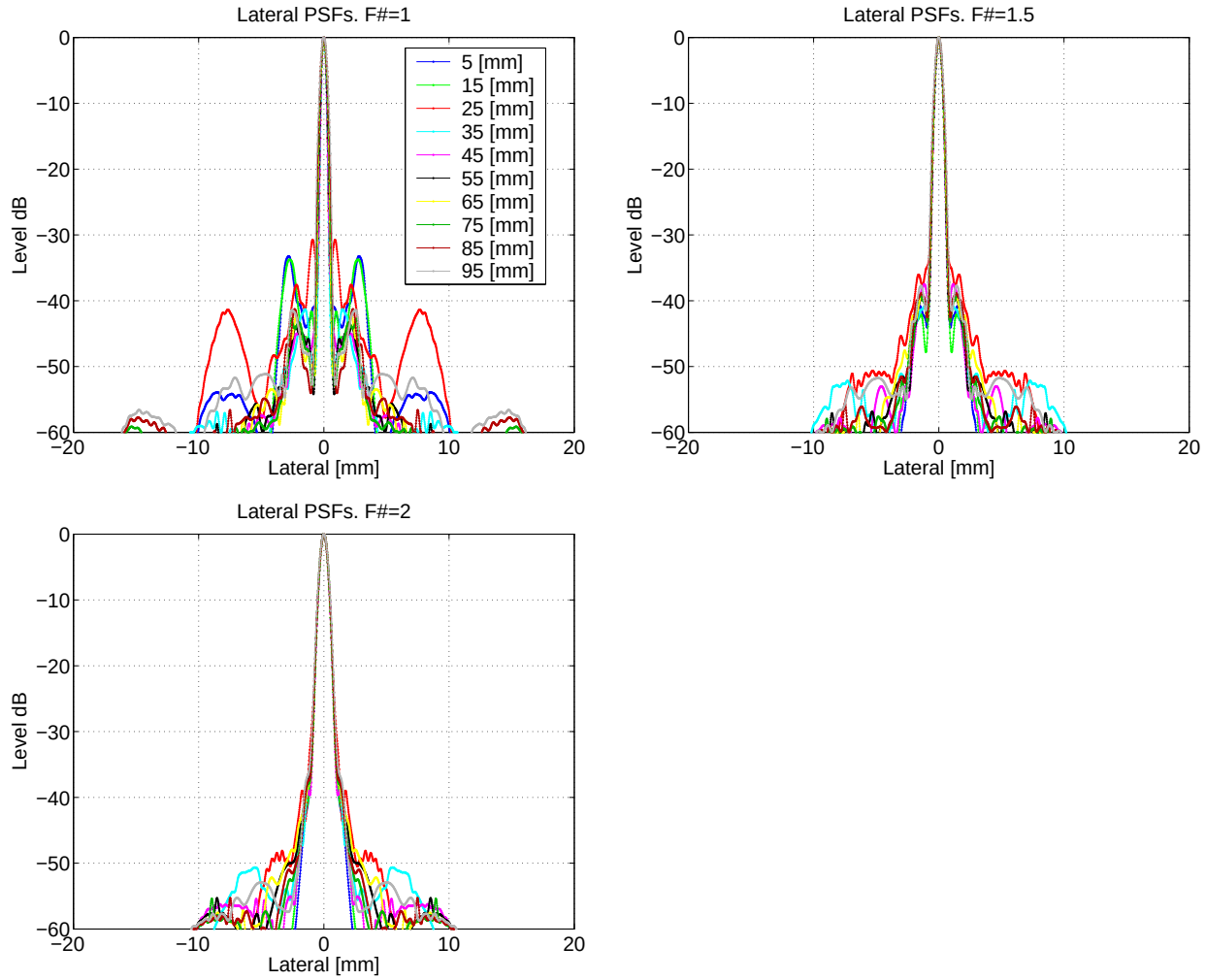

Figure A.21: Lateral PSF's at different depths are stacked up for different values of *F#*. VS at 10 mm, Simulation Model *II*.

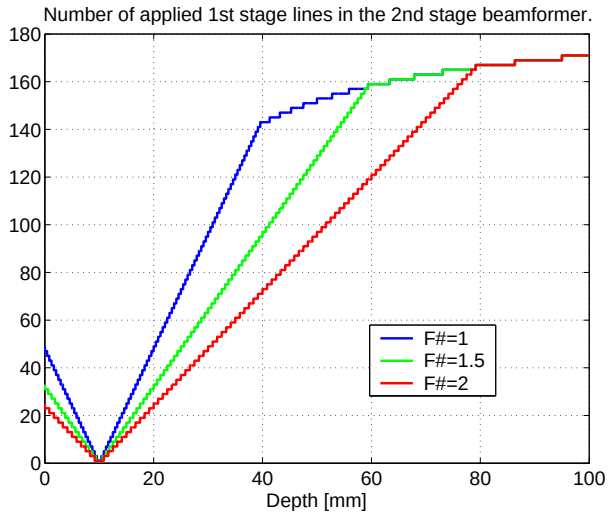

Figure A.22: The number of applied 1st stage lines in the 2nd stage beamformer for the center HRL. VS at 10 mm, Simulation Model *II*.

A.6 VS at 15 mm, Simulation Model *II*

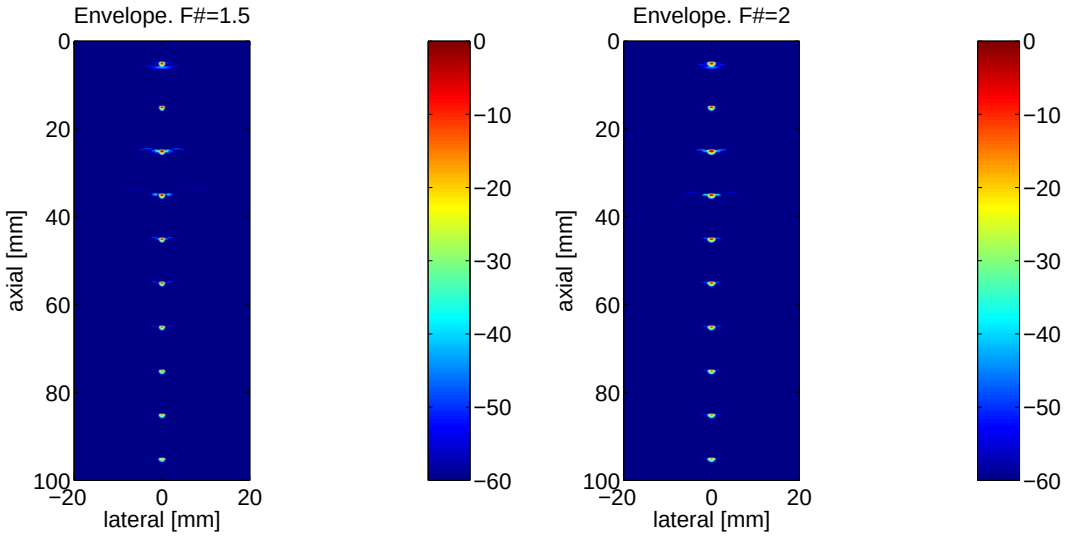

Figure A.23: Envelope detected and log-compressed images for different values of $F\#$ and with a dynamic range of 60 dB. VS at 15 mm, Simulation Model *II*.

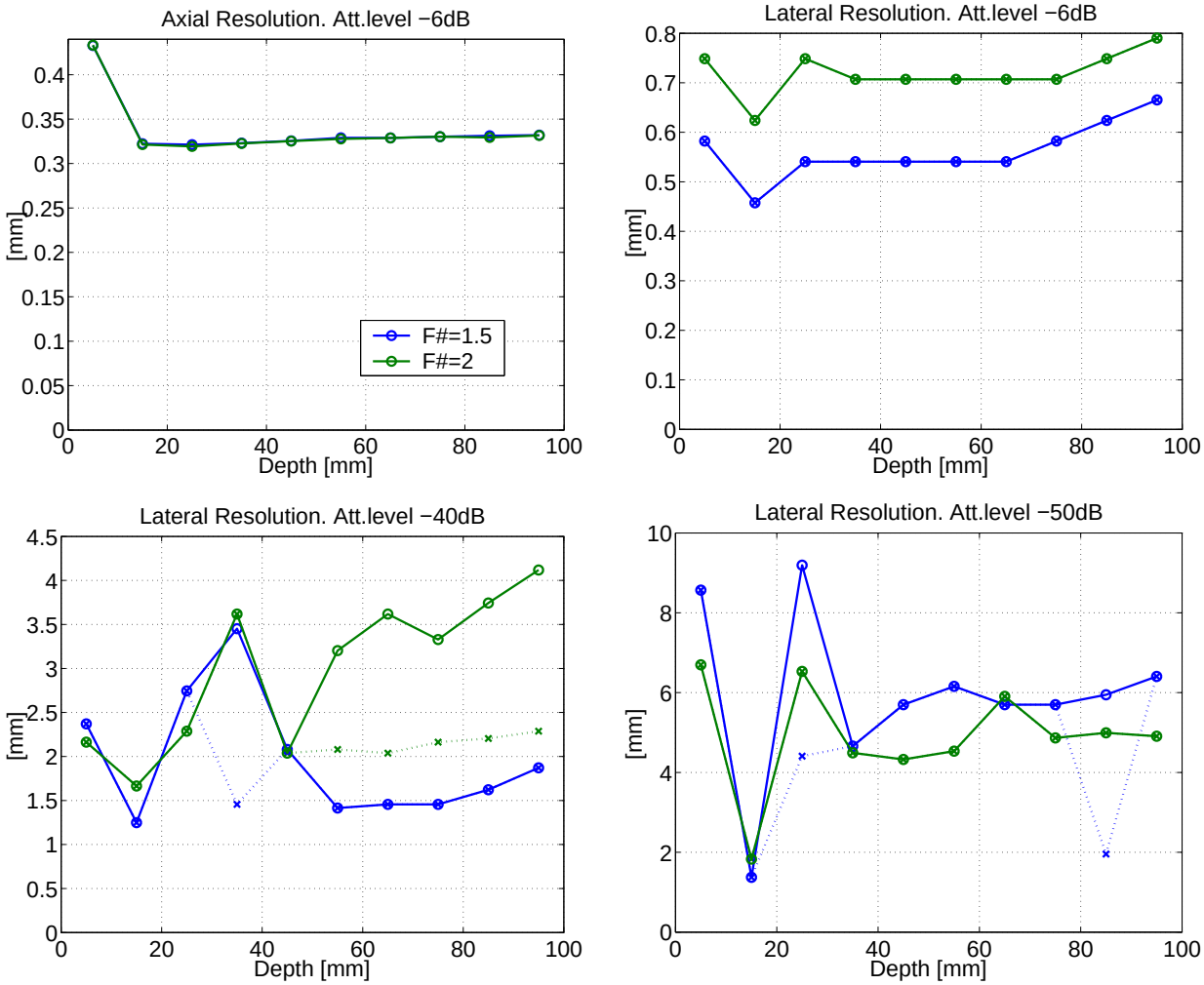

Figure A.24: Axial and lateral resolution as function of depth at levels of -6 dB, -40 dB, and -50 dB. If the lateral PSF has a distinct main-lobe and side-lobe distribution, the main-lobe resolution is shown as a dotted line. VS at 15 mm, Simulation Model *II*.

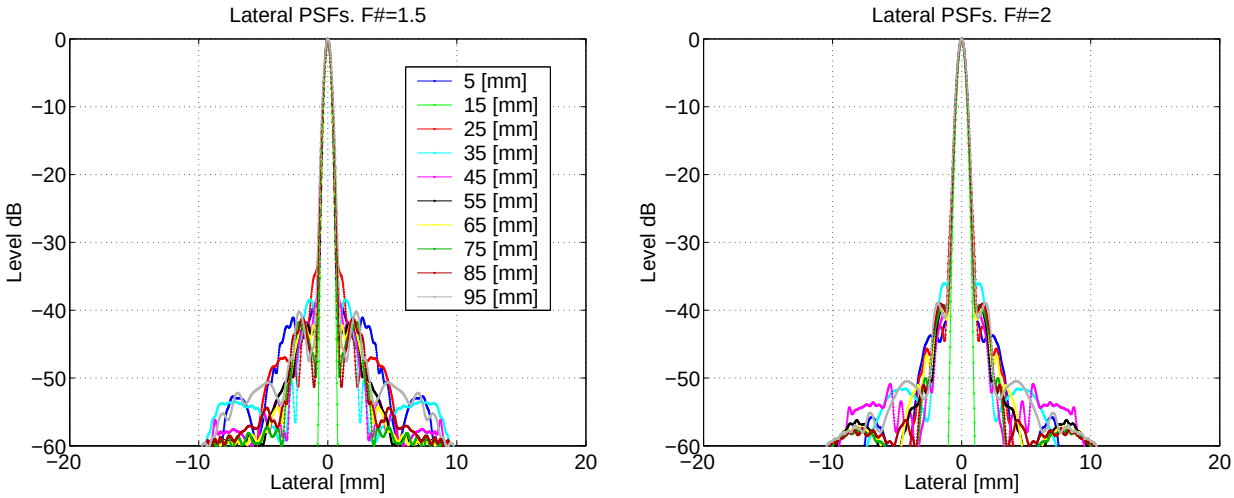

Figure A.25: Lateral PSF's at different depths are stacked up for different values of *F#*. VS at 15 mm, Simulation Model *II*.

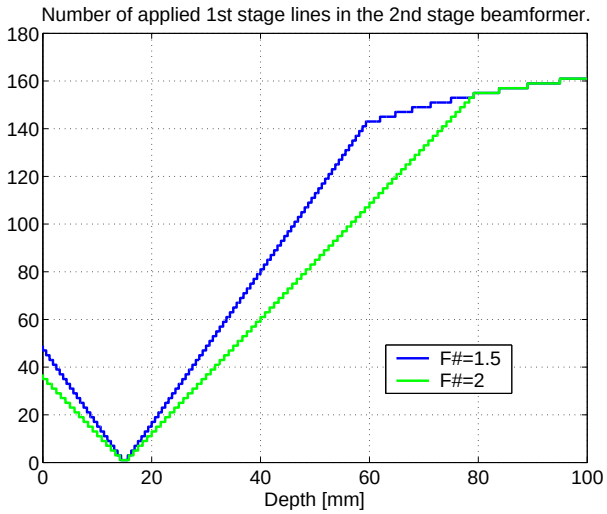

Figure A.26: The number of applied 1st stage lines in the 2nd stage beamformer for the center HRL. VS at 15 mm, Simulation Model *II*.

A.7 VS at 20 mm, Simulation Model *II*

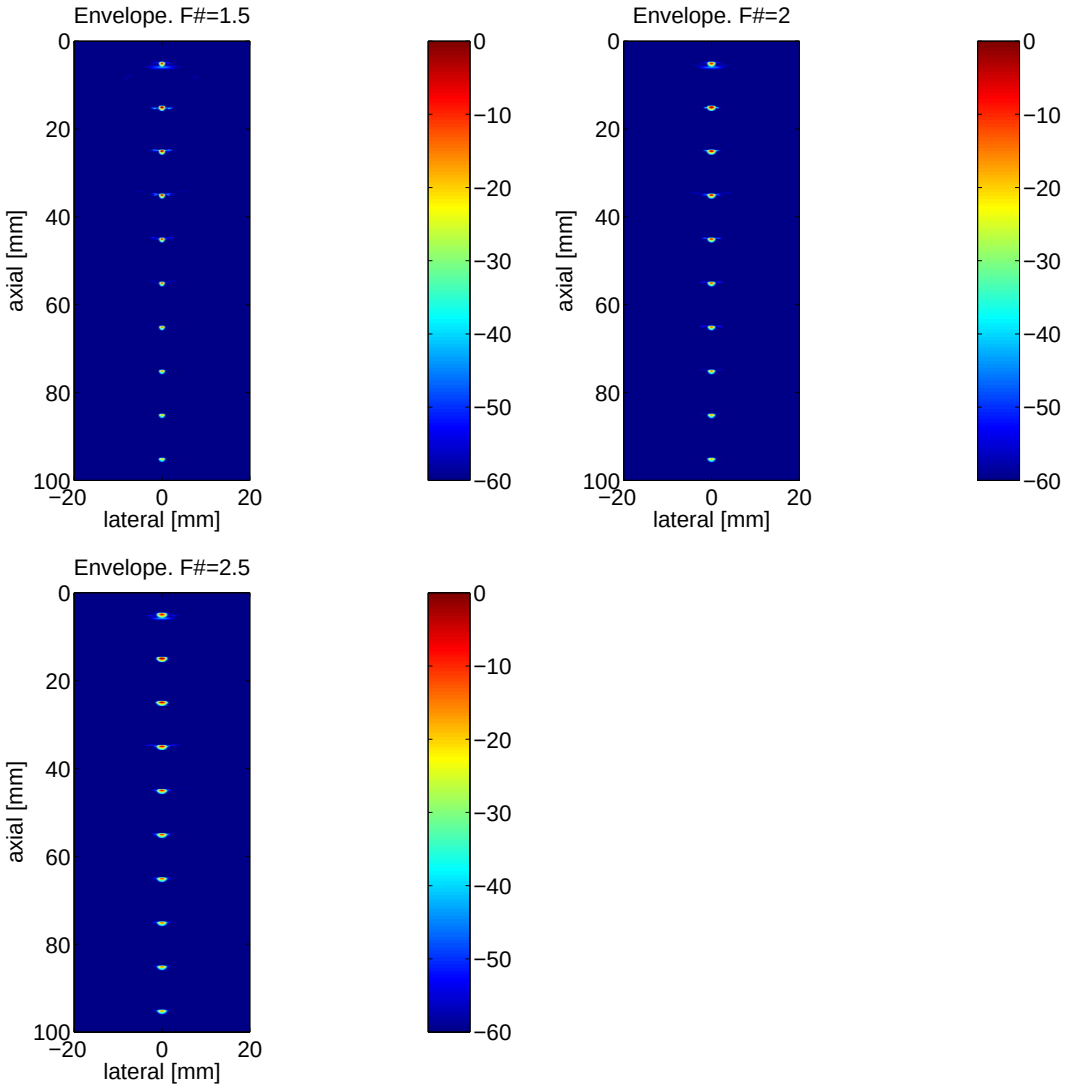

Figure A.27: Envelope detected and log-compressed images for different values of *F#* and with a dynamic range of 60 dB. VS at 20 mm, Simulation Model *II*.

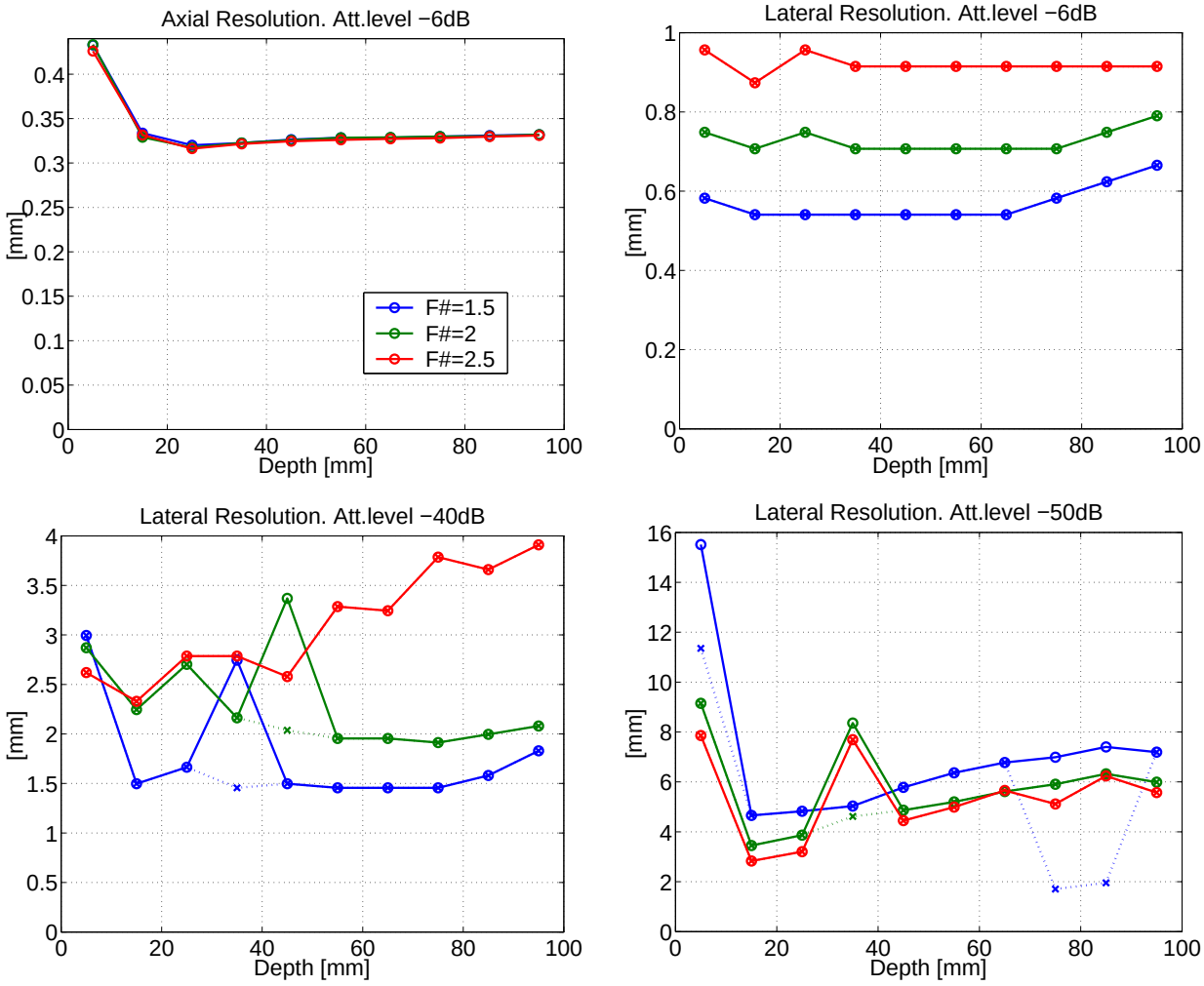

Figure A.28: Axial and lateral resolution as function of depth at levels of -6 dB, -40 dB, and -50 dB. If the lateral PSF has a distinct main-lobe and side-lobe distribution, the main-lobe resolution is shown as a dotted line. VS at 20 mm, Simulation Model *II*.

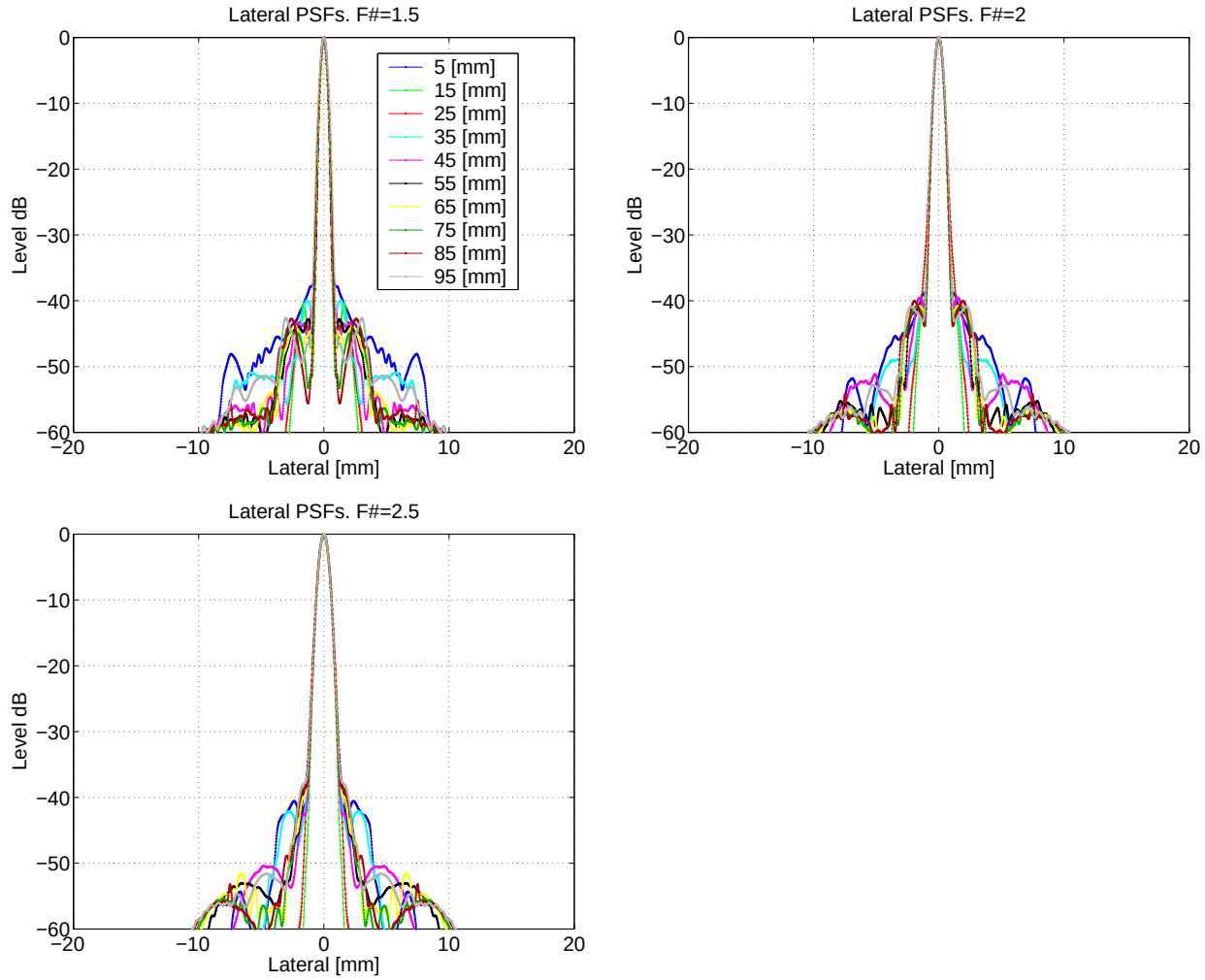

Figure A.29: Lateral PSF's at different depths are stacked up for different values of *F#*. VS at 20 mm, Simulation Model *II*.

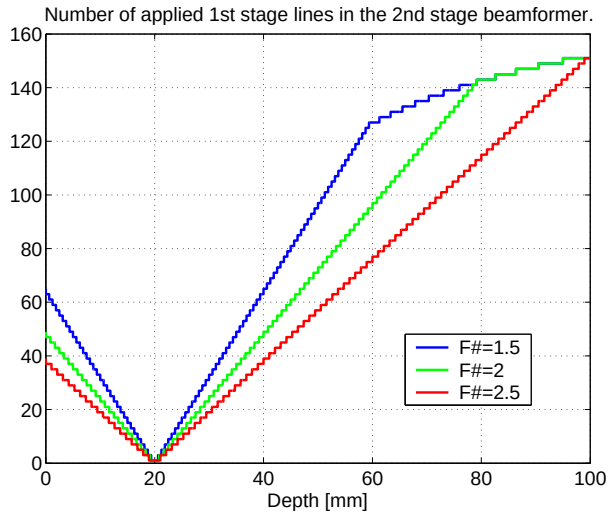

Figure A.30: The number of applied 1st stage lines in the 2nd stage beamformer for the center HRL. VS at 20 mm, Simulation Model *II*.

APPENDIX

B

Articles

B.1 Effective and Versatile Software Beamformation Toolbox

This article was published in *Progress in Biomedical Optics and Imaging - Proceedings of SPIE, 2007, pages 2023-2026, Oct. 2006.*. Conference Title *Medical Imaging 2007: Ultrasonic Imaging and Signal Processing. Issue Vol.6513 Page no. 651319*.

The poster presented at the conference received the *CUM LAUDE* Poster Award.

Effective and versatile software beamformation toolbox

Jacob Kortbek [a,b], Svetoslav Nikolov [b] and Jørgen Arendt Jensen [b]

[a]B-K Medical, Mileparken 34, 2730 Herlev, Denmark
[b]Center for Fast Ultrasound Imaging, Ørsted·DTU, Technical University of Denmark

ABSTRACT

Delay-and-sum array beamforming is an essential part of signal processing in ultrasound imaging. Although the principles are simple, there are many implementation details to consider for obtaining a reliable and computational efficient beamforming. Different methods for calculation of time-delays are used for different waveforms. Various inter-sample interpolation schemes such as FIR-filtering, polynomial, and spline interpolation can be chosen. Apodization can be any preferred window function of fixed size applied on the channel signals or it can be dynamic with an expanding and contracting aperture to obtain a preferred constant F-number. An effective and versatile software toolbox for off-line beamformation designed to address all of these issues has been developed. It is capable of exploiting parallelization of computations on a Linux cluster and is written in C++ with a `MATLAB` (MathWorks Inc.) interface. It is an aid to support simulations and experimental investigation of 3D imaging, synthetic aperture imaging, and directional flow estimation. A number of parameters are necessary to fully define the spatial beamforming and some parameters are optional. All spatial specifications are given in 3D space such as the physical positions of the transducer elements during transmit and receive and the positions of the points to beamform. The points of focus are defined as a collection of lines each having an origin, a direction, a distance between points and a length. The transducer, the points to beamform, and the apodization are defined as individual objects and a combination of these define the actual beamforming. Once the beamforming is defined, the time-delays and apodization values for every combination of transmit elements, receive elements and focus points can be calculated and stored in lookup-tables (LUT). Parametric beamforming can also be applied where calculations are done by demand, thus, reducing the storage demand dramatically. On a standard PC with a Pentium 4, 2.66 GHz processor running Linux the toolbox can beamform $100,000$ points in lines of various directions in 20 seconds using a transducer of 128 elements, dynamic apodization and 3rd order polynomial interpolation. This is a decrease in computation time of at least a factor of 15 compared to an implementation directly in `MATLAB` of a similar beamformer.

Keywords: medical ultrasound, beamforming, toolbox, image processing, 3D, parallel computation

1. INTRODUCTION

The image quality and diagnostic capabilities in general of medical ultrasound imaging rely to a great extent on the beamformer, which is the primary signal processing task of an ultrasound system. The delay-and-sum beamformer (DASB) is the dominant type of beamformer and comprises computation and application of channel delays and apodization in both transmit mode and receive mode. Even though the principle of the DASB is quite simple the implementation can be complex. The evolution of ultrasound beamformers from analog into digital implementations have been described by Thomenius[1] and numerous variations exist and new and improved methods of beamforming are continuing to appear. The beamformer design is a consequence of the combination of desired application, image quality demands, array type, and the processing resources available for real-time implementation. Concurrently with the development within real-time processing technology, new types of beamformers, which can utilize this increase in resources, become an obvious subject of investigations.

Several commercial and non-commercial toolboxes have been developed for different purposes within array signal processing.[2–4] This paper is about a software toolbox dedicated for off-line beamformation of ultrasound array signals, written in C++ and with a `MATLAB` (*The MathWorks, Inc.*) program interface. The name of the toolbox is *BFT2* and the initial version was developed by Sara Gustavsson[5] in 2002 and has been under continuous development ever since. It is motivated by the potential in improving the image quality of ultrasound imaging by investigating novel beamforming methods, and by offering colleagues an opportunity not to implement a beamformer from scratch and, thus accelerating the

Further author information: Jacob Kortbek, jk@oersted.dtu.dk

research. The maturity level of the toolbox at present time is such that it is applicable to most state of the art beamforming applications and it is reliable due to the feedback from the intensive use in several projects at *Center for Fast Ultrasound Imaging*(CFU).

The purpose of the beamformation toolbox (BFT) is to serve as an applicable entry into receive beamforming (or focusing) of real RF signals or complex base band signals acquired from any given application and acquisition sequence. It performs dynamic receive focusing in any arbitrary direction in 3D space and offers a range of choices between static or dynamic apodization and various interpolation schemes. Such a toolbox improves the reliability and can ensure a consistency in the way beamforming is implemented and the numerous details involved in this process. The RF data can be of different types and can originate from either a simulation program such as Field II,[6] from experimental equipment or from *in-vivo* experiments. Among the many applications of the toolbox are 3D imaging using 2D arrays or elevation focused 1D arrays. Also directional velocity vector estimation[7–9] in vascular imaging is an obvious candidate. Synthetic aperture (SA) imaging[10–12] and the many variations such as synthetic transmit aperture (STA),[13] synthetic receive aperture (SRA)[14–16] and hybrid combinations hereof are perhaps the most demanding beamforming tasks in medical ultrasound and can easily be explored.

The paper gives an insight into the software architecture of the toolbox and beamformer design principles and shares some of the many considerations in relation to beamformer development and implementation. The paper is organized as follows. Initially beamformer basics is described and the strategy for calculating the time-of-flight and the apodization for different applications is discussed. The software design of the implementation is characterized next and Section 2.1 elaborates on how the processing is organized and carried out and how the user can interact with the toolbox and control its parameters. Finally some examples of use and a measure of performance are presented.

2. BEAMFORMING STRATEGY

The general purpose of beamforming in terms of beam properties is to construct a narrow beam with a large range of depth. Beamforming in its simplest form is all about controlling the phase of a group of signals exploiting that the sum of these signals can be either constructive or destructive. In medical ultrasound beamforming is carried out during both transmit and receive and the type of beamforming varies first of all with the geometry of the applied transducer and the focal points. The main transducer categories are the linear array, focused array, and phased array beside the 2D arrays, but can in principle be any kind of arbitrary array.

In transmit beamforming appropriate delays and possibly apodization are applied to the individual transducer elements to obtain a single focal point at which the emitted waves sum up constructively. Receive beamforming is similar since appropriate delays are applied to the signals received from the individual transducer elements and then a weighted sum is performed. The main difference is that in transmit only a single focal point can be created at each emission, since the delays are applied before the emission and the waves are summed physically in the focal point. In receive multiple focal points can be obtained, by applying a new set of delay values to the received signals for each focal point.

The BFT does off-line processing of the received signals and, thus, performs receive focusing. One of the challenges in receive focusing is the strategy for calculating the time-of-flight (TOF). TOF is the propagation time of the emitted wave in its path from the transmit origin, $\vec{r}_e$ to the point of receive focus (FP), $\vec{r}_{fp}$ and return to one of the elements of the receive aperture, $\vec{r}_r$ as illustrated in Fig. 1.

$$t_{tof} = \frac{|\vec{r}_{fp} - \vec{r}_e| + |\vec{r}_r - \vec{r}_{fp}|}{c} \,. \tag{1}$$

Calculating proper receive delays and thus the TOF requires that the characteristics of the transmit beamforming are known. The TOF can be split into the transmit time t_{tof_t} and the receive time t_{tof_r}. $t_{tof} = t_{tof_t} + t_{tof_r}$. Assuming the speed of sound, c is known the receive time is uniquely determined from the receive path which is simply the path from the FP to receive aperture elements. The transmit path though is not well defined because the emitted pressure wave does not necessarily emanate from a point source as illustrated in Fig. 1 but is a consequence of numerous waves emitted from different elements at different times. The transmit time must thus be approximated accordingly.

Fig. 2 and Fig. 3 are illustrations of different situations where the strategy for calculating the TOF are not the same. In Fig. 2 a focused transmission with a transmit focal point (TFP) located at $\vec{r}_{tfp}$ is applied and the FP is located off-axis. The transmit origin, $\vec{r}_e$ is defined as the center element of the transmit sub-aperture. In compliance with the concept of virtual

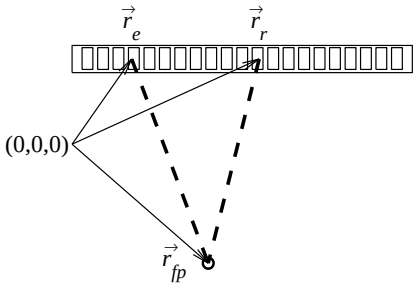

Figure 1. Wave propagation path (dotted line) for calculating the time-of-flight in receive focusing. The transmit origin, $\vec{r}_e$ and the receive point, $\vec{r}_r$ are illustrated as different elements of an array.

sources,[17–21] the transmit focal point can be considered as a point source emitting a spherical wave. By using this concept the transmit part t_{tof_t} of the TOF can be calculated unambiguously and the TOF becomes

$$t_{tof} = \frac{|\vec{r}_{tfp} - \vec{r}_e| \pm |\vec{r}_{fp} - \vec{r}_{tfp}| + |\vec{r}_r - \vec{r}_{fp}|}{c} \tag{2}$$

The $\pm$ in (2) refer to whether the FP is above or below the TFP. In Fig. 3 an unfocused plane wave is emitted and the transmit time t_{tof_t} in this case is simply proportional to the axial distance, $|z_{fp} - z_e|$ between the aperture and the FP and the TOF is then

$$t_{tof} = \frac{|z_{fp} - z_e| + |\vec{r}_r - \vec{r}_{fp}|}{c} \ . \tag{3}$$

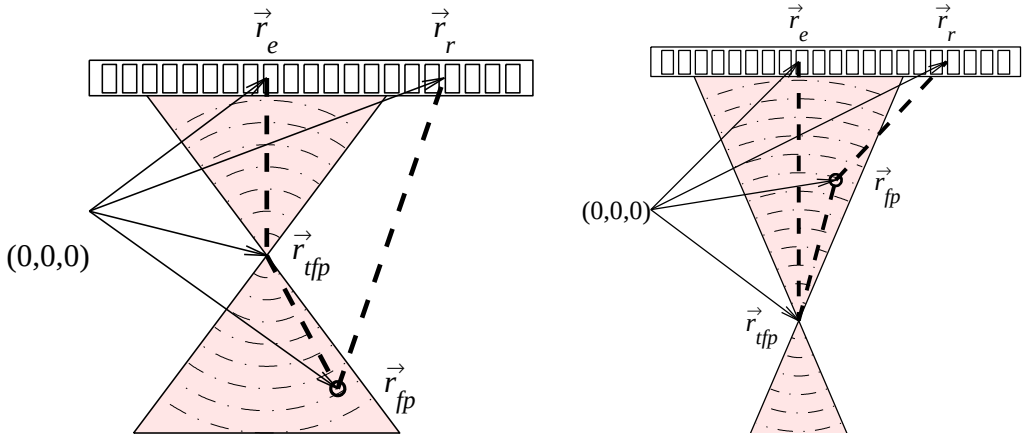

Figure 2. Wave propagation path (dotted line) for calculating the time-of-flight in receive focusing for a focused transmission. The transmit origin is perceived as the center element of the transmitting aperture. The TOF path is via the transmit focal point.

In DASB the strategy for beamforming a single point is to select one sample from each receive channel of the acquired data and then sum up a weighted set of these samples. By beamforming a group of points a scan line can be created. Different arrangements of scan lines are used for different applications. Examples of applications are illustrated in Fig. 4 and (a) demonstrate B-mode image lines and (b) & (c) directional beamforming for e.g. velocity vector estimation. In general a beamformed image point, $I(\vec{r})$ at position, $\vec{r}_{fp}$ can be expressed as

$$I(\vec{r}_{fp}) = \sum_{e=1}^{N_e} \mathcal{A}_e(\vec{r}_{fp}) \sum_{r=1}^{N_r} \mathcal{A}_r(\vec{r}_{fp}) s_{e,r}(t_{tof}(\vec{r}_e, \vec{r}_{tfp}, \vec{r}_{fp}, \vec{r}_r)) \ , \tag{4}$$

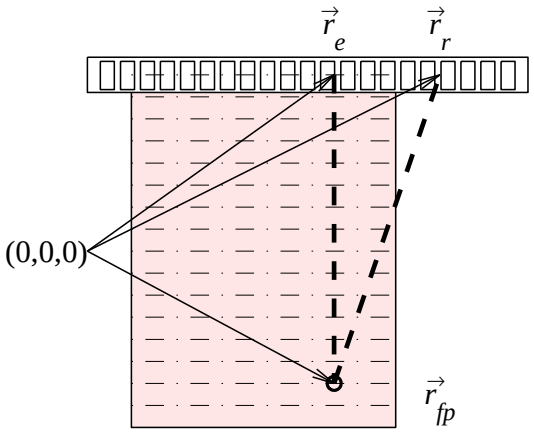

Figure 3. Wave propagation path (dotted line) for calculating the time-of-flight in receive focusing for a plane wave transmission. The transmit origin and the receive point are illustrated as different elements of an array. The transmit origin is assumed at the same lateral position as the receive point.

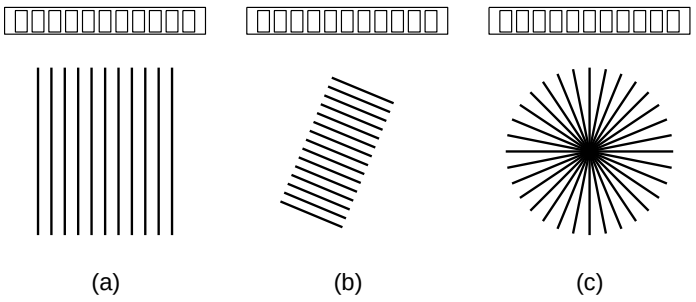

Figure 4. Receive points are located on straight lines. Different arrangements of lines are used for different applications. The examples shown illustrate B-mode imaging (a), directional beamforming for velocity estimation[7] (b) and directional beamforming for velocity vector angle estimation[8,9] (c).

where N_r is the number of receiving elements, $\mathcal{A}$ is the dynamic apodization function in transmit and receive and $s_{e,r}(t)$ is the time-domain received echo signal at receiving element r after the e'th emission. N_e is the number of emissions used to construct the image point, where the origin of each emission is spatially different from the other as is the case in STA. E.g for a conventional B-mode image point, $N_e = 1$.

As already stated the samples to select are determined by the TOF. Due to the continuous nature of the TOF the sample index will not necessarily coincide with the discrete time indices of the sampled channel data. Thus, a nearest neighbor approach or some form of inter-sample interpolation is needed and this has a influences on the image quality[22] and the hardware complexity for implementation. By using a proper interpolation scheme it is possible to reduce the sampling frequency or to improve performance.

With an aperture of finite size edge waves will affect the beam pattern by increasing the side lobes. Apodization is often applied in both transmit and receive to suppress the side lobes with a trade-off in lateral resolution, since the aperture width is inversely proportional to the main lobe width of the beam pattern. Receive apodization can take the form of a fixed tapering of channel signals, a step-wise depth dependent function or a fully dynamic function. The latter offers an opportunity to introduce an expanding and contracting aperture and maintain a constant preferred F-number and uniform beam pattern[23] until the entire aperture is applied.

2.1. Toolbox Software Design.

The software design of the toolbox is described next. The issues from the previous section and how they are handled and implemented are discussed. The toolbox is written in C++ and since it has a `MATLAB` (MathWorks Inc.) user interface `MATLAB` MEX-files are used to link between the C++ source code and the `MATLAB` environment. MEX-files are dynamically linked routines, which can be invoked from `MATLAB` just as a general built-in function.[24,25] The toolbox is designed for parallelization on a multi-processor cluster but can just as well run on a single processor system with a Windows or a Linux operating system. This part of the design is called *Parlib*[26] and the design philosophy and considerations regarding parallelization are not described further.

An overview of some of the functionality of the m-files (`MATLAB` programming code) and the MEX-file is illustrated in Fig. 5. The user interface is a group of user functions, which control the BFT. The most important functions are the definition functions which control the transmitting and receiving aperture, the scan lines, and the apodization. Each of these functions create an instance of a C++ class and a handle to the instance is returned.

The main content of the MEX-file is obviously the functions executing the user functions. The entry into the correct function is via the obligatory `mexFunction` which must exist in every C source MEX-file. In the `mexFunction` the correct task is found based on the input from user-function invoking the MEX-file. Moreover the MEX-file is in charge of storing all class instances. This is done by applying dynamically linked list and supporting functions for searching list members (class instances) and deleting list members.

The definition functions in the user interface are handled in different C++ classes. The APERTURE class stores the physical spatial coordinates in 3D space of the transducer elements or the coordinates of a virtual aperture. Different instances of this class are used to define both the transmit aperture and the receive aperture. The instance representing the receive aperture typically contains the coordinates of the physical transducer elements used during the receiving of echo signals. The transmit aperture however consists typically of a single coordinate to be able to calculate the transmit time t_{tof_t} as discussed previously in Section 2. If it contains several coordinates, a set of TOF values are calculated for each coordinate. A selection of one of these sets is made by the user, when the beamforming is executed based on the characteristics of the acquisition creating the data.

The APODIZATION class holds the information of the tapering of the samples from the individual receive data-channels. The apodization can be defined in two distinct ways. One option is completely flexible in the sense that arbitrary apodization values can be defined for an arbitrary number of depth intervals. With this option a simple and fixed tapering can be applied for FP's at all depth or extraordinary apodization functions e.g. the functions investigated by Jensen and Munk for vector velocity estimation[27] can easily be implemented. A dynamic apodization function with an expanding aperture can also be implemented with this option. This is done by supplying a table of the desired apodization values and manually calculating the depth intervals in which the different apodization values should be applied. This can be slightly cumbersome and for the purpose of creating a dynamic apodization function with a preferred F-number another option exist. Here a pre-defined analytical window function e.g. a Hamming or a Tukey is given as a text string along with a desired F-number and then the

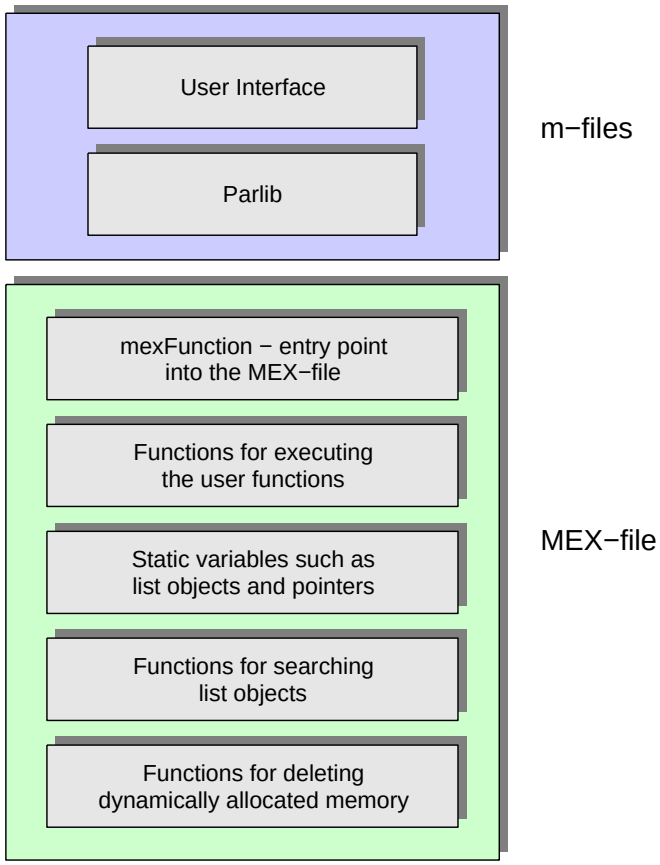

Figure 5. Overview of some of the functionality of the m-files and the MEX-file

APODIZATION class calculates the width of the active sub-aperture and the apodization values. If the width of the active sub-aperture exceeds the aperture width defined in the APERTURE class, then only the central part of the calculated values are applied as illustrated in Fig. 6. For a given FP the analytical calculation of the apodization value for aperture element, i, if e.g. a Hanning window is applied, is

$$\mathcal{A}(\gamma) = \begin{cases} 0.5(1-\cos(\pi\gamma+\pi)) & \text{for} \quad \gamma \leq 1 \\ 0 & \text{for} \quad \gamma > 1 \end{cases} \tag{5}$$

where γ is a normalized index which depends on the distance, D between the FP and a reference point on the aperture, the desired F-number, F and on the position of the element, $\vec{r}_i$ for which the apodization value is calculated relative to the center position of the aperture, $\vec{r}_c$

$$\gamma(r_i) = |(\vec{r}_i - \vec{r}_c)|2F/D \; . \tag{6}$$

When the apodization is defined as in the latter case the apodization values for each FP can be saved to `MATLAB` compatible files, if requested by the user.

The LINE class keeps the parameters and methods for generating the coordinates of the FP's in 3D space. The BFT is primarily designed to beamform FP's located on straight lines in any arbitrary direction as illustrated in Fig. 4. Equidistant points on a line can be characterized by an origin, $\vec{r}_0$, a direction, $\boldsymbol{\zeta}$, a length, L and the distance between consecutive points, Δr as illustrated in Fig. 7. The coordinate of the i'th point, $\vec{r}_i = (x,y,z)$ on the line is

$$\vec{r}_i = \vec{r}_0 + i\Delta r\boldsymbol{\zeta} \; . \tag{7}$$

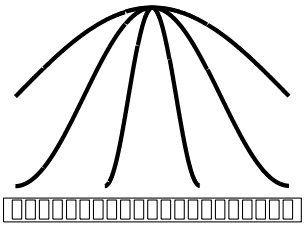

Figure 6. Dynamic apodization with expanding aperture.

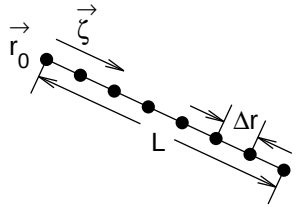

Figure 7. Line of equidistant receive focus points.

In the IMAGE class two instances of the APERTURE class and at least one instance from each of the classes APODIZATION and LINE are stored. These are the basic information needed for beamforming the acquired data. Besides the basics the strategy for calculating the TOF must be decided on as discussed previously in Section 2. A choice between the situations exemplified in Fig. 1, Fig. 2, and Fig. 3 and the corresponding TOF calculations expressed in (1), (2), and (3) must be taken and stored as a variable in the class instance. Furthermore a choice between the available inter-sample interpolation schemes must be made. These are nearest neighbor, linear, polynomial of various order, spline and up-sampling and filtering with a user-defined FIR-filter.[22] The calculation of the TOF is performed by IMAGE class. The method consists of nested loops going through lines, FP's, and finally transducer elements, such that the TOF can be calculated for all permutations of FP's, transmit aperture elements, and receive aperture elements. The TOF calculation in (1) and (2) involves a square root operation which is a computational heavy task to implement i hardware.[28] An alternative to calculating the TOF for each individual FP has been studied by Nikolov et al.[29,30]

The intention of the PARAMETER class is to hold general parameter values such as the sampling frequency, f_s and the speed of sound, c.

With all the parameters and definitions in place the beamforming can be initiated. In Fig. 8 an overview of the main information flow and C++ classes of the BFT is shown. The beamforming is initiated by the user function `bft2_bfm`, which is given an instance of the IMAGE class and obviously the data to beamform as inputs. Here it is also specified which element to use, if the transmit aperture consists of more than one element. It is also possible to specify that besides returning the DASB values the delayed pre-sum channel values should be returned. This is a powerful tool to investigate whether the channel data is summed coherently. A user option in the BFT determines whether all TOF values and apodization values should be pre-calculated and stored in look-up tables (LUT) after creating an instance of the IMAGE class or if each single value should be calculated on demand during the beamforming process. Using a LUT can be an advantage in terms of calculation speed when different sets of data have to be beamformed in the same way, since all the delay and apodization calculations are only made once. If many or extensive IMAGE instances are needed, the LUT will potentially occupy more system memory than available.

3. PERFORMANCE AND EXAMPLES OF USE

Some examples of use and a simple measure of performance are presented next. As stressed previously in Section 2 the strategy for calculating the TOF is of great significance in respect to phase coherent summation of channel data. An example of a Field II[6] simulation is given in Fig. 9. Here a single point target (PT) located at $\vec{r}_{pt} = (5,0,12)$ mm has been beamformed according to (3) and (2) respectively. The beamformed FP's are located on the axial line intersecting the

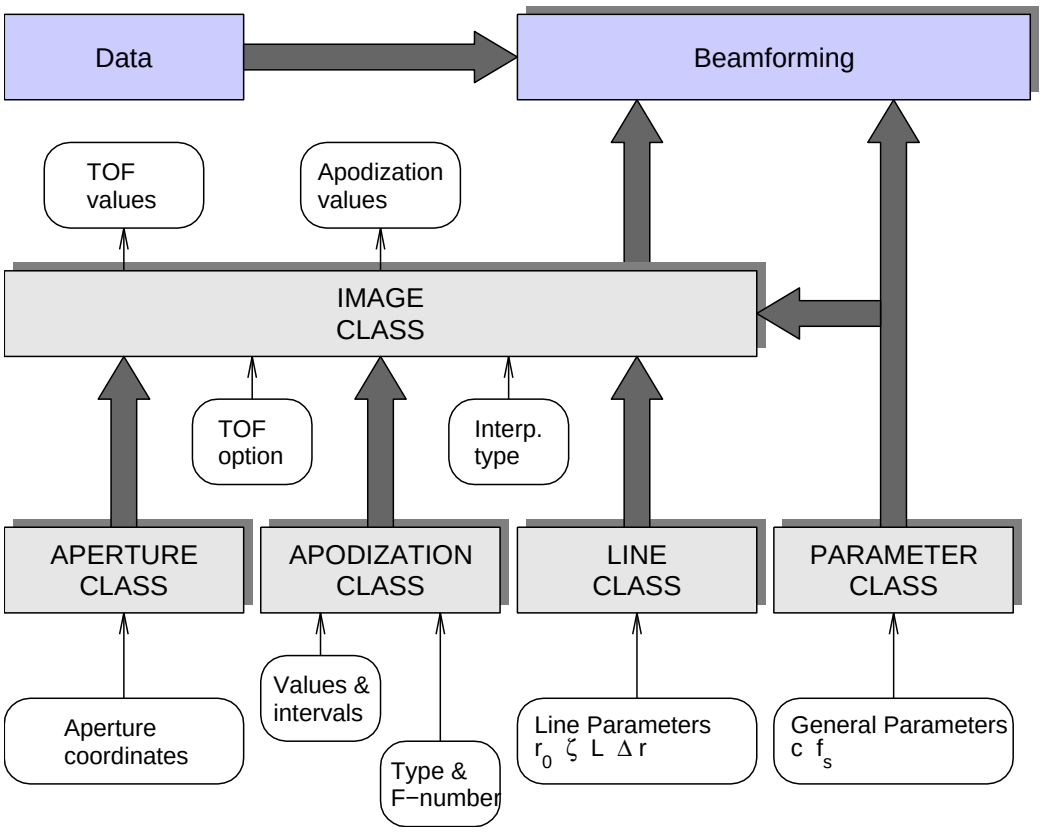

Figure 8. Information flow and C++ classes.

PT. The simulated application is a focused transmission using a linear array aperture of 128 elements, a 2-cycle sinusoid excitation and a transmit focal point at $\vec{r}_{tfp} = (0, 0, 5)$ mm. The beamformed pre-sum data are shown for all the receiving channels (columns). It appears that the beamformed channels are more coherent in phase around the PT when beamformed according to (2). This is in agreement with the strategy that the receive beamforming must comply with the transmit beamforming.

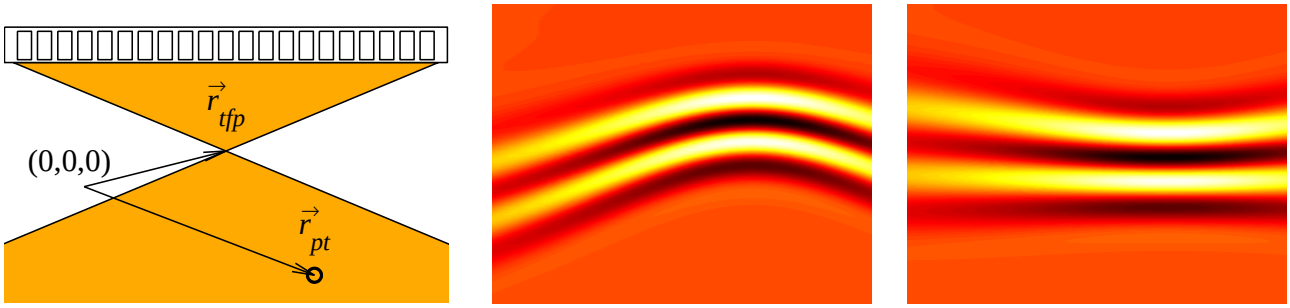

Figure 9. The response from a point target is simulated in Field II[6] with a focused transmission. The data are beamformed with two different strategies for calculating the TOF, (3) (left) and (2) (right). The beamformed data is shown for all the receiving channels (columns).

The BFT has been used in several occasions and for many different applications. Some examples of use are SA

B-mode imaging,[31] SA flow,[32,33] directional beamforming for velocity estimation,[7] directional beamforming for velocity vector angle estimation,[8,9] plane wave color flow imaging,[34] and coded SA.[35,36]

To get an impression of the performance in terms of calculation speed, a beamforming operation has been performed on a standard PC with a Pentium 4, 2.66 GHz processor running Linux. The BFT can beamform $100,000$ points in lines of various directions in 20.2 seconds with a standard deviation of 0.5 seconds using a transducer of 128 elements, dynamic apodization and 3rd order polynomial interpolation. This is a decrease in computation time of at least a factor of 15 compared to an implementation of a similar beamformer directly in `MATLAB`.

4. CONCLUSION

A software toolbox for off-line dynamic receive focusing of scan lines in any arbitrary direction in 3D space has been developed. It offers a choice between different methods for calculating time-delays, various inter-sample interpolation schemes, and apodization can be any preferred window function of fixed size or it can be fully dynamic with an expanding and contracting aperture to obtain a preferred F-number. The paper gives an insight into the software architecture of the toolbox and beamformer design principles and shares some of the many considerations in relation to beamformer development and implementation. The toolbox is versatile and has been used for many different applications such as directional velocity vector estimation and synthetic aperture imaging.

ACKNOWLEDGMENTS

This work was supported by grant 9700883, 9700563 and 26-04-0024 from the Danish Science Foundation and by B-K Medical, Denmark. The initial version of the BFT2 toolbox was written by Sara Gustavsson with S. Nikolov and J. A. Jensen as supervisors.

REFERENCES

1. K. E. Thomenius, "Evolution of ultrasound beamformers," in *Proc. IEEE Ultrason. Symp.*, **2**, pp. 1615–1621, 1996.
2. T. Pham and T. Whipps, "Acoustic signal processing toolbox for array processing," *Proceedings of SPIE - The International Society for Optical Engineering* **5096**, pp. 597–606, 2003.
3. S. Bjorklund and D. Rejdemyhr, "A matlab toolbox for radar array processing," *Signal Processing and Its Applications, 1999. ISSPA '99* **2**, pp. 547–550, 1999.
4. R. Hansen, T. Saebo, H. Callow, P. Hagen, and E. Hammerstad, "Synthetic aperture sonar processing for the hugin auvoceans 2005 - europe," *Oceans 2005 - Europe, IEEE* **2**, pp. 1090–1094, 2005.
5. S. Gustavsson, "Parallel algorithms for ultrasound beamformation," Master's thesis, Ørsted•DTU, Technical University of Denmark, Lyngby, Denmark, 2002.
6. J. A. Jensen, "Users' guide for the Field II program, version 2.70 of may 26, 1999," tech. rep., Department of Information Technology, DTU, 1999.
7. J. A. Jensen, "Directional velocity estimation using focusing along the flow direction: I: Theory and simulation," *IEEE Trans. Ultrason., Ferroelec., Freq. Contr.* , pp. 857–872, 2003.
8. J. A. Jensen, "Velocity vector estimation in synthetic aperture flow and B-mode imaging," in *IEEE International Symposium on Biomedical imaging from nano to macro*, pp. 32–35, 2004.
9. J. Kortbek and J. A. Jensen, "Estimation of velocity vector angles using the directional cross-correlation method," *IEEE Trans. Ultrason., Ferroelec., Freq. Contr.* **53**, pp. 2036–2049, 2006.
10. G. R. Lockwood, J. R. Talman, and S. S. Brunke, "Real-time 3-D ultrasound imaging using sparse synthetic aperture beamforming," *IEEE Trans. Ultrason., Ferroelec., Freq. Contr.* **45**, pp. 980–988, 1998.
11. S. I. Nikolov, *Synthetic aperture tissue and flow ultrasound imaging*. PhD thesis, Ørsted•DTU, Technical University of Denmark, 2800, Lyngby, Denmark, 2001.
12. K. Gammelmark, *Improving the Image Quality of Synthetic Transmit Aperture Ultrasound Images*. PhD thesis, Ørsted•DTU, Technical University of Denmark, 2800, Lyngby, Denmark, 2004.
13. C. R. Hazard and G. R. Lockwood, "Theoretical assessment of a synthetic aperture beamformer for real-time 3-D imaging," *IEEE Trans. Ultrason., Ferroelec., Freq. Contr.* **46**, pp. 972–980, 1999.
14. L. F. Nock and G. E. Trahey, "Synthetic aperture imaging in medical ultrasound with correction for motion artifacts," in *Proc. IEEE Ultrason. Symp.*, pp. 1597–1601, 1990.

15. L. F. Nock and G. E. Trahey, "Synthetic receive aperture imaging with phase correction for motion and for tissue inhomogenities - part I: basic principles," *IEEE Trans. Ultrason., Ferroelec., Freq. Contr.* **39**, pp. 489–495, 1992.
16. G. E. Trahey and L. F. Nock, "Synthetic receive aperture imaging with phase correction for motion and for tissue inhomogenities - part II: effects of and correction for motion," *IEEE Trans. Ultrason., Ferroelec., Freq. Contr.* **39**, pp. 496–501, 1992.
17. C. Passmann and H. Ermert, "Adaptive 150 MHz ultasound imaging of the skin and the eye using an optimal combination of short pulse mode and pulse compression mode," in *Proc. IEEE Ultrason. Symp.*, pp. 1291–1294, 1995.
18. C. Passmann and H. Ermert, "A 100-MHz ultrasound imaging system for dermatologic and ophthalmologic diagnostics," *IEEE Trans. Ultrason., Ferroelec., Freq. Contr.* **43**, pp. 545–552, 1996.
19. C. H. Frazier and W. D. O'Brien, "Synthetic aperture techniques with a virtual source element," *IEEE Trans. Ultrason., Ferroelec., Freq. Contr.* **45**, pp. 196–207, 1998.
20. S. I. Nikolov and J. A. Jensen, "Virtual ultrasound sources in high-resolution ultrasound imaging," in *Proc. SPIE - Progress in biomedical optics and imaging*, **3**, pp. 395–405, 2002.
21. S. I. Nikolov and J. A. Jensen, "Comparison between different encoding schemes for synthetic aperture imaging," in *Proc. SPIE - Progress in biomedical optics and imaging*, **3**, pp. 1–12, 2002.
22. J. Kortbek, H. Andresen, S. Nikolov, and J. A. Jensen., "Comparing interpolation schemes in dynamic receive ultrasound beamforming.," in *Proc. IEEE Ultrason. Symp.*, pp. 1972–1975, 2005.
23. J. C. Curlander and R. N. McDonough, *Synthetic Aperture Radar: Systems and Signal Processing*, John Wiley & Sons, Inc., 1991.
24. The MathWorks Inc., *MATLAB Application Program Interface Guide*, The MathWorks Inc., 1998.
25. The MathWorks Inc., *External Interfaces/API*, The MathWorks Inc., 2002.
26. A. Melchiorsen, "A library for parallel computations in Matlab," Master's thesis, Ørsted•DTU, Technical University of Denmark, Lyngby, Denmark, 2002.
27. J. A. Jensen and P. Munk, "A new method for estimation of velocity vectors," *IEEE Trans. Ultrason., Ferroelec., Freq. Contr.* **45**, pp. 837–851, 1998.
28. P. Montuschi, "Survey of square rooting algorithms," *IEEE Proceedings, Pt. E, No.1* **137**, 1990.
29. S. I. Nikolov, J. A. Jensen, and B. G. Tomov, "Recursive delay calculation unit for parametric beamformer," in *Proc. SPIE - Progress in biomedical optics and imaging*, **6147-13**, pp. 1–12, 2006.
30. S. I. Nikolov, B. G. Tomov, and J. A. Jensen, "Parametric beamformer for synthetic aperture ultrasound imaging," in *Proc. IEEE Ultrason. Symp.*, pp. 2172–2176, 2006.
31. H. Andresen, S. Nikolov, and J. A. Jensen, "Cardiac in-vivo measurements using synthetic transmit aperture ultrasound," in *Proc. IEEE Ultrason. Symp.*, p. Accepted, 2006.
32. N. Oddershede and J. A. Jensen, "Effects influencing focusing in synthetic aperture vector flow imaging," *IEEE Trans. Ultrason., Ferroelec., Freq. Contr.* , p. Accepted, 2006.
33. N. Oddershede and J. A. Jensen, "Motion compensated beamforming in synthetic aperture vector flow imaging," in *Proc. IEEE Ultrason. Symp.*, p. Accepted for publication, 2006.
34. I. Bolic, J. Udesen, F. Gran, and J. A. Jensen, "Plane wave fast color flow mode imaging: parameter study," in *Proc. SPIE - Progress in biomedical optics and imaging*, **6417-30**, pp. 1–11, 2006.
35. F. Gran and J. A. Jensen, "Directional velocity estimation using a spatio-temporal encoding technique based on frequency division for synthetic transmit aperture ultrasound," *IEEE Trans. Ultrason., Ferroelec., Freq. Contr.* **53(7)**, pp. 1289–1299, 2006.
36. F. Gran and J. A. Jensen, "Frequency division transmission and synthetic aperture reconstruction," *IEEE Trans. Ultrason., Ferroelec., Freq. Contr.* **53(5)**, pp. 900–911, 2006.

B.2 Comparing Interpolation Schemes in Dynamic Receive Ultrasound Beamforming

This article was published in Journal *Proceedings - IEEE Ultrasonics Symposium*. Conference Title *2005 IEEE Ultrasonics Symposium Issue Vol.4 Page no. 1972-1975. September 2005.*.

Comparing interpolation schemes in dynamic receive ultrasound beamforming

Jacob Kortbek[1,2], Henrik Andresen[1], Svetoslav Nikolov[1] and Jørgen Arendt Jensen[1]

1) Center for Fast Ultrasound Imaging, Ørsted•DTU,
Bldg. 348, Technical University of Denmark, DK-2800 Lyngby, Denmark.
2) B-K Medical, Mileparken 34, DK-2730 Herlev, Denmark.

***Abstract*— In medical ultrasound interpolation schemes are often applied in receive focusing for reconstruction of image points. This paper investigates the performance of various interpolation scheme by means of ultrasound simulations of point scatterers in Field II. The investigation includes conventional B-mode imaging and synthetic aperture (SA) imaging using a 192-element, 7 MHz linear array transducer with λ pitch as simulation model. The evaluation consists primarily of calculations of the side lobe to main lobe ratio, SLMLR, and the noise power of the interpolation error. When using conventional B-mode imaging and linear interpolation, the difference in mean SLMLR is 6.2 dB. With polynomial interpolation the ratio is in the range 6.2 dB to 0.3 dB using 2nd to 5th order polynomials, and with FIR interpolation the ratio is in the range 5.8 dB to 0.1 dB depending on the filter design. The SNR is between 21 dB and 45 dB with the polynomial interpolation and between 37 dB and 43 dB with FIR filtering. In the synthetic aperture imaging modality the difference in mean SLMLR ranges from 14 dB to 33 dB and 6 dB to 31 dB for the polynomial and FIR filtering schemes respectively. By using a proper interpolation scheme it is possible to reduce the sampling frequency and avoid a decrease in performance. When replacing linear interpolation with a more advanced interpolation scheme it is possible to obtain a reduction of 18 dB and 33 dB in the SLMLR for the B-mode and SA imaging, respectively, and an improvement in SNR of 24 dB.**

I. Introduction

In medical ultrasound receive focusing is a core signal processing element used for reconstruction of image points from the received transducer signals in both conventional and synthetic aperture imaging. In the delay-and-sum beamformer a sample is selected from each of the receive channels corresponding to the echo of the image point target. The sample index is based on the total transmit-receive time-of-flight. Due to the continuous nature of the time-of-flight, it will not necessarily lie at the discrete time indices of the sampled channel data. Thus, some form of interpolation is needed and this heavily influences the image quality and the hardware complexity for implementation. By using a proper interpolation scheme it is possible to reduce the sampling frequency or to improve performance.

The investigation in this paper is based on the work of Henrik Andresen [1] and quantifies the change in performance as a function of interpolation type applied by means of ultrasound simulations of point scatterers in Field II [2]. This paper introduces the beamformation toolbox, BFT2 which is used in the investigation. BFT2 [3],[4], developed at CFU is written in C and has a Matlab program interface. It performs dynamic receive focusing and offers choices between static or dynamic apodization and various interpolation schemes. The interpolation schemes investigated include linear, polynomial, and upsampling and FIR filtering. Various order polynomials and FIR filters are investigated.

II. Description

The investigation in this paper on the influence of the choice of interpolation scheme includes conventional B-mode imaging and synthetic aperture imaging (SAI). The ultrasound RF signals for the investigation is created using Field II and the beamforming is performed with BFT2. From a reference data set an evaluation data set is created, which is used for the evaluation. For the evaluation the point-spread function, PSF is useful when observing the characteristics of different imaging modalities. It is highly affected by the type of transmit-receive focusing used, and is, thus, also affected by the interpolation in receive beamforming. The lateral part of the PSF is especially interesting in terms of spatial distribution and amplitude of the side-lobe energy, which again directly affects the image contrast. The evaluation and comparison of interpolation schemes is done by partly observing the lateral PSF and quantizing the main-lobe and side-lobe energy distribution in terms of the full-width-half-maximum, FWHM and the side-lobe-main-lobe-ratio, SLMLR and partly by the noise power of the interpolation error. The FWHM and the SLMLR are calculated in the horizontal plane at the depth of each of the point scatterers and compared to the case where the reference data is used.

A. Simulation setup

The ultrasound RF signals for the investigation is created using Field II with a 192-element, 7 MHz linear array transducer with λ pitch as simulation model and a 3-cycle sinusoid as excitation. The simulation is based on point scatterers placed at a depth of 10 mm to 80 mm with 5 mm between each, placed along the center of the transducer. A reference RF data set has been created using a sampling frequency of 1 GHz and linear interpolation and the evaluation RF data set is created by decimating the reference data (picking out samples) to a sampling frequency of 40 MHz. Two data sets are created. One by using conventional B-mode imaging, and one by using

TABLE I

FILTER DESIGN PARAMETERS

Filter setup	Pass band ripple, dB	Stop band amplitude, dB	Filter order
1	±0.1	-30	30
2	±0.1	-40	34
3	±0.1	-50	38
4	±0.1	-70	48

SAI. The conventional B-mode imaging with a sliding aperture of 64 elements applies dynamic receive focus and dynamic Hanning apodization with an F-number of two. In transmit an F-number of two is applied which gives a single transmit focus at 26.6 mm close to the geometrical focal point of the transducer at 25 mm. In SAI each element will transmit a pulse in sequence, and all elements are used in receive and a Hanning apodization is applied over the entire aperture. The points selected for beamforming are along the center of the active aperture, creating a total of 129 lines for both imaging modalities, where the points along each line will be spaced 0.1 mm apart.

Linear, polynomial and upsampling and filtering are the interpolation schemes used in this paper. The polynomial interpolation estimates the value between samples by fitting a polynomial of order M to the M+1 nearest points, and the algorithm for implementation in BFT2 is taken from [5]. Polynomials of order two to five are examined. Instead of fitting a function type to the measured data, simply upsampling and low-pass filtering the data is another option [6]. The upsampling is set to a factor of eight and the low-pass filtering will be performed by an equiripple FIR-filter designed with Matlabs *Filter Design and Analysis Tool* with a pass band between 0 and $\frac{1}{16}$ relative to the upsampled Nyquist rate. The stop band is defined from $\frac{3}{16}$ to 1. The design parameters of the filters used can be seen in Table I.

III. SIMULATION RESULTS

The observation of main-lobe and side-lobe levels is part of the evaluation. The investigation shows that the main-lobe is practically the same for the reference data and the decimated data, hence the full width at half maximum (FWHM) does not vary significantly with the interpolation schemes. The FWHM is the lateral distance between the two points on the lateral PSF where the amplitude is -6 dB relative to the maximum of the PSF. However the side-lobe level does vary with the interpolation type and the SLMLR of the different interpolation schemes at the depth of each of the point scatterers is calculated and quantized into the difference between the mean SLMLR over all depths of the interpolated data and the reference data, $\Delta SLMLR$

$$\Delta SLMLR = \frac{1}{D}\sum_{i=1}^{D}\frac{E_{i_{SL}}}{E_{i_{ML}}} - \frac{1}{D}\sum_{i=1}^{D}\frac{E^{ref}_{i_{SL}}}{E^{ref}_{i_{ML}}}\,. \qquad (1)$$

D is the number of depths and E_i denotes the energy of the lateral part of the PSF at depth index i. The side-lobes are not necessarily distinct peaks in the lateral PSF and the definition of side-lobes in this paper is, thus, spatially determined as whenever the lateral distance from the point scatterer is larger than 5 mm. Another quantitative measure is the signal-to-noise ratio, SNR which is a measure of how much the interpolated signal differ from the reference signal, $SNR = 10\log(\frac{\mu^2}{(\widehat{\mu}-\mu)^2})$, where μ is the reference signal and $\widehat{\mu}$ is the interpolated signal.

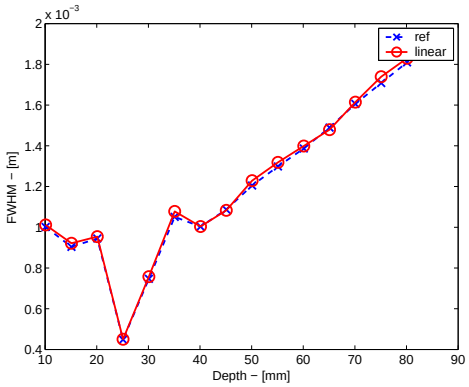

Fig. 1. B-mode FWHM as function of depth for reference data and interpolated data.

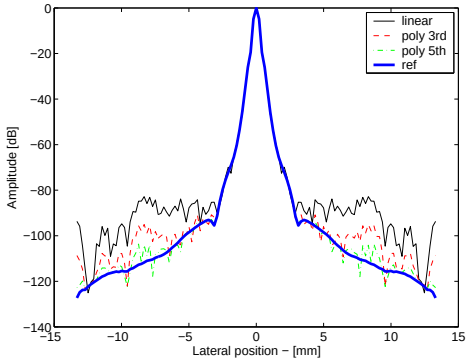

Fig. 2. B-mode lateral PSF at 25 mm axial position for reference data and interpolated data.

A. Conventional B-mode Imaging

The FWHM for the reference data and linear interpolated data can be seen in Fig. 1 and it is evident that a more advanced interpolation scheme will not have much further effect on the main-lobe. The point-spread-function, PSF along the lateral axis for the scatterer at 25 mm using the reference data, the linear interpolated data and the various order polynomial interpolated data can be seen in Fig. 2. The SLMLR can be seen in Fig. 3, and it shows that it is possible to attenuate the side-lobes to values near the reference data with the higher order polynomials or FIR filters in the region near the transmit focus. When the distance to the transmit focus is large the increased accuracy in the receive beamforming due to interpolation is diminished by the unfocused transmit field. The interpolated data primarily differ from the reference data close to the transmit focus. Since this will be reflected

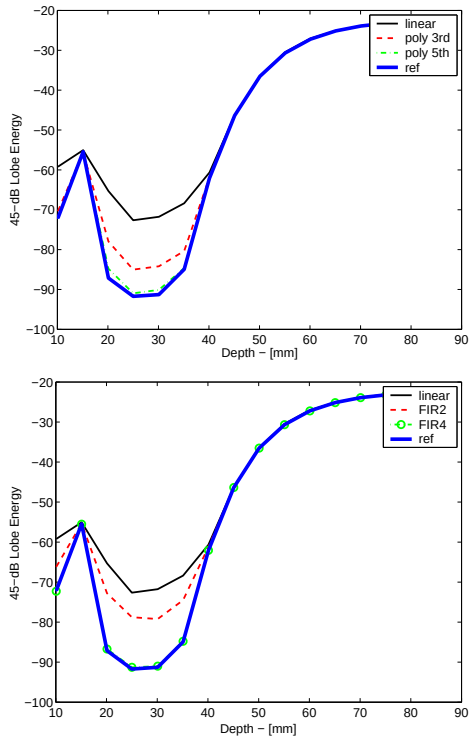

Fig. 3. B-mode SLMLR as a function of depth for different interpolation schemes.

TABLE II

B-MODE IMAGING. DIFFERENCE IN MEAN SLMLR AND SNR FOR DIFFERENT INTERPOLATION SCHEMES.

Interpolation Type	$\Delta SLMLR$, dB	Difference in SLMLR at 25 mm, dB	SNR, dB
Linear	6.2	19	21
2nd Order Pol.	6.2	19	21
3rd Order Pol.	2.0	6.7	34
4th Order Pol.	2.2	7.0	44
5th Order Pol.	0.3	0.8	45
1st FIR-filter	5.8	19	37
2nd FIR-filter	3.8	13	43
3rd FIR-filter	1.5	4.6	44
4th FIR-filter	0.1	0.4	43

in $\Delta SLMLR$ due to the averaging operation over depth the difference in SLMLR at 25 mm is also shown in Table II. It shows that the SLMLR near the transmit focus will decrease approximately 18 dB when switching from linear interpolation to a higher order polynomial or FIR filter interpolation. The $\Delta SLMLR$, the difference in SLMLR at the depth 25 mm and the SNR for the different schemes are all given in Table II.

The consequence of reducing the FIR-filter order, by putting less constrains on the pass band ripple has been investigated for the B-mode imaging modality. The parameters of the alternative filters can be seen in Table III. Compared to the filter setups in Table I, the filter orders are significantly lower. The quantified results are shown in Table IV. The difference in mean SLMLR and the SLMLR are practically unchanged

TABLE III

ALTERNATIVE FIR FILTER DESIGN PARAMETERS.

Filter setup	Pass band ripple, dB	Stop band amplitude, dB	Filter order
5	± 1	-30	18
6	± 1	-40	22
7	± 1	-50	28
8	± 1	-70	36

TABLE IV

B-MODE IMAGING. DIFFERENCE IN MEAN SLMLR AND SNR WITH ALTERNATIVE FIR FILTERS.

Interpolation Type	$\Delta SLMLR$, dB	Difference in SLMLR at 25 mm, dB	SNR, dB
5th FIR-filter	6.9	22	28
6th FIR-filter	5.2	16	29
7th FIR-filter	1.6	5.0	30
8th FIR-filter	0.4	0.9	30

compared to the higher order filters but a decrease in the SNR is present due to the larger pass band deviation.

B. Synthetic aperture Imaging

The results using the synthetic aperture imaging modality is presented similarly to the results of the sliding aperture B-mode imaging modality. The FWHM does not vary with interpolation type in this modality either. The PSF using the reference data, the linear interpolated data and various FIR-filtered data can be seen in Fig. 4. The SLMLR can be seen in Fig. 5 and it shows a significant attenuation due to interpolation in almost the entire image region and with the largest attenuation near the focus point of the transducer. The side-lobe levels are close to the levels of the reference data with the higher order FIR filters. The higher order polynomials are also getting close to the reference but not as close as with the FIR interpolation. The difference in mean SLMLR, the difference in SLMLR at the depth 25 mm and the SNR for the different schemes is given in Table V.

The levels of the SLMLR for the different interpolation types are similar within 10 dB in the two imaging modalities

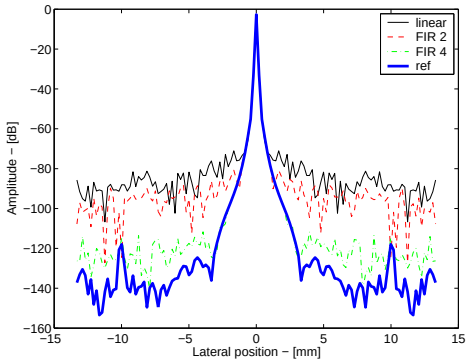

Fig. 4. SA-mode. Lateral PSF at 25 mm axial position for reference data and interpolated data.

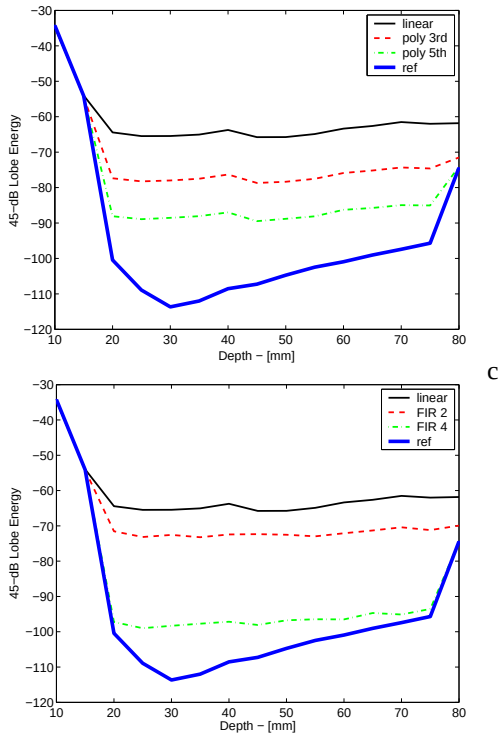

c

Fig. 5. SA-mode SLMLR as a function of depth for different interpolation schemes.

TABLE V

SYNTHETIC APERTURE IMAGING. DIFFERENCE IN MEAN SLMLR AND SNR FOR DIFFERENT INTERPOLATION SCHEMES.

Interpolation Type	$\Delta SLMLR$, dB	Difference in SLMLR at 25 mm, dB	SNR, dB
Linear	33	43	20
2nd Order Pol.	33	44	37
3rd Order Pol.	22	31	33
4th Order Pol.	23	32	48
5th Order Pol.	14	20	44
1st FIR-filter	31	41	45
2nd FIR-filter	26	36	46
3rd FIR-filter	18	26	44
4th FIR-filter	6	10	44

at depths close to the B-mode transmit focus. The SLMLR of the reference data though is much lower in SA than in conventional B-mode. E.g. at a depth of 25 mm the SLMLR is around -90 dB and -110 dB for the B-mode and the SA-mode, respectively. Due to this lower reference and due to the similarity between the SLMLR for the B-mode interpolated data and reference data at larger depths, the difference in mean SLMLR will be higher for the SA-mode than the B-mode.

IV. CONCLUSION

The main-lobe of the lateral point-spread function is practically the same, when using the reference data and the linear interpolated data. Hence, the FWHM in this investigation is not affected by the type of interpolation. When using conventional B-mode imaging and linear interpolation, the difference in mean SLMLR is 6.2 dB. With polynomial interpolation the difference is in the range 6.2 dB to 0.3 dB using 2nd to 5th order polynomials, and with FIR interpolation the difference is reduced from 5.8 dB to 0.1 dB depending on the filter design. The SNR is between 21 dB and 45 dB with the polynomial interpolation and between 37 dB and 43 dB with FIR filtering. The order of the FIR-filters can be decreased by reducing the demands on the pass band. The result of this is a decrease in the SNR, but the SLMLR is practically unchanged compared to the higher order filters. Thus, in B-mode imaging, the decimated data in combination with 4th order polynomial interpolation or a FIR filter of order 28 will yield a performance very near to the performance of using the reference data. In the synthetic aperture imaging modality the influence of the type of interpolation applied is even higher. Here the difference in mean SLMLR ranges from 14 dB to 33 dB and 6 dB to 31 dB for the polynomial and FIR filtering schemes respectively. The SNR is similar to the case of conventional B-mode imaging. By using a proper interpolation scheme it is possible to reduce the sampling frequency and avoid a decrease in performance. When replacing linear interpolation with a more advanced interpolation scheme it is possible to obtain a reduction in SLMLR of 18 dB and 33 dB in the B-mode and SA imaging, respectively, and an improvement in SNR of 24 dB.

ACKNOWLEDGMENT

This work was supported by grant 9700883, 9700563 and 26-04-0024 from the Danish Science Foundation and by B-K Medical, Denmark. The initial version of the BFT2 toolbox is written by Sara Gustavsson with Svetoslav Nikolov as supervisor.

REFERENCES

[1] H. Andresen. *Beamformation Interpolation Schemes using Field II*. Special Course Report. Ørsted•DTU, Technical University of Denmark, 2005.

[2] J. A. Jensen. Users' guide for the Field II program, version 2.70 of may 26, 1999. Technical report, Department of Information Technology, DTU, 1999.

[3] S. Gustavsson. Parallel algorithms for ultrasound beamformation. Master's thesis, Ørsted•DTU, Technical University of Denmark, Lyngby, Denmark, 2002.

[4] S. Gustavsson. Users guide for the beamformation toolbox ii, release 1.0. Technical report, Ørsted•DTU, Technical University of Denmark, Lyngby, Denmark, 2002.

[5] W. H Press et. Al. *Numerical Recipes in C*. Cambridge University Press, 1992.

[6] R. E. Crochiere and L. R. Rabiner. *Multirate digital signal processing*. Prentice-Hall, Englewood Cliffs, NJ, 1983.

B.3 Estimation of Velocity Vector Angles using the Directional Cross-Correlation Method

This article was published in Journal *IEEE Transactions on Ultrasonics, Ferroelectrics and Frequency Control, Vol.53 Issue.11, Page no. 2036-2049, November 2006.*

Estimation of Velocity Vector Angles Using the Directional Cross-Correlation Method

Jacob Kortbek and Jørgen Arendt Jensen, *Senior Member, IEEE*

***Abstract*—A method for determining both velocity magnitude and angle in any direction is suggested. The method uses focusing along the velocity direction and cross-correlation for finding the correct velocity magnitude. The angle is found from beamforming directional signals in a number of directions and then selecting the angle with the highest normalized correlation between directional signals. The approach is investigated using Field II simulations and data from the experimental ultrasound scanner RASMUS and a circulating flow rig with a parabolic flow having a peak velocity of 0.3 m/s. A 7-MHz linear array transducer is used with a normal transmission of a focused ultrasound field. In the simulations the relative standard deviation of the velocity magnitude is between 0.7% and 7.7% for flow angles between 45° and 90°. The study showed that angle estimation by directional beamforming can be estimated with a high precision. The angle estimation performance is highly dependent on the choice of the time $k_{\mathrm{tprf}} \cdot T_{\mathrm{prf}}$ (correlation time) between signals to correlate. One performance example is given with a fixed value of k_{tprf} for all flow angles. The angle estimation on measured data for flow at 60° to 90° yields a probability of valid estimates between 68% and 98%. The optimal value of k_{tprf} for each flow angle is found from a parameter study; with these values, the performance on simulated data yields angle estimates with no outlier estimates and with standard deviations below 2°.**

I. Introduction

Modern ultrasound systems can estimate the blood velocity in vivo in real time [1], [2]. This is done by acquiring ultrasound signals from the same direction a number of times, and then correlating the signals. The shift in phase as a function of time can be determined using an autocorrelation estimator and this yields the velocity [3]. A second approach is to determine the shift in position using the cross-correlation function; dividing with the time between emissions [4], [5] gives the velocity. Both approaches find only the shift along the ultrasound beam direction, and thus only the projected velocity along this direction. Velocities transverse to the beam are not detected, and velocities in different directions are not depicted correctly. There is, thus, a need for methods that can detect the correct velocity magnitude and direction as a function of spatial position.

Several authors have devised methods for estimating the correct velocity. Fox [6] suggested using two crossing beams to have two independent measurements. This, however, necessitates the use of a large aperture to obtain a sufficient angle between the beams to ensure a precise determination of the transverse component. Trahey and coworkers [7] suggested using speckle tracking over a region of the image to track the motion in any direction. This necessitates the use of fast beam formation to generate the large amounts of data. Introduction of a lateral oscillation has also been suggested so that the phase shift in the lateral directions also can be found using a modified autocorrelation method [8], [9]. Several other methods have been suggested [10], [11], but none have so far yielded a satisfactory performance to be commercially implemented.

This paper suggests a method for determining the velocity direction based on finding the motion along the velocity direction using cross-correlation. The velocity magnitude is determined here by focusing signals along the direction of the flow, as suggested in [12], [13]. This can be done if the correct direction is known. This is currently found by inspecting the B-mode image, and then using this angle in the beam formation. This is cumbersome and difficult to use, if the beam-to-flow angle changes throughout the image. Using the directional beamforming approach, angle estimation based on finding the direction of the maximum correlation is suggested in this paper, founded on the idea from [14]. Directional signals for a number of directions are beamformed, and the velocity and peak normalized correlation value are found. The direction with the highest correlation is then chosen as the angle estimate. The basics of the velocity estimation scheme is briefly described in Section II, and the angle estimation method is introduced in Section III. Investigations of the approach using simulations are given in Section IV-A and from measured data on a flow rig in Section IV-B.

II. Directional Velocity Estimation

This section gives a brief introduction to the principles from [12] of directional velocity estimation using focusing along the flow direction. The concept of spatial directional signals is introduced, and it is shown how the velocity can be estimated from these.

As described, the conventional cross-correlation method can estimate only the velocity component projected onto the direction of the ultrasound propagation, since the beam formation is done along this direction. In directional velocity estimation, the beam formation is done along the flow direction, and the correct velocity amplitude can, thus, be found also for a purely transverse direction.

Manuscript received November 28, 2005; accepted May 10, 2006.
The authors are with Ørsted•DTU, Technical University of Denmark, DK-2800 Lyngby, Denmark (e-mail: jk@oersted.dtu.dk).
Digital Object Identifier 10.1109/TUFFC.2006.144

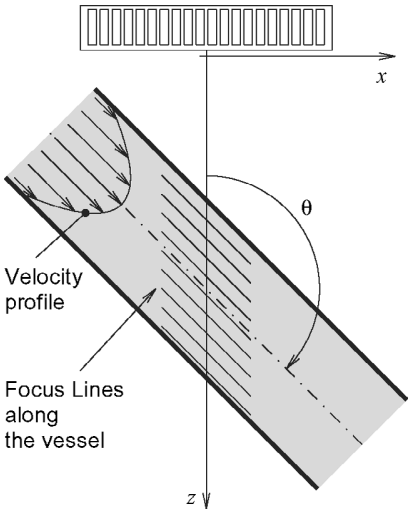

Fig. 1. Focus lines for constructing spatial directional signals.

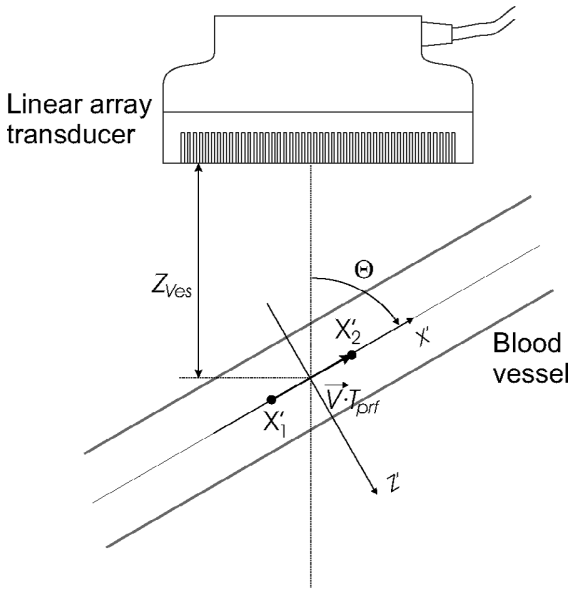

Fig. 2. Rotated coordinate system (x', z') oriented along the flow direction, and with origin at the center of the vessel at a distance Z_{ves} from the transducer.

The basic principle is to focus the responses received by the transducer along focus lines in the flow direction, which is referred to as directional signals in the spatial domain. In Fig. 1, a blood vessel and examples of focus lines are shown. The spatial signals for two consecutive emissions are then cross-correlated and the shift between them is found. This is a shift in spatial position of the scatterers, and dividing by the time between emissions, thus, directly gives the velocity magnitude. Just as for the conventional systems, the angle between the propagating direction of the emitted beam and the flow direction must be known before the beam formation can be done.

The directional signals are denoted $g(x')$, where x' is the x-coordinate in a rotated coordinate system aligned along the flow rather than along the ultrasound beam direction as shown in Fig. 2. Here the x'-axis of the new coordinate system is parallel to the flow direction, and the origin of the coordinate system is placed at the center of the vessel at depth Z_{ves}. The original coordinate system (x, z) has origin at the center of the transducer, the x-axis is parallel with the transducer, and the z-axis represents the depth. The y-axis represents the elevation plane, and this is the same for both coordinate systems. The relation between the rotated coordinate systems and the original coordinate system is given by

$$\begin{aligned} x &= \sin(\theta) \cdot x' + \cos(\theta) \cdot z', \\ y &= y', \\ z &= -\cos(\theta) \cdot x' + \sin(\theta) \cdot z' + Z_{ves}, \end{aligned} \tag{1}$$

or in matrix notation,

$$\begin{bmatrix} x \\ z \end{bmatrix} = \mathbf{R_{xz}} \cdot \begin{bmatrix} x' \\ z' \end{bmatrix} + \begin{bmatrix} 0 \\ Z_{ves} \end{bmatrix}, \tag{2}$$

where $\mathbf{R_{xz}}$ is the rotation matrix:

$$\mathbf{R_{xz}} = \begin{bmatrix} \sin(\theta) & \cos(\theta) \\ -\cos(\theta) & \sin(\theta) \end{bmatrix}. \tag{3}$$

The angle θ is defined in Fig. 2. In the new coordinate system, the velocity vector is $\vec{v} = (v_{x'}, 0, 0)$, which has only one non-zero component, $v_{x'} = |\vec{v}|$, provided the correct angle is used. The position of the scatterers can now be expressed through a scalar, where the first position is x'_1, and the position after T_{prf} seconds is $x'_2 = x'_1 + v_{x'} T_{\text{prf}}$. The directional signals are used to find the velocity. The first signal is given by $g_1(x')$, and the second obtained T_{prf} seconds later is $g_2(x')$. The two signals are related by

$$g_2(x') = g_1(x' - v_{x'} T_{\text{prf}}). \tag{4}$$

Cross-correlating the two signals gives

$$R_{12}(\xi_{x'}) = \int_X g_1(x') g_2(x' + \xi_{x'}) dx', \tag{5}$$

where X is the length of the directional signals. Using (4) the cross-correlation can be rewritten as

$$\begin{aligned} R_{12}(\xi_{x'}) &= \int_X g_1(x') g_1(x' - v_{x'} T_{\text{prf}} + \xi_{x'}) dx' \\ &= R_{11}(\xi_{x'} - v_{x'} T_{\text{prf}}), \end{aligned} \tag{6}$$

which is the shifted autocorrelation $R_{11}(\xi_{x'})$ of $g_1(x')$, which has a global maximum at $\xi_{x'} = v_{x'} T_{\text{prf}}$. The maximum of the cross-correlation function

$$\xi_{x'_{\max}} = \arg\max_{\xi_{x'}} \{R_{12}(\xi_{x'})\} \tag{7}$$

is, thus, the shift in spatial position of the scatterers over the time interval T_{prf}. This makes it possible to calculate the velocity estimate along the flow direction, given by

$$\hat{v}_{x'} = \frac{\xi_{x'_{\max}}}{T_{\text{prf}}}. \tag{8}$$

The cross-correlation can be improved by averaging over several estimates of R_{12} under the assumption that the velocity of the scatterers can be considered constant for several pulses. A number of cross-correlations N_{xc} can, thus, be used in the estimation. When applying averaging, $R_{12}(\xi_{x'})$ in (5) and (7) is substituted with

$$R_{12}(\xi_{x'}) = \sum_{i=1}^{N_{xc}} \mathcal{R}\left\{g_i(x', z'), g_{i+1}(x', z')\right\}, \tag{9}$$

where $\mathcal{R}$ is the cross-correlation operator. The correct flow angle must be determined for this to work, and this is the topic of Section III.

The beam formation of the directional signals is performed as described in [12], [13]. The discrete directional signals are obtained by focusing signals received by the transducer elements in a set of points. These points are located on a straight line in any arbitrary direction and, e.g., aligned along the flow direction for velocity estimation. The focusing of any of these points is based on the total transmit-receive time-of-flight, and a sample of the directional signal corresponding to the point $\mathbf{r_x}$ is calculated as

$$g(\mathbf{r_x}) = \sum_{j=1}^{N_E} s_j(t_{\mathbf{r_x}}) = \sum_{j=1}^{N_E} s_j\left(\frac{|\mathbf{r_t} - \mathbf{r_x}| + |\mathbf{r_x} - \mathbf{r_j}|}{c}\right), \tag{10}$$

where N_E is the number of transducer elements, $s_j(t)$ is the received signal from transducer element $\mathbf{j}$, $t_{\mathbf{r_x}}$ is the time instance at which to select a value from the signal $s_j(t)$, $\mathbf{r_t}$ is the position of the transmit source, and $\mathbf{r_j}$ is the position of the j'th transducer element.

III. Angle Estimation

Conventional velocity estimation systems rely on knowledge of the angle between the flow vector and the direction of the emitted ultrasound beam, and traditionally this knowledge comes from the B-mode image. In the ideal situation, the vessel is rigid and straight without sudden geometric changes within the range of the B-mode image, or at least within the velocity estimation range. In this case, the beam-to-flow angle could be determined with satisfactory results from the B-mode image. Unfortunately, this is not a realistic case. The blood vessels are branching and curving, and typically no unique direction can be found for the whole image. This leads to a wrong correction value for the projected velocity component, and the consequence is an increase in bias and standard deviation. The approach also fails for angles close to 90°. This motivates the investigation of an automatic approach to angle estimation.

The spatial directional signals are obtained by focusing the received responses in points along the flow direction. Directional signals obtained from two consecutive acquired responses properly aligned with the flow direction have a high correlation. The primary contribution to the decorrelation between the signals is the spatial shift due to the movement of the scatterers. Another minor contribution is due to new scatterers entering the directional signal at one end and others leaving at the other end. Now consider the case where the directional signals are not aligned along the flow direction. The distribution of the scatterers for the second directional signal is no longer just a shift in position of the previous scatterer distribution. The relative positions between the scatterers have changed, due to the different velocities for the different scatterers. The consequence is that the correlation between the two directional signals is reduced compared to the case of focusing along the flow direction. This change in correlation is the property used for the angle estimation. The method is, thus, to obtain directional signals in a number of directions, and quantify the correlation between signals in each direction. From this procedure a correlation function is constructed showing the normalized correlation as a function of search angle. The maximum of this function indicates the direction with the highest correlation between consecutive signals; hence the flow direction.

The cross-correlation is an obvious choice for the correlation function. However, the cross-correlation peak amplitude is not directly a valid measure. The cross-correlation output values are dependent on the amplitudes of the directional signals, and the amplitudes will differ due to different scatterer distributions at the focal points, and due to the spatial energy distribution of the transmitted ultrasound beam. Instead, the correlation peak should be found from normalized cross-correlation. The normalization factor could be the power of the signal, and this approach is formulated as

$$\begin{aligned} R_{12_n}(l, \phi) &= \frac{R_{12}(l, \phi)}{P_{12}(\phi)}, \\ R_{12_{\max}}(\phi) &= \max\left(R_{12_n}(l, \phi)\right), \\ \hat{\theta}_k &= \arg\max_{\phi}\left\{R_{12_{\max}}(\phi)\right\}, \end{aligned} \tag{11}$$

where $R_{12_n}(l, \phi)$ is the normalized cross-correlation estimate between directional signals $g_1(x', \phi)$ and $g_2(x', \phi)$, and

$$\begin{aligned} P_{12}(\phi) &= \sqrt{R_{11}(0, \phi) \cdot R_{22}(0, \phi)} \\ &= \sqrt{\sum_{x'} g_1(x', \phi)^2 \cdot \sum_{x'} g_2(x', \phi)^2} \end{aligned} \tag{12}$$

represents the power of the signals. The term ϕ denotes the angle of the directional signal, and $R_{12_{\max}}(\phi)$ is the maximum value of the normalized cross-correlation estimate as a function of beam-angle. The discrete angle estimate $\hat{\theta}_k$ is found where $R_{12_{\max}}(\phi)$ has its peak value.

The discrete cross-correlation estimates can yield erroneous peaks when a limited amount of data is used, and if noise is present in the data. This has been investigated in [12]; the influence of noise on the angle estimation is expected to be similar. The cross-correlation estimate can

be improved by averaging over several directional signals. If averaging is used, $R_{12_n}(l,\phi)$ in (11) can be rewritten as

$$R_{12_n}(l,\phi) = \sum_i \frac{R_{i,i+1}(l,\phi)}{P_{i,i+1}(\phi)}, \tag{13}$$

where i represents the pulse-echo lines, and the final correlation function from (11) is, thus, formulated as

$$R_{12_{\max}}(\phi) = \max\left(\sum_i \frac{R_{i,i+1}(l,\phi)}{P_{i,i+1}(\phi)}\right). \tag{14}$$

The quantization of the cross-correlation is determined from the spatial sampling frequency, when constructing the directional signals. If the spatial sampling interval is sparse, the performance can be improved by interpolation around the peak value of $R_{12_n}(l,\phi)$. Fitting a second-order polynomial to the samples around the peak $R_{12}(l_p,\phi)$, where l_p denotes the lag at which the peak occurs, will give a more precise maximum value [4], hence a more precise angle estimation.

The correlation between the directional signals can also be described using the correlation coefficient ρ. Correlation is the degree to which two or more components are linearly associated, and the statistical term is the covariance

$$\operatorname{cov}(x_1,x_2) = \langle (x_1-\overline{x}_1)(x_2-\overline{x}_2)\rangle \tag{15}$$

between components x_1 and x_2, and where $\langle\ \rangle$ is the expectation operator. The correlation coefficient is simply the covariance normalized with the product of the standard deviations of the two components, and is defined as

$$\rho = \frac{\operatorname{cov}(x_1,x_2)}{\sigma_{x_1}\sigma_{x_2}}, \tag{16}$$

where $\rho \in [-1,1]$ and $\rho = 1$ corresponds to perfect linear relation or full correlation.

The strategy for the angle estimation involves two steps when the correlation coefficient is used for the correlation function. Before calculating the correlation coefficient, the two directional signals, for which the correlation coefficient is needed, are aligned. Otherwise the correlation coefficient will be small, even at the true angle, due to the spatial shift from the movement of the scatterers. The alignment is determined from the discrete lag at the cross-correlation peak l_p. To increase accuracy, a 2nd order polynomial is fitted around the peak [4] to find a new interpolated lag value l_p^{int}:

$$l_p^{\text{int}} = l_p - \frac{R_{12_n}(l_p+1) - R_{12_n}(l_p-1)}{2\left(R_{12_n}(l_p+1) - 2R_{12_n}(l_p) + R_{12_n}(l_p-1)\right)}. \tag{17}$$

Due to the new continuous lag, the alignment operation involves a first-order linear interpolation or a higher-order interpolation scheme between the samples in one of the signals g_1 or g_2. The correlation function using the correlation coefficient is, thus, defined as

$$\rho(\phi) = \sum_i \frac{\operatorname{cov}\left(g_i(x',\phi), g_{i+1}(x'+l_p^{\text{int}},\phi)\right)}{\sigma_{g_i(x',\phi)}\sigma_{g_{i+1}(x'+l_p^{\text{int}},\phi)}}, \tag{18}$$

and the final angle estimation using this function is

$$\hat{\theta}_k = \arg\max_{\phi}\left\{\rho(\phi)\right\}, \tag{19}$$

where the estimate has been improved by averaging over several estimates of ρ using several pulse-echo lines i.

If the expectation operator is approximated by the temporal average, and assuming $\overline{x}_1 = \overline{x}_2 = 0$, then the correlation coefficient of (16) can be written as

$$\rho = \frac{\sum x_1 x_2}{\sqrt{\sum x_1^2}\sqrt{\sum x_2^2}}, \tag{20}$$

and the correlation function can be calculated by rewriting (18) into

$$\rho(\phi) = \sum_i \frac{\sum_{x'} g_i(x',\phi)\cdot g_{i+1}(x'+l_p^{\text{int}},\phi)}{\sqrt{\sum_{x'} g_i(x',\phi)^2 \cdot \sum_{x'} g_{i+1}(x'+l_p^{\text{int}},\phi)^2}}, \tag{21}$$

or in terms of the cross-correlation,

$$\rho(\phi) = \sum_i \frac{R^*_{i,i+1}(0,\phi)}{P^*_{i,i+1}(\phi)}, \tag{22}$$

where * denotes operation on the aligned signals.

The two approaches to calculating the correlation function in (14) and (21) (or (22)), respectively, are closely related but there are some differences. The quantifier in (21) benefits from the directional signals being accurately aligned before multiplication and summing contrary to the quantifier in (14). Here the summing of cross-correlation functions will suffer from a sparse spatial sampling and they will not sum fully coherently. The quantifier in (21) though requires additional computation due to the interpolation involved in the alignment. The influence of the choice of quantifier on the angle estimation performance is discussed in Section IV.

The directional lines are placed with an angular distance $\Delta\phi$, and the estimates are, thus, initially restricted to be discrete estimates $\hat{\theta}_k$ with the same resolution. Continuous estimates $\hat{\theta}$ can be obtained by employing interpolation similar to (17) around the peak of the correlation function to find a continuous index for the peak and then using linear interpolation between the neighboring discrete angles. This will reduce the number of directions to beamform signals in. Prior knowledge of the actual flow angle can also be used in confining the angle search range, with the purpose of limiting the computational task. Iterative schemes could be used, where a temporary estimate based on interpolation between results from a few search

angles is used. A new search, in a new confined search range around this temporary estimate, can now be made with an increased search resolution. This process continues until the desired precision is obtained or until the limit on the accuracy of the method has been reached.

In the angle and velocity estimator, the correlation is traditionally calculated based on consecutive directional signals. Considering the velocity estimator, for low velocities or high pulse repetition frequencies, the shift between signals is low, yielding a value of $\xi_{x'_{\max}}$ from (8) close to zero. This will make the relative estimation variance high since noise will dominate the estimate. It can be an advantage to correlate signals, where the time between acquisitions is higher. The directional signals used for the cross-correlations are then selected with a time interval $T_{cc} = k_{\text{tprf}} \cdot T_{\text{prf}}$ between the correlated signals. T_{cc} is referred to as the correlation time and the proportionality k_{tprf} is referred to as the correlation time factor. The correlation time factor is, thus, a representation of how many directional signals are bypassed before the correlation is performed. All indices equal to $i+1$ in all previous equations for both velocity and angle estimation must then be substituted by $i + k_{\text{tprf}}$, and, e.g., (5) is then written as

$$R_i(\xi_{x'}) = \int_X g_i(x')\, g_{i+k_{\text{tprf}}}(x' + \xi_{x'})dx', \quad i = 1 \ldots N_{xc}, \tag{23}$$

where g_i is the i'th directional signal. Considering the angle estimator, the same dependency on the choice of k_{tprf} applies, and it appears to be an important parameter which affects performance radically, and the optimal value varies with the flow angle. This will be discussed in more detail in Section IV. The results presented here are all produced with a fixed value for velocity estimation and a fixed value for angle estimation, if nothing else is noticed.

The consequence of using a wrong beam-to-flow angle is different in conventional velocity estimation [1], [2] than with the directional beamforming approach proposed in this paper. With the conventional velocity estimation approach, the estimate available is the velocity projected along the ultrasound beam direction, and this estimate must, thus, be compensated with the beam-to-flow angle to obtain the correct velocity amplitude along the flow. If the angle estimate is not correct, a bias will occur in the velocity estimate. The bias will increase for the same absolute angle estimation error as the true flow angle increases toward 90°. This can be seen from the expression of the relative change in velocity estimate

$$\frac{\Delta v}{v} = \frac{\cos(\phi)}{\cos\left(\hat{\phi}\right)} - 1. \tag{24}$$

With the velocity estimation approach suggested in this paper, the beam-to-flow angle estimate is used for beamforming the focus lines, and the consequence on the velocity bias is related only to the cosine relation between the true angle and the estimated angle. In Fig. 3, the relative change in velocity estimate is shown as a function of beam-to-flow estimation error for both velocity estimation approaches, with angle errors of ±10° assuming velocity projection. For the conventional approach, the relative change is shown for $\theta = 45°$ and $\theta = 60°$.

IV. Results

In Section IV-A and Section IV-B, the results from simulations and measurements are presented. The emphasis is placed on the velocity vector angle estimation algorithm. All results are obtained at tube angles of $\theta = \{45°, 60°, 75°, 90°\}$ and the angle estimation is performed at the vessel center. Furthermore, a study of performance as a function of the parameters N_{xc} and k_{tprf} is presented. Some of the parameters and processing involved in calculating and presenting the estimation results are described below.

A number N_{xc} of directional lines are cross-correlated for each velocity profile estimate and angle estimate. Echo cancellation is performed by subtracting the mean value of the directional signals used for the estimation.

Specifically for the velocity profile estimation, discrimination between flow and stationary signal is necessary to remove estimates that are based primarily on noise. This rejection scheme is based on the ratio $E_r(z_k)$ between the energy of the directional signals after echo cancellation E_{ec} and before echo cancellation E:

$$E_r(z_k) = \frac{E_{\text{ec}}}{E} = \frac{\sum_{i=1}^{N_{\text{pe}}} \sum_{j=1}^{N_g} g_{i_{\text{ec}}}^2(j, z_k)}{\sum_{i=1}^{N_{\text{pe}}} \sum_{j=1}^{N_g} g_i^2(j, z_k)}, \tag{25}$$

where N_g is the number of samples in the directional signals, N_{pe} is the number of pulse-echo lines used for the estimate, and z_k is the discrete index proportional to the depth. A purely stationary target will yield noise only after echo cancelling, and the ratio will, thus, be low; a proper threshold value is therefore selected for the discrimination.

The results presented are quantified by calculating bias, standard deviations, and probabilities. The velocity profile for a parabolic laminar flow can be described as [2]

$$v(r) = v_0 \left(1 - \left(\frac{r}{R}\right)^2\right), \tag{26}$$

where R is the tube radius, v_0 is the maximum velocity attained at the center of the tube, and r is the radial distance from the center of the tube. This is the profile used in the simulated flow, and it is used as reference when calculating the velocity estimation performance in the experimental measurements. The bias and standard deviation are calculated over the profile as a function of depth:

$$\begin{aligned} B_{\text{est}}(z_k) &= \overline{\hat{v}}(z_k) - v(z_k), \\ \sigma_{\text{est}}(z_k) &= \sqrt{\frac{1}{N_{\text{est}} - 1} \sum_{i=1}^{N_{\text{est}}} \left(\hat{v}_i(z_k) - \overline{\hat{v}}(z_k)\right)^2}, \end{aligned} \tag{27}$$

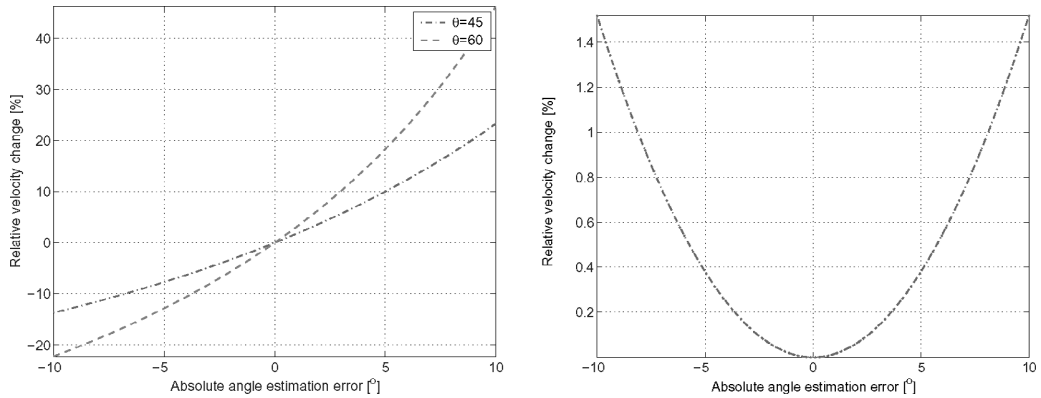

Fig. 3. Velocity estimation error due to a wrong beam-to-flow angle estimate: conventional velocity estimation approach for two different flow directions (left); directional velocity estimation approach (right).

where z_k is the discrete depth where the directional signals are obtained, N_{est} is the total number of velocity profile estimates, $v(z_k)$ is the true profile, and $\overline{\hat{v}}(z_k)$ is the mean profile estimate. From the bias profile $B_{\text{est}}(z_k)$ and standard deviation profile $\sigma_{\text{est}}(z_k)$, the relative mean bias and the relative mean standard deviation are calculated for the whole profile as

$$B_{\text{rel}} = \frac{1}{v_0 \cdot N_{\text{lines}}} \sum_{z_k} B_{\text{est}}(z_k),$$
$$\sigma_{\text{rel}} = \frac{1}{v_0} \sqrt{\frac{1}{N_{\text{lines}}} \sum_{z_k} \sigma^2_{\text{est}}(z_k)}, \tag{28}$$

where N_{lines} is the number of directional lines, or the number of velocity estimates in one profile.

Since the kernel of the angle estimation algorithm is the cross-correlation, there is a risk of having estimates that are based on erroneous peaks. These estimates can take values much different from the true angle. If no attention is made to these outlier estimates, the bias and the standard deviation of all estimates will be highly influenced by these and will not represent the performance properly. When angle estimates in some form of blood flow imaging are visualized, a few false estimates in a group of almost correct estimates can easily be handled by the human eye. As a consequence of these aspects, the angle estimates are divided into two groups: one group with estimates that are within a specified acceptable deviation θ_{dev} from the true angle, and one group with the complementary estimates, which are considered outliers. A probability of having a continuous estimate $\hat{\theta}$ within θ_{dev} from the true angle is calculated as

$$P_{\text{ok}} = P(\theta - \theta_{\text{dev}} \leq \hat{\theta} \leq \theta + \theta_{\text{dev}}),$$

where $\theta_{\text{dev}} = 15°$ by choice. All estimates outside this range are considered outliers. The bias B_{est} and standard deviation σ_{est} are calculated based on that subset of estimates only, which are within θ_{dev} from the true angle:

$$B_{\text{est}} = \overline{\hat{\theta}} - \theta,$$
$$\sigma_{\text{est}} = \sqrt{\frac{1}{N_{\text{sub}} - 1} \sum_{i=1}^{N_{\text{sub}}} \left(\hat{\theta}_i - \overline{\hat{\theta}}\right)^2}, \tag{29}$$

where N_{sub} is the number of estimates in the subset, and $\overline{\hat{\theta}}$ is the mean estimate within the subset.

TABLE I
DEFAULT PARAMETERS FOR THE VELOCITY PROFILE AND ANGLE ESTIMATION ALGORITHM.

Spatial sampling interval for directional signals	$\lambda/10$
Spatial extent of directional signals (correlation interval)	$-10\lambda : 10\lambda$
Number of correlations for each estimate $\theta = \{45°, 60°, 75°, 90°\}$	{10, 10, 10, 20}
Angular distance between directional lines for angle estimation	5°
Correlation time factor k_{tprf} for angle estimation	8
Position of angle estimate	Center of vessel
Velocity search range	1 m/s
Correlation time factor k_{tprf} for velocity estimation	2

The default parameters for velocity and angle estimation are found in Table I.

In Section III two different ways of quantifying the correlation between the directional signals were described. One was to use the normalized amplitude from the cross-correlation, and the other was to use the correlation coefficient. All angle estimation results presented here are produced with the correlation coefficient for the correlation function if nothing else is noticed. A complete comparison study of the performance with the two different quantifiers has not been made, but examples of the differences will be given in Section IV-B,3.

TABLE II
DEFAULT PARAMETERS USED IN ALL SIMULATIONS.

Number of transmit elements	128
Number of receive elements	128
Transducer center frequency	7 MHz
Pitch of transducer element	0.208 mm
Height of transducer element	4.5 mm
Kerf	0.035 mm
Assumed speed of sound	1540 m/s
Transmit apodization	Hanning
Receive apodization	Rectangular (none)
Excitation pulse	1-period sinusoid
Pulse repetition frequency	10 kHz
RF sampling frequency	100 MHz
Radius of vessel	10 mm
Distance to vessel center	40 mm
Transmit focus	80 mm
Peak velocity in flow, v_0	0.3 m/s

TABLE III
VELOCITY PROFILE ESTIMATES FROM FIELD II SIMULATIONS.*

θ	Relative mean bias [%]	Relative mean standard deviation [%]	Estimates in profile
45°	0.4	0.7	29
60°	1.2	1.0	29
75°	3.5	1.8	27
90°	−3.6	7.7	27

*Results are calculated from estimates inside the vessel only.

A. Simulation Results Using Field II

The main purpose of the simulations is to verify the functionality of the algorithms, and to evaluate how good the performance can get under favorable conditions. In Field II the conditions are ideal, and the simulation results are obtained from acquired data free from noise. The velocity and angle estimates are estimated from the same simulated data, with transmit focus at twice the depth of the vessel center. The simulation results are presented similar to the measurement results, using the same parameters with a few exceptions. The default parameter values for the simulations are found in Table II.

1. Velocity Profile Estimation on Simulated Data: The results are based on 1000 pulse-echo signals which lead to 165 and 89 profile estimates for the beam-to-flow angles of 45° to 75° and 90°, respectively. The profiles are calculated using the flow/stationary rejection scheme, and the beam-to-flow angle is assumed known.

The mean velocity profile and an indication of the deviation from this mean profile are illustrated in Fig. 4 for all four flow angles. The performance is calculated from the estimates inside the vessel only and can be found in Table III. Both the bias and the standard deviation increase with flow angle, and the standard deviation for transverse flow is noticeable larger than for the other angles.

TABLE IV
RESULT OF ANGLE ESTIMATION FROM SIMULATION IN FIELD II.

Flow angle, θ	Probability, P_{ok}	Bias, B_{est}	Standard deviation σ_{est}
45°	100%	−0.6°	2.9°
60°	100%	−1.5°	2.2°
75°	97%	−4.9°	2.8°
90°	89%	0.3°	0.7°

TABLE V
RESULT OF ANGLE ESTIMATION FROM SIMULATIONS WITH OPTIMAL VALUES OF THE CORRELATION TIME k_{TPRF}.

Flow angle, θ	k_{tprf}	Probability, P_{ok}	Bias, B_{est}	Standard deviation, σ_{est}
45°	18	100%	−0.4°	1.9°
60°	18	100%	−0.9°	1.7°
75°	18	100%	−1.0°	0.4°
90°	6	100%	0.4°	0.9°

2. Angle Estimation on Simulated Data: The simulation results in this section are based on the default simulation parameters from Table II and the default angle estimation parameters from Table I.

The results are based on 1000 pulse-echo acquisitions which lead to 110 and 70 angle estimates for the beam-to-flow angles 45°, 60°, 75°, and 90°, respectively. The performance is shown in Table IV.

The performance decreases as the flow angle increases from $\theta = 45°$ to $\theta = 90°$. At $\theta = 90°$ there are dominant secondary peaks at the correlation function which divides the estimates into a few groups, giving relatively many outliers at specific angles. However, those estimates that are within the acceptable deviation have a low bias and standard deviation. It should be emphasized that this performance dependency on flow angle is different with another choice of correlation time factor k_{tprf}. Since the choice of k_{tprf} has a strong influence on performance, a study of this influence is performed and described in Section IV-B,3, based on measured data. A similar study is performed on simulated data with values of k_{tprf} from 2 to 18 to find those values which optimize the performance for flow angles of $\theta = \{45°, 60°, 75°, 90°\}$. The results of the angle estimation with these optimal values are shown in Table V with the only purpose of illustrating the absolute potential of the method under favorable conditions.

B. Experimental Measurements

This section describes the measurement setup and presents the angle estimation results from the experiments.

1. Measurement Setup: The experimental ultrasound scanner RASMUS [15] and a 7-MHz linear array trans-

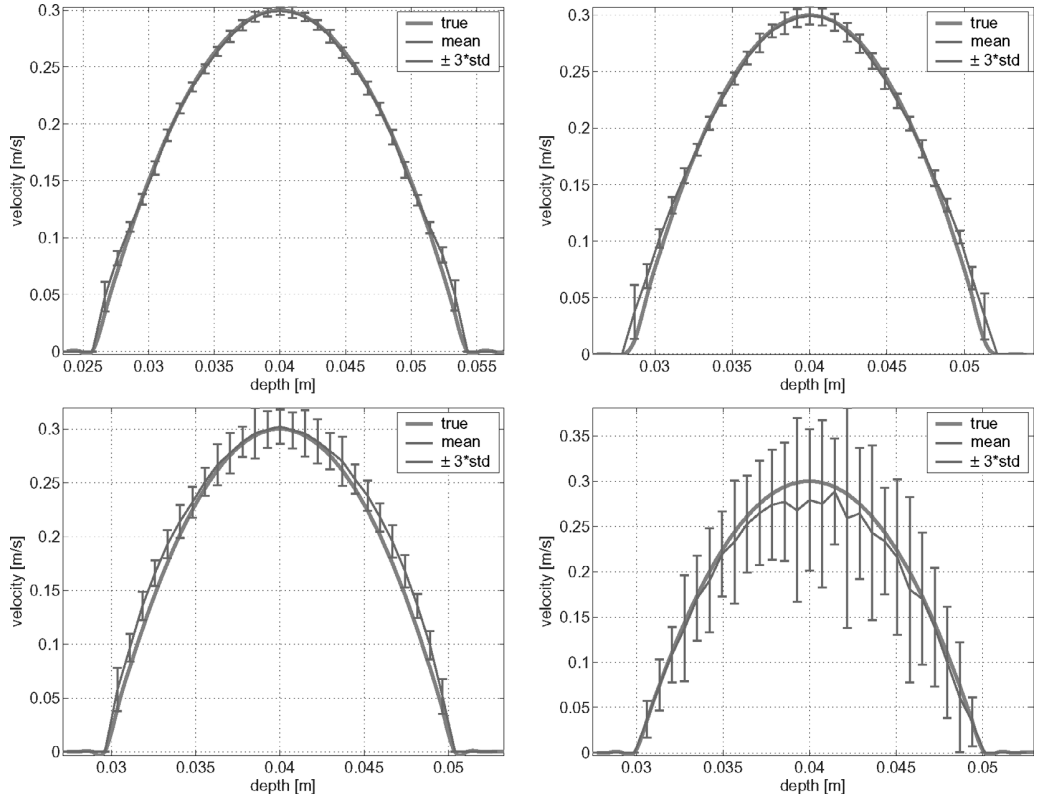

Fig. 4. Velocity profile estimation from simulations in Field II: mean profile and standard deviation of profile estimates. Flow/stationary rejection scheme is used. $\theta = 45°$ (upper left), $\theta = 60°$ (upper right), $\theta = 75°$ (lower left), $\theta = 90°$ (lower right).

ducer, type 8804, from B-K Medical (DK-2730 Herlev, Denmark), are used for all measurements. The system acquires RF data from the individual transducer channels and these data are transferred to a PC, where they are saved and processed off-line. The RASMUS system contains 128 transmitting channels and 64 receiving channels with a 40-MHz sampling frequency, and has 12-bit resolution for each individual channel. With the built-in 2-to-1 multiplexer, the system can cover 128 individual receive channels in two receptions.

All measurements are made using a circulating flow rig with a blood-mimicking fluid. A pump is connected to a steel tube of approximately 1 m, which enters a water tank; there the steel tube enters another tube made of heat shrink, which mimics a blood vessel. This tube is connected to a similar steel tube before it exits the water tank. Inside the water tank a fixture for the transducer is inserted. The angle of the transducer and the distance to the tube can be adjusted. The distance from the center element of the transducer to the tube is the same regardless of the angle. The measurements are obtained at the angles 45°, 60°, 75°, and 90°, where 90° corresponds to a transverse flow measurement.

The measurement setup consists of a blood-mimicking fluid and a PC-controlled pump (CompuFlow1000, Shelley Medical Imaging Technologies, London, Ontario, Canada) [16]. In CompuFlow1000 a piston is moved and maintains a constant flow for a period of time. The reference velocity is based solely on volume flow input to the control PC. Inaccuracy in the control system and the loss throughout the flow rig system will contribute to a bias in the estimate. For all measurements, a number of parameters has been fixed and these are found in Table VI.

TABLE VI
DEFAULT MEASUREMENT PARAMETERS USED FOR ALL MEASUREMENTS.

Number of transmit elements	128
Number of receive elements	64/128 (combined)
Pitch of transducer element	0.208 mm
Height of transducer element	4.5 mm
Kerf	0.035 mm
Transmit apodization	Hanning
Receive apodization	Rectangular (none)
Excitation pulse	2-cycle sinusoid
Pulse repetition frequency	10 kHz/5 kHz (combined)
RF sampling frequency	40 MHz
Transducer center frequency	7 MHz
Assumed speed of sound	1480 m/s
Radius of vessel	6.4 mm
Distance to vessel center	37 mm
Peak velocity in flow	≈ 0.3 m/s

The system is capable of receiving data from 64 channels simultaneously. By use of the built-in 2-to-1 multiplexer, the system can receive data from 128 channels in 2 emissions. For the odd-numbered emissions the first 64 channels of the transducer are used in receive, and for the

TABLE VII
CHANNELS USED IN RECEIVE MODE.

Emission number	1	2	3	4	5	6	...	N_{shots}
Receive channels	1:64	65:128	1:64	65:128	1:64	65:128	...	

TABLE VIII
EXCEPTION FROM THE DEFAULT PARAMETERS OF TABLE I USED FOR ANGLE ESTIMATION ON MEASURED DATA.

Number of correlations for each estimate $\theta = \{45°, 60°, 75°, 90°\}$	{20, 20, 20, 20}

TABLE IX
RESULT OF ANGLE ESTIMATION FROM MEASUREMENTS USING THE CORRELATION COEFFICIENT FOR THE CORRELATION FUNCTION.

Flow angle, θ	Probability, P_{ok}	Bias, B_{est}	Standard deviation, σ_{est}
45°	62%	−1.5°	8.1°
60°	95%	−2.8°	4.3°
75°	98%	−2.0°	2.0°
90°	68%	0.4°	1.0°

even-numbered emissions the last 64 channels are used, as shown in Table VII.

The first 128-channel combined data matrix C_1 are available after the 2nd emission by simply putting together the data from the emission 1, d_1 and data from emission 2, d_2. The second 128-channel data matrix C_2 is available after the 3rd emission by putting together d_3 and d_2. The list of 128-channel combined data $\mathbf{C}$ can thus be written as

$$\begin{aligned}\mathbf{C} &= \{C_1, C_2, C_3, \ldots, C_{N_{\text{shots}}-1}\} \\ &= \{[d_1, d_2], [d_3, d_2], [d_3, d_4], [d_5, d_4], [d_5, d_6], \ldots, \\ &\quad [d_{N_{\text{shots}}-1}, d_{N_{\text{shots}}}]\}.\end{aligned}$$

Notice that the even-numbered combined data are obtained differently than the odd-numbered data. The cross-correlation of combined and beamformed signals should, thus, be done only between even-numbered or odd-numbered C-data.

2. Angle Estimation on Measured Data: The results in this section are based on the default parameters from Table I and the exception in Table VIII. Three thousand pulse-echo acquisitions are processed, which leads to 213 angle estimates.

The estimation performance is found in Fig. 5 for the four different flow angles. They show the probability P_{ok} and the distribution of those continuous estimates that are not classified as outliers. A summary of the quantized performance can be found in Table IX. The performance at $\theta = 45°$ is radically worse than at the other angles. Velocity profile estimates have been calculated based on the same acquisition data, and here there was a similar decrease in performance. One thing to notice about the measurement setup is that there is a relatively large difference in physical position of the transducer for the different tube angles. The distance from the center element to the tube is the same regardless of the angle, but for $\theta = 45°$ the transducer element in one end is very close to the tube, which could have a negative effect in form of re-reflections. Re-reflections inside the water tank can also have some influence on the results, and this will also vary with the angle of the transducer. Another thing to notice is that the simulation did not show any decrease in performance for $\theta = 45°$ compared to the other angles.

The correlation function is the basis of the angle estimation. The correlation functions for all estimates are superimposed for a given flow angle in Fig. 6. This figure shows how certain or reliable the estimates are. The shape of the correlation function and specifically the amplitude distribution and the position of the peaks are interesting. From this figure it is also evident that the performance for $\theta = 45°$ is worse than at the other angles. At the other angles the peak around the true angle is much more distinct and the coefficient attenuates faster as ϕ moves away from the true angle. For $\theta = 90°$ there are two dominant peaks adjacent to the peak at $\theta = 90°$. This shape is consistent with the lower-left histogram in Fig. 5 where the estimates are divided into one dominant group around $\theta = 90°$ and two minor groups around $\theta = 65°$ and $\theta = 115°$, which was also the case with the simulated data.

3. Angle Estimation Parameter Study: In this section, studies of performance as a function of k_{tprf} and N_{xc} are carried out. The study of k_{tprf} will be done with $N_{xc} = 20$ and the study of N_{xc} with $k_{\text{tprf}} = 8$ for all flow angles.

The angle estimation results in Section IV-B,2 were all produced with a fixed value of k_{tprf}, and the study in this section will show how different values affect performance. In Fig. 7, the study of k_{tprf} for all flow angles is shown. In each figure, P_{ok} is plotted as a function of k_{tprf}, and so are the bias b_{est} and the standard deviation σ_{est}. It is evident from these figures that the choice of k_{tprf} has a strong influence on performance and that the optimal value varies with the flow angle. The optimal value is in some degree a subjective choice of whether to optimize P_{ok}, b_{est}, or σ_{est}, but desirable values for the given data set for $\theta = \{45°, 60°, 75°, 90°\}$ are $k_{\text{tprf}} = \{18, 18, 20, 4\}$. For the angles $\theta = \{45°, 60°, 75°\}$ the estimation benefits from having a high value quite contrary to the case for $\theta = 90°$, where a low value is preferable. This is likely due to the low lateral oscillation of the field and the fast de-correlation at the true angle, when increasing the correlation time. However, these chosen values can be considered optimal only for the

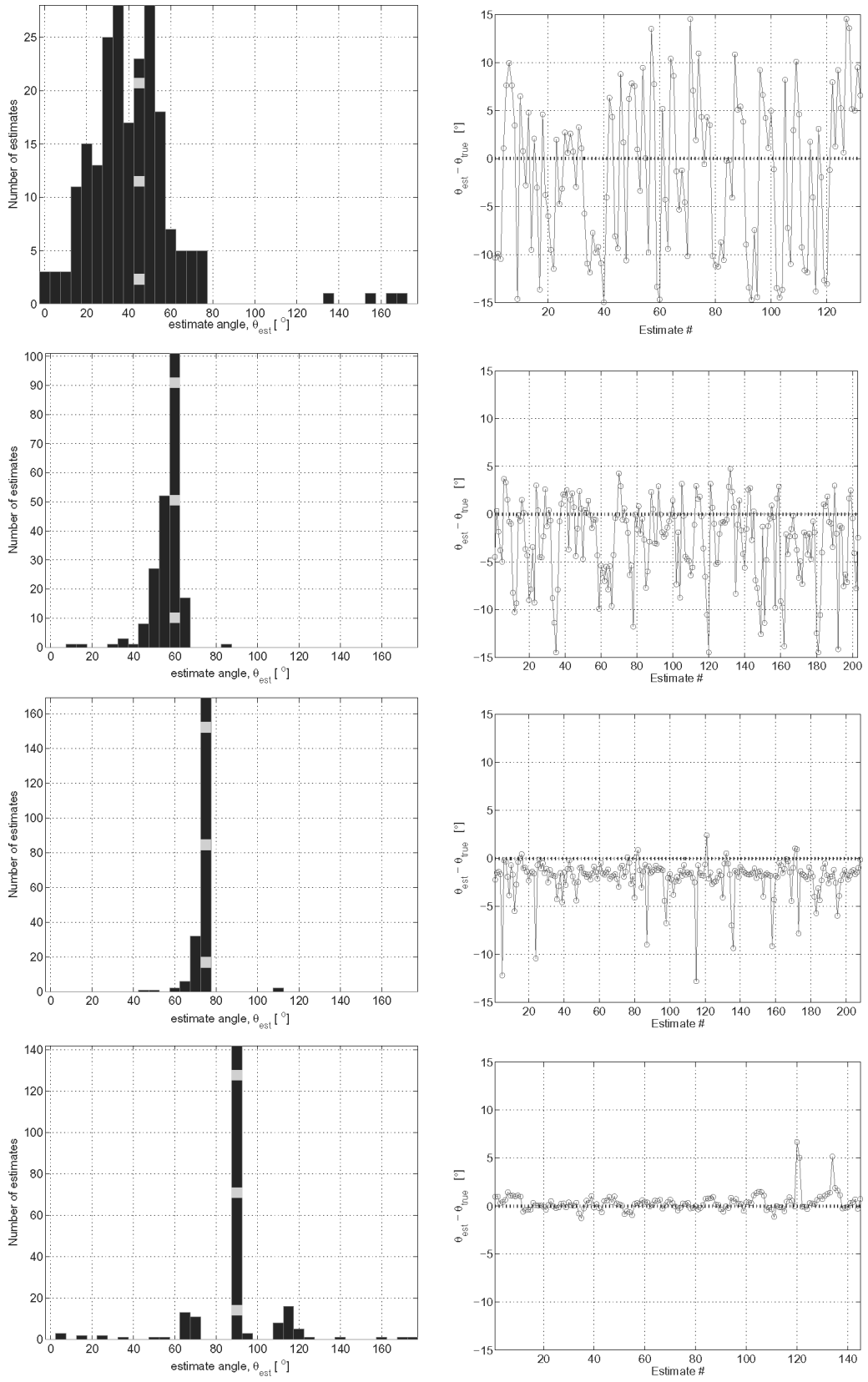

Fig. 5. Angle estimation from measurements for $\theta = 45°$, $60°$, $75°$, and $90°$: a histogram of the discrete estimates (left); deviation between accepted continuous estimates and the true angle (right).

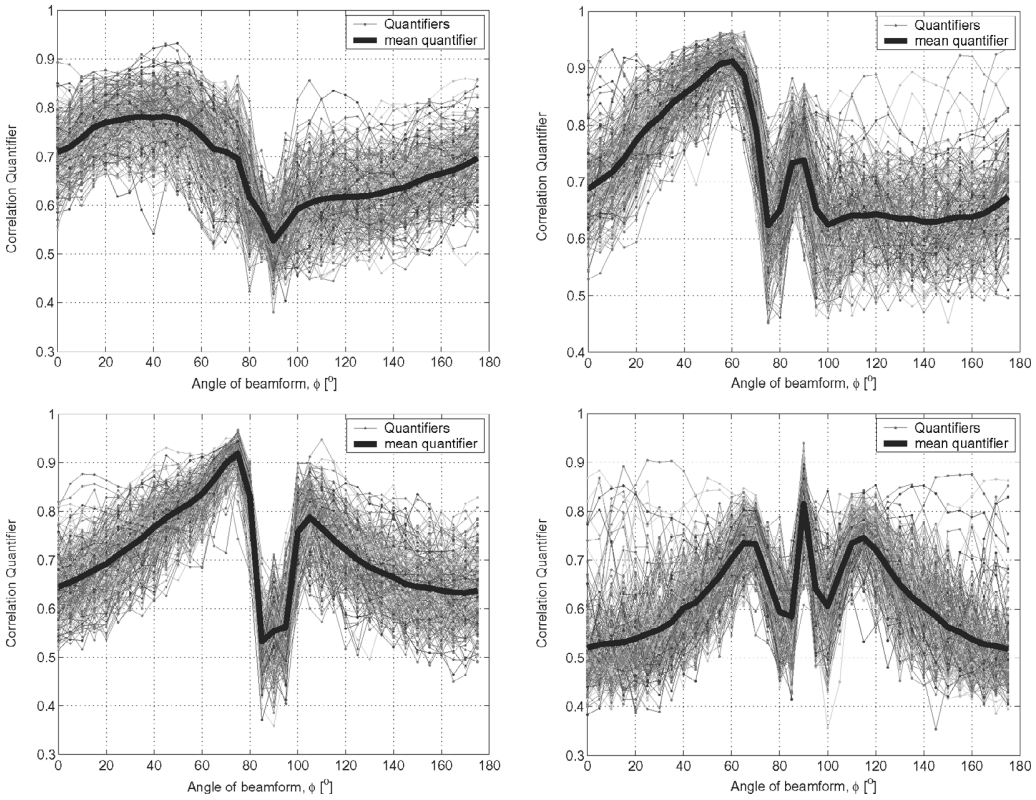

Fig. 6. Angle Estimation: coefficient functions for all estimates are superimposed for $\theta = 45°$ (upper left), $\theta = 60°$ (upper right), $\theta = 75°$ (lower left), and $\theta = 90°$ (lower right).

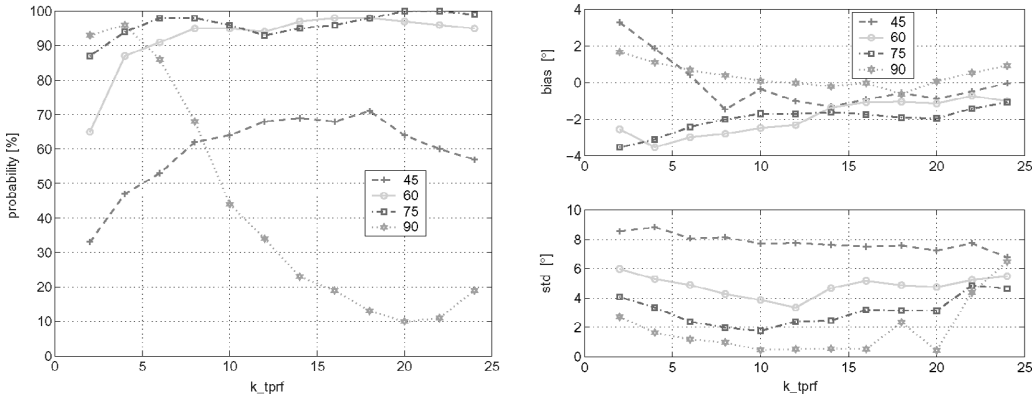

Fig. 7. Performance as a function of k_{tprf} for $\theta = 45°$, 60°, 75°, and 90°: probability of having an estimate within ±15° from the true angle (left); bias B_{est} and standard deviation σ_{est} of that subset of continuous estimates that are within ±15° from the true angle (right).

data used in the parameter study. Using another set of data with a different flow velocity or different signal-to-noise ratio, the set of optimal values would likely be different. The angle estimation performance with $k_{\mathrm{tprf}} = \{18, 18, 20, 4\}$ is shown in Table X to illustrate the performance under favorable conditions.

The same parameter study on k_{tprf} has been done using the correlation function based on finding the peak amplitude of the averaged cross-correlation function, as described in Section III. From this study the conclusion on desirable values of k_{tprf} is unchanged, and a plot show-

TABLE X
RESULT OF ANGLE ESTIMATION FROM MEASUREMENTS WITH OPTIMAL VALUES OF THE CORRELATION TIME k_{TPRF}.

Flow angle, θ	k_{tprf}	Probability, P_{ok}	Bias, B_{est}	Standard deviation, σ_{est}
45°	18	71%	−0.6°	7.6°
60°	18	98%	−1.1°	4.9°
75°	20	100%	−2.0°	3.1°
90°	4	96%	1.1°	1.6°

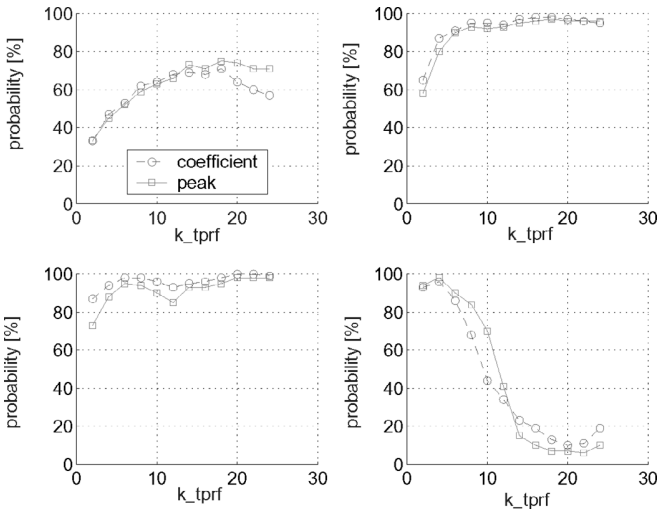

Fig. 8. Performance as a function of k_{tprf} with two different types of correlation functions for $\theta = 45°$ (upper left), $\theta = 60°$ (upper right), $\theta = 75°$ (lower left), and $\theta = 90°$ (lower right). Probability of having an estimate within $\pm 15°$ from the true angle.

TABLE XI
RESULT OF ANGLE ESTIMATION FROM MEASUREMENTS USING THE CROSS-CORRELATION PEAK AMPLITUDE FOR THE CORRELATION FUNCTION.

Flow angle, θ	Probability, P_{ok}	Bias, B_{est}	Standard deviation, σ_{est}
45°	59%	−1.6°	7.7°
60°	93%	−3.9°	4.7°
75°	94%	−2.5°	2.3°
90°	84%	0.8°	1.4°

ing P_{ok} as a function of k_{tprf} for both types of correlation functions is shown in Fig. 8.

The result of the angle estimation using the peak correlation for the correlation function and $k_{\text{tprf}} = 8$, just as in Table IX and Fig. 5 is shown in Table XI. Only small differences exist when comparing Table IX with Table XI and when observing Fig. 8. The benefits of using the correlation coefficient over the correlation peak amplitude is, thus, questionable when the additional computational task is considered.

If the time in between consecutive directional signals used for the cross-correlation is very small, the two directional signals will be very similar. As stated in Section III, the distribution of scatterers making up the second of the two directional signals is basically the same as the distribution making up the first directional signal. This is due to the extent of the point-spread function. There is a high correlation between the signals also, if they are obtained at an angle different from the flow angle. At some point, the time in between the signals is so large that the physical movement of the scatterers is on the order of the extent of the point-spread function. The signals obtained at angles different from the flow angle will, thus, have a very low correlation because of different scatter distributions. The signals obtained at the flow angle do not have this problem, and the main contribution to the de-correlation is the shift. This is where the optimal value for the correlation time is found, namely, where there is a large difference between the correlation at the flow angle and the other angles, which makes it possible to discriminate. Further time increase will merely result in further de-correlation of the signals at the flow angle, and since the signals at the other angles at this point are almost completely uncorrelated, the discrimination will be more difficult. To illustrate this, the mean correlation function as a function of k_{tprf} is shown in Fig. 9 for all flow angles. There is a general decrease in correlation with increasing values of k_{tprf}, as expected, and the decrease rate is stronger at angles different from the true angle. For $\theta = 90°$ the decrease rate at the true angle relative to the other search angles is stronger than for $\theta = 45°$, 60°, and 75°. This is in agreement with the lower desirable value of k_{tprf} for $\theta = 90°$ than for $\theta = 45°$, 60°, and 75° found previously.

If the flow is stationary, the estimate will improve from averaging over a number of correlations N_{xc}, and the improvement will increase with a broader averaging. The study of performance as a function of N_{xc} is still interesting, though, since it will show the relation between the performance and the necessary computational task. This study is presented in the same way as the above study of k_{tprf} and with $k_{\text{tprf}} = 8$, just as for the results in Table IX and Fig. 5. The results from all flow angles are shown in Fig. 10. With attention to the results for $\theta = 60°$, 75°, and 90°, it seems possible to decrease the number of outliers radically until P_{ok} reaches approximately 90%, where further increase of N_{xc} has only little effect.

V. CONCLUSION

When focusing along the velocity direction is used for velocity estimation, the velocity profile estimates from simulations have relative mean standard deviations between 0.7% and 7.7% for flow between 45° and 90°. The simulation study and measurement study both showed that angle estimation by directional beamforming can be estimated with a high precision, potentially yielding velocity estimates with a better accuracy. The angle estimation performance is strongly influenced by the choice of correlation time, and a proper choice varies with flow angle and will vary with flow velocity amplitude, though the latter is not shown in this paper. Flow angles of $\theta = \{45°, 60°, 75°\}$ require a high value of the correlation time whereas for $\theta = 90°$ a low value is required. By using the optimal choice of correlation time for the different flow angles based on a parameter study, the potential of the method has been revealed. With these favorable conditions the simulations produced 100% valid estimates (no outliers) and a bias and standard deviation below 2° for all flow angles. Using the measurements, more than 96% valid estimates

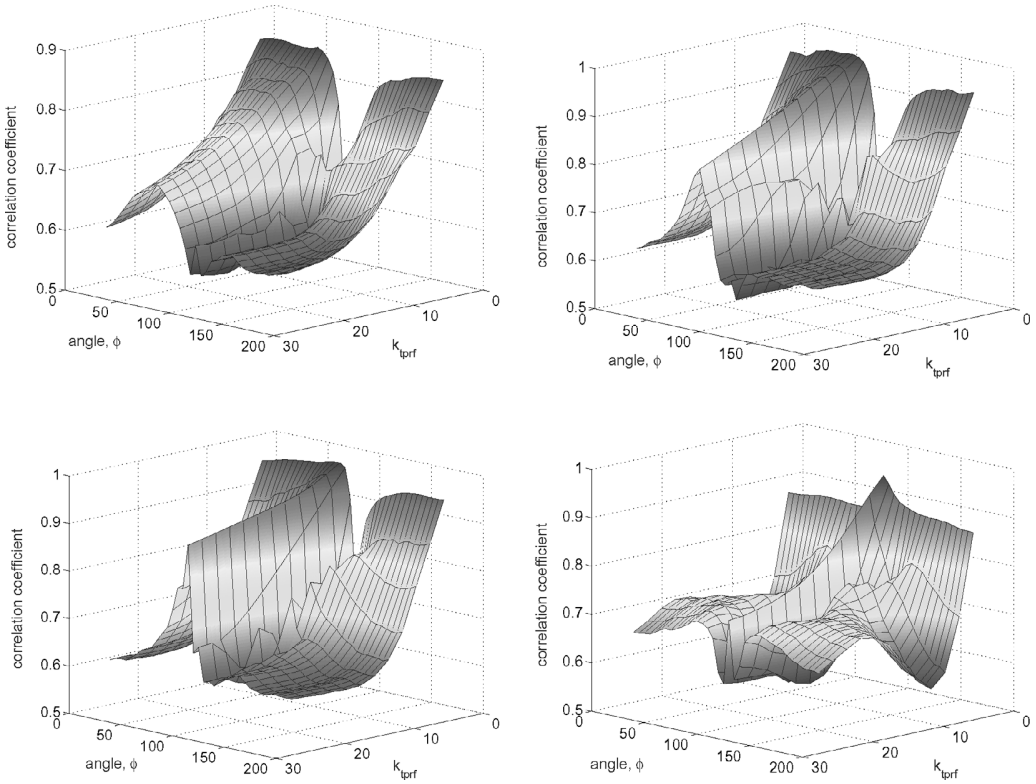

Fig. 9. Mean correlation function as a function of k_{tprf} for $\theta = 45°$ (upper left), $\theta = 60°$ (upper right), $\theta = 75°$ (lower left), and $\theta = 90°$ (lower right).

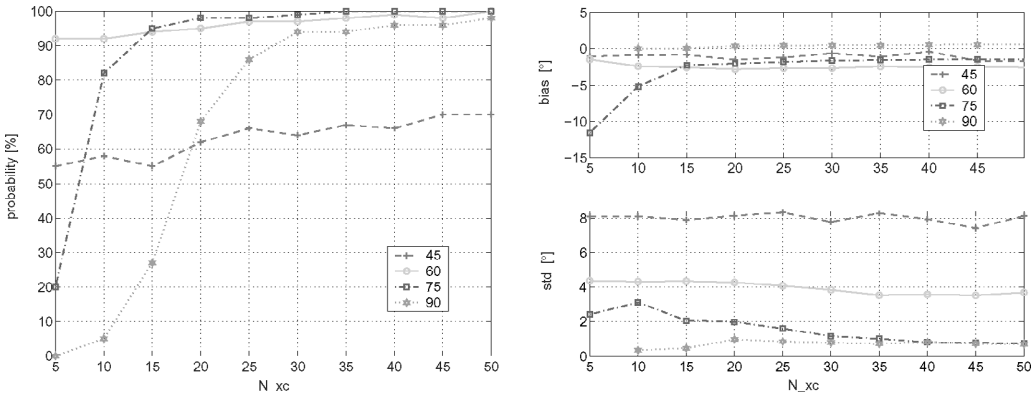

Fig. 10. Performance as a function of N_{xc} for $\theta = 45°$, 60°, 75°, and 90°: probability of having estimates within ±15° from the true angle (left); bias B_{est} and standard deviation σ_{est} of that subset of estimates that are within ±15° from the true angle (right).

were produced for the flow angles $\theta = \{60°, 75°, 90°\}$ and with a bias below 2° and a standard deviation below 5°. The techniques used are based on an assumption of a laminar flow. A turbulent flow will evidently complicate matters of angle estimation and can be a topic of future investigations.

References

[1] D. H. Evans, W. N. McDicken, R. Skidmore, and J. P. Woodcock, *Dopper Ultrasound, Physics, Instrumentation, and Clinical Applications*. New York: John Wiley & Sons, 1989.

[2] J. A. Jensen, *Estimation of Blood Velocities Using Ultrasound: A Signal Processing Approach*. New York: Cambridge University Press, 1996.

[3] C. Kasai, K. Namekawa, A. Koyano, and R. Omoto, "Real-time two-dimensional blood flow imaging using an autocorrelation technique," *IEEE Trans. Sonics Ultrason.*, vol. 32, pp. 458–463, 1985.

[4] S. G. Foster, "A pulsed ultrasonic flowmeter employing time domain methods," Ph.D. dissertation, Department of Electrical Engineering, University of Illinois, Urbana, IL, 1985.

[5] O. Bonnefous and P. Pesqué, "Time domain formulation of pulse-Doppler ultrasound and blood velocity estimation by cross correlation," *Ultrason. Imag.*, vol. 8, pp. 73–85, 1986.

[6] M. D. Fox, "Multiple cross-beam ultrasound Doppler velocimetry," *IEEE Trans. Sonics Ultrason.*, vol. SU-25, pp. 281–286,

1978.
[7] G. E. Trahey, J. W. Allison, and O. T. von Ramm, "Angle independent ultrasonic detection of blood flow," *IEEE Trans. Biomed. Eng.*, vol. BME-34, pp. 965–967, 1987.
[8] J. A. Jensen and P. Munk, "A new method for estimation of velocity vectors," *IEEE Trans. Ultrason., Ferroelect., Freq. Contr.*, vol. 45, pp. 837–851, 1998.
[9] M. E. Anderson, "Multi-dimensional velocity estimation with ultrasound using spatial quadrature," *IEEE Trans. Ultrason., Ferroelect., Freq. Contr.*, vol. 45, pp. 852–861, 1998.
[10] H. F. Routh, T. L. Pusateri, and D. D. Waters, "Preliminary studies into high velocity transverse blood flow measurement," in *Proc. IEEE Ultrason. Symp.*, 1990, pp. 1523–1526.
[11] V. L. Newhouse, D. Censor, T. Vontz, J. A. Cisneros, and B. B. Goldberg, "Ultrasound Doppler probing of flow transverse with respect to beam axis," *IEEE Trans. Biomed. Eng.*, vol. BME-34, pp. 779–788, 1987.
[12] J. A. Jensen, "Directional velocity estimation using focusing along the flow direction: I. Theory and simulation," *IEEE Trans. Ultrason., Ferroelect., Freq. Contr.*, vol. 50, pp. 857–872, 2003.
[13] J. A. Jensen and R. Bjerngaard, "Directional velocity estimation using focusing along the flow direction: II. Experimental investigation," *IEEE Trans. Ultrason., Ferroelect., Freq. Contr.*, vol. 50, pp. 873–880, 2003.
[14] J. A. Jensen, "Velocity vector estimation in synthetic aperture flow and B-mode imaging," in *Proc. IEEE Int. Symp. Biomed. Imag. Nano to Macro*, vol. 1, 2004, pp. 32–35.
[15] J. A. Jensen, O. Holm, L. J. Jensen, H. Bendsen, S. I. Nikolov, B. G. Tomov, P. Munk, M. Hansen, K. Salomonsen, J. Hansen, K. Gormsen, H. M. Pedersen, and K. L. Gammelmark, "Ultrasound research scanner for real-time synthetic aperture image acquisition," *IEEE Trans. Ultrason., Ferroelect., Freq. Contr.*, vol. 52, no. 5, pp. 881–891, May 2005.
[16] K. V. Ramnarine, D. K. Nassiri, P. R. Hoskins, and J. Lubbers, "Validation of a new blood mimicking fluid for use in Doppler flow test objects," *Ultrasound Med. Biol.*, vol. 24, pp. 451–459, 1998.

Jacob Kortbek earned his Bachelor of Science degree in electrical engineering in 1999. From 1999 until 2002 his was employed as a development engineer at Bang & Olufsen in Denmark. He received his Master of Science degree in electrical engineering in 2004 from the Technical University of Denmark and is currently employed as an industrial Ph.D. student at B-K Medical and Ørsted•DTU at the Technical University of Denmark doing research in synthetic aperture ultrasound imaging.

Jørgen Arendt Jensen (M'93–SM'02) earned his Master of Science degree in electrical engineering in 1985 and the Ph.D. degree in 1989, both from the Technical University of Denmark. He received the Dr.Techn. degree from the university in 1996. He has published a number of papers on signal processing and medical ultrasound and the book "Estimation of Blood Velocities Using Ultrasound", Cambridge University Press, in 1996. He is also the developer of the Field II simulation program. He has been a visiting scientist at Duke University, Stanford University, and the University of Illinois at Urbana-Champaign. He is currently a full professor of Biomedical Signal Processing at the Technical University of Denmark at Ørsted•DTU and head of the Center for Fast Ultrasound Imaging. He is also adjunct professor at the Faculty of Health Sciences, University of Copenhagen. He has given courses on blood velocity estimation at both Duke University and the University of Illinois and teaches biomedical signal processing and medical imaging at the Technical University of Denmark. He has given several short courses on simulation, synthetic aperture imaging, and flow estimation at international scientific conferences. He has received several awards for his research. He is also the co-organizer of a new biomedical engineering education offered by the Technical University of Denmark and the University of Copenhagen. His research is centered around simulation of ultrasound imaging, synthetic aperture imaging and blood flow estimation and constructing systems for such imaging.

B.4 Determination of Velocity Vector Angles using the Directional Cross-Correlation Method

This article was published in Journal *Proceedings - IEEE Ultrasonics Symposium*. Conference Title *2005 IEEE Ultrasonics Symposium Issue Vol.2 Page no. 1339-1343; September 2005.*

Determination of velocity vector angles using the directional cross-correlation method

Jacob Kortbek[1,2] and Jørgen Arendt Jensen[1]

1) Center for Fast Ultrasound Imaging, Ørsted•DTU,
Bldg. 348, Technical University of Denmark, DK-2800 Lyngby, Denmark.
2) B-K Medical, Mileparken 34, DK-2730 Herlev, Denmark.

***Abstract*— A method for determining both velocity magnitude and angle in any direction is suggested. The method uses focusing along the velocity direction and cross-correlation for finding the correct velocity magnitude. The angle is found from beamforming directional signals in a number of directions and then select the angle with the highest normalized correlation between directional signals. The approach is investigated using Field II simulations and data from the experimental ultrasound scanner RASMUS and with a parabolic flow having a peak velocity of 0.3 m/s. A 7 MHz linear array transducer is used with a normal transmission of a focused ultrasound field. The velocity profile estimates from simulations have relative mean standard deviations between 0.7% and 7.7% for flow between 45° and 90°. The angle estimation performance is highly dependent on the choice of the time $k_{tprf} \cdot T_{prf}$ (*correlation-time*) between signals to correlate, and a proper choice varies with flow angle and flow velocity. One performance example is given with a fixed value of k_{tprf} for all flow angles. The angle estimation on measured data for flow at 60° to 90°, yields a probability of valid estimates between 68% and 98% and with standard deviations between 1° and 4°. The optimal value of k_{tprf} for each flow angle is found from a parameter study to reveal the potential of the method and with these values the performance on simulated data yields angle estimates with no outlier estimates and with standard deviations below 2°.**

I. Introduction

Modern ultrasound systems can estimate the blood velocity in-vivo in real time [1], [2]. This is done by acquiring ultrasound signals from the same direction a number of times, and then correlate the signals. The shift in phase as a function of time can be determined using an autocorrelation estimator and this yields the velocity [3]. A second approach is to determine the shift in position using the cross-correlation function and dividing with the time between emissions [4], [5] gives the velocity. Both approaches only finds the shift along the ultrasound beam direction, and only the projected velocity along this direction is, thus, found. Velocities transverse to the beam are not detected, and velocities in different directions are not depicted correctly. There is, thus, a need for methods that can detect the correct velocity magnitude and direction as a function of spatial position.

Several authors have devised methods for estimating the correct velocity. Fox (1978) suggested using two crossing beams to have two independent measurements. Trahey and co-workers suggested using speckle tracking over a region of the image to tracke the motion in any direction. It has also been suggested to introduce a lateral oscillation, so that the phase shift in the lateral directions also can be found using a modified autocorrelation method [8], [9]. Several other methods have been suggested [10], [11], but none have so far yielded a satisfactory performance to be commercially implemented.

This paper suggest a method for determining the velocity vector. The velocity magnitude is determined by finding the motion along the velocity direction using cross-correlation of signals focused along the direction of the flow as suggested in [12], [13]. This can be done, if the correct direction is known which is currently found by inspecting the B-mode image, and then use this angle in the beam formation. This is cumbersome and difficult to use, if the beam-to-flow angle changes throughout the image. Using the directional beam forming approach, an angle estimation approach based on finding the direction of the maximum correlation is suggested in this paper. Directional signals for a number of directions are beam formed, and the direction with the highest correlation is then chosen as the angle estimate. The basics of the velocity estimation scheme is briefly described in Section II, and the angle estimation method is introduced in Section III. Investigations of the approach using simulations are given in Section IV-A and from measured data on a flow rig in Section IV-B.

II. Directional velocity estimation

In directional velocity estimation the beam formation is done along the flow direction, and the correct velocity amplitude can, thus, be found, also for a purely transverse direction [12]. The basic principle is to focus the responses received by the transducer along focus-lines in the flow direction, which is referred to as *directional signals* in the spatial domain. The spatial signals for two consecutive emissions are then cross-correlated and the shift between them is found. This is a shift in spatial position of the scatterers, and dividing by the time between emissions, thus, directly gives the velocity magnitude. Just as for the conventional systems the angle between the propagating direction of the emitted beam and the flow direction must be known before the beam formation can be done [12].

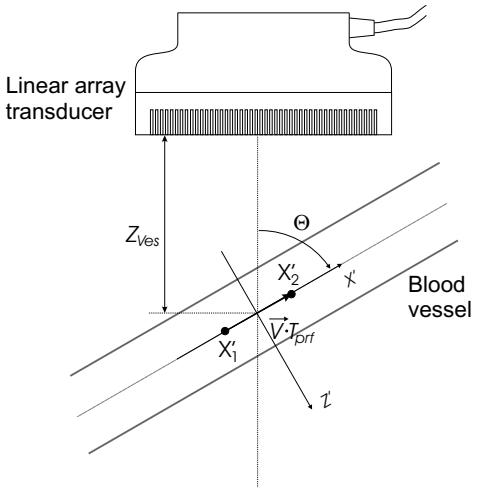

Fig. 1. Rotated coordinate system (x', z') oriented along the flow direction, and with origo at the center of the vessel at a distance Z_{ves} from the transducer.

III. Angle estimation

The spatial directional signals, g can e.g. be obtained by focusing the received responses in points along the flow direction as shown in Fig. 1. Directional signals obtained from two consecutive acquired responses properly aligned with the flow direction have a high correlation. The primary contribution to the de-correlation between the signals is the spatial shift due to the movement of the scatterers. In other words, the distribution of scatterers for the second directional signal is basically the same as the distribution for the first directional signal, except from the shift for a laminar flow. Now consider the case where the directional signals are not aligned along the flow direction. The distribution of the scatterers for the second directional signal is no longer just a shift in position of the previous scatterer distribution. The relative positions between the scatterers have changed, due to the different velocities for the different scatterers. The consequence is that the correlation between the two directional signals is reduced compared to the case of focusing along the flow direction. This change in correlation is the property used for the angle estimation. The method is, thus to obtain directional signals in a number of directions, and quantify the correlation between signals in each direction. From this procedure a *correlation-function* is constructed showing the normalized correlation as a function of search angle. The maximum of this function indicates the direction with the highest correlation between consecutive signals hence the direction of flow.

The normalized cross-correlation peak amplitude is a valid choice for the correlation-function. In this paper a slightly different approach is taken. The correlation between the directional signals is described using the *correlation coefficient*, ρ. Correlation is the degree to which two or more components are linearly associated and the statistical term is the covariance $\mathrm{cov}(x_1, x_2) = \langle (x_1 - \overline{x}_1)(x_2 - \overline{x}_2) \rangle$ between components, x_1 and x_2, and where $\langle\rangle$ is the expectation operator. The correlation coefficient is simply the covariance normalized with the product of the standard deviations of the two components, and is defined as

$$\rho = \frac{\mathrm{cov}(x_1, x_2)}{\sigma_{x_1}\sigma_{x_2}}\,, \tag{1}$$

where $\rho \in [-1, 1]$ and $\rho = 1$, corresponds to perfect linear relation or full correlation.

The strategy for the angle estimation involves two steps, when the correlation coefficient is used for the correlation-function. Before calculating the correlation coefficient the two directional signals, for which the correlation coefficient is needed, are aligned. Otherwise the correlation coefficient will be small even at the true angle due to the spatial shift from the movement of the scatterers. The alignment is determined from the discrete lag at the cross-correlation peak, l_p. To increase accuracy a 2^{nd} order polynomial is fitted around the peak [4] to find a new interpolated lag value, l_p^{int}. Due to the new continuous lag, the alignment operation involves another interpolation between the samples in one of the signals g_1 or g_2 using a first order linear interpolation. The correlation-function is, thus, defined as

$$\rho(\phi) = \sum_i \frac{\mathrm{cov}\left(g_i(x', \phi), g_{i+1}(x' - l_p^{int}, \phi)\right)}{\sigma_{g_i(x',\phi)}\sigma_{g_{i+1}(x'-l_p^{int},\phi)}}\,, \tag{2}$$

and the final angle estimation using this function is then

$$\widehat{\theta}_k = \arg\max_{\phi} \left\{\rho(\phi)\right\}\,, \tag{3}$$

where the estimate has been improved by averaging over several estimates of ρ, using several pulse-echo lines, i.

If the expectation operator is approximated by the temporal average and assuming $\overline{x}_1 = \overline{x}_2 = 0$ then the correlation coefficient of (1) can be written as

$$\rho = \frac{\sum x_1 x_2}{\sqrt{\sum x_1^2}\sqrt{\sum x_2^2}}\,, \tag{4}$$

which means that the correlation-function can be calculated by rewriting (2) into

$$\rho(\phi) = \sum_i \frac{\sum_{x'} g_i(x', \phi) \cdot g_{i+1}(x' - l_p^{int}, \phi)}{\sqrt{\sum_{x'} g_i(x', \phi)^2 \cdot \sum_{x'} g_{i+1}(x' - l_p^{int}, \phi)^2}}\,, \tag{5}$$

The directional lines are placed with an angular distance, $\Delta\phi$, and the estimates are thus initially restricted to be discrete estimates, $\widehat{\theta}_k$ with the same resolution. Continuous estimates, $\widehat{\theta}$ can be obtained by employing polynomial interpolation around the peak of the correlation-function to find a continuous index for the peak and then use linear interpolation between the neighboring discrete angles. This will reduce the number of directions to beamform signals in.

In the angle and velocity estimator the correlation is traditionally calculated based on consecutive directional signals. Considering the velocity estimator, for low velocities, angles close to 90° or high pulse repetition frequencies, the phase

difference between signals is low yielding a lag at the cross-correlation peak which is close to zero. This will make the estimation variance high, and it can be an advantage to correlate signals, where the time between acquisitions is higher. The directional signals used for the cross-correlations are then selected with a time interval, $T_{cc} = k_{tprf} \cdot T_{prf}$ between the correlated signals. T_{cc} is referred to as the *correlation-time* and the proportionality, k_{tprf} is referred to as the *correlation-time-factor*. All indices equal to $i+1$ in all previous equations for both velocity and angle estimation must thus be substituted by $i + k_{tprf}$. The angle estimator is also dependant on the choice of k_{tprf} and it appears to affect performance radically and the optimal value varies with the flow angle. The results presented here are all produced with a fixed value for velocity estimation, and a fixed value for angle estimation if nothing else is noticed.

IV. Results

In Section IV-A and IV-B the results from simulations and measurements are presented. The emphasis is placed on the velocity vector angle estimation algorithm. All results are obtained at the tube angles, $\theta = \{45°, 60°, 75°, 90°\}$ and the angle estimation is performed at the center of the vessel. Some of the parameters and processing involved in calculating and presenting the estimation results are described below.

A number, N_{xc} of directional lines from different pulse-echo lines are cross-correlated for each velocity profile estimate and angle estimate. Echo cancellation is performed by subtracting the mean value of the directional signals used for the estimation, and for the velocity profile estimation a rejection scheme is used to discriminate between flow and stationary signal. The results presented are quantified by calculating bias, standard deviations, and a probability of having a valid estimate. The velocity profile for a parabolic laminar flow is described in [2], and this is the profile used in the simulated flow, and it is used as reference when calculating the velocity estimation performance in the experimental measurements. The bias and standard deviation are calculated over the profile as a function of depth, z_k. From the bias-profile, $B_{est}(z_k)$, and standard-deviation-profile, $\sigma_{est}(z_k)$, the relative mean bias and the relative mean standard deviation are calculated, both relative to the maximum velocity of the profile.

Since the kernel of the angle estimation algorithm is the cross-correlation there is a risk of having estimates which are based on erroneous peaks [2]. These estimates can take values much different from the true angle. If no attention is made to these outlier estimates the bias and the standard deviation of all estimates will be highly influenced by these and will not represent the performance properly. As a consequence of this the angle estimates are divided into two groups. One group with estimates that are within a specified acceptable deviation, θ_{dev}, from the true angle and one group with the complementary estimates, which are considered outliers. A probability of having a continuous estimate, $\widehat{\theta}$ within θ_{dev} from the true angle is calculated,

$$P_{ok} = P(\theta - \theta_{dev} \leq \widehat{\theta} \leq \theta + \theta_{dev}) \,,$$

TABLE I

Default parameters for the velocity profile and angle estimation algorithm.

Spatial sampling interval for directional signals	$\lambda/10$
Spatial extent of directional signals	$-10\lambda : 10\lambda$
Number of correlations for each estimate $\theta = \{45°, 60°, 75°, 90°\}$	$\{10, 10, 10, 20\}$
Angular distance between directional lines for angle estimation	$5°$
Correlation-time-factor, k_{tprf} for angle estimation	8
Velocity search range	1 m/s
Correlation-time-factor, k_{tprf} for velocity estimation	2

TABLE II

Default parameters used in all simulations.

Number of transmit/receive elements	128/128
Transducer center frequency	7 MHz
Pitch of transducer element	0.208 mm
Height of transducer element	4.5 mm
Kerf	0.035 mm
Assumed speed of sound	1540 m/s
Transmit apodization	Hanning
Receive apodization	Rectangular (none)
Excitation Pulse	1 period sinusoid
Pulse repetition frequency	10 kHz
RF sampling frequency	100 MHz
Radius of vessel	10 mm
Distance to vessel center	40 mm
Transmit focus	80 mm
Peak velocity in flow, v_0	0.3 m/s

where $\theta_{dev} = 15°$ by choice. All estimates outside this range are considered outliers. The bias, B_{est}, and standard deviation, σ_{est} are calculated based on that subset of estimates only, which are within θ_{dev} from the true angle.

The default parameters for velocity and angle estimation are found in Table I.

A. Simulation results using Field II

The main purpose of the simulations is to verify the functionality of the algorithms, and to evaluate how good the performance can get under favorable conditions. In Field II the conditions are ideal, and the simulation results are obtained from acquired data free from noise. The velocity and angle estimates are estimated from the same simulated data, with transmit focus at twice the depth of the vessel center. The default parameter values for the simulations are found in Table II.

1) Velocity profile estimation on simulated data: The results are based on 1000 pulse-echo signals which leads to 165 and 89 profile estimates for the beam-to-flow angles of $45°$ to $75°$ and $90°$, respectively. The profiles are calculated using the flow/stationary rejection scheme [2], and the beam-to-flow angle is assumed known. The quantized performance is calculated from the estimates inside the vessel only and can be found in Table III. Both the bias and the standard deviation increase with the flow angle, and the standard deviation for

TABLE III

VELOCITY PROFILE ESTIMATES FROM FIELD II SIMULATIONS. RESULTS ARE CALCULATED FROM ESTIMATES INSIDE THE VESSEL ONLY.

θ	Relative Mean Bias [%]	Relative Mean Standard Deviation [%]	Estimates in profile
$45°$	0.4	0.7	29
$60°$	1.2	1.0	29
$75°$	3.5	1.8	27
$90°$	-3.6	7.7	27

transverse flow is noticeable larger than for the other angles.

2) Angle estimation on simulated data: The simulation results in this section are based on the default simulation parameters from Table II and the default angle estimation parameters from Table I.

The results are based on 1000 pulse-echo acquisitions, which leads to 110 and 70 angle estimates for the beam-to-flow angles $45°, 60°, 75°$, and $90°$, respectively. The performance is shown in Table IV.

TABLE IV

RESULT OF ANGLE ESTIMATION FROM SIMULATION IN FIELD II .

θ	P_{ok}	B_{est}	σ_{est}
$45°$	100%	-0.6°	2.9°
$60°$	100%	-1.5°	2.2°
$75°$	97%	-4.9°	2.8°
$90°$	89%	0.3°	0.7°

The performance decreases as the flow angle increases from $\theta = 45°$ to $\theta = 90°$. At $\theta = 90°$ there are dominant secondary peaks at the correlation-function which divides the estimates into a few groups that gives relatively many outliers at specific angles. Those estimates that are within the acceptable deviation though have a low bias and standard deviation. It should be emphasized that this performance dependency on flow angle is different with another choice of correlation-time-factor, k_{tprf}. Since the choice of k_{tprf} has a strong influence on performance a study of this influence has been performed in order to find those values which optimizes the performance for the flow angles $\theta = \{45°, 60°, 75°, 90°\}$. The result of the angle estimation with these optimal values are shown in Table V with the only purpose of illustrating the absolute potential of the method under favorable conditions.

TABLE V

RESULT OF ANGLE ESTIMATION FROM SIMULATIONS WITH OPTIMAL VALUES OF THE CORRELATION-TIME, k_{tprf}.

θ	k_{tprf}	P_{ok}	B_{est}	σ_{est}
$45°$	18	100%	-0.4°	1.9°
$60°$	18	100%	-0.9°	1.7°
$75°$	18	100%	-1.0°	0.4°
$90°$	6	100%	0.4°	0.9°

TABLE VI

DEFAULT MEASUREMENT PARAMETERS USED FOR ALL MEASUREMENTS.

Number of transmit elements	128
Number of receive elements	64 / 128 (combined)
Pitch	0.208 mm
Height	4.5 mm
Kerf	0.035 mm
Transmit apodization	Hanning
Receive apodization	Rectangular (none)
Excitation Pulse	2-cycle sinusoid
Pulse repetition frequency	10 kHz / 5 kHz (combined)
RF sampling frequency	40 MHz
Transducer center frequency	7 MHz
Assumed speed of sound	1480 m/s
Radius of vessel	6.4 mm
Distance to vessel center	37 mm
Peak velocity in flow	≈ 0.3 m/s

B. Experimental Measurements

This section describes the measurement setup and presents the angle estimation results from the experiments.

1) Measurement setup: The experimental ultrasound scanner, RASMUS [14], and a 7 MHz linear array transducer, type 8804, from BK-Medical were used for all measurements. The system acquires RF data from the individual transducer channels and this data is transferred to a PC, where it is saved and ready for off-line processing. The RASMUS system contains 128 transmitting channels and 64 receiving channels with a 40 MHz sampling frequency, and has 12 bits resolution for each individual channel. With the build-in 2-to-1 multiplexer the system can cover 128 individual receive channels in two emissions. All measurements are made using a circulating flow rig with a blood mimicking fluid and a PC-controlled pump called *CompuFlow1000* [15] [16]. The pump is connected to a steel tube of approximately 1 m, which enters a water tank, where the steel tube enters another tube, which mimics a blood vessel. Inside the water tank a fixture for the transducer is inserted. The angle of the transducer, and the distance to the tube can be adjusted. The distance from the center element of the transducer to the tube is the same regardless of the angle. The measurements are obtained at the angles $45°, 60°, 75°, 90°$, where $90°$ corresponds to a transverse flow measurement. For all measurements, a number of parameters has been fixed and these are found in Table VI.

2) Angle Estimation on measured data: The results in this section are based on the default parameters from Table I with the exception that the number of correlations for each estimate, $N_{xc} = 20$ for all flow angles. 3000 pulse-echo acquisitions are processed, which leads to 213 angle estimates. The quantized estimation performance is shown in Table VII. The performance at $\theta = 45°$ is radically worse, than at the other angles. Velocity profile estimates has been calculated based on the same acquisition data, and here there was a similar decrease in performance. One thing to notice about the measurement setup is, that there is a relative large difference in physical position of the transducer for the different tube

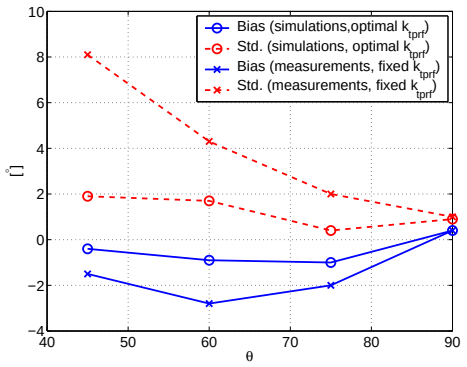

Fig. 2. Bias and standard deviation of Angle estimation under different conditions.

angles. The distance from the center element to the tube is the same regardless of the angle, but for $\theta = 45°$ the transducer elements in one end is very close to the tube, which could have a negative effect in form of re-reflections. Re-reflections inside the water tank can also have some influence on the results, and this will also vary with the angle of the transducer. Another thing to notice is that the simulation did not show any decrease in performance for $\theta = 45°$ compared to the other angles. The

TABLE VII

RESULT OF ANGLE ESTIMATION FROM MEASUREMENTS.

θ	P_{ok}	B_{est}	σ_{est}
45°	62%	-1.5°	8.1°
60°	95%	-2.8°	4.3°
75°	98%	-2.0°	2.0°
90°	68%	0.4°	1.0°

quantized performance in form of bias and standard deviation from Table V and Table VII are shown in Fig. 2. Here it is clear that there is a difference in performance when using the optimal values of the correlation-time and when using a fixed value for all flow angles. Beside these differences there is also a difference in the probability, P_{ok}, which is not shown in this figure.

V. CONCLUSION

A method for velocity vector estimation in conventional ultrasound imaging has been presented using a new approach to angle estimation. The simulation study and measurement study both showed that angle estimation by directional beamforming is possible. The angle estimation performance is strongly influenced by the choice of correlation-time, and a proper choice varies with flow angle and will vary with flow velocity amplitude though the latter is not shown in this paper. The flow angles $\theta = \{45°, 60°, 75°\}$ requires a high value of the correlation-time whereas for $\theta = 90°$ a low value is required. By using the optimal choice of correlation-time for the different flow angles based on a parameter study the potential of the method has been revealed. With these favorable conditions the simulations produced 100% valid estimates (no outliers) and a bias and standard deviation below $2°$ for all flow angles. Using the measurements more than 96% valid estimates were produced for the flow angles $\theta = \{60°, 75°, 90°\}$ and with a bias below $2°$ and a standard deviation below $5°$.

ACKNOWLEDGMENT

This work was supported by grant 9700883, 9700563 and 26-04-0024 from the Danish Science Foundation and by B-K Medical, Denmark.

REFERENCES

[1] D. H. Evans, W. N. McDicken, R. Skidmore, and J. P. Woodcock. *Doppler Ultrasound, Physics, Instrumentation, and Clinical Applications*. John Wiley & Sons, New York, 1989.

[2] J. A. Jensen. *Estimation of Blood Velocities Using Ultrasound: A Signal Processing Approach*. Cambridge University Press, New York, 1996.

[3] C. Kasai, K. Namekawa, A. Koyano, and R. Omoto. Real-time two-dimensional blood flow imaging using an autocorrelation technique. *IEEE Trans. Son. Ultrason.*, 32:458–463, 1985.

[4] S. G. Foster. *A pulsed ultrasonic flowmeter employing time domain methods*. PhD thesis, Dept. Elec. Eng., University of Illinois, Urbana, Ill., 1985.

[5] O. Bonnefous and P. Pesqué. Time domain formulation of pulse-Doppler ultrasound and blood velocity estimation by cross correlation. *Ultrason. Imaging*, 8:73–85, 1986.

[6] M. D. Fox. Multiple crossed-beam ultrasound Doppler velocimetry. *IEEE Trans. Son. Ultrason.*, SU-25:281–286, 1978.

[7] G. E. Trahey, J. W. Allison, and O. T. von Ramm. Angle independent ultrasonic detection of blood flow. *IEEE Trans. Biomed. Eng.*, BME-34:965–967, 1987.

[8] J. A. Jensen and P. Munk. A new method for estimation of velocity vectors. *IEEE Trans. Ultrason., Ferroelec., Freq. Contr.*, 45:837–851, 1998.

[9] M. E. Anderson. Multi-dimensional velocity estimation with ultrasound using spatial quadrature. *IEEE Trans. Ultrason., Ferroelec., Freq. Contr.*, 45:852–861, 1998.

[10] H. F. Routh, T. L. Pusateri, and D. D. Waters. Preliminary studies into high velocity transverse blood flow measurement. In *Proc. IEEE Ultrason. Symp.*, pages 1523–1526, 1990.

[11] V. L. Newhouse, D. Censor, T. Vontz, J. A. Cisneros, and B. B. Goldberg. Ultrasound Doppler probing of flows transverse with respect to beam axis. *IEEE Trans. Biomed. Eng.*, BME-34:779–788, 1987.

[12] J. A. Jensen. Directional velocity estimation using focusing along the flow direction: I: Theory and simulation. *IEEE Trans. Ultrason., Ferroelec., Freq. Contr.*, pages 857–872, 2003.

[13] J. A. Jensen and R. Bjerngaard. Directional velocity estimation using focusing along the flow direction: II: Experimental investigation. *IEEE Trans. Ultrason., Ferroelec., Freq. Contr.*, pages 873–880, 2003.

[14] J. A. Jensen, O. Holm, L. J. Jensen, H. Bendsen, S. I. Nikolov, B. G. Tomov, P. Munk, M. Hansen, K. Salomonsen, J. Hansen, K. Gormsen, H. M. Pedersen, and K. L. Gammelmark. Ultrasound research scanner for real-time synthetic aperture image acquisition. *IEEE Trans. Ultrason., Ferroelec., Freq. Contr.*, 52 (5), May 2005.

[15] K. V. Ramnarine, D. K. Nassiri, P. R. Hoskins, and J. Lubbers. Validation of a new blood mimicking fluid for use in Doppler flow test objects. *Ultrasound Med. Biol.*, 24:451–459, 1998.

[16] www.simutec.com.

B.5 Synthetic Aperture Focusing applied to Imaging Using a Rotating Single Element Transducer

This article was published in Journal *Proceedings - IEEE Ultrasonics Symposium*. Conference Title *2007 IEEE Ultrasonics Symposium Issue Vol.?, Page no. 1504-1507. October 2007.*

Synthetic aperture focusing applied to imaging using a rotating single element transducer

Jacob Kortbek*†, Jørgen Arendt Jensen* and Kim Løkke Gammelmark†
*Center for Fast Ultrasound Imaging, Ørsted•DTU,
Bldg. 348, Technical University of Denmark, DK-2800 Lyngby, Denmark
†B-K Medical, Mileparken 34, DK-2730 Herlev, Denmark.

***Abstract*—This paper applies the concept of virtual sources and mono-static synthetic aperture focusing (SAF) to 2-dimensional imaging with a single rotating mechanically focused concave element with the objective of improving lateral resolution and signal-to-noise ratio (SNR). The geometrical focal point of the concave element can be considered as a point source emitting a spherical wave in a limited angular region. The SAF can be formulated as creating a high resolution line as a sum over low resolution lines (LRL). A LRL is the contribution from a single emission. Simulation in Field II is based on moving the concave element of radius 2.5 mm along a circle of radius 10 mm. Elements with different concave curvatures are used to obtain geometrical focusing depths at 10 mm, 15 mm, and 20 mm. Point targets in the range from 5 mm to 65 mm are used as image objects. The high resolution images (HRI) are shown and the radial and angular resolution are extracted at -6 dB and -40 dB. The performance of the setup with a VS at 20 mm is superior to the other setups. Due to the rotation, the synthesized aperture only experiences a moderate expansion, which is not sufficient to reduce the extent of the wide point spread function of a single emission. The effect of SAF with focal depth at 20 mm is negligible, caused by the small number of LRL applied. The great profit of the SAF is the increase in SNR. For the setup with focal depth at 20 mm the SAF SNR gain is 11 dB. The SNR gain of a setup with a VS at radius 10 mm or 15 mm over conventional imaging with a VS at 20 mm, is also 11 dB.**

I. Introduction

Inspired by synthetic aperture radar techniques, synthetic aperture ultrasound imaging has been investigated thoroughly for many years. In synthetic transmit aperture (STA) imaging a single element is used in transmit to create a spherical wave that propagates in all directions. In receive a multi-element aperture is applied. The backscattered signals come from all imaging points and can be used to construct a low-resolution image (LRI), hence an image constructed from a single emission. Several emissions from single elements across the aperture can be used to create several LRI's which can be added into a high-resolution image (HRI). In the mono-static approach [1] the same element serves as a transmitter and a receiver. Variations of synthetic transmit aperture and sparse synthetic aperture techniques has been investigated with improvements in both frame rate, penetration, and lateral resolution. A synthetic aperture technique suitable for a hand held system using a multi-element transmit and receive aperture was described by Karaman et al. [2]. Lockwood and Hazard described a sparse synthetic aperture beamforming technique for three-dimensional ultrasound imaging using a few transmit pulses for each image [3], [4]. A synthetic aperture method for a circular aperture was investigated by O'Donnell and Thomas [5]. The concept of using the transmit focal point as a virtual aperture was introduced by Passmann and Ermert [6]. Virtual sources in synthetic aperture focusing (SAF) was further investigated by Frazier and OBrien [7], Nikolov and Jensen [8], [9], and Bae and Jeong [10].

This paper applies the concept of virtual sources and synthetic aperture techniques to 2-dimensional imaging with a single rotating mechanically focused concave element. Such an imaging system can e.g. be found in an anorectal ultrasound transducer. With such a transducer emission and reception are done while the transducer element continuously rotates and the received RF signals are stored. It is proposed to apply mono-static synthetic aperture focusing (SAF) on these data with the objective of improving lateral resolution and signal-to-noise ratio (SNR). This is investigated using simulations in Field II [11], [12] and SAF is carried out using the Beamformation Toolbox, *BFT2* [13]. Images of point targets are created and the radial and angular resolution in the polar coordinate system is extracted. The potential improvement in SNR is also evaluated. The SAF method is described in Section II. The simulation setup and simulation results are found in Section III, and the investigation is concluded in Section IV.

II. Method

In the mono-static case of linear array SAF, a single element is used in both transmit and receive. The transmitting element can be considered a point source emitting a spherical wave. The wave traverses all image points and an entire LRI can be formed after each emission. Several emissions from across the aperture can be used to construct a HRI. The HRI has a better resolution than the LRI, since the multiple emissions synthesize an effective aperture of a certain lateral width.

This focusing scheme can not directly be applied to imaging with a rotating mechanically focused element. To begin with the lateral translation of the transmit source is smaller for the rotating system than for the linear array making the synthesized width of the aperture smaller. Secondly the concave rotating element can not be considered a point source because of the physical extent of the element and the geometrical focusing due to the concave shape. Instead the geometrical

focal point can be considered as a point source emitting a spherical wave in a limited angular region. The focal depth of the transducer element or more exact the focusing $F_\#$ determines the opening angle, hence the width of the wave field and the point spread function (PSF). An illustration of propagating waves from 3 different emissions is shown in Fig. 1 for a transducer element with a focal depth of 10 mm.

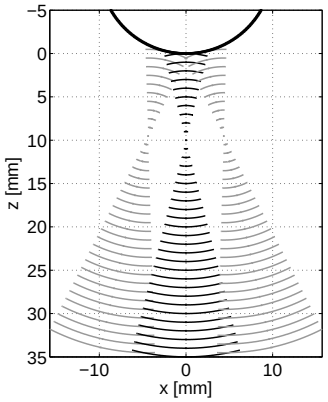

Fig. 1. An illustration of propagating waves from 3 different emissions for a transducer element with a focal depth of 10 mm.

A LRI of the entire imaging area can not be formed after each emission due to the spatially limited wave propagation. Instead, for each image point in a high resolution image line (HRL) it must be determined which emissions that have a wave field that encompasses the image point. These emissions contribute to the HRL, and samples from each of them are selected according to the SAF delays, and added together. In other words a single HRL is composed of the sum of a number of low resolution lines (LRL). A single LRL is, thus, the contribution from a given emission to a HRL. The term LRL is used for an RF-line which have been processed using SAF and which contains at least one non-zero sample which carries information of one of the image points of the HRL.

The SAF can be formulated as a sum over LRL. A single sample of the HRL, representing the image point at the location $\vec{r}_{ip}$ with angular coordinate ϕ and radial coordinate r becomes

$$h(\phi, r) = \sum_{\theta} \mathcal{A}(\theta, r) l_\theta(r)\,, \tag{1}$$

where $h(\phi, r)$ is the HRL sample, and $l_\theta(r)$ is the LRL sample from the emission with propagation direction θ. Both with radial coordinate r. The variable $\mathcal{A}$ is an apodization function which controls the weighting of the contribution from each of the LRL. It is a function a the radial coordinate, since the number of contributing emissions increases with range. The synthesized aperture increases with range resulting in a less range dependent lateral resolution. The LRL can be formulated using the RF-line, $s_\theta(r')$

$$l_\theta(r) = s_\theta(r')\,. \tag{2}$$

r' is the radial coordinate at which to select a sample from the RF-line and is not the same radial coordinate as in the HRL. r' can be found from the distance function, $r' = d(\vec{r}_{v_\theta}, \vec{r}_{ip})$ which calculates the transmit-receive time-of-flight for the SAF, and thus the sample index for the RF-line, $s_\theta(r')$. The transducer element at the position $\vec{r}_{t_\theta}$ is physically focused at the VS at the position $\vec{r}_{v_\theta}$ with a focal distance of d_v from the element. The element is focused in both transmit and receive and the distance function becomes a sum of transmit and receive travel paths

$$\begin{aligned} d(\vec{r}_{v_\theta}, \vec{r}_{ip}) = & \quad |\vec{r}_{v_\theta} - \vec{r}_{t_\theta}| \pm |\vec{r}_{ip} - \vec{r}_{v_\theta}| \\ & \pm |\vec{r}_{v_\theta} - \vec{r}_{ip}| + |\vec{r}_{t_\theta} - \vec{r}_{v_\theta}| \\ = & \quad 2|\vec{r}_{v_\theta} - \vec{r}_{t_\theta}| \pm 2|\vec{r}_{ip} - \vec{r}_{v_\theta}| \\ = & \quad 2d_v \pm 2|\vec{r}_{ip} - \vec{r}_{v_\theta}| \end{aligned} \tag{3}$$

The $\pm$ in refer to whether the image point is above or below the VS. A single sample of the HRL can thus be formulated using (1) and (2)

$$h(\phi, r) = \sum_{\theta} \mathcal{A}(\theta, r) s_\theta(d(\vec{r}_{v_\theta}, \vec{r}_{ip}))\,. \tag{4}$$

A single element of limited extent can be considered as a wave source emitting a spherical wave, which will cover the entire image area. With complete overlap between the covered image areas all emission can be utilized to create a HRI. Having a physically focused transducer element the VS is conceived as the wave source. With a transducer element of fixed size the focal depth determines the opening angle, α and the confined image area covered by the wave field. The consequence is that not all emissions can be utilized to create a HRI. Having a rotating element instead of a translating element even further limits the number of applicable emissions. From geometrical observation the opening angle can be expressed as $\alpha = 2\arctan\frac{1}{2F_\#}$, which is a valid approximation [14]. The confined image area covered by the wave field is, thus, a function of the $F_\#$. With a higher $F_\#$ the point spread function becomes narrower improving the resolution for the single RF-line. This portrays a conflict between using a low $F_\#$ and adding a large number of LRL, and using a high $F_\#$ and reducing the number of applied LRL. Performance results for these different configurations are presented in Section III.

III. Simulation Results

The SAF scheme is investigated using Field II [11], [12]. The simulations are based on moving a single concave element of radius 2.5 mm along a circle of radius 10 mm. Elements with different concave curvatures are used to obtain geometrical focusing depths at 10 mm, 15 mm, and 20 mm. The scattering media consists of point targets (PT) in the range from 5 mm to 65 mm with a distance of 10 mm. The transducer element is rotated with a fixed angle of 0.63° corresponding to moving the element $\lambda/2$ between each acquisition. It is assumed that the transducer element is not moving during emission and reception. The 7 MHz pulse, and the one-way impulse response are weighted single-cycle sinusoids.

The envelope HRI's are shown in this section. The radial and angular resolution are extracted at -6 dB and -40 dB. For

each PT the resolution is calculated as the width at which the envelope amplitude has decreased to the specified level relative to the maximum level at that given PT. For the lateral resolution the envelope amplitude is taken as the maximum amplitude within a radial range of $\pm$ 3 mm around the PT. Likewise for the radial resolution the envelope amplitude is taken as the maximum amplitude across the entire angular range of the image.

The variable $\mathcal{A}$ from (4) controls the weighting of the contribution from each of the LRL and is a function a the radial coordinate. The actual number of contributing LRL is shown in Fig. 2 for the transducer elements with focusing depths at 10 mm, 15 mm, and 20 mm. As the focal depth increases, and the opening angle decreases, the number of contributing LRL decreases.

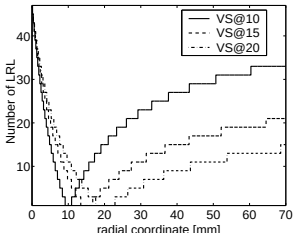

Fig. 2. The number of contributing LRL for the transducer elements with focusing depths at 10 mm, 15 mm, and 20 mm.

Images with different setups are shown in Fig. 3. In the first three images the focusing depths of the element are 10 mm, 15 mm, and 20 mm, respectively and SAF has been applied. In the last image the element has a focusing depths of 20 mm and SAF is not applied. The differences between the images are better demonstrated in Fig. 4 where the radial and angular resolution are extracted. The performance of the setup with a VS at 20 mm is superior to the other setups. This reflects the conflict stated earlier between using a low $F_{\#}$ and adding a large number of LRL, and using a high $F_{\#}$ and reducing the number of LRL. Due to the rotation the synthesized aperture only experiences a moderate expansion even for the setup with a focal depth of 10 mm. The modest expansion is not sufficient to reduce the extent of the wide point spread function of a single emission. At least not to a level which is competitive to the relatively narrow PSF of the setup with focal depth at 20 mm. The effect of SAF with focal depth at 20 mm is negligible. This is also caused by the small number of LRL. Only 15 LRL are used at a range of 70 mm as shown in Fig. 2.

The SAF technique rely on phase coherent addition of the LRL. The LRL's composing the center HRL around the PT at 35 mm are plotted in Fig. 5. The setup is with an element with focal depth of 10 mm. It is apparent that the LRL's are completely phase aligned and add up constructively.

Provided that the image object does not move in between acquisitions and assuming uncorrelated electronic noise at the receivers the SNR improvement using SAF is

$$\Delta SNR(r) = 10\log_{10}(N_{r_v}(r))\,. \tag{5}$$

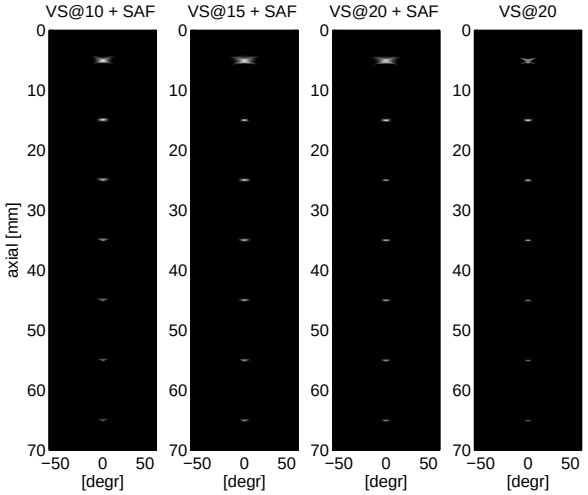

Fig. 3. Images from 4 different setups. In the first three images the focusing depths of the elements are 10 mm, 15 mm, and 20 mm respectively and SAF has been applied. In the last image the element has a focusing depths of 20 mm and SAF is not applied.

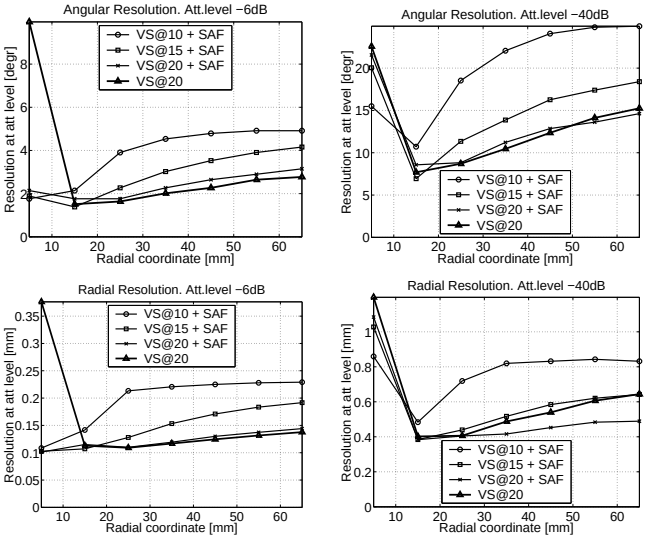

Fig. 4. Radial resolution (bottom) and angular resolution (top) at -6 dB (left) and -40 dB (right)

$N_{r_v}(r)$ is the number of emissions which contributes to the HRL for a transducer element with a VS at radius r_v as shown in Fig. 2. With a VS at 20 mm $N_{r_v}(r) = 13$ at radius, $r = 60$ mm. This yields a SAF SNR improvement of $\Delta SNR = 11$ dB. With a lower $F_{\#}$ the number of contributing emissions increases, but the width of the wave field does also increase. Provided that the transmitted power is equally distributed over the width of the field, the SAF SNR improvement of a setup with a VS at radius r_v over conventional imaging with a VS at 20 mm can be expressed as

$$\Delta SNR_{r_v}(r) = 10\log_{10}\left(N_{r_v}(r)\frac{W_{r_{20}}(r)}{W_{r_v}(r)}\right)\,. \tag{6}$$

$W_{r_{20}}$ and W_{r_v} are the -6 dB widths of the wave fields

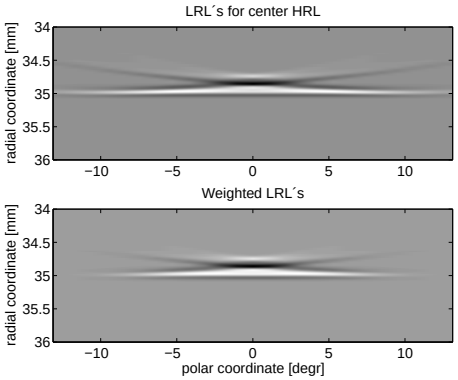

Fig. 5. A single HRL is composed of the sum of a number of low resolution lines (LRL). Here the LRL's composing the center HRL around the PT at 35 mm are shown. The setup is with an with focal depth of 10 mm. Without apodization (top) and with Hamming apodization (bottom).

measured in whole wave lengths for the elements with VS's at radius 20 mm and at radius r_v, respectively. The widths are calculated using the opening angle, α. The width-ratio and the SNR improvement are shown in Fig. 6 for elements with VS's at radius $r_v = 10$ mm, $r_v = 15$ mm, and $r_v = 20$ mm. At greater range the width-ratio is 2.5, and 1.5 with elements having VS's at radius $r_v = 10$ mm, $r_v = 15$ mm respectively, while $N_{r_v}(r)$ is 33 and 21. This results in an improvement in SNR of 11 dB in both cases just as the improvement of using SAF on the setup with the VS at radius 20 mm. The SNR improvement can be converted directly to an increase in penetration or an increase in emitted frequency yielding a higher resolution.

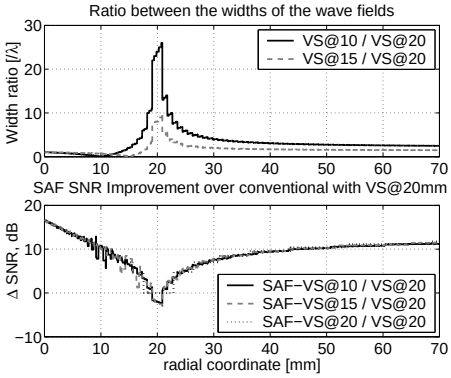

Fig. 6. The ratio between the width of different wave fields (top) and SAF SNR improvement over conventional imaging with a VS at radius 20 mm (bottom).

IV. Conclusion

Through simulations in Field II mono-static synthetic aperture focusing of pulse-echo data from a rotating concave element has been investigated. The radial and angular resolution have been extracted using transducer elements with a focal depth of 10 mm, 15 mm, and 20 mm. Due to the rotation, the synthesized aperture only experiences a moderate expansion. This is not sufficient to reduce the extent of the wide point spread function of a single emission. At least not to a level which is competitive to the relatively narrow PSF of the setup with focal depth at 20 mm. The effect of SAF with focal depth at 20 mm is also negligible due to the small number of LRL added.

The advantage of the SAF is the increase in SNR. For the setup with focal depth at 20 mm the SAF SNR gain is 11 dB. The SNR gain of a setup with a VS at radius 10 mm or 15 mm over conventional imaging with a VS at 20 mm is also 11 dB. The SNR improvement can be converted directly to an increase in penetration or an increase in emitted frequency yielding a higher resolution.

Acknowledgment

This work was supported by grant 9700883, 9700563 and 26-04-0024 from the Danish Science Foundation and by B-K Medical, Denmark.

References

[1] J. T. Ylitalo and H. Ermert, "Ultrasound synthetic aperture imaging: monostatic approach," *IEEE Trans. Ultrason., Ferroelec., Freq. Contr.*, vol. 41, pp. 333–339, 1994.

[2] M. Karaman, P. C. Li, and M. O'Donnell, "Synthetic aperture imaging for small scale systems," *IEEE Trans. Ultrason., Ferroelec., Freq. Contr.*, vol. 42, pp. 429–442, 1995.

[3] G. R. Lockwood, J. R. Talman, and S. S. Brunke, "Real-time 3-D ultrasound imaging using sparse synthetic aperture beamforming," *IEEE Trans. Ultrason., Ferroelec., Freq. Contr.*, vol. 45, pp. 980–988, 1998.

[4] C. R. Hazard and G. R. Lockwood, "Theoretical assessment of a synthetic aperture beamformer for real-time 3-D imaging," *IEEE Trans. Ultrason., Ferroelec., Freq. Contr.*, vol. 46, pp. 972–980, 1999.

[5] M. O'Donnell and L. J. Thomas, "Efficient synthetic aperture imaging from a circular aperture with possible application to catheter-based imaging," *IEEE Trans. Ultrason., Ferroelec., Freq. Contr.*, vol. 39, pp. 366–380, 1992.

[6] C. Passmann and H. Ermert, "A 100-MHz ultrasound imaging system for dermatologic and ophthalmologic diagnostics," *IEEE Trans. Ultrason., Ferroelec., Freq. Contr.*, vol. 43, pp. 545–552, 1996.

[7] C. H. Frazier and W. D. O'Brien, "Synthetic aperture techniques with a virtual source element," *IEEE Trans. Ultrason., Ferroelec., Freq. Contr.*, vol. 45, pp. 196–207, 1998.

[8] S. I. Nikolov and J. A. Jensen, "Virtual ultrasound sources in high-resolution ultrasound imaging," in *Proc. SPIE - Progress in biomedical optics and imaging*, vol. 3, 2002, pp. 395–405.

[9] ——, "3D synthetic aperture imaging using a virtual source element in the elevation plane," in *Proc. IEEE Ultrason. Symp.*, vol. 2, 2000, pp. 1743–1747.

[10] M. H. Bae and M. K. Jeong, "A study of synthetic-aperture imaging with virtual source elements in B-mode ultrasound imaging systems," in *IEEE Trans. Ultrason., Ferroelec., Freq. Contr.*, vol. 47, 2000, pp. 1510–1519.

[11] J. A. Jensen and N. B. Svendsen, "Calculation of pressure fields from arbitrarily shaped, apodized, and excited ultrasound transducers," *IEEE Trans. Ultrason., Ferroelec., Freq. Contr.*, vol. 39, pp. 262–267, 1992.

[12] J. A. Jensen, "Field: A program for simulating ultrasound systems," *Med. Biol. Eng. Comp.*, vol. 10th Nordic-Baltic Conference on Biomedical Imaging, Vol. 4, Supplement 1, Part 1, pp. 351–353, 1996b.

[13] J. Kortbek, S. I. Nikolov, and J. A. Jensen, "Effective and versatile software beamformation toolbox," in *Proc. SPIE - Medical Imaging - Ultrasonic Imaging and Signal Processsing*, 2007, pp. 651 319,1–10.

[14] N. Oddershede and J. A. Jensen, "Effects influencing focusing in synthetic aperture vector flow imaging," *IEEE Trans. Ultrason., Ferroelec., Freq. Contr.*, vol. 54, no. 9, pp. 1811–1825, September 2007.

B.6 Synthetic Aperture Sequential Beamforming

This article is awaiting filing of a patent application before publishing.

Synthetic Aperture Sequential Beamforming

Jacob Kortbek
Ørsted•DTU, Center for Fast Ultrasound, Technical University of Denmark & B-K Medical, Denmark

Jørgen Arendt Jensen
Ørsted•DTU, Center for Fast Ultrasound, Technical University of Denmark

Kim Løkke Gammelmark
B-K Medical, Denmark

(Dated: January 3, 2008)

The main motivation for synthetic aperture sequential beamforming (SASB) is to apply synthetic aperture techniques without the need for storing RF-data and with a restricted system complexity. The objective is to improve lateral resolution and obtain a more range independent resolution compared to conventional ultrasound imaging. SASB is a two-stage procedure using two separate beamformers. The initial step is to construct and store a set of B-mode image lines using a single focal point in both transmit and receive. The focal points are considered virtual sources making up a virtual array. The second stage applies the focused image lines from the first stage as input data. The size of the virtual array is dynamically expanded as the image range increases and a range independent lateral resolution is obtained. The SASB method has been investigated using simulations in Field II and by off-line processing of data acquired with a commercial scanner. The lateral resolution increases with a decreasing $F\#$, but for a linear array with λ-pitch grating lobes appear if $F\# \leq 2$. The performance of SASB with the VS at 20 mm and $F\# = 1.5$ is compared with conventional dynamic receive focusing (DRF). The axial resolution is the same for the two methods. For the lateral resolution there is improvement in FWHM of at least a factor of 2 and the improvement at -40 dB is at least a factor of 3. With SASB the resolution is almost constant throughout the range. For DRF the FWHM increases almost linearly with range and the resolution at -40 dB is fluctuating with range. The decrease in performance at the transducer edges is more profound for SASB than for DRF and especially at greater depths it is obvious that the lateral resolution is laterally dependent. The theoretical potential improvement in SNR of SASB over DRF has been estimated based on the measured SNR data and an assumption of a stationary image object, and a correct phase-alignment in the 2nd stage beamformer. The improvement is attained at the entire range and at a depth of 80 mm the improvement is 8 dB.

I. INTRODUCTION

Inspired by synthetic aperture (SA) radar techniques[1–3], SA ultrasound imaging has been investigated thoroughly for many years. In synthetic transmit aperture (STA) imaging[4,5] a single element is used to transmit a spherical wave that occupies the entire region of interest. The backscattered signals are registered using a multi-element receive aperture and RF-samples from all channels are stored. Delay-and-sum (DAS) beamforming can be applied to these data to construct a low-resolution image (LRI), hence an image constructed from a single emission. Several emissions from single elements across the aperture will synthesize a larger aperture and the LRI's from these emissions can be added into a single high-resolution image (HRI). The HRI is dynamically focused in both transmit and receive yielding an improvement in resolution[6]. This has been confirmed with side-by-side comparisons with conventional ultrasound imaging in pre-clinical trials by Pedersen et. al[7]. This imaging technique sets high demands on processing capabilities, data transport, and storage and makes implementation of a full SA system very challenging and costly. The method investigated in this paper is yet another variation on SA processing. The objective is to reduce the demands on the system making it a more realistic task to implement, while still preserving benefits in imaging performance.

Many variations of synthetic aperture focusing (SAF) and examples of implementation have been reported with improvements in both frame rate, penetration, and lateral resolution. A simple real-time single channel system with a multiplexer for array imaging was described by Peterson and Kino[8] back in 1984. In the mono-static approach[6] the same element serves as a transmitter and a receiver. A SA technique suitable for a hand held system using a multi-element transmit and receive aperture was described by Karaman et al.[4]. Lockwood and Hazard described a sparse SA beamforming technique for three-dimensional ultrasound imaging using a few transmit pulses for each image[9,10]. A SA method for a circular aperture was investigated by O'Donnell and Thomas[11].

The concept of using the transmit focal point as a virtual source (VS) or a virtual aperture was introduced by Passmann and Ermert[12]. Virtual sources in SAF was further investigated by Frazier and O´Brien[13], Nikolov and Jensen[14,15], and Bae and Jeong[16]. It was shown that the virtual source coincides with the focal point of the transducer, and that a depth independent resolution can be achieved.

Mono-static SA focusing applied to imaging with a single rotating mechanically focused concave element was investigated by Kortbek et al.[17]. Such an imaging system can e.g. be found in an anorectal ultrasound transducer. One objective of this study was to improve lateral resolution. This was done by storing the RF-lines from every emission and feeding these to a SA beamformer. Due to the small radius of rotation, the synthesized aperture only experiences a moderate lateral expansion. This was not sufficient to reduce the wide extent of the point spread function of a single emission, thus, improvement in lateral resolution was not significant.

The same SAF technique is applied in this paper, but to

linear array imaging. Here the synthesized aperture becomes considerable larger with a lateral translation of the VS than with a rotation. Instead of having a VS created from a single concave element physically focused in both transmit and receive the VS is now created from a sub-aperture - a group of elements. This offers more flexibility since the position and the opening angle of the VS are determined by the electronic focusing instead of the physical concave shape of the single element transducer. The receive focusing is a simple fixed focusing with receive focal point in the transmit focal point. This first beamformer, thus, mimics the focusing that is a consequence of the concave single element transducer. The focused RF-lines from every emission are stored and transferred to a SA beamformer just as the one applied with the rotating transducer. Two beamformers are, thus, applied sequentially - a simple fixed focus beamformer and a SA beamformer denoted Synthetic Aperture Sequential Beamforming (SASB).

One objective of SASB is to improve the penetration depth. The primary objective though is to improve lateral resolution and obtain a more range independent resolution compared to conventional ultrasound imaging. The improvement is naturally not as great as with a full SA setup. Contrary to a full SA setup only a single RF-line is beamformed and stored for each emission. This reduces the system requirements significantly. For simplicity the method is investigated using a linear array, but it might as well apply to other types of imaging. The investigation comprises performance evaluation at a large imaging range. This is done without consideration for the typical use of the specific transducer but as a mean to demonstrate the properties of the method.

The SASB method is described in more detail in Section II. Section III presents results from the Field II[18,19] simulation study. A parameter study shows the performance and artifacts of the method and compare with conventional dynamic receive focusing (DRF). Section IV presents imaging examples and signal-to-noise ratio (SNR) calculations with data acquired from phantom measurements with a commercial scanner.

II. METHOD

Synthetic aperture sequential beamforming (SASB) is a two-stage procedure which can be applied to B-mode imaging with any array transducer. The initial step is to construct and store a set of B-mode image lines using a conventional sliding sub-aperture. These 1st stage lines are obtained with a single focal point near the transducer in both transmit and receive. The second stage consist of an additional beamformer using the focused image-lines from the first stage as input data. The concept of virtual sources and means of calculating the focusing delays are briefly discussed in Section II.A before presenting the SASB in more detail in Section II.B.

A. Virtual sources and focusing delays

In delay-and-sum receive focusing appropriate delays are applied to the responses of the individual transducer elements originating from the focusing point and coherently adding these responses. The delays are found from the round trip time-of-flight (TOF), which is the propagation time of the emitted wave in its path from the transmit origin, $\vec{r}_e$ to the focusing point (FP), $\vec{r}_{fp}$ and return to one of the elements of the receive aperture, $\vec{r}_r$ as illustrated in Fig. 1. This could be the case of mono-static SAF.

$$t_{tof} = \frac{|\vec{r}_{fp} - \vec{r}_e| + |\vec{r}_r - \vec{r}_{fp}|}{c} \ . \tag{1}$$

The transmit origin is not necessarily well defined, if the emitted pressure wave does not emanate from a single element point source as illustrated in Fig. 1. In multi-element synthetic aperture imaging[4] a multi-element transmit sub-aperture is introduced as an alternative to mono-static SAF to ensure sufficient transmitted energy. Here the pressure wave is the result of numerous waves emitted from a multiple elements. With a focused transmission the focal point is introduced as a virtual source, since a spherical wave emanates from this point in a limited angular region. With a known position of the source this allows for the SAF delays to be calculated.

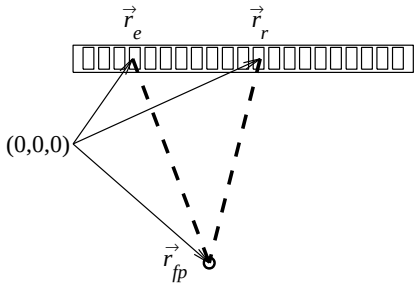

FIG. 1. Wave propagation path (dotted line) for calculating the time-of-flight in receive focusing. The transmit origin, $\vec{r}_e$ and the receive point, $\vec{r}_r$ are illustrated as different elements of an array.

Applying a VS instead of a single element source has a consequence for the calculations of SA focusing delays. Time-delay calculations for different applications was discussed by Kortbek et al.[20]. In dynamic receive beamforming a new set of delay values is calculated for each focusing point (FP). Assuming the speed of sound c is known, the delay value, t_d for the receiving element with position $\vec{r}_r$ is calculated in accordance with Fig. 2 (left)

$$t_{d_{fp}}(\vec{r}_r) = \frac{|\vec{r}_{tfp} - \vec{r}_e| \pm |\vec{r}_{fp} - \vec{r}_{tfp}|}{c} + \frac{|\vec{r}_r - \vec{r}_{fp}|}{c} \tag{2}$$

The transmit origin, $\vec{r}_e$ is the center element of the transmit sub-aperture. $\vec{r}_{tfp}$ and $\vec{r}_{fp}$ is the position of the transmit focal point and the receive focusing point respectively. The $\pm$ in (2) refer to whether the FP is above or below the VS. With SASB the first stage beamformer has a fixed receive focus and the delay values, t_d are calculated in accordance with Fig. 2 (right)

$$\begin{aligned} t_{d_{fp}}(z_v) = & \quad \frac{1}{c}\Big(|\vec{r}_{tfp} - \vec{r}_e| \pm |\vec{r}_{fp} - \vec{r}_{tfp}| \\ & \pm |\vec{r}_{tfp} - \vec{r}_{fp}| + |\vec{r}_r - \vec{r}_{tfp}|\Big) \\ = & \quad \frac{1}{c}\Big(2z_v \pm 2|\vec{r}_{tfp} - \vec{r}_{fp}|\Big) \end{aligned} \tag{3}$$

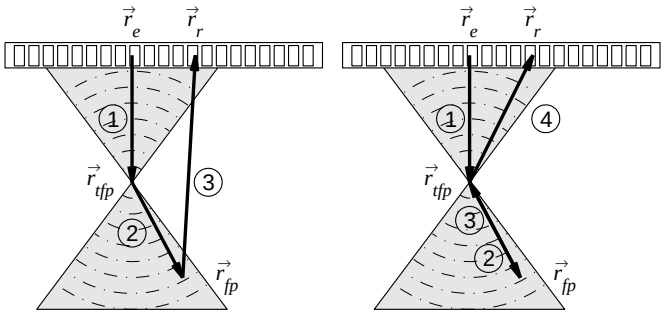

FIG. 2. Wave propagation path (solid line) for calculating the receive focusing time delays for a focused transmission. The transmit origin is perceived as the center element of the transmitting aperture. Dynamic receive focusing (left) and fixed receive focusing (right).

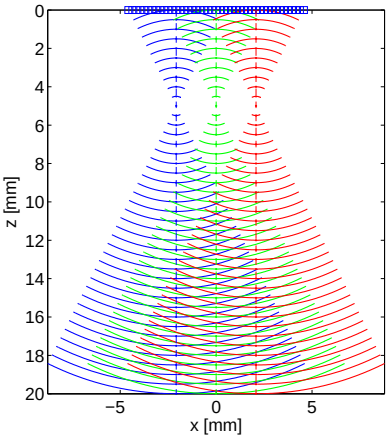

FIG. 3. Example of wave propagation and 1st stage image lines from 3 different emissions. Each point on the image lines contains information from the spatial positions which are indicated by the arc of a circle intersecting the point. A single high resolution image point of the SASB method is obtained by extracting information from all of those 1st stage image lines which contain information about that point.

z_v is the distance from the aperture to the VS. With dynamic receive beamforming the differences between the individual channel delays changes with the position of the focusing point due to the term $|\vec{r}_r - \vec{r}_{fp}|$ in (2). A new set of delay values are, thus, calculated for each focusing point. With fixed receive focusing as in (3) only a single set of delay values is calculated and for each focusing point a constant is added. This is an important issue in respect to the complexity of the beamformer. With dynamic focusing the delay calculations involve among others the computational costly square root operation.

B. Two stage beamforming

The 1st stage RF-lines, which are the output from the first beamformer, are obtained with a single focal point near the transducer in both transmit and receive. This focal point is considered as a VS emitting a spherical wave front spatially confined by the opening angle. Each point in the focused image line contains information from a set of spatial positions. These are defined by the arc of a circle limited by the opening angle that crosses the image point and has a center in the focal point as illustrated in Fig. 3. A single image point is therefore represented in multiple 1st stage lines obtained from multiple emissions. This is exploited in the second stage. Each HRI consists of a number of high resolution image lines - the output lines from the 2nd stage beamformer. In this paper, N denotes the number of emissions, which is the same as the number of 1st stage lines and also the number of high resolution lines. Each sample in a high resolution line (HRL) is constructed in the second beamformer by selecting a sample from each of those 1st stage lines, which contain information from the spatial position of the image point and summing a weighted set of these samples.

The number of elements in the transmit sub-aperture, the depth of the focal point and, thus, the $F\#$ determines the opening angle, hence the width of the transmitted wave field and the point spread function (PSF). A LRI of the entire imaging area can not be formed after each emission due to the spatially limited wave propagation. Instead, for each image point in a HRL it must be determined which emissions that have a wave field encompassing the image point. These emissions contribute to the HRL, and samples from each of them are selected according to the SAF delays, and added together. In other words a single HRL is composed of the sum of a number of low resolution lines. A single low resolution line (LRL) is, thus, the contribution from a given emission to a HRL. The term LRL is used for an RF-line, which has been processed using SAF and which contains at least one non-zero sample that carries information from one of the image points of the HRL.

The SAF can be formulated as a sum over LRL's. A single sample of the HRL, representing the image point at the location $\vec{r}_{ip}$ with lateral coordinate x and axial coordinate z, can be expressed as

$$h(x,z) = \sum_{k}^{K(z)} \mathcal{W}(x_k,z) l_{x_k}(z)\,. \tag{4}$$

$h(x,z)$ is the HRL sample, and $l_{x_k}(z)$ is the LRL sample from the emission with lateral position x_k. The variable $\mathcal{W}$ is an apodization function with $K(z)$ values, which controls the weighting of the contribution from each of the LRL's. It is a function of the axial position of the image point since the number of contributing emissions, $K(z)$ increases with range. K determines the number of VS's applied for a given HRI point and is a measure of the size of the synthesized aperture. $K(z)$ can be calculated directly from the geometry shown in Fig. 4 as

$$K(z) = \frac{L(z)}{\Delta} = \frac{2(z-z_v)\tan(\alpha/2)}{\Delta} \tag{5}$$

showing that K increases linearly with range. This facilitates a range independent lateral resolution. $L(z)$ is the lateral width of the wave field at a depth, z, and Δ is the distance between the VS's of two consecutive emissions. α is the opening angle of the VS. It is the angular span for which the phase of the wave field can be considered constant. The opening angle can

be expressed as

$$\alpha = 2\arctan\frac{1}{2F\#}, \tag{6}$$

which is a valid approximation[21]. With L_A denoting the size of the sub-aperture $F\# = z_v/L_A$. The LRL can be formulated

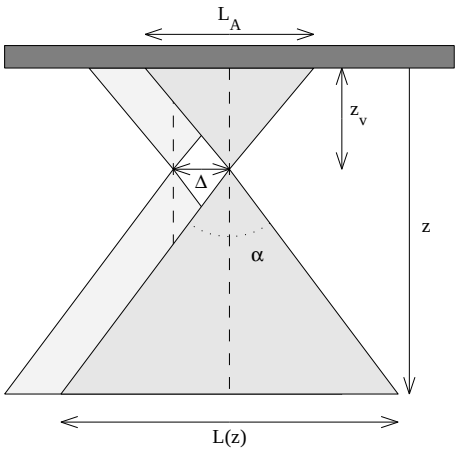

FIG. 4. Geometry model of the emitted wave fields from two consecutive emissions. The lateral width, $L(z)$ of the wave field at a depth, z determines the number of LRL's which can be added in the 2nd stage beamformer for an image point at depth, z.

using the RF-line, $s_{x_k}(z')$

$$l_{x_k}(z) = s_{x_k}(z'). \tag{7}$$

z' is the axial position at which to select a sample from the RF-line and is not the same axial position as in the HRL. z' can be found from the distance function, $z' = d(\vec{r}_{v_{x_k}}, \vec{r}_{ip})$ which calculates the transmit-receive round trip travel path for the SAF, and thus the sample index for the RF-line, $s_{x_k}(z')$. The transducer elements are electronically focused at the VS at the position $\vec{r}_{v_{x_k}}$ with a focal distance of z_v from the aperture. The aperture is focused in both transmit and receive and the distance function becomes a sum of transmit and receive travel paths

$$d(\vec{r}_{v_{x_k}}, \vec{r}_{ip}) = 2z_v \pm 2|\vec{r}_{ip} - \vec{r}_{v_{x_k}}| \tag{8}$$

The $\pm$ in (8) refer to whether the image point is above or below the VS. A single sample of the HRL can thus be formulated using (4) and (7)

$$h(x,z) = \sum_{x_k}^{K(z)} \mathcal{W}(x_k, r) s_{x_k}(d(\vec{r}_{v_{x_k}}, \vec{r}_{ip})). \tag{9}$$

The formulation of the method in this section assumes an aperture with an infinite number of elements. This becomes apparent when observing (5). At greater depth $K(z)$ will exceed the number of available 1st stage lines, N. At depths beyond the point where $K(z) = N$ the synthesized aperture will no longer increase with depth. The $F\#$ will increase and the lateral resolution will no longer be range independent beyond that depth. Another consequence of a limited element count is that the opening angle of the VS decreases as the position of the VS approaches the transducer edges as indicted in Fig. 5. The synthesized aperture decreases for the HRL's near the edges, since K decreases. The lateral resolution is, thus, laterally dependent. The apodization function $\mathcal{W}$ is also laterally dependent with a finite aperture. The HRI is composed of a sum of LRI's from multiple transmissions as formulated in (9). The formulation assumes that the image object is stationary during all transmission, which is not the case in-vivo. Tissue motion and motion artifacts are nevertheless not completely destructive to SA imaging. The susceptibility to motion of SA imaging has been investigated by several authors[22–30], and techniques to address the problems with tissue motion have been demonstrated.

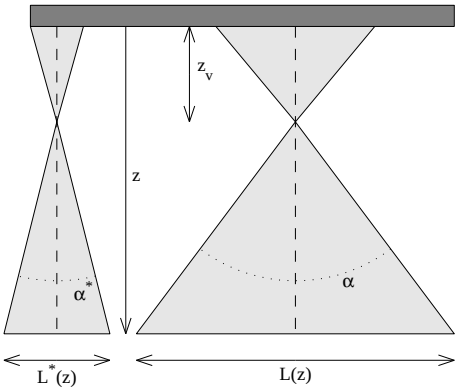

FIG. 5. Geometry model of the emitted wave fields from two emissions. The opening angle of the VS decreases as the position of the VS approaches the transducer edges. This has an influence on the calculation of $K(z)$ and makes the lateral resolution laterally dependent.

C. Implementation

In SAF data from multiple emissions are applied. This could essentially decrease the image frame rate if a full set of emissions is needed to construct a HRI. Nikolov and Jensen proposed SA recursive imaging[31] to be able to construct a new frame after each emission. In SASB acquisition of a full set of N emissions is also a necessity before a HRI can be constructed. By storing the N most recent 1st stage lines a new HRL can be constructed after each emission. This is feasible by having a temporal offset between the reconstructed HRL and the acquired RF-line corresponding to $N/2$ emissions. The RF-lines across the aperture are denoted $j = 1,2,\ldots N$ and the HRL's are denoted $J = 1,2,\ldots N$. The HRL $J = n$ can be constructed while acquiring the RF-line, j

$$j = \begin{cases} n + N/2 & \text{for} \quad 1 \le n \le N/2 \\ n - N/2 & \text{for} \quad N/2 < n \le N \end{cases}$$

Following this scheme the 1st stage lines which potentially can contribute to a given HRL, is always available.

A view on implementation of the SASB at a block function level demonstrates a requirement for two beamformers and memory for storage of the 1st stage image lines to feed

the 2nd stage beamformer. The 1st stage beamformer is simple since the receive delay-profiles are the same for all image points except for a depth dependant additive constant. It only requires calculation of a single profile or a look up table (LUT) with a single entry. It could easily be analog and thereby save many ADC's. The 2nd stage beamformer has the complexity of a general dynamic receive focusing beamformer. For each depth a separate entry in a LUT for a profile is required or the delay profile must be calculated. Apodization is also a desirable requirement for the 2nd stage beamformer to suppress off-axis energy lobes. Since $K(z)$ increases linearly with depth the apodization is dynamic. The apodization is also a function of the lateral position of the HRL due to the finite aperture and it can profitably be calculated as a parametric function. The number of channels in the 2nd stage beamformer is determined by the number of acquired 1st stage lines and a combination of the demand for penetration and resolution.

III. SIMULATION RESULTS

In this section the method is investigated using simulations in Field II[18,19] and SAF is carried out using the Beamformation Toolbox, *BFT2*[20]. Images of point targets using different realizations of SASB are created. The axial and lateral resolution are extracted and compared to conventional B-mode imaging. The simulations are made with a model of a linear array 7 MHz transducer with properties similar to a commercial transducer.

A. Setup

The parameters which are the most decisive for the performance of the SASB imaging method are the depth z_v (the focal depth), and the $F\#$ of the VS. A parameter study is done by varying the combination of z_v with values of $5, 10, 15, 20$ mm and the $F\#$ with values in the range 0.5 to 2.5. The study is done with a fixed set of transducer parameters and processing parameters shown in Table I.

In the main parameter study the value of $N_e = 401$ has been set to exclude the effects of a finite aperture to demonstrate the ability of the method to generate a range independent resolution. The number of 1st stage image lines and also 2nd stage image lines is the same as the number of transducer elements. Only LRL's symmetric around the HRL are valid candidates for the 2nd stage processing. The apodization function for a given depth $\mathcal{W}(z)$ may differ between two neighboring HRL's if the number of symmetric LRL's is different.

In this study a single cycle sinusoid is used as excitation and a weighted double cycle sinusoid is used to simulate the transducer impulse response. Another less extensive study is performed with more practical realizable parameters. The number of elements is $N = 191$. A double cycle sinusoid forms the excitation, and the measured impulse response of the applied transducer type is used. The scattering media consists of stationary point targets (PT) placed in the center of the image in the range from 5 mm to 95 mm with a distance of 10 mm.

Parameter		Value
Various		
Sampling frequency	f_s	120 MHz, (20 MHz)
Transducer		
Pitch	Δ	0.208 mm
Center frequency	f_c	7 MHz, (5 MHz)
Bandwidth, relative	B	0.6
Elevation Focus	z_{ele}	25 mm
Number of elements	N	401, (191)
Excitation		1, (2) cycles
Impulse response		1-cycle, (measured IR)
1st stage processing		
Focusing		fixed, (xmt/rcv)
Number of channels, xmt/rcv	N_{1st}	63/63
Transmit Sub-aperture		Symmetric only
Transmit apodization	$\mathcal{A}_{xmt}$	Hamming, (Boxcar)
Focal depth (virtual source)	z_v	$5, 10, 15, 20$ mm
Receive Apodization	$\mathcal{A}_{rcv}$	Hamming
Receive Sub-aperture		same as transmit
Number of image lines	N	401, (191)
Distance between lines	Δ	0.208 mm
2nd stage processing		
Focusing		Synthetic aperture
Number of channels	N_{2nd}	401, (191, 127, 63)
SA Weighting	$\mathcal{W}$	Hamming
Number of image lines	N	401, (191)
Distance between lines	Δ	0.208 mm
Applied 1st stage lines		Symmetric only

TABLE I. Applied values for the simulation parameter study. Values in brackets are applied for various performance illustrations. If nothing else is noticed the value without brackets are applied.

B. Resolution study

Different realizations of SASB are simulated to evaluate performance and limitations. The position of the VS and the opening angle determines the image area covered by a single emission. If the covered area increases, the number of 1st stage lines, which can be used for the 2nd stage beamforming, also increases, yielding a larger synthesized aperture. This explicitly sets demands on the size of the array and the number of required 2nd stage beamformer channels if a range independent resolution is the objective. The study will show that other complications exist with the combination of a shallow focal depth and a large opening angle.

The envelope HRI's are shown in this section. The axial and lateral resolution are extracted at the image center for several depths. The resolution is quantified at -6 dB, the Full Width at Half Maximum (FWHM), and at -40 dB. For each PT the resolution is calculated as the width at which the envelope amplitude has decreased to the specified level relative to the maximum level at that given PT. For the lateral resolution the envelope amplitude is taken as the maximum amplitude within a axial range of $\pm$ 3 mm around the PT. Likewise for the axial resolution the envelope amplitude is taken as the maximum amplitude across the entire lateral range of the image. A poor lateral resolution is the consequence of having a PSF with a wide main lobe and/or high side-lobe levels. The illustrations of the quantified lateral resolution reflects this by also showing the main-lobe resolution as a dotted line, but only if the lateral

PSF has a distinct main-lobe and side-lobe distribution. That is if the lateral PSF drops below the -40 dB level and rises above this level again at a greater wider lateral position.

The PSF at the output of the 1st stage beamformer has a large extent because of the fixed receive focusing. The curvature is determined by the distance between the VS's and the point of the PSF. Consider the point at position $\vec{r}_p = (x,z) = (0,z_p)$. The curvature, $z_c(x)$ is

$$z_c(n) = z_p + \sqrt{(z_p - z_v)^2 + (|n|\,\Delta)^2}\,. \qquad (10)$$

The variable x has been substituted by $n\Delta$, where $-N/2 \leq n \leq N/2$ is the VS number counting from the VS at $x = 0$. The contour plot of the PSF is shown in Fig. 6 with a VS at 5 mm and with $F\# = 0.5$, and $F\# = 2$. The shape of the PSF is the same in both cases, but the width of the PSF differs due to the different opening angles. $z_c(n)$ from (10) has been plotted on top of the contour plot to illustrate the coherence. A PT is placed at $z = 65$ mm and z_c has been plotted for two points at $z_p = 64$ mm and $z_p = 66$ mm, respectively. The curvatures of these plots are the same as for the PSF.

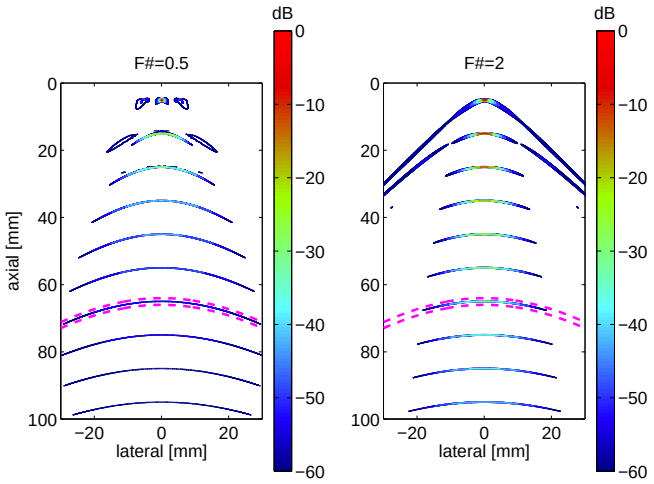

FIG. 6. Contour plots of the envelope of the output from the 1st stage beamformer. $F\# = 0.5$ (left), and $F\# = 2$ (right). The VS is at 5 mm. The curvature of the PSF is determined by the distance between the VS's and the point of the PSF. This is calculated analytically and shown as dotted lines for two points just above and below the PT at $z = 65$ mm.

The envelope images after 2nd stage processing of these data sets are shown in Fig. 7 with a 60 dB dynamic range. The images are constructed with $N = 401$ which equals an image width of approximately 83 mm, but the displayed images have been cropped to a width of 40 mm. If the dominant side-lobes are discounted to begin with the resolution seems range independent. The lateral resolution decreases as the $F\#$ increases as expected because of the decrease in the width of the synthesized aperture.

The number of applied 1st stage lines in the 2nd stage beamformer at a given depth determines the width of the synthesized aperture. This is expressed by $K(z)$ from (5). This was for the image-center line only, and assumed an infinite aperture. The theoretical required number of lines, and the actual number of applied lines for the center HRL is shown in Fig. 8 for the different setups represented in Fig. 7. The linear dependence on depth is only a reality until a certain depth. At this depth the required number of applied VS's approaches a level where the VS's near the transducer edges are included. The opening angles of these VS's decrease due to the limited aperture and the slope of $K(z)$ drops off. This drop-off occurs at 42 m and 84 mm for $F\# = 0.5$ and $F\# = 1$ respectively. For $F\# = 1.5$ and $F\# = 2$ the linearity is maintained through range.

The quantified resolution of the HRI in Fig. 7 is shown in Fig. 9. The resolution is practically constant at -6 dB and -40 dB through range for all values of $F\#$, with a few exceptions. The exceptions are for those PT in near proximity to the VS when $F\# = 0.5$. Here the side-lobe level is very dominant.

Side-lobes are also noticeable for $F\# = 1$ when looking at the HRI in Fig. 7. They are below the -40 dB level though and do not show in Fig. 9. They do show when looking at the -50 dB level in Fig. 10. Again the main-lobe resolution (dotted line) is practically constant but the difference between the main-lobe resolution and the resolution including the side-lobes (solid line) is significant.

1. *Investigating grating-lobes*

The off-axis energy-lobes in Fig. 7 for $F\# = 0.5$ are dominant. Taking a closer look at the phase of those LRL's which are summed in the 2nd stage beamformer can disclose the origin of this artifact. The part of the image containing the PT at 15 mm is shown in Fig. 11. Three different HRL's are investigated. They are marked with dotted lines in Fig. 11. SASB relies on phase coherent addition of the LRL's as expressed in (4). The LRL's composing the center HRL are plotted in Fig. 12. It is apparent that the LRL's are completely phase aligned and add up constructively as expected. The figure shows the LRL's before and after the weighting function. It also shows the HRL, hence the summation of the LRL's and the corresponding envelope. Finally the envelope of the weighted HRL is shown relative to the maximum of the HRI in Fig. 11.

The LRL's composing the HRL at $x = 3.1$ mm are plotted in Fig. 13. The LRL's are shown before the weighting and a zoom in on a few of the LRL's after the weighting function is shown. The phase shift between consecutive LRL's is close to half a pulse-echo wave length and this destructive summation yields an envelope level near -60 dB.

The LRL's composing the HRL at $x = 6.7$ mm are plotted in Fig. 14. The phase shift between consecutive LRL's has increased to almost an entire pulse-echo wave length and the LRL's add up constructively to an envelope level above -40 dB. In this simulated setup the pulse-echo signal consists of only a few periods, hence only a few non-zero contributions are included in the summation of the LRL's. If the pulse-echo signal contains several periods several non-zero LRL's will be present in the sum, yielding an even higher envelope level.

The artifacts shown are best described as grating lobes, since they arise due to lateral spatial under-sampling. Consider having a setup with a phased array transducer with a $\lambda/2$ pitch and, thus, twice the lateral density of VS's. The illustration of LRL's prior to summation equivalent to the one shown

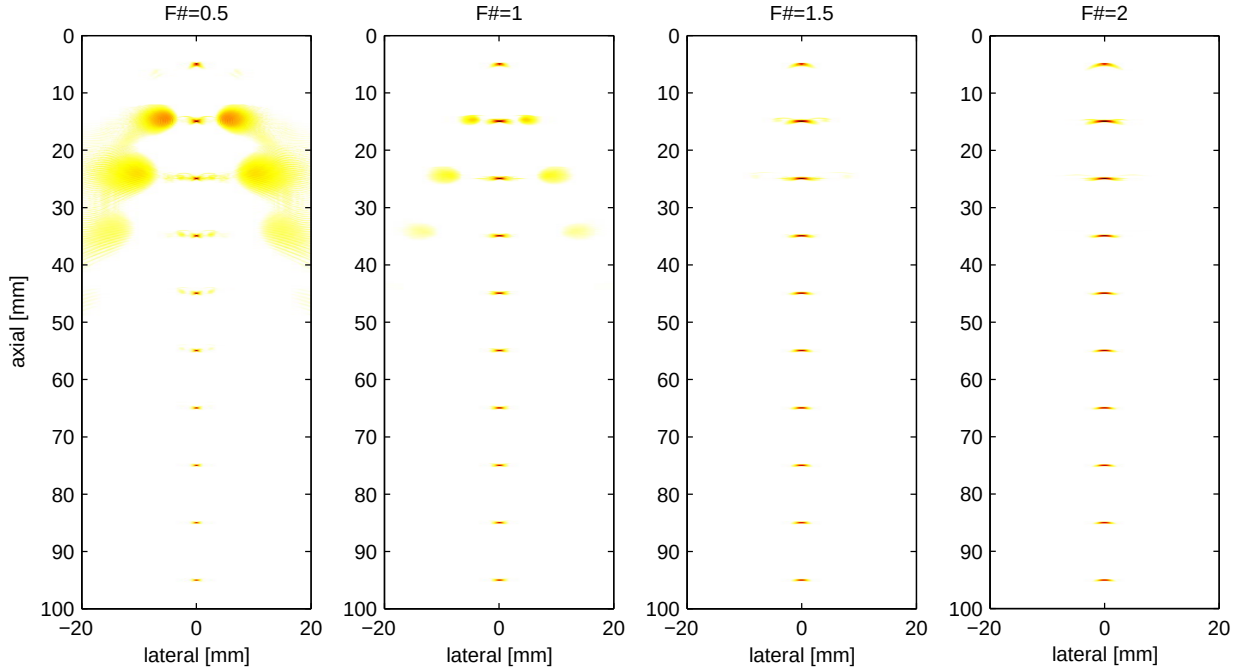

FIG. 7. Envelope Images with the VS at 5 mm and with different values of $F\#$. Dynamic Range is 60 dB.

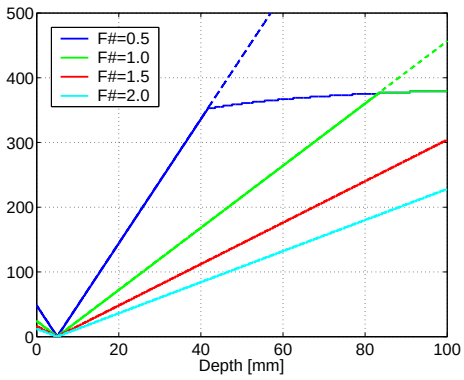

FIG. 8. The number of applied 1st stage lines in the 2nd stage beamformer for the center HRL. Shown for the four different setups represented in Fig. 7. Required number to obtain range independent resolution (dotted lines). Actual number of applied lines (solid lines).

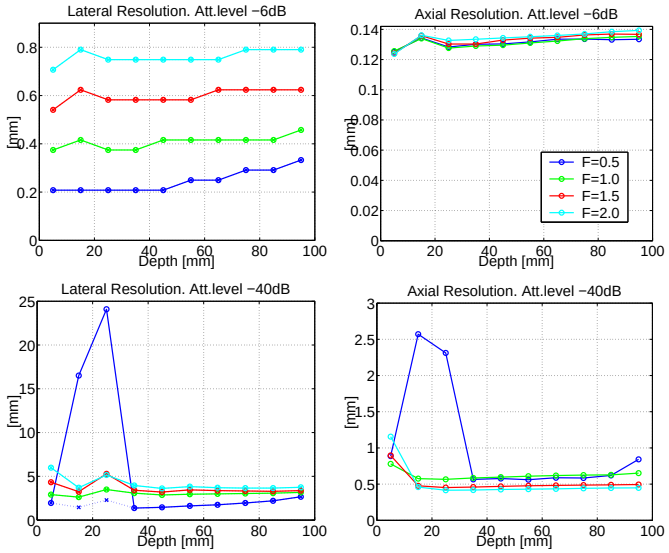

FIG. 9. Resolution as function of depth at -6 dB (top) and -40 dB (bottom). Lateral resolution (left) and axial resolution (right). If the lateral PSF has a distinct main-lobe and side-lobe distribution, the main-lobe resolution is shown as a dotted line. Shown for the four different setups represented in Fig. 7.

in Fig. 14 will contain LRL's with a phase shift between consecutive LRL's of only half a wave length. Every second LRL will be equal to the ones shown in Fig. 14 but every other LRL will have a phase which is in between the two. The result is destructive summation instead of unintentional constructive summation, and the massive grating lobes are avoided. This is exemplified in Fig. 15. Two HRI's are constructed using a linear array with λ-pitch and a linear phased array with $\lambda/2$-pitch respectively. Both having 401 elements, a VS at 5 mm, and with $F\# = 0.75$. The linear array is, thus, twice the width of the phased array, but the image has been cropped to the same width as the phased array image. The difference between the images is striking, since the grating lobes are avoided by increasing the lateral spatial sampling in the 1st stage processing.

The VS's can be conceived as elements in a virtual array. In SASB the wave fields from several emissions are sampled by the virtual array and coherently added. Grating lobes arise at a combination of a sparse spatial sampling by the virtual array and wave fields with incident angles beyond a certain limit. Both of these parameters can be controlled in SASB to prevent

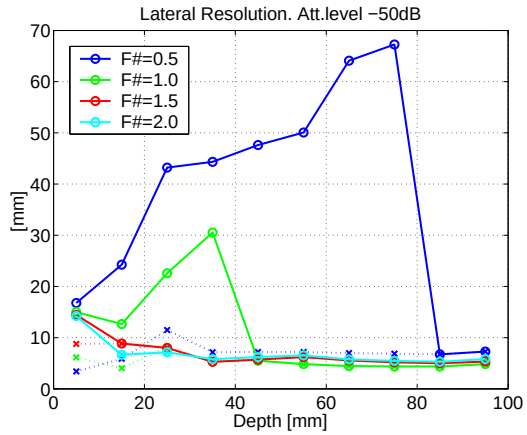

FIG. 10. Lateral Resolution as function of depth at -50 dB. The main-lobe resolution (dotted line), and the resolution including the side-lobes (solid line). Shown for the four different setups represented in Fig. 7.

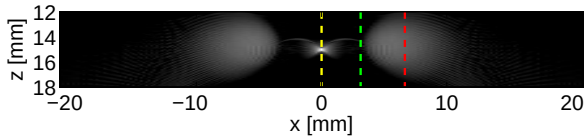

FIG. 11. A zoom in on the HRI shown in Fig. 7 for $F\# = 0.5$. Three different HRL's are marked with dotted lines. The LRL's composing these HRL's are shown in Fig. 12, Fig. 13, and Fig. 14.

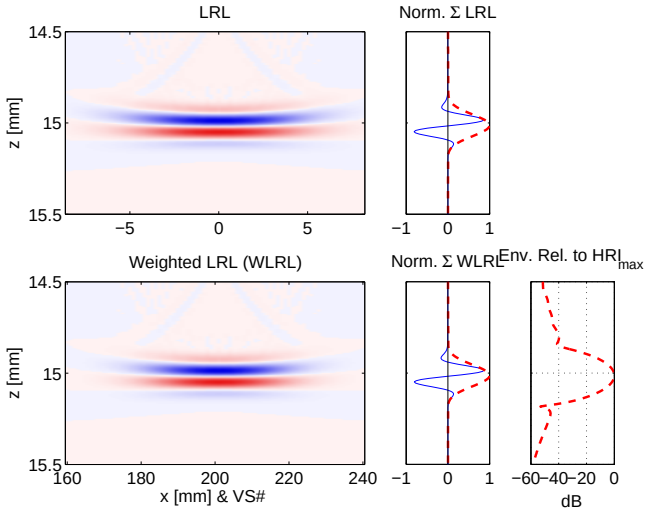

FIG. 12. The LRL's composing the center HRL of the HRI shown in Fig. 11. The LRL's are shown before and after the weighting function. The summation of the LRL's and the corresponding envelope are also shown.

grating lobes. For a given array and a fixed distance between the VS's the range of incident angles must be restricted. This is possible by putting a limit to the opening angle of the VS.

The restriction on the opening angle to avoid grating lobes

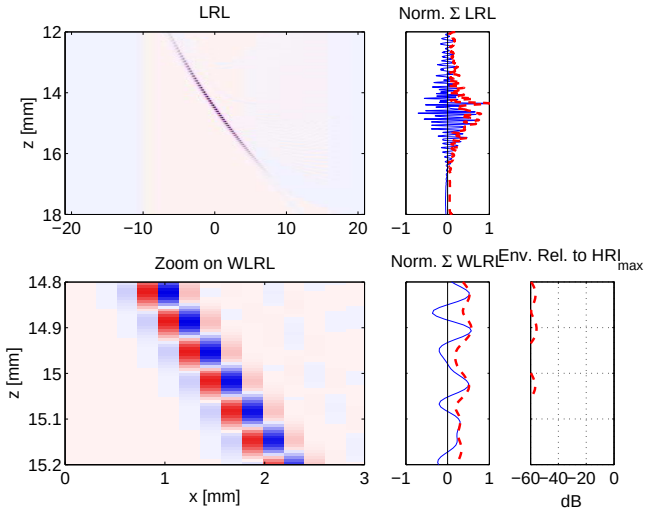

FIG. 13. The LRL's composing the off-center HRL at the lateral position $x = 3.1$ of the HRI shown in Fig. 11. A zoom in on a few of the weighted LRL's is shown to visualize destructive summation of the LRL's.

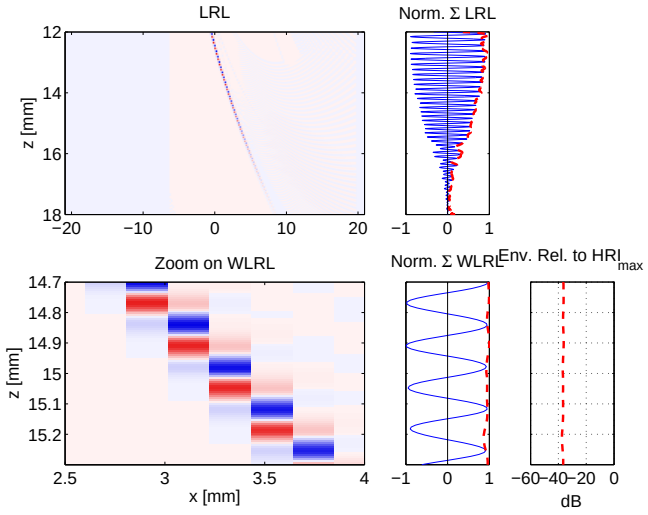

FIG. 14. The LRL's composing the off-center HRL at the lateral position $x = 6.7$ of the HRI shown in Fig. 11. A zoom in on a few of the weighted LRL's is shown to visualize a phase-shift of almost an entire pulse-echo wave length, yielding constructive summation, and an envelope level above -40 dB.

can be determined from an analysis of the LRL's constituting the off-center HRL's. The appearance of these LRL's can be predetermined to some extent. In Fig.14 the LRL's constituting the center HRL at the lateral position $x_h = 0$ are phase-coherently aligned. They are aligned at the depth, $z_p = 15$ mm, where a PT at $\vec{r}_p = (x,y) = (0,z_p)$ is placed. The line of phase equality is perpendicular to the line with origin in the VS of the center HRL and going to $\vec{r}_p$. This line has a length $z_r = z_p - z_v$, where z_v is the depth of the VS. In Fig.14 the LRL's constituting an off-center HRL at the lateral position x_h

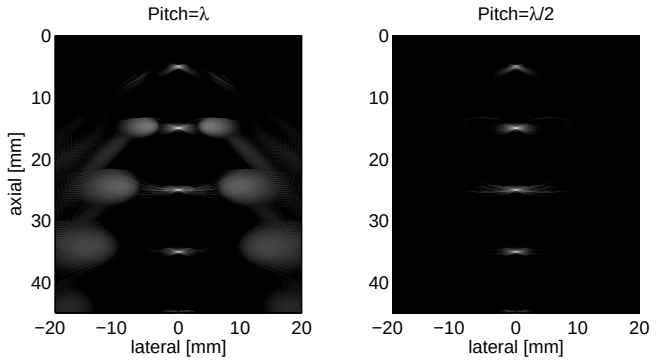

FIG. 15. Two SASB images are constructed using a linear array (left) and a linear phased array (right). Both having 401 elements, a VS at 5 mm, and with $F\# = 0.75$. The linear array is twice the width of the phased array, but the image has been cropped to the same width as the phased array image. Dynamic range is 70 dB.

are no longer aligned phase-coherently. As a simple approximation these LRL's can be found by a rotation of the aligned LRL's. They are rotated such that the line of phase equality is perpendicular to the line with origin in the VS of the off-center HRL and again with length z_r. The angle of this line is

$$\theta_r = \arcsin(\frac{x_h}{z_r}). \tag{11}$$

This geometry is illustrated in Fig. 16 superimposed on the log-compressed envelope of a set of LRL's. The LRL's constitutes the HRL's at $x_h = 1$ mm and $x_h = 4$ mm in the range 12-18 mm. Beyond this range the envelope image is cropped. It seems reasonable, that the line of phase equality is perpendicular to the line originating at the VS.

The rotation of the aligned LRL's is only an approximation, which is valid in the proximity of $x = 0$. The positions of phase equality is not a straight line entirely. The curvature increases for LRL's with increasing distance to the HRL when the distance between the FP and the VS decreases. This would be the case if VS's with large opening angles are applied. The consequence of having a curvature that deviates considerably from the straight line approximation is that the axial shift between consecutive LRL's is greater than estimated for the outermost LRL's. This indicates a requirement for a limited opening angle. It is also an argument for using apodization in the 2nd stage beamformer, which will reduce the influence of the LRL's with increasing distance to the HRL.

The exact positions are also indicated in Fig. 16 for $x_h = 4$ mm as a dashed line cutting through the path of constant phase. The exact positions are determined by observing the focusing indices of each channel in the 2nd stage beamforming, and the indices representing the PT at $\vec{r}_p$ in each channel. These indices are shown in Fig. 17 for the same setup as in Fig. 16 and for a few FP's all placed in the same off-center HRL. For each FP it is registered at which LRL's the intersection between the FP-index and the PT-index takes place. In the reverse process the depth of the intersection between the FP-index and the PT-index is registered for each LRL. This is also shown in Fig. 17, and it is the same way the exact positions of

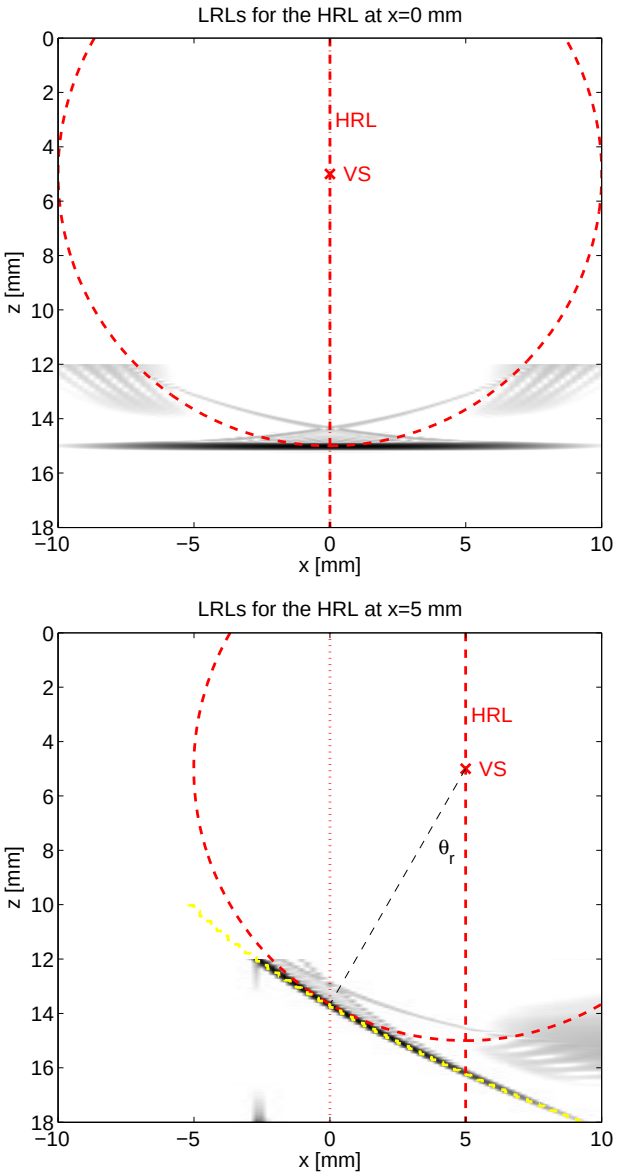

FIG. 16. The log-compressed envelope of the LRL's constituting the HRL's at $x_h = 0$ mm (top) and $x_h = 4$ mm (bottom) is shown in the range 12-18 mm with a dynamic range of 50 dB. The VS is at the depth $z_v = 5$ mm and $F\# = 0.5$. A PT is positioned at the point $\vec{r}_p = (x,y) = (0,z_p)$ with depth, $z_p = 15$ mm. The appearance of the LRL's for the off-center HRL can be approximated by a rotation of the LRL's of the center HRL. The center of rotation is the VS of the off-center HRL, and the rotation radius is $z_r = z_p - z_v$. The angle of rotation $\theta_r = \arcsin(x_h/z_r)$ is also indicated.

phase equality is indicated in Fig. 16.

By applying the approximation about the rotated LRL's it is possible to estimate the phase shift between consecutive LRL's with a simple expression. The axial shift between consecutive LRL's is

$$x = \tan\theta_r \Delta. \tag{12}$$

Substituting θ_r with half the opening angle, $\alpha' = \alpha/2$ the axial

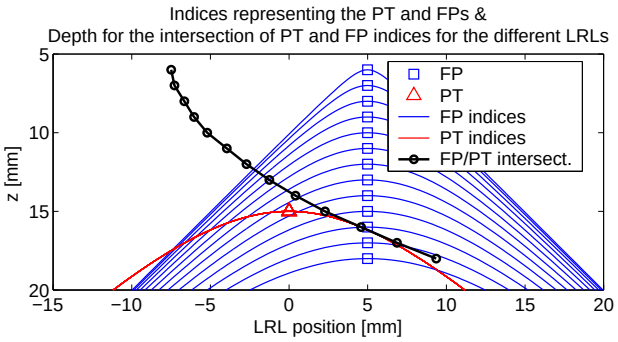

FIG. 17. Focusing indices of each channel in the 2nd stage beamforming for a few FP's ranging from 6 mm to 18 mm from an off-center HRL. Indices representing the PT in each channel. For each LRL the depth of the intersection between the FP-index and the PT-index is shown.

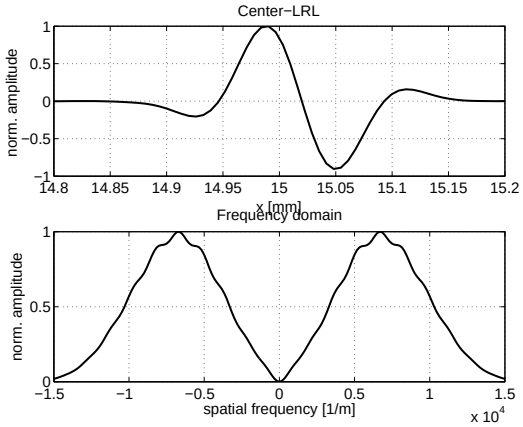

FIG. 18. Center HRL with the VS at 5 mm and $F\# = 0.5$. Shown in a limited range near the PT at 15 mm (top). The spatial frequency content (bottom).

shift can be expressed as

$$x = \tan(\alpha')\Delta = \frac{\Delta}{2F\#}. \tag{13}$$

If the spatial shift does not exceed half the wavelength of the pulse-echo signal, $\lambda_{pe} = \lambda/2 = c/f_0/2$ grating lobes are avoided. This condition can be used to put restrictions on the $F\#$ of the VS

$$F\# \geq \frac{\Delta}{\lambda/2} \quad \text{for } x \leq \lambda/4. \tag{14}$$

The opening angle of the VS limits the range of angles of the wave field. If a transducer with $\Delta = \lambda$ are used in SASB grating lobes are avoided if $F\# \geq 2$.

An approximation of the actual pulse-echo response and the spatial frequency content is extracted from the center LRL, and shown in Fig. 18. It is shown for the setup with VS at 5 mm and $F\# = 0.5$ and for the PT at 15 mm, but the spatial frequency content does not differ noticeably from the other setups and depths. The dominant spatial pulse-echo wavelength is $\lambda_{pe} = 0.15$ mm. With $\Delta = 0.208$ mm the VS must be designed with $F\# \geq 1.39$ with the restriction of (14). For $F\# = 0.5$, $F\# = 1$, $F\# = 1.5$, and $F\# = 2$ the spatial shift between consecutive LRL's measured in units of λ_{pe} is 1.39, 0.70, 0.46, and 0.35 respectively according to (13). The criterion for avoiding grating lobes is obeyed for $F\# = 1.5$, and $F\# = 2$ only. This is also reflected in Fig. 7, and Fig. 10, where the grating lobes evidently are attenuated for $F\# = 1.5$ and $F\# = 2$ compared to the setup where $F\# = 0.5$, and $F\# = 1$. In Fig. 15 a phased array with $\Delta = 0.104$ is applied. In this setup the VS must be designed with $F\# \geq 0.70$ with the restriction of (14). In Fig. 15 this criterion is obeyed with $F\# = 0.75$, and the grating lobes are avoided.

$K(z)$ from (5) determines the number of VS's applied and the size of the synthesized aperture. It is a function of the position of the VS and the opening angle and, thus, the $F\#$. It was shown previously that the grating lobes were appropriately attenuated for the linear array with $F\# = 1.5$ when the VS was at 5 mm. The lateral resolution with $F\# = 1.5$ and different positions of the VS is shown in Fig. 19, and $K(z)$ is shown in Fig. 20. The resolution functions are very similar but not the same in the four different setups because of the different number of applied VS's.

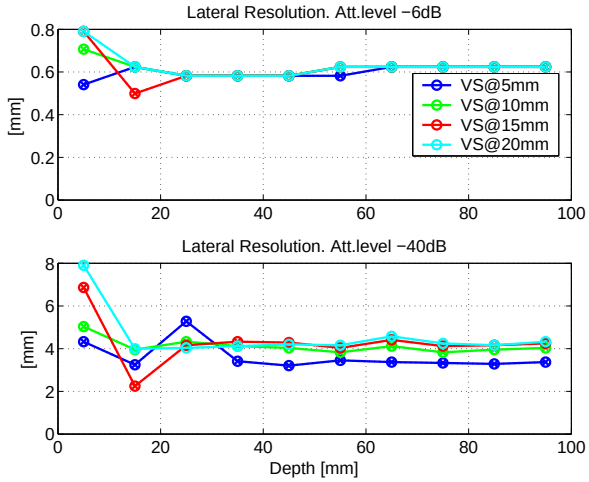

FIG. 19. Lateral resolution with $F\# = 1.5$ as a function of depth at -6 dB (top) and -40 dB (bottom).

2. Influence of transducer impulse response.

The performance results presented in the previous sections were based on a transducer with $N = 401$, a short excitation signal, and a simple impulse response. The performance using a more realistic transducer simulation model is presented in this section and a comparison between the two is made. Envelope images with the VS at 20 mm, $F\# = 2$, and with the two different simulation models are shown in Fig. 21. The new simulation model has $N = 191$. The excitation signal has two periods, and the impulse response has been measured yielding a longer pulse-echo (PE) response. The difference between the two images is significant. The axial resolution has decreased as a consequence of the extended PE response. The lateral resolution has improved in the entire range also beyond

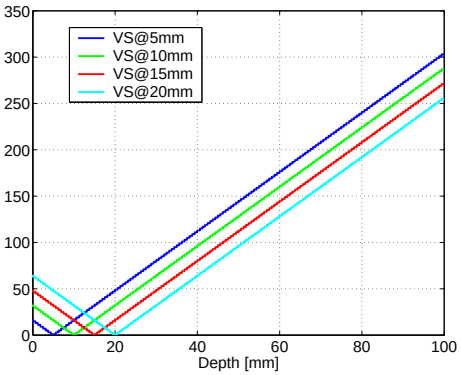

FIG. 20. The number of applied 1st stage lines in the 2nd stage beamformer for the center HRL when $F\# = 1.5$.

depths of 80 mm, where $K(z)$ ceases to increase linearly. The axial and lateral resolution are extracted, and shown in Fig. 22. The improvement in lateral resolution at -40 dB is at least a factor of 2.

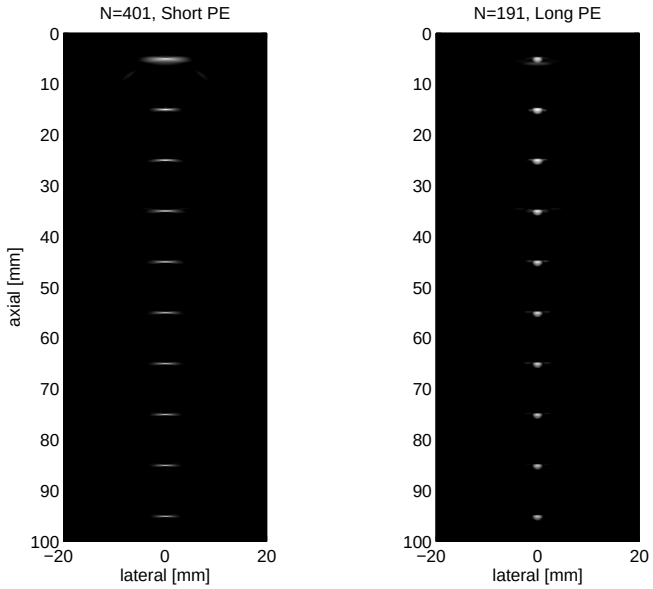

FIG. 21. Envelope images with the VS at 20 mm and with $F\# = 2$. Two different simulation models are used. $N = 401$, and a short pulse-echo (PE) response (left). $N = 191$, and a long pulse-echo response (right). The image using $N = 401$ has been cropped to the same width as the image using $N = 191$. Dynamic Range is 60 dB.

To illustrate the cause of the difference in performance, the LRL's composing the HRI's are investigated. The investigation concerns only the range from 53 mm to 57 mm which include a single PT at a depth of 55 mm. The HRI's in this range are shown in fig 23, superimposed with vertical dashed lines indicating those HRL's for which the LRL's are shown.

The LRL's for the center HRL are shown in Fig. 24. The LRL's for the off-center HRL are shown in Fig. 25. In these figures the LRL's after LRL-weighting are shown. They also show the summation of the LRL's and the corresponding envelope. Finally the envelope of the weighted HRL is shown

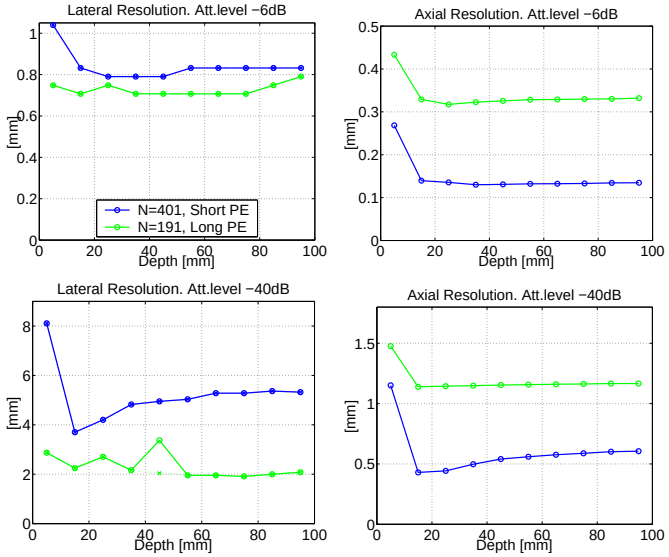

FIG. 22. Resolution as function of depth at -6 dB (top) and -40 dB (bottom). Lateral resolution (left) and axial resolution (right). If the lateral PSF has a distinct main-lobe, and side-lobe distribution, the main-lobe resolution is shown as a dotted line. The resolution is extracted from the HRI's in Fig. 21.

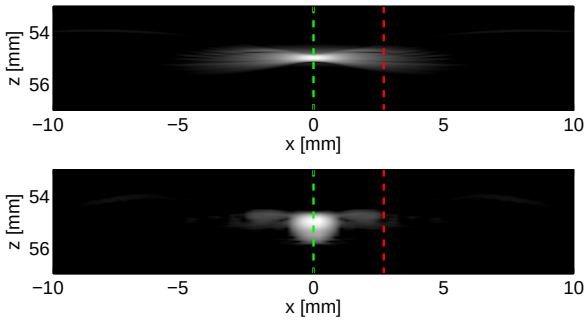

FIG. 23. Envelope images with the VS at 10 mm, and with $F\# = 2$ from Fig. 21. Short PE response (top), and long PE response (bottom). Shown in the range from 53 mm to 57 mm, and superimposed with vertical dashed lines indicating those HRL's for which the LRL's are shown. The LRL's are shown in Fig. 24 and Fig. 25.

relative to the maximum of the HRI's in Fig. 23. The LRL's sum completely constructive for the center HRL in both setups.

For the off-center HRL's the LRL's sum destructively toward zero level. With a short pulse-echo response the off-center HRL is composed of the sum of a only a few positive and negative half-periods. The amplitudes of these half-periods varies with range and lateral position. The amplitude of the HRL, thus, varies with range. The variation over range is considerable due to the sparse number of cycles in the sum.

With a longer pulse-echo response the off-center HRL is composed of the sum of several positive and negative half-periods. The amplitudes of these half-periods decay smoothly over range and lateral position and on average sum destructively to a zero level. The HRL is of oscillating nature with the same center frequency as the pulse-echo response, which

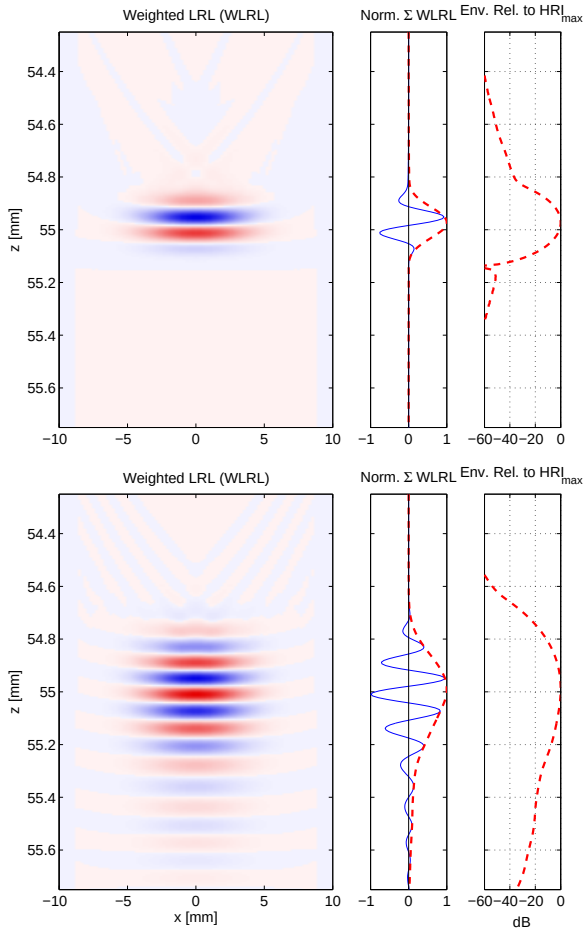

FIG. 24. The LRL's composing the center HRL of the two HRI's shown in Fig. 23. The LRL's are shown after the weighting function. The summation of the LRL's and the corresponding envelope are also shown.

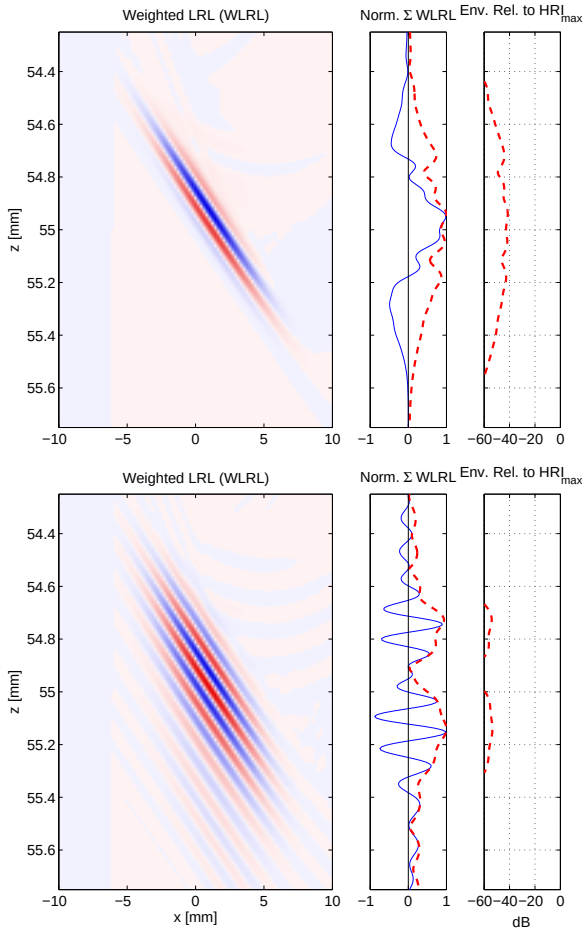

FIG. 25. The LRL's composing the off-center HRL of the two HRI's shown in Fig. 23. The LRL's are shown after the weighting function. The summation of the LRL's and the corresponding envelope are also shown.

VS depth	$F\# = 1.5$	$F\# = 2$
5 mm	17	13
10 mm	33	25
15 mm	49	37
20 mm	65	49

TABLE II. The number of array elements used during transmission as a function of VS position and $F\#$.

is not the case for the setup with the short PE response.

3. *Comparison to dynamic receive focusing.*

The performance of SASB is among others a function of VS position and $F\#$. These parameters also determine the number of elements used during transmission. This has an influences on the emitted energy and the signal to noise ratio. It was shown in Section III.B.1 that the grating lobes were appropriately attenuated for $F\# = 1.5$ and $F\# = 2$. The number of elements used as a function of VS position and $F\#$ is shown in Table II

The choice of configuration for comparison with DRF is based on the results presented in Fig. 26. Here the lateral resolution for a number of configurations is shown. In all configurations the results are based on the realistic transducer simulation model introduced in Section III.B.2. The performance with the VS at 20 mm and $F\# = 1.5$ is superior to the other configurations in almost the entire range. It is thus a rational choice for a good performance and a comparison with DRF.

Fig. 27 show images with DRF and SASB side by side, and Fig. 28 show the quantified lateral resolution for different configurations. The quantified axial resolution does not differ between the different configurations and is not shown. Different positions of the transmit focal point in DRF has been applied for a fair comparison. The VS is at 20 mm and $F\# = 1.5$ for all cases of SASB. In Fig. 27, and in the previous sections the number of channels in the 2nd stage beamformer is unlimited, so that $N_{2nd} = N$. In Fig. 28 additional SASB results are presented where the number of channels has been limited to $N_{2nd} = 127$, and $N_{2nd} = 63$.

There is an substantial improvement in resolution using SASB compared to DRF. It accounts for both the FWHM and the resolution at -40 dB. The improvement in FWHM is at least a factor of 2 and the improvement at -40 dB is at least

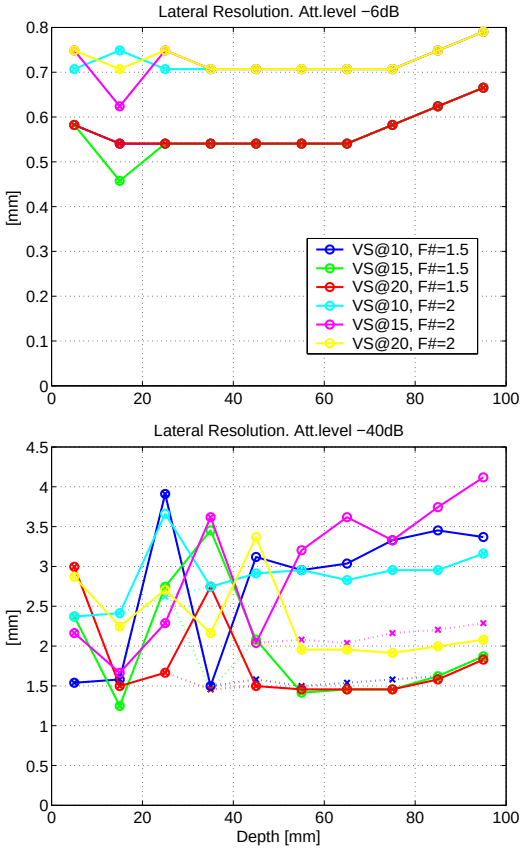

FIG. 26. Lateral resolution of SASB as function of depth at -6 dB (top) and -40 dB (bottom). If the lateral PSF has a distinct main-lobe, and side-lobe distribution, the main-lobe resolution is shown as a dotted line. In all configurations the results are based on the realistic transducer simulation model introduced in Section III.B.2.

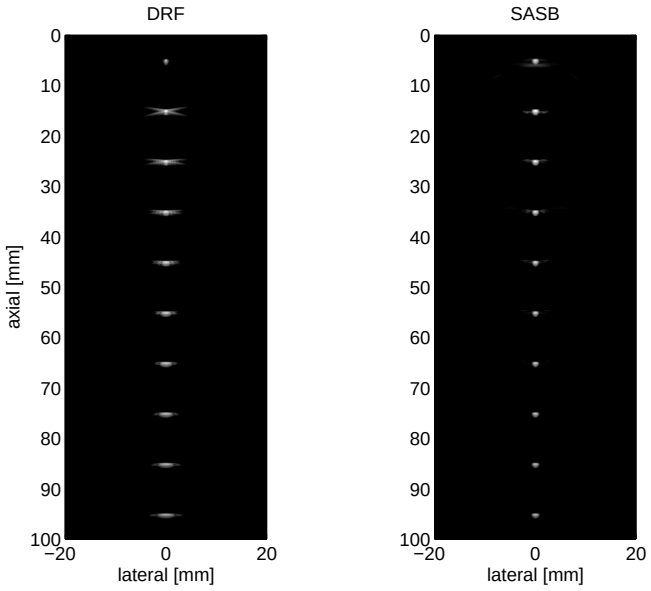

FIG. 27. Envelope images using DRF (left) and SASB (right). For DRF the transmit focal point is at 70 mm. For SASB the VS is at 20 mm and $F\# = 1.5$. Dynamic Range is 60 dB.

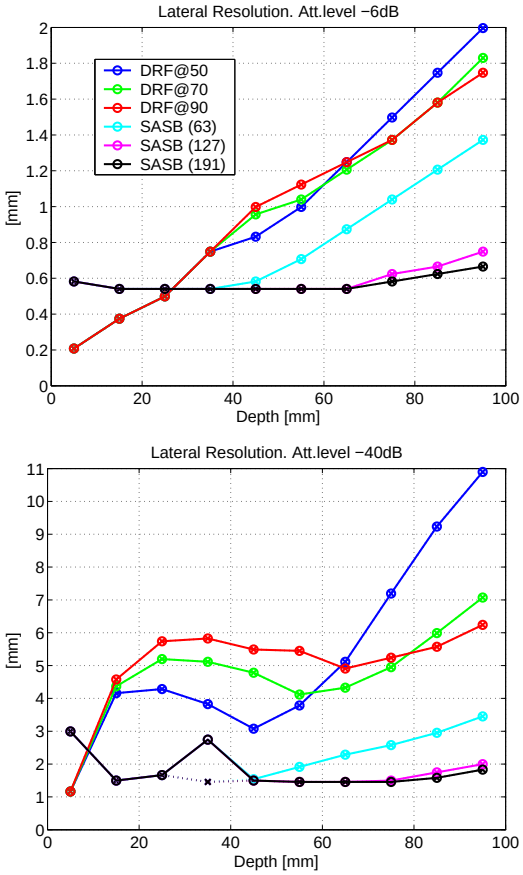

FIG. 28. Lateral resolution of DRF and SASB as function of depth at -6 dB (top) and -40 dB (bottom). If the lateral PSF has a distinct main-lobe, and side-lobe distribution, the main-lobe resolution is shown as a dotted line. In all configurations the results are based on the realistic transducer simulation model introduced in Section III.B.2. For DRF the transmit focal point is at 50 mm, 70 mm, and 90 mm. For SASB the VS is at 20 mm and $F\# = 1.5$. SASB results are presented using different number of available 2nd stage beamformer channels. $N_{2nd} = 63$, $N_{2nd} = 127$, and $N_{2nd} = 191$.

a factor of 3. The improvement of SASB over DRF is a reality except for a few exceptions. At depths until 20 mm the FWHM is superior with DRF. With SASB the resolution is almost constant throughout the range. For DRF the FWHM increases almost linearly with range and the resolution at -40 dB is fluctuating with range.

By putting restrictions on the number of 2nd stage beamformer channels the system complexity is reduced. It will have a negative consequence on resolution, since the synthesized aperture decreases. When the number of channels is restricted to $N_{2nd} = 63$, and $N_{2nd} = 127$ then the depths at which $K(z)$ ceases to increase linearly is at 40 mm and 61 mm respectively. This is also apparent when observing the resolution in Fig. 28 when these restrictions are applied. Both the FWHM and the resolution at -40 dB cease to be constant at these depths. Even when the number of channels is restricted to $N_{2nd} = 63$ the performance of SASB is superior to DRF.

IV. MEASUREMENT RESULTS

A commercial scanner and a linear array transducer with parameters similar to the ones in Table I have been used to acquire data. A tissue phantom with wire targets and 0.5 dB/MHz/cm attenuation is used as imaging object. RF-data using DRF and 1st stage SASB is acquired with a 5 MHz center frequency and stored. 2nd stage SASB processing, envelope detection, and logarithmic compression is done off-line for both DRF and SASB. An envelope image of the acquired 1st stage SASB data is shown in Fig. 29. It resembles the shape of the contours shown in Fig. 6 as expected. Notice the arcs are turned upside down before and after the focal point at 20 mm. A side by side comparison between the DRF image and the SASB image is also shown in Fig. 29. With DRF the transmit focal point is at 65 mm, and with SASB the VS is at 20 mm $F\# = 2$.

The images based on measured data confirms the results from the simulations. At the center of the image the resolution of SASB is superior to DRF and is practically range independent. A zoom in on the PT at 69 mm for the DRF and SASB images from Fig. 29 is shown in Fig. 30. Here the difference in resolution is prominent. The resolution in the near field is slightly better for DRF as stated in Section III.B.3 and in Fig. 28.

Artifacts at the transducer edges occur for both DRF and SASB but are more profound for SASB and especially at greater depths. The speckle pattern is present at a greater range in the SASB image compared to the DRF image indicating greater penetration.

At greater depths the emitted wave field in SASB is wide compared to DRF. The intensity is lower and so is the SNR of the 1st stage SASB-data. The SNR increases because of the summation of a number of LRL's. Provided that the image object does not move in between acquisitions and assuming uncorrelated electronic noise at the receivers the potential SNR improvement at the center HRL compared to 1st stage RF-data is

$$\Delta SNR(z) = 10\log_{10}\left(\sum_{k}^{K(z)} \mathcal{W}(x_k, z)\right). \tag{15}$$

The signal to noise ratio as a function of depth for a set of acquired DRF-data and a set of 1st stage SASB-data has been estimated, and is shown in Fig. 31. For DRF the transmit focus is at 45 mm and for SASB the VS is at 20 mm with $F\# = 2$. 20 data sets have been acquired for both DRF and SASB using a tissue phantom with an attenuation of 0.5 dB/[MHz cm]. The signal part is estimated by averaging the measured signals. A set of noise signals is estimated by subtracting the estimated signal part from the measured signals. The SNR is

$$\begin{aligned} SNR(z) &= \frac{\mathcal{E}\{Y(z)\}^2}{\mathcal{E}\left\{[Y(z) - \mathcal{E}\{Y(z)\}]\right\}^2} \\ &\simeq \frac{\left(\frac{1}{M}\sum_{m=1}^{M} y_m(z)\right)^2}{\frac{1}{M}\sum_{m=1}^{M}\left[y_m(z) - \frac{1}{M}\sum_{m=1}^{M} y_m(z)\right]^2}. \end{aligned} \tag{16}$$

$\mathcal{E}$ is the expectation operator. $Y(z)$ denotes the M number of measured data sets, and $y_m(z)$ is the m'th data set. The theoretical potential improvement in SNR, $\Delta SNR(z)$ from (15) is also shown in Fig. 31 with a boxcar and a Hamming window as SA weighting. For $z = 80$ mm the value of $\Delta SNR(z)$ can be calculated using (6) and (5) and is 19 dB. The potential SNR of the SASB is superior to DRF at the entire range and an improvement of 8 dB is realized at a depth of 80 mm.

V. CONCLUSION

The main motivation for SASB is to apply synthetic aperture techniques with a restricted system complexity. The objective is to improve lateral resolution and obtain a more range independent resolution compared to conventional ultrasound imaging.

The SASB method has been investigated using simulations in Field II and by off-line processing of data acquired with a commercial scanner. The parameters which are the most decisive for the performance are the depth of the VS (the focal depth), and the $F\#$ of the VS. The lateral resolution increases with a decreasing $F\#$, but grating lobes arise at a combination of a sparse spatial sampling by the virtual array and wave fields with incident angles beyond a certain limit. It is possible to restrict the range of incident angles by putting a limit to the opening angle of the VS. For a transducer with a pitch of $\Delta = \lambda$ grating lobes are avoided if $F\# \geq 2$. For a phased array transducer with $\Delta = \lambda/2$ grating lobes are avoided if $F\# \geq 1$.

Simulations have been done with two different pulse-echo responses having different bandwidths. The performance difference between the two simulation models is significant. The lateral resolution is significantly better for the simulation model with the longer pulse-echo response and the improvement is at least a factor of 2 at -40 dB. With a longer pulse-echo response the off-center HRL is composed of the sum of several positive and negative half-periods of the LRL's and on average sum destructively to a zero level. This is not the case for a short pulse-echo response. Here the off-center HRL is composed of the sum of a only a few positive and negative half-periods and, thus, sum less destructively.

The performance of SASB with the VS at 20 mm and $F\# = 1.5$ is compared with conventional dynamic receive focusing (DRF). The axial resolution is the same for the two methods. There is an substantial improvement in lateral resolution using SASB compared to DRF. It accounts for both the FWHM and the resolution at -40 dB. The improvement in FWHM is at least a factor of 2 and the improvement at -40 dB is at least a factor of 3. The improvement of SASB over DRF is a reality except for a few exceptions. At depths until 20 mm the FWHM is superior with DRF. With SASB the resolution is almost constant throughout the range. For DRF the FWHM increases almost linearly with range and the resolution at -40 dB is fluctuating with range. By putting restrictions on the number of 2nd stage beamformer channels the system complexity is reduced. It will have a negative consequence on resolution since the synthesized aperture decreases, but even when the number of channels is restricted to $N_{2nd} = 63$ the performance of SASB is still superior to DRF.

SASB has been applied to data acquired with a commercial scanner and a tissue phantom with wire targets. The images confirms the results from the simulations. At the center of the image the resolution of SASB is superior to DRF and is practically range independent. The resolution in the near

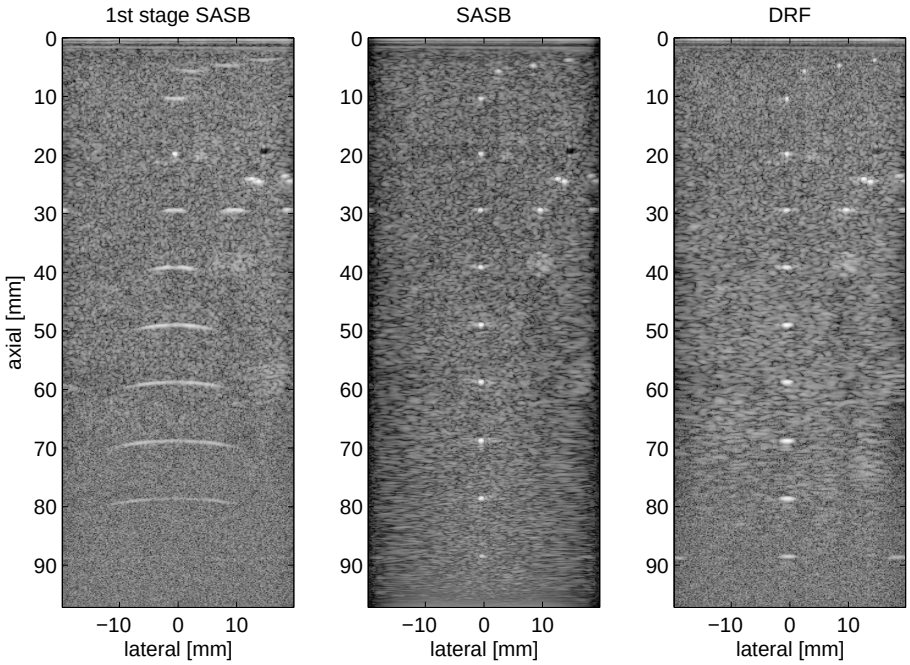

FIG. 29. Envelope images using 1st stage SASB (left), SASB (center), and DRF (right). RF-data is acquired using a commercial scanner, and processing is done off-line. For DRF the transmit focal point is at 65 mm. For SASB the VS is at 20 mm and $F\# = 2$. Dynamic Range is 60 dB.

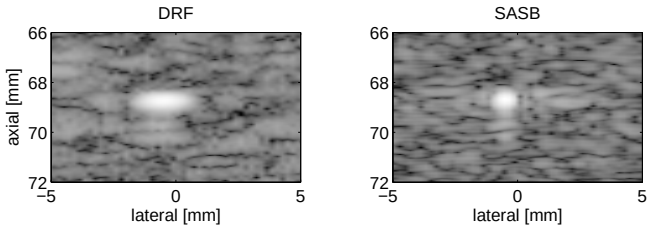

FIG. 30. A zoom in on the DRF and SASB images from Fig. 29.

field is slightly better for DRF. A feasible solution could be to construct the final image by applying DRF above the VS and SASB beyond the VS.

A decrease in performance at the transducer edges occur for both DRF and SASB. They are more profound for SASB and especially at greater depths it is obvious that the lateral resolution is laterally dependent. A solution could be to apply DRF at the edges as a supplement to SASB.

The speckle pattern is present at a greater range in the SASB image compared to the DRF image indicating greater penetration. The signal to noise ratio as a function of depth for a set of acquired DRF-data and a set of 1st stage SASB-data has been estimated. The theoretical potential improvement in SNR of SASB over DRF has been estimated based on the measured SNR data and an assumption of a stationary image object, and a correct phase-alignment in the 2nd stage beamformer. The improvement is attained at the entire range and at a depth of 80 mm the improvement is 8 dB.

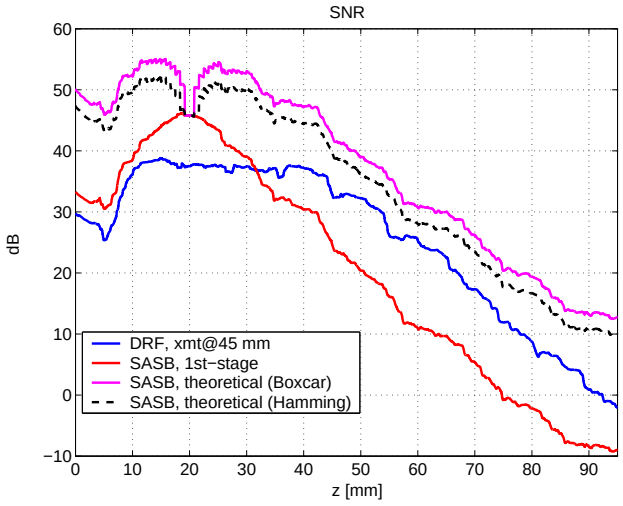

FIG. 31. Estimated SNR as a function of depth. Data sets are acquired with a commercial scanner and a tissue phantom for both DRF (blue) and 1 stage SASB (red). The theoretical SNR of the 2nd stage SASB is also shown with and without the SA-weighting (black and magenta).

Acknowledgments

This work was supported by grant 9700883, 9700563 and 26-04-0024 from the Danish Science Foundation and by B-K Medical, Denmark.

[1] L. J. Cutrona, W. E. Vivian, E. N. Leith, and G. O. Hall. A

high resolution radar combat-surveillance system. *IRE Trans. Mil. Elect.*, MIL-5(2):127–131, 1961.

[2] C. W. Sherwin, J. P. Ruina, and D. Rawcliffe. Some early developements in synthetic aperture radar systems. *IRE Trans. Mil. Elect.*, MIL-6(2):111–115, 1962.

[3] J. C. Curlander and R. N. McDonough. *Synthetic Aperture Radar: Systems and Signal Processing*. John Wiley & Sons, Inc., 1991.

[4] M. Karaman, P. C. Li, and M. O'Donnell. Synthetic aperture imaging for small scale systems. *IEEE Trans. Ultrason., Ferroelec., Freq. Contr.*, 42:429–442, 1995.

[5] R. Y. Chiao, L. J. Thomas, and S. D. Silverstein. Sparse array imaging with spatially-encoded transmits. In *Proc. IEEE Ultrason. Symp.*, pages 1679–1682, 1997.

[6] J. T. Ylitalo and H. Ermert. Ultrasound synthetic aperture imaging: monostatic approach. *IEEE Trans. Ultrason., Ferroelec., Freq. Contr.*, 41:333–339, 1994.

[7] M. H. Pedersen, K. L. Gammelmark, and J. A. Jensen. In-vivo evaluation of convex array synthetic aperture imaging. *Ultrasound Med. Biol.*, 33:37–47, 2007.

[8] D. K. Peterson and G. S. Kino. Real-time digital image reconstruction: A description of imaging hardware and an analysis of quantization errors. *IEEE Trans. Son. Ultrason.*, 31:337–351, 1984.

[9] G. R. Lockwood, J. R. Talman, and S. S. Brunke. Real-time 3-D ultrasound imaging using sparse synthetic aperture beamforming. *IEEE Trans. Ultrason., Ferroelec., Freq. Contr.*, 45:980–988, 1998.

[10] C. R. Hazard and G. R. Lockwood. Theoretical assessment of a synthetic aperture beamformer for real-time 3-D imaging. *IEEE Trans. Ultrason., Ferroelec., Freq. Contr.*, 46:972–980, 1999.

[11] M. O'Donnell and L. J. Thomas. Efficient synthetic aperture imaging from a circular aperture with possible application to catheter-based imaging. *IEEE Trans. Ultrason., Ferroelec., Freq. Contr.*, 39:366–380, 1992.

[12] C. Passmann and H. Ermert. A 100-MHz ultrasound imaging system for dermatologic and ophthalmologic diagnostics. *IEEE Trans. Ultrason., Ferroelec., Freq. Contr.*, 43:545–552, 1996.

[13] C. H. Frazier and W. D. O'Brien. Synthetic aperture techniques with a virtual source element. *IEEE Trans. Ultrason., Ferroelec., Freq. Contr.*, 45:196–207, 1998.

[14] S. I. Nikolov and J. A. Jensen. Virtual ultrasound sources in high-resolution ultrasound imaging. In *Proc. SPIE - Progress in biomedical optics and imaging*, volume 3, pages 395–405, 2002.

[15] S. I. Nikolov and J. A. Jensen. 3D synthetic aperture imaging using a virtual source element in the elevation plane. In *Proc. IEEE Ultrason. Symp.*, volume 2, pages 1743–1747, 2000.

[16] M. H. Bae and M. K. Jeong. A study of synthetic-aperture imaging with virtual source elements in B-mode ultrasound imaging systems. In *IEEE Trans. Ultrason., Ferroelec., Freq. Contr.*, volume 47, pages 1510–1519, 2000.

[17] J. Kortbek, J. A. Jensen, and K. L. Gammelmark. Synthetic Aperture Focusing Applied to Imaging Using a Rotating Single Element Transducer. In *Proc. IEEE Ultrason. Symp.*, Oct. 2007 (Accepted).

[18] J. A. Jensen and N. B. Svendsen. Calculation of pressure fields from arbitrarily shaped, apodized, and excited ultrasound transducers. *IEEE Trans. Ultrason., Ferroelec., Freq. Contr.*, 39:262–267, 1992.

[19] J. A. Jensen. Field: A program for simulating ultrasound systems. *Med. Biol. Eng. Comp.*, 10th Nordic-Baltic Conference on Biomedical Imaging, Vol. 4, Supplement 1, Part 1:351–353, 1996b.

[20] J. Kortbek, S. I. Nikolov, and J. A. Jensen. Effective and Versatile software Beamformation Toolbox. In *Proc. SPIE - Medical Imaging - Ultrasonic Imaging and Signal Processsing*, pages 651319,1–10, 2007.

[21] N. Oddershede and J. A. Jensen. Effects influencing focusing in synthetic aperture vector flow imaging. *IEEE Trans. Ultrason., Ferroelec., Freq. Contr.*, 54(9):1811–1825, September 2007.

[22] L. F. Nock and G. E. Trahey. Synthetic receive aperture imaging with phase correction for motion and for tissue inhomogenities - part I: basic principles. *IEEE Trans. Ultrason., Ferroelec., Freq. Contr.*, 39:489–495, 1992.

[23] G. E. Trahey and L. F. Nock. Synthetic receive aperture imaging with phase correction for motion and for tissue inhomogenities - part II: effects of and correction for motion. *IEEE Trans. Ultrason., Ferroelec., Freq. Contr.*, 39:496–501, 1992.

[24] H. Ş. Bilge, M. Karaman, and M. O'Donnell. Motion estimation using common spatial frequencies in synthetic aperture imaging. In *Proc. IEEE Ultrason. Symp.*, pages 1551–1554, 1996.

[25] M. Karaman, H. Ş. Bilge, and M. O'Donnell. Adaptive multielement synthetic aperture imaging with motion and phase aberation correction. *IEEE Trans. Ultrason., Ferroelec., Freq. Contr.*, 42:1077–1087, 1998.

[26] C. R. Hazard and G. R. Lockwood. Effects of motion artifacts on a synthetic aperture beamformer for real-time 3D ultrasound. In *Proc. IEEE Ultrason. Symp.*, pages 1221–1224, 1999.

[27] J. S. Jeong, J. S. Hwang, M. H. Bae, and T. K. Song. Effects and limitations of motion compensation in synthetic aperture techniques. In *Proc. IEEE Ultrason. Symp.*, pages 1759 –1762, 2000.

[28] S. I. Nikolov and J. A. Jensen. K-space model of motion artifacts in synthetic transmit aperture ultrasound imaging. In *Proc. IEEE Ultrason. Symp.*, pages 1824–1828, 2003.

[29] K. L. Gammelmark and J. A. Jensen. Multielement synthetic transmit aperture imaging using temporal encoding. *IEEE Trans. Med. Imag.*, 22(4):552–563, 2003.

[30] K. L. Gammelmark and J. A. Jensen. Duplex synthetic aperture imaging with tissue motion compensation. In *Proc. IEEE Ultrason. Symp.*, pages 1569–1573, 2003.

[31] S. I. Nikolov, K. Gammelmark, and J. A. Jensen. Recursive ultrasound imaging. In *Proc. IEEE Ultrason. Symp.*, volume 2, pages 1621–1625, 1999.

APPENDIX

C

Co-authored Articles

C.1 In-Vivo Vector Velocity Imaging Using Directional Cross-Correlation

This article was published in Journal *Proceedings - IEEE Ultrasonics Symposium*. Conference Title *2006 IEEE Ultrasonics Symposium, Issue Vol.? Page no. 2023-2026; October 2006.*

In-vivo Vector Velocity Imaging Using Directional Cross-Correlation

Iben Kraglund Holfort[1], Jacob Kortbek[1,2] and Jørgen Arendt Jensen[1]

1) Center for Fast Ultrasound Imaging, Ørsted•DTU,
Build. 349, Technical University of Denmark, DK-2800 Lyngby, Denmark.
2) B-K Medical, Mileparken 34, DK-2730 Herlev, Denmark.

***Abstract*— Previous investigations have shown promising results in using the directional cross-correlation method to estimate velocity vectors. The velocity vector estimate provides information on both velocity direction and magnitude. The direction is estimated by beamforming signals along directions in the range $[0°; 180°[$ and identifying the direction that produces the largest correlation across emissions. An estimate of the velocity magnitude is obtained from the spatial shift between signals beamformed along the estimated direction.**

This paper expands these investigations to include estimations of the vector velocities of a larger region by combining the estimations along several scan lines. In combination with a B-mode image, the vector velocities are displayed as an image of the investigated region with a color indicating the magnitude, and arrows showing the direction of the flow.

Using the RASMUS experimental ultrasound scanner, measurements have been carried out in a water tank using a 7 MHz transducer. A 6 mm tube contained the flow and a Danfoss, MAG 3000, magnetic flow meter measured the volume flow. The tube has a parabolic flow profile with a peak velocity of 0.29 m/s. During the experiments fixed beam-to-flow angles at $\{60°, 75°, 90°\}$ have been applied. The images are obtained using a pulse repetition frequency of 15 kHz, and the images contain 33 lines with 60 emissions for each line.

Corresponding to the three fixed beam-to-flow angles, the angle estimates along the center scan line have a bias of $\{-3.9°, -12.8°, -18.1°\}$ and standard deviation of $\{10.0°, 18.2°, 32.2°\}$. The estimates of the velocity magnitude have bias of $\{4.4\%, 8.1\%, -5.4\%\}$ and standard deviation of $\{9.7\%, 14.3\%, 13.4\%\}$ relative to the peak velocity. The amount of in-tube angle estimates in the range of $\pm 10°$ from the true angle are $\{74\%, 77\%, 66\%\}$.

In-vivo measurements are carried out on a human volunteer. These measurements include the common carotid artery and the femoral bifurcation.

I. Introduction

In conventional blood flow estimation, the velocities are dependent on the direction of the emitted beam, as only the axial component of the velocity vector is estimated. The directional cross-correlation method suggested by Jensen in [1]-[2] is capable of estimating the two-dimensional velocity vector. The two-dimensional velocity vector is independent on the beam direction and provides information on the magnitude as well as the direction of the flow.

In this paper, the directional cross-correlation method is investigated. Based on the theory in [1]-[2], a fully automatic velocity vector estimation algorithm is developed and implemented. Experimental investigations are carried out; these include an experimental setup using a water tank with three different fixed beam-to-flow angles and in-vivo. The in-vivo measurements include the common carotid artery and the femoral bifurcation

II. Velocity Vector Estimation

The two-dimensional velocity vector is obtained by estimating flow direction and velocity magnitude separately as described below.

A. Velocity Estimation

The magnitude of the velocity vector is estimated by identifying the spatial shift of a directional signal over time. Beamforming along the estimated flow direction, two directional signals, $g_1(x')$ and $g_2(x')$, are obtained. Assuming laminar flow, the two directional signals are identical, except for a displacement, due to the movement of the blood scatterers.

The spatial shift between the two signals is found by cross-correlating the two signals

$$\begin{aligned} R_{12}(\tau) &= \frac{1}{L}\int_L g_1(x')\, g_2(x'+\tau)\, dx' \quad (1)\\ &= \frac{1}{L}\int_L g_1(x')\, g_1(x' - |\vec{v}|\, T_{prf} + \tau)\, dx' \\ &= R_{11}(\tau - |\vec{v}|\, T_{prf}), \quad (2)\end{aligned}$$

where L is the length of the directional signal, $R_{11}(\tau)$ and $R_{12}(\tau)$ denote the auto-correlation and the cross-correlation functions, respectively. $R_{12}(\tau)$ is a shifted version of the auto-correlation of the signal $g_1(x')$. The auto-correlation function normally peaks at $\tau = 0$, but due to the subtraction of the term $|\vec{v}|\, T_{prf}$, R_{11} reaches its maximum at $\tau_{peak} = |\vec{v}|\, T_{prf}$. Thus, the magnitude of the velocity vector is found by identifying the lag corresponding to the maximum peak

$$\tau_{peak} = \arg\max_{\tau}\{R_{12}(\tau)\}. \quad (3)$$

The magnitude of the velocity along the flow direction is then

$$|\vec{v}| = \frac{\tau_{peak}}{T_{prf}}, \quad (4)$$

where T_{prf} is the pulse repetition interval.

B. Angle Estimation

The direction of the flow is obtained by estimating the beam-to-flow angle, θ. Based on an assumption of laminar flow, the flow direction provides the largest amount of correlation between the two directional signals. The amount of correlation can be quantified by the correlation coefficient. Let $g_1(x')$ and $g_2(x')$ denote the two directional signals beamformed along the direction, ϕ. By denoting the mean values of each of the signals, μ_1 and μ_2, the correlation coefficient can be estimated by [3]

$$\rho = \max \left\{ \frac{R_{12}(\tau) - \mu_1\mu_2}{\sqrt{[R_{11}(0) - \mu_1^2][R_{22}(0) - \mu_2^2]}} \right\}, \qquad (5)$$

where $R_{11}(0)$ and $R_{22}(0)$ denote the auto-correlation functions at lag 0, and $R_{12}(\tau)$ is the cross-correlation function given by (1). The auto- and cross-correlation functions in (5) are obtained along the direction ϕ.

By beamforming directional signals at angles $\phi \in [0°; 180°[$, the angle estimate can be found from the largest correlation

$$\hat{\theta}_d = \arg\max_{\phi}\{\rho(\phi)\}, \qquad (6)$$

where $\hat{\theta}_d$ is the discrete estimated beam-to-flow angle.

To improve the accuracy of the discrete estimate, $\hat{\theta}_d$, is interpolated using the following expression

$$\hat{\theta} = \hat{\theta}_d - \frac{\rho(\hat{\theta} + \Delta\phi) - \rho(\hat{\theta} - \Delta\phi)}{2(\rho(\hat{\theta} + \Delta\phi) - 2\rho(\hat{\theta}) + \rho(\hat{\theta} - \Delta\phi))}\Delta\phi \qquad (7)$$

where $\Delta\phi$ is the angular distance between two consecutive beamform angles.

III. Measurements

To validate the implemented velocity vector algorithm, a set of measurements have been carried out using the experimental ultrasound scanner, RASMUS [4]. The standard parameters for all measurements are stated in Table I.

A. Experimental Setup

An experimental setup uses a water tank with a tube as illustrated in Fig. 1. The transducer is placed at a fixed beam-to-flow angle, θ, within the water tank. The tube is connected to a pump, and the volume flow rate of the fluid is controlled by a valve and registered by a Danfoss MAG 1100 flow meter. The flow is assumed to be laminar and have a parabolic flow profile, which is characterized by [5]

$$v(z') = v_0 \left(1 - \left(\frac{z'}{R}\right)^2\right), \quad z' \in [-R; R] \qquad (8)$$

where z' denotes the direction perpendicular to the flow direction, R is the radius of the vessel and v_0 is the peak velocity in the center of the vessel. v_0 is determined by the chosen volume flow rate of the pump.

Measurements are carried out using the three beam-to-flow angles, $\theta = \{60°, 75°, 90°\}$, where $\theta = 90°$ is transverse flow.

Type	Linear array
Center frequency, f_0	7 MHz
Pitch of transducer element	208 μm
Height of transducer element	4.5 mm
Kerf	35 μm
Elevation focus	25 mm
Number of transducer elements	128
Apodization, Transmit/Receive	Hamming/None
Number of elements, Transmit/Receive	64 / 64
Excitation pulse, $e(t)$	$\sin(2\pi f_0 t)$
Number of excitation periods	2
Sampling frequency, f_s	40 MHz
Pulse repetition frequency, f_{prf}	15 kHz
Speed of sound, c (in water tank/in-vivo)	1485 m/s / 1540 m/s
Wavelength, $\lambda = c/f_0$ (in water tank/in-vivo)	212 μm / 220 μm
Radius of tube, R	6.0 mm
Peak velocity in flow profile, v_0	0.29 m/s
Volume flow rate, Q	60 l/h
Beam-to-flow angles, θ	$\{60°, 75°, 90°\}$
Depth of focus point, z_f	$\{56, 44, 36\}$ mm
f-number, $f_\#$	$\{4.2, 3.3, 2.7\}$

TABLE I

STANDARD PARAMETERS USED IN THE CONDUCTED MEASUREMENTS.

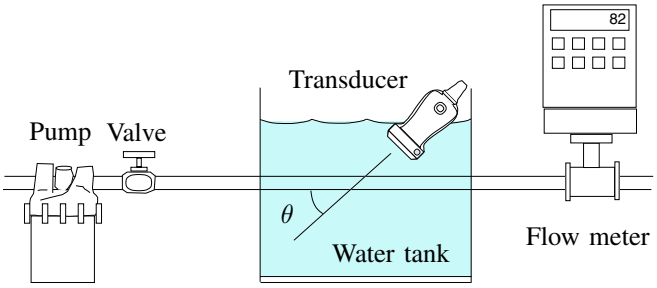

Fig. 1. Illustration of the experimental setup. From [6].

B. Measurement Sequence

The measurements have been carried out using 64 active elements, which are both transmitting and receiving. These 64 elements obtain data, which provides information for one scan line. To obtain data for a full image, the active part of the aperture is displaced along the lateral direction. A total of 33 scan lines with 60 emissions for each line have been acquired resulting in a frame rate of $\simeq 7.5$ Hz.

C. Experimental Validation

The performance of the implemented velocity vector estimation algorithm has been investigated along the center scan line. The performance measures, bias and standard deviation, are stated in Table II. The velocity estimates have been estimated using two different approaches; along the fixed direction, θ, and along the estimated direction, $\hat{\theta}$.

Along the fixed direction, the velocity estimation demonstrates a very satisfying performance for all three test angles, including transverse flow. A decrease in performance, especially for the transverse flow, is identified, when estimating the velocities along the estimated directions. This decrease is a direct consequence of the performance of the angle estimates. Thus, the fully automatic velocity vector estimation algorithm

is limited by the performance of the angle estimation.

Vector flow images have been produced. The velocity vector estimates are visualized using a color to display the magnitude, and an arrow pointing in the direction of the flow. The arrows are scaled by the magnitude of the velocity.

In Fig. 2, the vector flow image of the $\theta = 75°$ measurement is shown. The intensity of the colors and the scaling of the arrows indicate a parabolic flow profile. The general direction of the flow is easily recognized. The distribution of the estimated angles have been investigated. The percentages within $\theta \pm 10°$ are stated in Table III. For all three test angles, the majority of the angle estimates fall within this interval.

θ	60°	75°	90°
Velocity estimates along fixed angles			
B_v	4.39%	8.09%	−5.41%
σ_v	9.66%	14.27%	13.40%
Velocity estimates along estimated angles			
B_v	−3.70%	−11.29%	−25.55%
σ_v	15.12%	18.46%	33.21%
Angle estimates			
B_θ	−3.91°	−12.82°	−18.11°
σ_θ	10.03°	18.24°	32.24°

TABLE II

BIAS AND STANDARD DEVIATION FOR THE VECTOR VELOCITY ESTIMATION ALGORITHMS ALONG THE CENTER SCAN LINE. UNITS ARE IN % RELATIVE TO THE PEAK VELOCITY, v_0, OR IN DEGREES.

θ	60°	75°	90°
$P(\hat{\theta} \in \theta \pm 10°)$	74.33%	77.35%	66.03%

TABLE III

PERCENTAGE OF IN-TUBE ANGLE ESTIMATES WITHIN $\theta \pm 10°$.

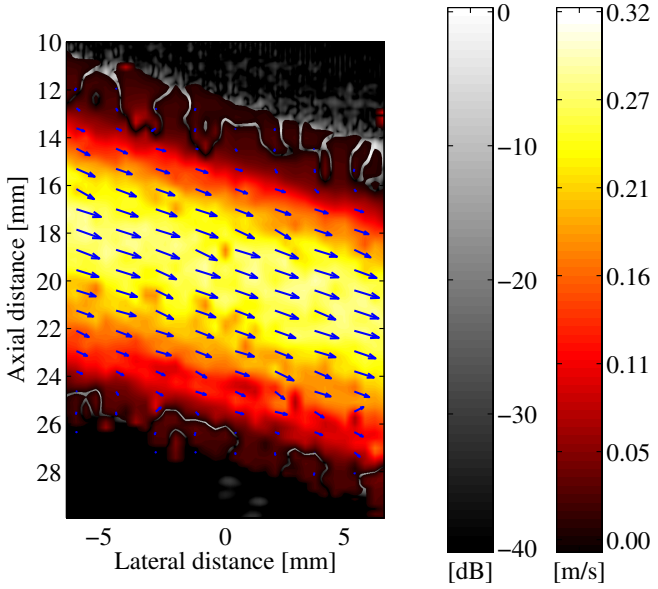

Fig. 2. Vector flow image of the $\theta = 75°$ measurement.

IV. IN-VIVO MEASUREMENTS

Measurements have been carried out on a human volunteer. All measurements are from a healthy 25-year-old female volunteer. The measurements have investigated the blood flow in the common carotid artery and the femoral bifurcation.

Prior to the in-vivo blood flow measurements, the intensities of the actual measurement sequence have been measured. This is a requirement to accommodate the restriction [7] set by the U.S. Food and Drug Administration (FDA). The measured intensities are $I_{spta.3} = 39$ mW/cm^2, $I_{sppa.3} = 9$ W/cm^2 and $MI = 0.14$, which all are well within FDA limits.

For each of the measurements, a sequence of 28 vector flow images have been acquired. These have been combined into movies visualizing the pulsating blood flow in the two arteries. In the following, two single frames from the two movies are shown.

A. Common Carotid Artery

The two vector flow images, Fig. 3, visualize the blood flow in the common carotid artery. In both vector flow images, the general direction of the flow is easily recognized, and the velocities fall in the range of $[0; 0.5]$ m/s.

To estimate the cardiac cycle, the variation of the mean velocity as shown in Fig. 4 is investigated. Each point represents a frame in the acquired sequence. The peak systoles are easily recognized. However, due to the sparse representation, the peak systoles cannot be regarded as more than indications. As a consequence, the first peak has not been acquired. This peak is indicated by the dashed curve.

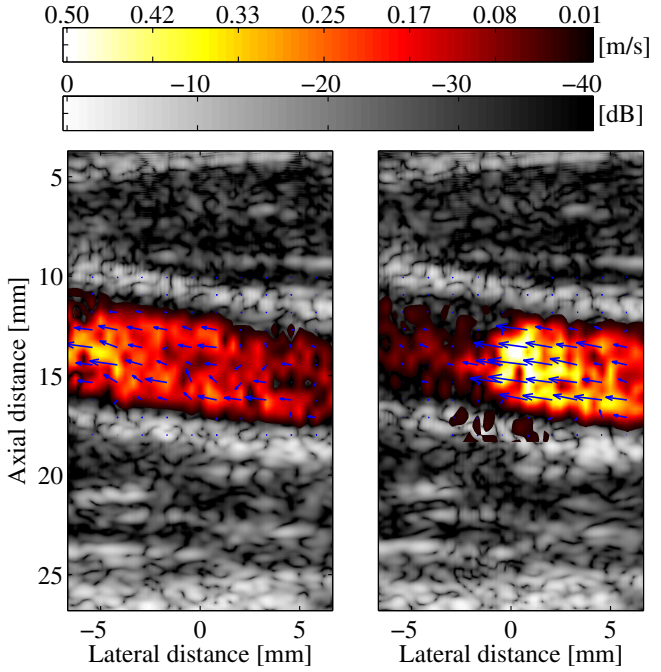

Fig. 3. Vector flow images of the blood flow in the common carotid artery. The two images correspond to peak systoles in the cardiac cycle, and they are acquired at $t = 0.54$ s (left) and $t = 1.74$ (right).

Based on the estimated cardiac cycle, a heart rate of 89.5 bpm is estimated from the time difference between two peaks. Again, due to the sparse representation, the heart rate is merely a rough estimate. The resting normal heart rate is 60-80 bpm [8]. The measured rate is somewhat high, which could be due to stress during the measurement sequence.

The mean blood flow velocity during the systole and diastole in the greater arteries is in the range of 5-18 cm/s [8]. The temporal mean velocity during the entire cardiac cycle is 9.7 cm/s and indicated by the horizontal dashed line in Fig. 4.

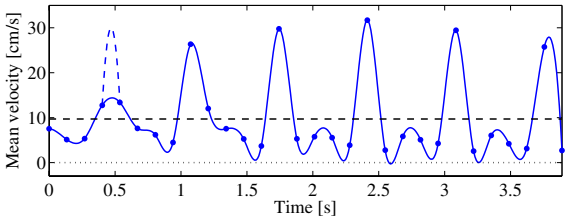

Fig. 4. Variation of the mean velocity in the common carotid artery.

B. Femoral Bifurcation

The estimated blood flow in the femoral bifurcation is visualized by the two vector flow images in Fig. 5. In general, the estimated mean velocities in the femoral arteries are somewhat lower than in the common carotid artery. There are several explanations for this phenomenon, e.g., the reduction of the hydrostatic pressure in the vessels due to a supine position of the test subject.

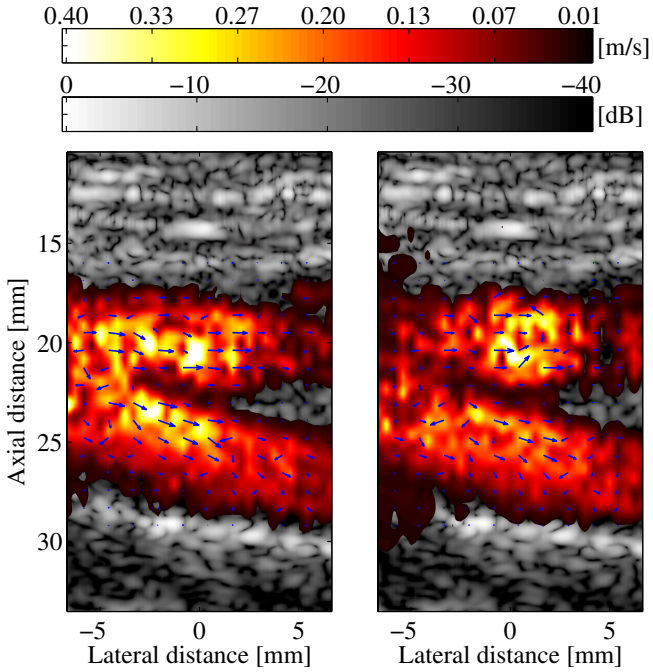

Fig. 5. Vector flow images of the blood flow in the femoral bifurcation. The two images correspond to peak systoles in the cardiac cycle.

The estimated direction of the flow is not as distinct as in the previous measurement. The majority of the angle estimates indicate the direction of the flow from the bifurcation point into the two branches. However, several angle estimates are not consistent with the assumed flow direction. Especially in the deep branch, the angle estimates appear underestimated.

In [9], investigations of the blood flow in the carotid bifurcation using the Transverse Oscillation method have shown a turbulent flow pattern at the bifurcation point and in the internal carotid artery. The turbulent behavior is not evident in Fig. 5. However, this could explain the less distinct flow direction.

V. Conclusions

Based on the theory of the directional cross-correlation method, a fully automatic velocity vector estimation algorithm has been developed and implemented in Matlab. The algorithm has been validated against measurements using an experimental setup. The validation has provided satisfying performance measures. In-vivo measurements have been carried out on a human volunteer for the common carotid artery and the femoral bifurcation. Based on these measurements, vector flow images and movies have been produced.

Acknowledgment

This work was supported by grant 9700883, 9700563 and 26-04-0024 from the Danish Science Foundation and by B-K Medical A/S.

References

[1] J. A. Jensen. Directional velocity estimation using focusing along the flow direction: I: Theory and simulation. *IEEE Trans. Ultrason., Ferroelec., Freq. Contr.*, pages 857–872, 2003.

[2] J. A. Jensen. Velocity vector estimation in synthetic aperture flow and B-mode imaging. In *IEEE International Symposium on Biomedical imaging from nano to macro*, pages 32–35, 2004.

[3] J. S. Bendat and A. G. Piersol. *Engineering Applications of Correlation and Spectral Analysis*. John Wiley & Sons, New York, 2nd edition, 1993.

[4] J. A. Jensen, O. Holm, L. J. Jensen, H. Bendsen, S. I. Nikolov, B. G. Tomov, P. Munk, M. Hansen, K. Salomonsen, J. Hansen, K. Gormsen, H. M. Pedersen, and K. L. Gammelmark. Ultrasound research scanner for real-time synthetic aperture image acquisition. *IEEE Trans. Ultrason., Ferroelec., Freq. Contr.*, 52 (5):881–891, May 2005.

[5] J. A. Jensen. *Estimation of Blood Velocities Using Ultrasound: A Signal Processing Approach*. Cambridge University Press, New York, 1996.

[6] J. A. Jensen and R. Bjerngaard. Directional velocity estimation using focusing along the flow direction: II: Experimental investigation. *IEEE Trans. Ultrason., Ferroelec., Freq. Contr.*, pages 873–880, 2003.

[7] FDA. Information for manufacturers seeking marketing clearance of diagnostic ultrasound systems and transducers. Technical report, Center for Devices and Radiological Health, United States Food and Drug Administration, 1997.

[8] A. Despopoulos and S. Silbernagl. *Color Atlas of Physiology*. Thieme, 1986.

[9] J. Udesen. *2-D blood vector velocity estimation using a phase shift estimator.* PhD thesis, Ørsted•DTU, Technical University of Denmark, 2800, Lyngby, Denmark, 2005.

C.2 In Vivo Vector Flow Imaging Using Improved Directional Beamforming

This article was published in Journal *Proceedings - IEEE Ultrasonics Symposium*. Conference Title *2007 IEEE Ultrasonics Symposium, Issue Vol.? Page no. 2438-2441; October 2007.*

In Vivo Vector Flow Imaging Using Improved Directional Beamforming

Lasse Henze[1], Iben Kraglund Holfort [1], Jacob Kortbek [12], Kristoffer Lindskov Hansen[3] and Jørgen Arendt Jensen[1]

1) Center for Fast Ultrasound Imaging, Ørsted•DTU, Bldg. 348,
Technical University of Denmark, DK-2800 Kgs. Lyngby, Denmark
2) B-K Medical, Mileparken 34, 2730 Herlev, Denmark
3) University hospital of Copenhagen, Rigshospitalet Blegdamsvej 9, DK-2100 Copenhagen

***Abstract*— Directional beamforming has shown promising results for creating vector flow images. The method measures both the flow angle and the magnitude of the velocity. The flow angle is estimated by focusing lines in a range of angles from 0 to 180 degrees. The true angle is identified as the angle that produces the largest correlation coefficient across emissions. The magnitude of the velocity is found by cross-correlating consecutive lines focused along the direction of flow, to find the spatial shift corresponding to the velocity. In initial in vivo experiments, the method has however shown weaknesses by yielding outliers when a substantial clutter signal is present after clutter filtering. This is especially a problem when the flow angle is close to 90 degrees as the slow time frequencies from the flow signal is similar to that of the clutter, making clutter filtration difficult. When the angle determination fails, the correct velocity can no longer be found. The purpose of this work is to improve the robustness of the directional beamforming method, making precise in vivo measurement possible. A more robust angle estimator is proposed. Spatial averaging in the axial direction is applied over a depth of 2 wavelengths. Instead of traditionally beamforming a single line, three lines are beamformed with an interline distance of a wavelength. To improve clutter filtering a post correlation clutter filter is applied, by removing peaks in the correlation functions corresponding to low velocities, since these peaks are believed not to be a result of the measured flow. The method has been tested on a flow phantom, using the RASMUS experimental scanner. The flow had a parabolic velocity distribution with a peak velocity of 0.1 m/s, and a flow angle of 90 degrees. The measurement were made with a 6.2 MHz linear array transducer, using 30 emissions and 128 transducer elements for each estimate. Using the same measurement setup, an initial in vivo study has been carried out. The measurements have been performed on the carotid artery of 11 human volunteers. To validate the method MR angiography has been performed on all human volunteers as a gold standard. For the phantom measurement 76.30 % of the angle estimates are within +- 5 degrees of the actual angle, when using the traditional setup. Using our new approach 98.32 % of the angle estimates are within +-5 degrees from the true angle. The comparison between the stroke volume measurements in the carotid artery calculated using directional beamforming and MR angiography, gives a correlation coeficient of 0.84. Phantom and in vivo measurements has been carried out with a more robust implementation of the directional beamforming method. With the applied changes, the method has shown improved results for in vivo measurements.**

I. Introduction

In traditional ultrasonic velocity estimation systems, only the axial velocity component is estimated. So to find the absolute velocity, the beam to flow angle must be found. The absolute velocity is an important clinical parameter, so the ability to measure it accurately is of great value. Jensen [1] suggested to cross-correlate lines beamformed in the flow direction, to directly measure the magnitude of the velocity vector. The method performs well, even for pure transverse flow, but needs a priori knowledge of the flow angle. To find the flow angle Kortbek and Jensen [2] suggested to beamform lines in a range of directions, from 0 to 180 degrees, and then search for the direction with the largest correlation over time. It was shown in simulations and phantom measurements that the method was capable of finding both the correct flow angle and velocity magnitude using few emissions. However when Holfort [3] performed initial in vivo experiment is was shown that the angle estimator breaks down when a substantial amount of clutter is present after clutter filtering. When the angle determination fails, the correct velocity can no longer be found. The purpose of this work is to improve the robustness of the angle estimator to enable accurate velocity vector estimation. This is performed by applying spatial averaging, and improving clutter filtering.

II. Methods and materials

A. Angle Estimation

To find the flow angle, directional signals are beamformed in a range from 0 to 180 degrees as shown in Fig 1. The directional signal is given by $S_i(x'_\phi)$, where i is the emission number ϕ is the beam angle, as seen on the figure and x' is the spatial location on the line

The directional signal, corresponding to the true flow angle, for emission i, contains the same blood scatterers, as for emission $i+1$, excepts for the few scatterers that has left the signal in the end or entered at the start. This will make the correlation between consecetive signals high. For the remaining angles, a different distribution of scatters will be examined for each emission, due to the misalignment between the signals and the direction of flow. As a result the correlation will be low. The directional signal corresponding to the true flow angle, can therefore be identified as the signal that produces the largest normalized correlation coefficient over emissions. The correlation coefficient for different angles is calculated using

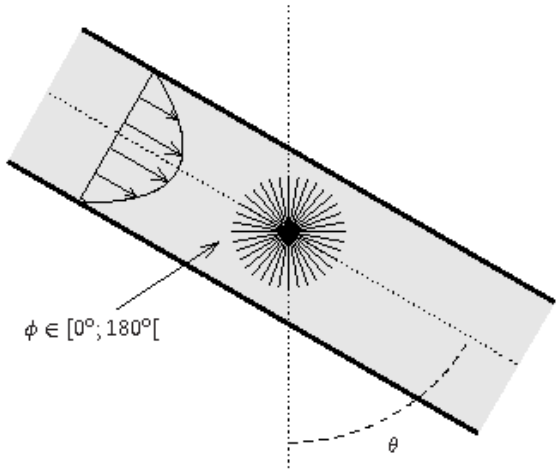

Fig. 1. Setup for the method. Directional signals are beamformed from 0 to 180 degrees at the estimation point. The directional signals are correlated over emissions. The signal with the largest correlation is identified as the direction of flow. When the direction of flow is found, the magnitude of the velocity is found by cross-corelating consecutive signals to find the spatial shift corresponding to the blood velocity.

$$P(\phi) = \max\{\sum_{i=1}^{N-1} C(S_i(x'_\phi), S_{i+1}(x'_\phi))\}, \tag{1}$$

where N is the total number of emissions and C is the normalized correlation coefficient defined by

$$C(a,b) = \frac{R_{ab}(k) - \mu_a\mu_b}{\sqrt{[R_{aa}(0) - \mu_a^2][R_{bb}(0) - \mu_b^2]}}, \tag{2}$$

where R_{ab} is the cross-correlation between signal a and b, μ_a is the mean of a and μ_b is mean of b. The sum in (1) is introduced to perform averaging.

The angle can now be estimated by searching for the largest correlation coefficient,

$$\theta_e = (\arg\max_\phi\{P(\phi)\}) \tag{3}$$

B. Velocity Estimation

When the direction of flow is known, the magnitude of the velocity can be found. Two signals taken from consecutive emissions, beamformed along the direction of flow, is related to each other by a spatial shift x'_s given by

$$S_i(x'_\phi) = S_{i+1}(x'_\phi - 2VT_{prf}) \tag{4}$$

where V is magnitude of the velocity and T_{prf} is the time between emission. The spatial shift is found be locating the peak of the cross-correlation function taken between two consecutive signals.

$$x'_s = \arg\max_k \sum_{i=1}^{N-1} R_{S_iS_{i+1}}(k), \tag{5}$$

The velocity is now given by

$$V = \frac{x'_s}{T_{prf}} \tag{6}$$

For a more in depth description of the basic method see [2]

C. Spatial Averaging

To improve the robustness, spatial averaging is applied on the angle estimator in the axial dimension. The spatial averaging is applied by beamforming three lines for every angle. The three lines are beamformed with in a range of 2 λ. The new angle estimator is give by

$$P(\theta) = \max\{\sum_{j_z=1}^{3}\sum_{i=1}^{N-1} C(S_{i,\theta,(j_z-2)\lambda}(t), S_{i+1,\theta,(j_z-2)\lambda}(t))\}, \tag{7}$$

The length of the directional signals, in the used setup, is 20λ, so the applied spatial averaging will only marginally reduce the spatial resolution of the estimator.

D. Post Correlation Clutter Filtering

To improve clutter filtering, peaks in the correlation function taken in (2) identified to be a product of the clutter is removed. The Directional signals are composed of two major components, one flow component, coming from the blood scatterers and one clutter component, coming from the stationary tissue,

$$S_i(x') = F_i(x') + N(x'), \tag{8}$$

where $F_i(x')$ is the flow component and $N(x')$ is the clutter component. It is assumed that the clutter and blood component is uncorrelated and that the clutter component is stationary over emissions. When the cross-correlation is taken in (2) between two consecutive emissions, it corresponds to the cross-correlation of the flow signal, added with the auto-correlation of the clutter signal

$$R_{S_i(x'),S_{i+1}(x')} = R_{F_i(x'),F_{i+1}(x')} + R_{N(x'),N(x')} \tag{9}$$

It is known from basic signal processing, that the auto-correlation function peaks at lag zero and from (4) it is known that the cross-correlation of the flow signal, for the true angle, peaks at lag $2V\frac{T_{prf}}{c}$. So the post correlation clutter filtering is done by ignoring peaks laying around lag zero in (2).

By doing this, peaks emerging as a result of the clutter is removed, without affecting the true peak coming as a result of the measured flow.

E. Measurements

To test the performance of the method, phantom and in-vivo measurements have been carried out on the experimental ultrasound scanner RASMUS [4]. The parameters used for all measurements can be seen in Table I.

Phantom measurements have been performed on a circulating flow rig as seen on Fig 2. A long tube is connected to a flow pump. The transducer is placed in a fixture, with a known beam to flow angle. An electro magnetic flow meter is placed around the tube to read the flow, as a reference. Measurements has been carried out for a beam to flow angle of 90 degrees.

An transmit focus is placed in double the depth of the tube, to get a wide transmit beam. The vector flow images has been created by measuring 16 flow lines pr image, with an axial spacing of λ between each estimate. 64 elements is used in transmit and 128 elements is used in receive. The used scanner has access to 128 channels, so a sliding aperture can only be achieved in transmit. To avoid tilting of the point spread function, a boxcar apodization is applied in receive to force a symmetric receive aperture.

The in-vivo measurements have been carried out on the carotid artery of 11 healthy human volunteers. To validate the method MR angiography has been performed on all 11 volunteers as an gold standard. To enable a comparison, the volume flow over a heart cycle has been calculated. The volume flow has been calculated using the assumption of rotational symmetry. All in-vivo measurements has been performed by an experienced medical doctor.

Prior to the in-vivo measurements, the intensities of the transmit setup have been measured using a hydrophone. All measured intensities where below the limits set by the U.S Food an Drug Administration [5].

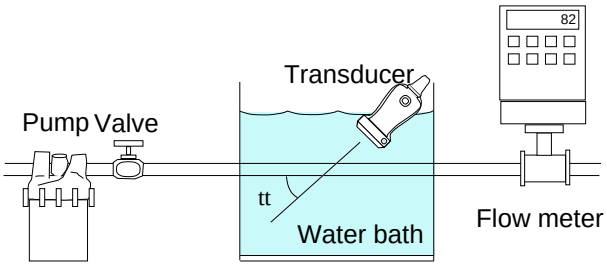

Fig. 2. Setup of the used flowrig. A pump secures a steady parabolic flow in the tube. A fixture holds the transducer at a known beam to flow angle. An electro magnetic flow meter measures the volume flow as a reference.

III. Experimental Results

A. Phantom Measurements

The top graph in Fig. 3 shows the angle estimates, for the phantom measurement, calculated using the traditional setup. Angle estimates from 10 images each containing 16 flow lines are plotted. 76.3 % of the estimates are within $\pm$ 5 % from the correct angle. The angle estimates, at the side of the tube, are slightly worse than the estimates in the middle. The method performs best on the central flow lines. This is because they have the largest recieve aperture.

The bottom of Fig.3 shows angle estimates, calculated with the improvements. 98.32 % of the estimates are with in $\pm$ 5 % from the correct angle. A slight worsenning of the estimates can again be observed at the side of the tube, but not to the same extend as in the top figure. A fairly even performance is observed over the individual flow lines. Using the improvements a satisfactory result is optained for the phantom measurements.

TABLE I
Standard parameters For Phantom and In-vivo measurements

Type		Linear array
Transducer center frequency	f_0	7 MHz
Wavelength	λ	0.22 mm
Pitch of transducer elements	w	0.208 mm
Height of transducer elements	h_e	4.5 mm
Kerf	ke	0.035 mm
Number of active elements(receive/transmit)	N_e	128/64
Apodization(receive/transmit)		Boxcar/Hanning
Number of excitation periods		2
Elevation focus	R_e	25 mm
Radius of tube	R	6 mm
Peak velocity in flow profile	v_0	0.15 m/s
Beam to flow angles	θ	90°
RF lines for estimation	N	32
Length of directional signals		20 λ
Sampling frequency	f_s	40 MHz
Number of oscillations	N_o	2
Speed of sound	c	1480/1540 m/s

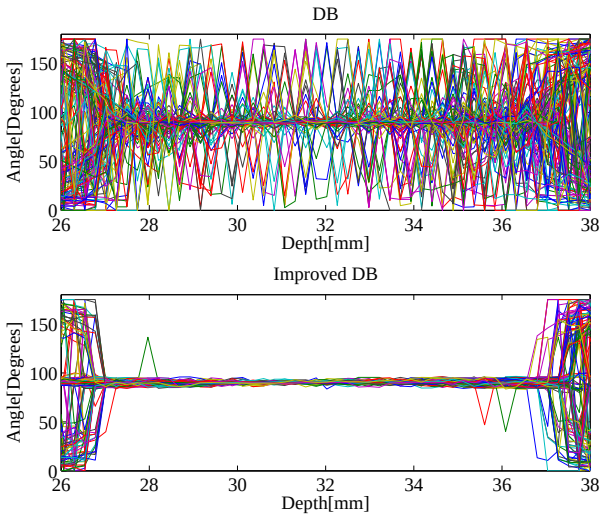

Fig. 3. Angle estimates from the phantom measurements, for a beam to flow angle of 90 degrees. The top figure shows the estimates calculated with a direct implementation of Directional beamforming. The bottom figure shows the estimates calculated with the improved version of Directional beamforming.

B. In-vivo Measurements

The top of Fig 4 shows a velocity vector image of the common carotid artery and jugular vein, calculated using the traditional setup. The brightness of the color and the length of the arrows, shows the magnitude of the velocity and the direction of the arrows shows the flow angle. The main direction of flow in the artery and vein can be observed, but the image is dominated by errors.

The bottom of Fig 4 shows, for the same frame as the top of the figure, a velocity vector image, calculated using the new method. A more believable result is obtained and only few estimates can visually be determined to be errors.

Fig 5 shows the regression line for stroke volume, estimated using Directional beamforming and MR angiography. The MR measurements directly measures the volume flow, where as the ultrasound measurements is based on the assumption of a rotational symmetric velocity field. The vertical line on each of the data points, show the possible distribution of volume flow estimates, if the MR measurements where based on the same assumptions as the ultrasound measurements. The correlation coefficient is calculated to be 0.84, with a 95 % confidence interval from 0.49 to 0.96.

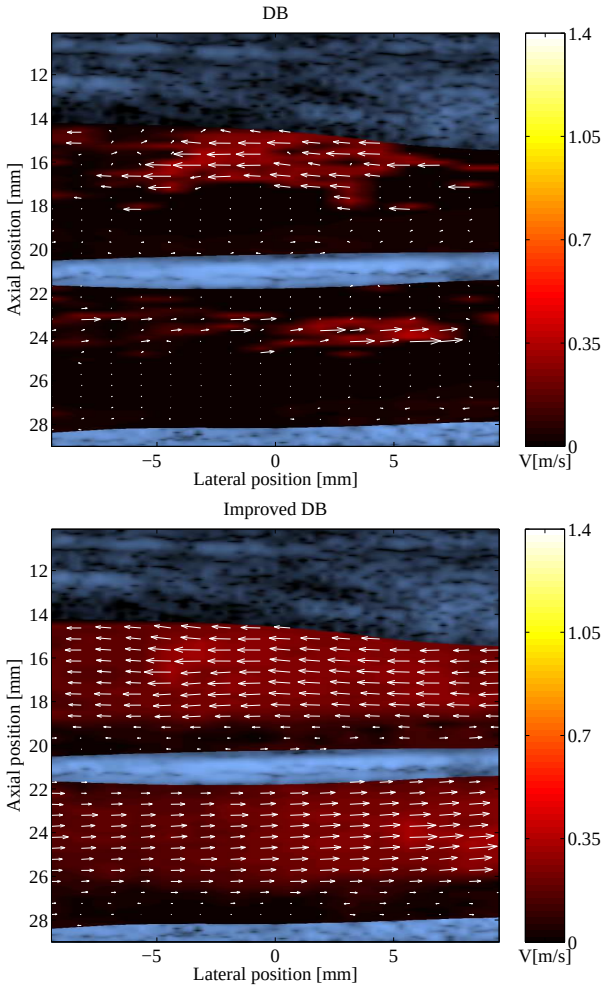

Fig. 4. In vivo scan of the carotid artery and jugular vein. The top figure shows the estimates calculated with a direct implementation of Direction beamforming. The bottom figure shows the estimates calculated with the improved version of Direction beamforming.

IV. Conclusion

A more robust version of Directional beamforming has been implemented. The method has been tested in circulating flowrig. 11 successful in vivo measurements have been carried out. MR angiography has been performed as a reference. A corelation coefficient of 0.84 has been achieved for stroke volume estimated using MR and ultrasound. The preliminary results look encouraging for further research.

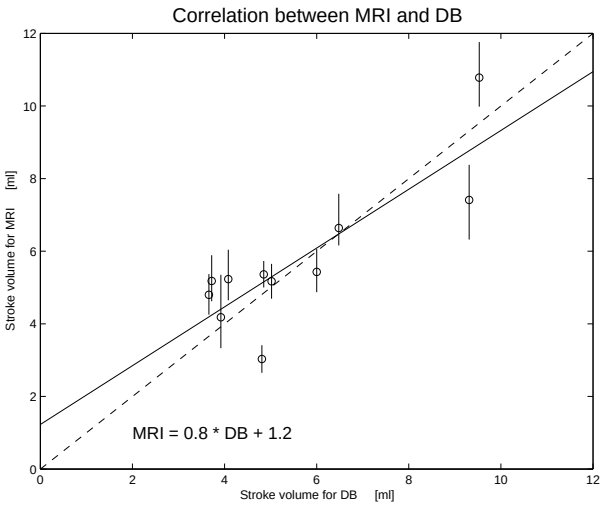

Fig. 5. Regression line for volume flow estimated with MR and ultrasound. The vertical line on each of the data points shows the uncertainty of the ultrasound estimates, due to the assumption of rotational symmetry.

V. Acknowledgment

This work was supported by the Faculty of Health Science, University of Copenhagen, by grant 274-05-0327 from the Danish Research Agency, the Radio-parts foundation and by B-K Medical A/S, Denmark.

References

[1] J. A. Jensen, "Directional velocity estimation using focusing along the flow direction: I: Theory and simulation," *IEEE Trans. Ultrason., Ferroelec., Freq. Contr.*, pp. 857–872, 2003.

[2] J. Kortbek and J. A. Jensen, "Estimation of velocity vector angles using the directional cross-correlation method," *IEEE Trans. Ultrason., Ferroelec., Freq. Contr.*, vol. 53, pp. 2036–2049, 2006.

[3] I. K. Holfort, J. Kortbek, and J. A. Jensen, "In-vivo Vector Velocity Imaging Using Directional Cross-Correlation," in *Proc. IEEE Ultrason. Symp.*, Oct. 2006, pp. 2023–2026.

[4] J. A. Jensen, O. Holm, L. J. Jensen, H. Bendsen, S. I. Nikolov, B. G. Tomov, P. Munk, M. Hansen, K. Salomonsen, J. Hansen, K. Gormsen, H. M. Pedersen, and K. L. Gammelmark, "Ultrasound research scanner for real-time synthetic aperture image acquisition," *IEEE Trans. Ultrason., Ferroelec., Freq. Contr.*, vol. 52 (5), pp. 881–891, May 2005.

[5] FDA, "Information for manufacturers seeking marketing clearance of diagnostic ultrasound systems and transducers," Tech. Rep., Center for Devices and Radiological Health, United States Food and Drug Administration, 1997.